Investigation of magneto-transport properties of Mn4N-based nitrides for efficient current-induced domain wall motion

Taro Komori

THÈSE

Pour obtenir le grade de

DOCTEUR DE L'UNIVERSITÉ GRENOBLE ALPES
et University of Tsukuba

École doctorale : **Physique**
Spécialité : **Nanophysique**
Unité de recherche : Laboratoire Spintronic et Technologie des Composants (**SPINTEC**) et Envirinmentally Frinedly Materials in the Next Generations Lab (**University of Tsukuba**)

Étude des propriétés de magnétotransport des nitrures à base de Mn_4N pour un mouvement efficace de paroi du domaine induit par courant

Investigation of magneto-transport properties of Mn4N-based nitrides for efficient current-induced domain wall motion

Présentée par :

Taro KOMORI

Direction de thèse :

Olivier FRUHCART Directeur de recherche, Université Grenoble Alpes	Directeur ou Directrice de thèse
Takashi SUEMASU Professeur, University of Tsukuba	Co-Directeur de thèse

Rapporteurs :

Yasuhiro NIIMI
Professeur, Osaka University
Florent TOURNUS
Charge de recherche, Université Lyon 1, CNRS

Thèse soutenue publiquement le **30/03/23** devant le jury composé de :

Nora DEMPSEY Directrice de recherche, Institut Néel, CNRS	Examinatrice
Hideto YANAGIHARA Professeur, University of Tsukuba	Président
Laurent RANNO Maitre de conferences, Institut Néel, CNRS	Examinateur
Sébastien PETIT-WATELOT Maitre de conferences, Institut Jean Lamour	Examinateur
Yasuhiro NIIMI Professeur, Osaka University	Rapporteur
Florent TOURNUS Charge de recherche, Université Lyon 1, CNRS	Rapporteur

Titre : titre (en français) Étude des propriétés de magnétotransport des nitrures à base de Mn_4N pour un mouvement efficace de paroi du domaine induit par courant

Mots clés : Mouvement de paroi magnétique / Spintronique / Nitures

Résumé : Le mouvement des parois de domaine induit par courant (CIDWM) est l'un des domaines de recherche les plus importants en spintronique car il peut être appliqué à de nouveaux dispositifs magnétiques tels que les mémoires de type racetrack, etc. Ils sont des technologies attrayantes grâce à leur non-volatilité et leur fonctionnement rapide. Du point de vue de l'ingénierie des matériaux, notre groupe s'est concentré sur les films minces de Mn_4N et $Mn_{4-x}Ni_xN$. Nous avons enregistré des vitesses de paroi de 900 m/s dans Mn_4N, et de 3000 m/s dans $Mn_{4-x}Ni_xN$ au voisinage de sa compensation de moment angulaire (à $x \sim 0,2$) à température ambiante. Ce sont les CIDWM les plus rapides par couples de transfert de spin (STT) purs. Dans ce contexte, nous avons étudié les propriétés magnétiques et de magnéto-transport de ces composés pour comprendre en particulier l'interaction entre les électrons de conduction et les électrons localisés et avons tenté de réaliser des CIDWM pilotés par des SOTs pour un fonctionnement plus efficace.

Le chapitre 1 se concentre sur la théorie du magnétisme et les couples qui induisent le CIDWM. Nous avons également montré l'avantage de la compensation dans les ferrimagnets pour le CIDWM et fait son état de l'art dans la littérature.

Dans le chapitre 2, nous présentons un aperçu du Mn_4N. Tout d'abord, nous expliquons les propriétés fondamentales du Mn_4N et concluons qu'elles sont bénéfiques pour le CIDWM. Ensuite, nous présentons nos expériences de CIDWM dans le Mn_4N et le $Mn_{4-x}Ni_xN$, dans lesquelles nous mettons en évidence le lien entre la vitesse rapide et la compensation du moment angulaire du $Mn_{4-x}Ni_xN$. Nous présentons également les études précédentes et nos propres études sur les composés à base de Mn_4N.

Dans le chapitre 3, nous menons la croissance de films épitaxiaux de Mn_4N sur différents substrats afin d'étudier l'origine de l'anisotropie perpendiculaire (PMA) dans le Mn_4N. Notre étude précédente a abouti à l'hypothèse que la PMA dérive de la contrainte de traction dans le plan du Mn_4N, cependant, cette corrélation n'a pas encore été prouvée. Nous avons réussi à moduler la contrainte de traction par l'épaisseur et le désaccord de maille entre le Mn_4N et le substrat de croissance. Au final, nous avons trouvé une corrélation claire entre la PMA et l'amplitude du rapport des constantes de réseau (c/a).

Dans le chapitre 4, nous étudions les propriétés de magnéto-transport du $Mn_{4-x}Ni_xN$ par de mesures de magnétorésistance anisotrope (AMR) et d'effet Hall anormal (AHE). L'AMR a révélé un changement de l'état des électrons d en fonction de la température, qui diminue avec l'insertion de Ni. Nos calcul ab-initio des PDOSs de $Mn_{4-x}Ni_xN$ a prouvé qu'il dérive d'un changement drastique du niveau de Fermi et du changement du PDOS de Mn même à faible composition de Ni. Nous avons analysé l'AHE et révélé qu'une grande déviation intrinsèque contribue à l'AHE à basse température dans le Mn_4N alors que les diffusions extrinsèques deviennent dominantes à haute température et dans le $Mn_{4-x}Ni_xN$.

Dans le chapitre 5, nous visons la croissance d'hétérostructure de métal lourd (HM) (Pt ou W) et de Mn_4N pour tenter de réaliser un CIDWM piloté par les SOTs à partir de l'effet Hall de spin. Nous avons observé des domaines magnétiques larges et stables dans ces échantillons, cependant, nous avons également constaté que les renversements d'aimantation sont affectés par du piégeage, qui peuvent provenir des conditions interfaciales tels que la formation d'alliage et l'endommagement par le processus de pulvérisation de la couche HM. Nous avons atteint une vitesse de DW de 420 m/s. Cependant, nous n'avons pas pu trouver un effet clair des SOTs sur le CIDWM.

En conclusion, la modulation de la PMA par la contrainte et des propriétés de magnéto-transport par les dopants va élargir les possibilités du Mn_4N. L'utilisation des SOTs pour le Mn_4N sera tentée avec l'aide du champ dans le plan et l'optimisation des hétérostructures.

Title: Investigation of magneto-transport properties of Mn_4N-based nitrides for efficient current-induced domain wall motion

Keywords: Domain wall motion / Spintronics / Nitrides / Ferrimagnetism

Abstract: Current-induced domain wall motion (CIDWM) is one of the most important spintronics research fields because it can be applied to new magnetic devices such as a racetrack memory, spin-transfer majority gate, and so on. They constitute an attractive technology thanks to their non-volatility and fast operation. From material engineering, our group has focused on Mn_4N and $Mn_{4-x}Ni_xN$ films as new candidates for CIDWM. We recorded the DW velocity of 900 m/s in Mn_4N, and 3000 m/s in $Mn_{4-x}Ni_xN$ at the vicinity of its angular momentum compensation (at $x \sim 0.2$) at room temperature. These are the fastest records among CIDWM by pure spin-transfer torques (STTs). In this context, we investigated their magnetic and magneto-transport properties to understand especially the interaction between conduction and localized electrons and attempted to perform SOTs-driven CIDWM for more efficient operation.

Chapter 1 focuses on the theory of magnetism, especially ferrimagnets, and the torques which induce CIDWM. We also showed the advantage of the compensation in ferrimagnets for CIDWM and benchmark CIDWM in the literature.

In chapter 2, we present an overview of Mn_4N and Mn_4N-based compounds. First, we explain the fundamental properties of Mn_4N and concluded that they are beneficial for CIDWM. Then, we present our experiments of CIDWM in Mn_4N and $Mn_{4-x}Ni_xN$, in which we evidence the link between the observed fast DW velocity and the angular momentum compensation of $Mn_{4-x}Ni_xN$. We also introduce previous reports and our own studies on Mn_4N-based compounds and explain the compensation in other nitrides such as $Mn_{4-x}Co_xN$.

In chapter 3, we attempt the growth of Mn_4N epitaxial films on various substrates to investigate the origin of PMA in Mn_4N. Our previous study reached the assumption that its PMA derives from the in-plane tensile strain of Mn_4N, however, this correlation was not been proven yet. We succeeded in the modulation of the tensile strain by the thickness and the lattice mismatch between Mn_4N and the growth substrate. In the end, we found a clear correlation between PMA and the magnitude of the ratio of lattice constants of Mn_4N (c/a). We thereby concluded that PMA derives from the spontaneous in-plane tensile strain of Mn_4N films and that it is possible to control its PMA by applying external stress to films.

In chapter 4, we investigate the magneto-transport properties of $Mn_{4-x}Ni_xN$ from anisotropic magnetoresistance (AMR) and anomalous Hall effect (AHE) measurements. From AMR, we found a change of the d electrons state by temperature, which became less effective with Ni insertion. Our ab-initio calculation of PDOSs of $Mn_{4-x}Ni_xN$ proved that it derives from a drastic shift in the Fermi level and the change in the PDOS of Mn even by small Ni composition. Also, we analyzed the scaling of AHE and discovered that large intrinsic deflection contributes to the AHE in Mn_4N at low temperatures while extrinsic scatterings become dominant at high temperatures or in $Mn_{4-x}Ni_xN$.

In chapter 5, we aim at the growth of the heterostructure of heavy metal (HM) (Pt or W) and Mn_4N to attempt SOTs-driven CIDWM from the spin Hall effect. We observed large and stable magnetic domains in these samples, however, we also found that the magnetization reversals are affected by DW pinnings, which may come from the interfacial condition such as alloying and damaging by the sputtering process of the HM layer. We process them into multiwires for CIDWM investigation and achieved DW velocity of 420 m/s. However, we could not find a clear effect of SOTs on CIDWM. We propose that measurements with an in-plane field should be performed to form chiral Néel DWs, a prerequisite for the use of SOTs by SHE.

To conclude, the modulation of PMA by the strain and of the magneto-transport properties by dopants will broaden the possibility of Mn_4N. The use of SOTs for Mn_4N will be attempted with the assistance of the in-plane field and the optimization of the heterostructure.

Table of Contents

List of Figures

Introduction

After the ARPANET, the predecessor of the Internet, was connected between the University of California, Los Angels and Stanford Research Institute in 1969, the information society showed an incredible growth pace. In 1999, the idea of Internet of Things (IoT) was proposed by Dr. K. Ashton, where all the things are connected to the Internet and they get to control one another by exchanging information. Internet of Humans (IoH) was recently proposed, influenced by IoT to protect the safety of individuals and improve the efficiency of human work through the Internet. The launch of the 5th Generation of Mobile Communication System in 2020 is expected to realize these ideas in our lives.

However, the rapid increase in the amount of data exchange which became more noticeable with the spread of telecommuting due to the pandemic of COVID19 causes various problems. For example, Dynamic Random Access Memories (DRAMs) which play a key role as the main storage in modern computers or mobile devices are volatile. Thus, they always require the supply of electric power to keep the data even when the devices are not in operation, resulting in a huge loss of energy. From the viewpoint of integration, NAND Flash memories, DRAMs, and SRAMs have been further integrated following Moore's law. Nevertheless, they're facing the limit of this law which is attributable to uncontrollable dopants in semiconductors on the nm scale. In this context, the research on non-volatile memories such as Magnetic Random Access Memories (MRAMs) and the integration beyond the limit of Moore's law have been important topics for decades.

In the introduction, we would like to present how spintronics is expected to tackle these problems, especially current-induced domain wall motion (CIDWM). The first section introduces the brief history and achievements of spintronics. The second section will focus on CIDWM and explain why this is the key technology of spintronics to enable more strive of the information society. The third section, in the end, proposes anti-perovskite ferrimagnetic Mn-based nitrides, which we expect as new candidates for CIDWM materials and are the main themes of our work.

Spintronics

Spintronics is nowadays categorized as the research field in which we utilize the features of electric charge and spin angular momentum simultaneously both from fundamental and applications perspectives. Figure 1 shows the chronology of spintronics from the viewpoints of both metals and semiconductors. The birth of spintronics is considered to be set by the discovery of giant magnetoresistance (GMR) by A. Fert and P. Gruberg in 1988 [1], in which the resistivity changes in a ferromagnet (FM)/non-magnet (NM)/FM heterostructure depends on the relative direction of magnetizations in two FMs. In 1998, the magnetic head for hard disc drives (HDDs) got to be the first practical application of GMR. This was replaced by ones based on tunnel magnetoresistance (TMR) [2, 3], in which the larger change in the resistivity is observed in

FM/insulator/FM layers in 2004 [4, 5]. Importantly, in the 2000s, the magnetization reversals induced by spins of conduction electrons became the interest of many groups thanks to the success in the magnetization reversals by spin injection in 1999 [6–8]. The control of magnetizations by current, not by a magnetic field is advantageous for the integration of magnetic devices into wider applications. Focusing on the field of semiconductors, S. Datta and B. A. Das proposed the idea of spin-field effect transistor (FET) in 1990[9]. In spin-FET, the source and drain are made from ferromagnets, and the gate voltage controls the flow of current between them. This device will be advantageous not only thanks to low power consumption but also to the possibility to function as a transistor and memory simultaneously. After that, ferromagnetic semiconductor materials such as (In, Mn)As[10] and (Ga, Mn)As[11] were fabricated. In the 2000s, based on these ideas, control of magnetizations with voltages[12, 13], including with lights[14], was reported by several research groups.

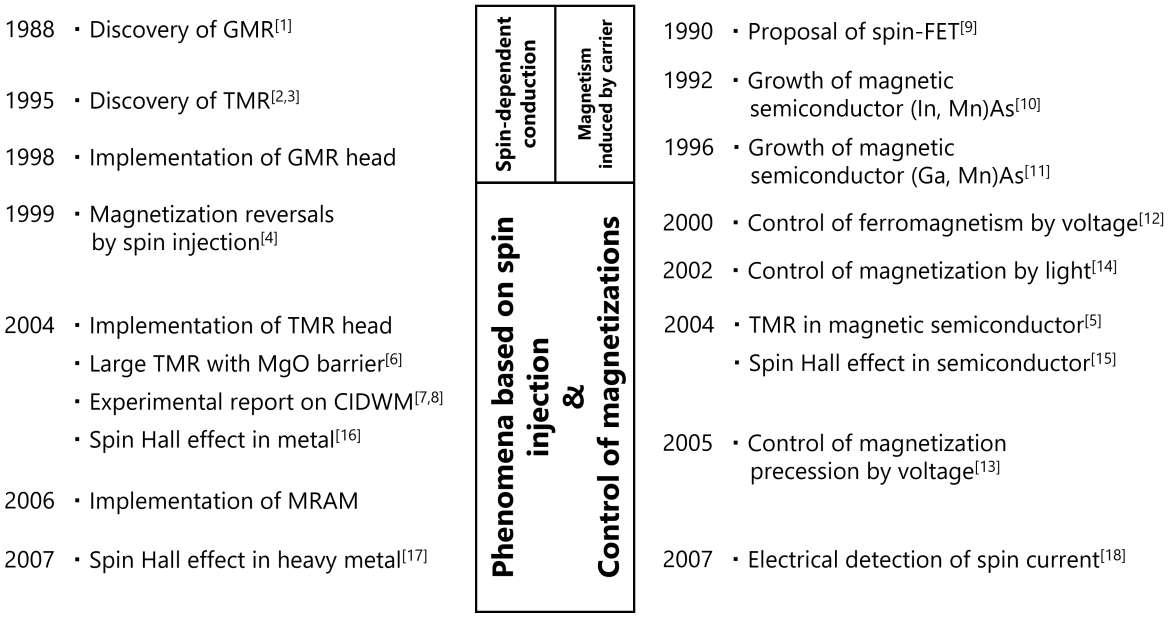

Figure 1: *The chronology of spintronics from the viewpoints of metals (left-side) and semiconductors (right-side) from the discovery of GMR effect to the experimental demonstration of spin current up to 2007.*

In the chronology of Figure 1, spin current which takes place by spin Hall effect started to attract a lot of attention from 2004[15–18]. Spin current is a net flow of spin angular momentum of electrons. There are two situations, where this flow is also accompanied by a net flow of charge, which is called a spin-polarized charge current, and when there is no net charge flow, for example when spin up and spin down diffuse in opposite directions, which is then called pure spin current. The former is generated in ferromagnets due to the exchange interaction, while the second is in materials with strong spin-orbit coupling. Figure 2 shows the chronology of spintronics after 2007, when "Spin current" was registered as Grant-in-Aid for Scientific Research on Priority Areas (KAKENHI), Japan. The spin current opened the door of new fields of spintronics[19–23]. For example, spin-caloritronics represented by spin Seebeck effect and spin Peltier effect is the study in which we try to generate spin current by heat energy or vice versa[24, 25]. Especially, spin-orbitronics, which takes advantage of the spin-orbit interactions to interconvert charge and spin current, has been one of the main topics of spintronics in the last decade. There are two basic mechanisms for this interconversion, the spin Hall effect that usually appears in bulk materials and the Rashba effect that emerges under the broken crystalline symmetry at interfaces.[26, 27]. One of the successes in spin-

orbitronics is magnetization reversals or domain wall motion by spin-orbit torques (SOTs) which are generated by the exchange of angular momentum between spin current and localized electrons[28]. Spintronics is expected to be a key technology to sustain the information society by providing non-volatile, scalable, and low energy memories for solutions.

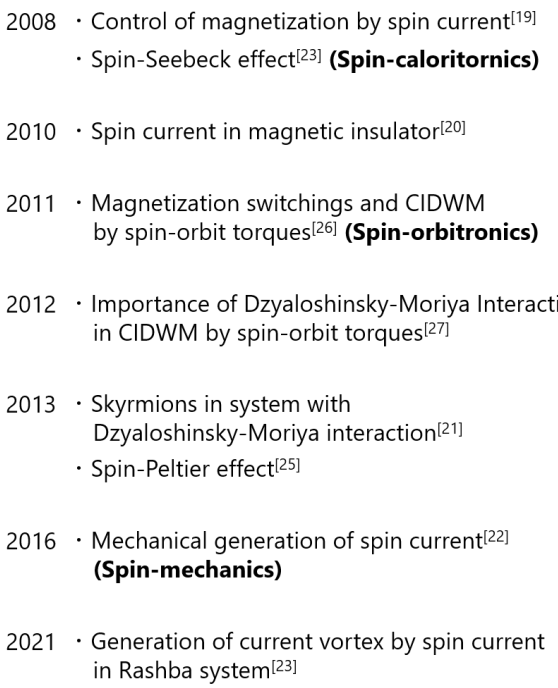

Figure 2: *The chronology of spintronics after 2007, when "Spin current" was registered as Grant-in-Aid for Scientific Research on Priority Areas (KAKENHI), Japan*

Current-induced domain wall motion (CIDWM)

Ferromagnets and ferrimagnets contain magnetic domains, regions where the magnetizations are in the same direction. The boundary between magnetic domains is called a magnetic domain wall (DW).

For example, in magnetic films in which the magnetization aligns perpendicular to the plane, the magnetizations rotate by 180° in DWs and they are antiparallel in domains next to each other[29–31]. By associating each direction of the magnetization with "0" and "1" of digital signal, magnetic domains are expected to be information vectors in magnetic memories, logic devices, sensors, and so on. Magnetic domains or DWs were reported to move with the assistance of magnetic fields[32–34]. However, the use of magnetic fields for DW motion is disadvantageous due to large power consumption and incompatibility for the integration. Moreover, domains that are aligned parallel to the magnetic field enlarge while those that are antiparallel shrink. In 1984, Berger theoretically predicted DW motion by spin-transfer torques (STTs) which are generated by the transfer of angular momentum between conduction electrons and localized electrons, when injecting a spin-polarized electrical current[35]. Thereafter, DW motion by the current was experimentally demonstrated in the 2000s[7, 36, 37]. After these achievements, current-induced domain wall motion (CIDWM) and magnetization switching have been one of the main focuses of spintronics in the last two decades, aiming at applications to the DW racetrack memories[38, 39], DW MRAMs[40] and DW based logic devices[41–44]. DW racetrack memories are expected to replace hard disc drives (HDDs) while DW MRAMs

can acts as DRAM replacements due to their high speed and non-volatility thanks to their non-volatility high-speed operation. Also, spin logic devices will be the replacement for conventional ones such as transistors.

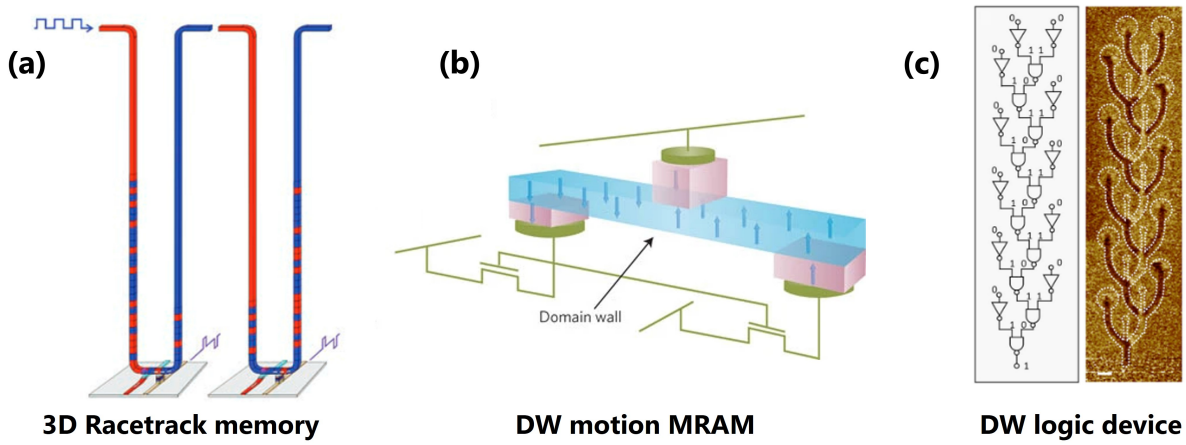

Figure 3: *The variety of new devices which will be implemented by CIDWM (a) 3D Racetrack memory[38] (b) DW motion MRAM[40] (c) DW logic device such as an artificial synapse[44]*

STTs[45, 46] and spin-orbit torques (SOTs)[26, 28, 47] are two mechanics for CIDWM. As mentioned above, STTs acting on DWs are generated from the transfer of angular momentum between the conduction electrons, polarized by the local magnetizations through the *s-d* interaction, and the localized electrons. On the other hand, the use of SOTs for CIDWM requires a heterostructure of heavy metal and magnetic layers in order to generate a spin current by the spin Hall effect or the spin accumulation by the Rashba effect. The spin current in the heavy metal flows into the magnetic layer and SOTs are generated to drive DW motion. Dzyaloshinski-Moriya interaction (DMI) is also an important factor so that the relationship of directions of spins in spin current and localized electrons becomes suitable for CIDWM by SOTs[27]. Such interaction can also induce magnetic skyrmions in thin films[21].

CIDWM in ferrimagnetic and Mn-based nitrides

Although CIDWM is a promising spintronics technology to enable new types of memories and logic devices, the threshold current density required for CIDWM should be lower and its efficiency should be improved as well. Considering the application of devices in circuits with complementary metal oxide semiconductors (CMOSs), DW must move with current density (j) on the scale of 10^{10} A/m^2 so that the oxide layer in CMOS doesn't get broken by high current density[48].

In this context, CIDWM in ferrimagnets, with reduced magnetizations, has attracted the attention of spintronics from the 2010s. Ferrimagnets consist of two sublattices or more with magnetic moments pointing in opposite directions and have non-zero magnetizations which are much smaller than those of ferromagnets. Since STTs and SOTs become efficient for CIDWM in materials with small magnetizations, ferrimagnets are more advantageous than ferromagnets [46, 49]. In some ferrimagnets, the magnetization and the angular momentum can be modulated by temperature or composition ratio and reached to points where magnetic moments and/or angular momentum compensate each other[50]. They are called the magnetic compensation point (MCP) and angular momentum compensation (ACP) point[51, 52]. Especially, at ACP,

very fast and efficient DW and magnetization switchings can be achieved thanks to the negligible precessional torque[53–57].

While fast and efficient CIDWM has been reported in ferrimagnetic GdCo[53, 54], TbCo[58, 59], YIG-based materilas[60, 61] and so on, our group has focused on rare-earth free ferrimagnetic Mn_4N films as new candidates for CIDWM devices. They have small saturation magnetization ($\simeq$ 80kA/m),quite large perpendicular magnetic anisotropy[62–65] which devote to the reduction of threshold j[66] for CIDWM and large spin polarization ($\simeq$ +0.8 effective polarization for CIDWM[67]) which enables high efficiency of STTs[46]. What's more, Mn atoms can be partially replaced with other transition metal elements, leading to a change in the various properties such as electric and magnetic properties. Notably, $Mn_{4-x}Ni_xN$[68–72] and $Mn_{4-x}Co_xN$[73–75] possess a room temperature compensation point. Therefore, Mn_4N and its based nitrides are materials to enable fast and efficient CIDWM. Moreover, they are highly desirable for implementation because they cost less for fabrication and are environmentally friendly. Indeed, we achieved DW velocity of 3,000 m/s in $Mn_{4-x}Ni_xN$ multiwires purely by STTs, which is the highest value among the records without the use of magnetic fields[71].

In our research project, we worked on the investigation of the magnetic and magneto-transport properties of Mn_4N and Mn_4N-based nitrides. We also attempted SOTs-driven CIDWM in Mn_4N multiwires to enable more efficient CIDWM. In this thesis, chapter 1 explains the theory of magnetism and CIDWM. We also present the latest study and achievements on CIDWM and propose obstacles for improvement. In chapter 2, we focus on Mn_4N and Mn_4N-based nitrides, especially $Mn_{4-x}Ni_xN$. We show not only their fundamental properties but also our previous works and achievements with these materials. In chapter 3, we report the growth of Mn_4N films on various substrates and the relationship between the PMA and the in-plane tensile strains which derive from the lattice mismatch. In chapter 4, we report the investigation of magneto-transport properties of $Mn_{4-x}Ni_xN$, especially anisotropic magnetoresistance (AMR) and anomalous Hall effect (AHE). In chapter 5, we show our attempt to enable SOTs-driven CIDWM in Mn_4N multiwires using spin current generated by the spin Hall effect in heavy metal. In the end, chapter 6 summarizes the achievements of these works and shows future perspectives to continue our research on Mn_4N and Mn_4N-based nitrides.

Chapter

Ferrimagnetism and domain wall motion 1

In this chapter, we introduce the basics of ferrimagnetism and current-induced domain wall motion (CIDWM). Section 1.1 focuses on the concept of ferrimagnetism and that of angular and magnetic compensation which enables fast and efficient CIDWM. Section 1.2 deals with magnetic anisotropy, especially perpendicular magnetic anisotropy (PMA) which enables the decrease of threshold current density for CIDWM. Section 1.3 shows the basics of magnetic domain walls (DWs) and how they are formed in magnets. Finally, Section 1.4 discusses the mechanism and state of the art of CIDWM.

1.1 Ferrimagnets

Ferrimagnetism is often considered to present the features of both ferromagnetism and antiferromagnetism. Figure 1.1 shows the schematics of their respective magnetic alignments. Ferrimagnets have at least two sublattices and each of them behaves like ferromagnets. However, the exchange interaction between these sublattices stabilizes their antiparallel alignments like in antiferromagnets. While the magnetization of sublattice cancels out each other in antiferromagnets, there are small but non-zero magnetizations in ferrimagnets due to the difference of the magnetization of each sublattice[76]. Thanks to their low damping, ferrimagnetic garnets are applied to the use of spin waves[77], and ferrites are applied to microwave technology[78].

In the following sections, we introduce the background of the exchange interaction, the spin configuration, and the compensation in ferrimagnets.

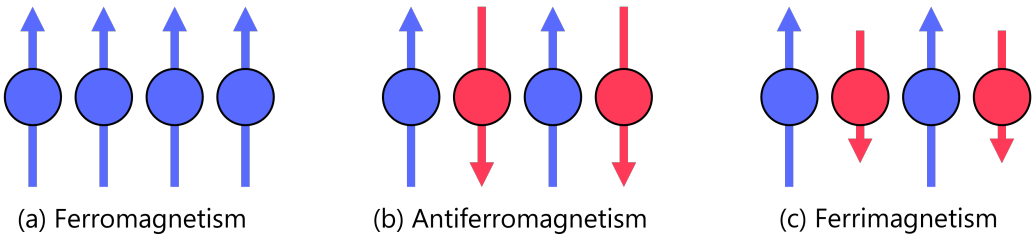

Figure 1.1: *Three types of magnetic alignment to represent magnetism. (a) Ferromagnetism where spins align in the same direction. (b) Antiferromagnetism with anti-parallel alignment with net zero magnetization (c) Ferrimagnetism with anti-parallel alignment with non-zero net magnetization*

1.1.1 Magnetism and exchange interaction

Exchange interaction is the interaction between identical particles, found and proposed by Heisenberg and Dirac in 1926[79, 80]. This interaction is often one of the most dominant factors to decide the spacial alignment of the moments of atoms. One of the means to understand its origin is to use quantum mechanical consideration of a simple two-electron system. Let us assume that there's no or negligibly small spin-orbit coupling in these electrons, which means that the Hamiltonian is spin-independent. Therefore, we can use the standard quantum mechanical procedure to separate the parameters of the space Ψ and the spin χ, which is given as

$$\Psi(r1, r2, s1, s2) = \psi(r1, r2)\chi(s1, s2) \tag{1.1}$$

The Schrödinger equation for these parameters is given as

$$H\psi = -\frac{\hbar}{2m}(\nabla_1^2 + \nabla_2^2) + V(r1, r2)\psi = E\psi \tag{1.2}$$

where $\hbar$ is the reduced Planck constant, m is the mass of the particle and V is the potential energy, respectively. Thanks to the Hamiltonian being spin-independent, the eigenfunctions, solutions of the equation, and the corresponding energy states are also spin-independent. Considering Pauli's exclusion principle, however, spin dependence emerges as seemingly spin-independent problem if the particles are fermions, which is the case of electrons. For two electrons, this principle forces the total wavefunction to be antisymmetric. The wavefunction can be divided into two parts, the orbital and the spin parts. This means that the spin wavefunction must be antisymmetric if the orbital wavefunction is symmetric. Since spin can have only two S_z states, the spin wavefunction is a linear combination of any four two-spin states, $|1, 1\rangle = \uparrow\uparrow$, $|1, 0\rangle = (\uparrow\downarrow + \downarrow\uparrow)/\sqrt{2}$, $|1, -1\rangle = \downarrow\downarrow$, $|0, 0\rangle = (\uparrow\downarrow - \downarrow\uparrow)/\sqrt{2}$. The former three combinations of the spin states are symmetric and are called triplet states which have a total spin $s = 1$. The last combination of the spin states is asymmetric and is called a singlet state which has a total spin $s = 0$. In this way, the symmetric wavefunctions must be combined with the antisymmetric wavefunctions for the principle to be met. The eigenfunctions of the spin-independent Hamiltonian and the corresponding energy states should be dependent on the relative orientation of the two spins of the electrons. This is the origin of the exchange interaction, in which the energy of the system is dependent on the mutual orientation of the spins of two particles, usually the neighboring ones.

The approximate representation of the exchange interaction of two magnetic moments i and j with spins S_i and S_j is given by the Hamiltonian below.

$$\hat{H}^{spin} = -J_{ij}S_i \cdot S_j \tag{1.3}$$

Here, J_{ij} is the exchange integral of particles i and j and represents the difference in the energy between the parallel and the antiparallel spin states. S_{ij} is the spin angular momenta of the atoms or ions composing the solid system. The effective magnetic field, called as the exchange field as well, acting on spin i is the sum of the nearest neighboring terms derived from the particle system.

$$B_E(i) \propto \Sigma J_{ij}S_j \tag{1.4}$$

The interaction is attributable to the overlap of the neighboring atomic orbitals, and thus it has an impact only in a short range and acts as an effective magnetic field. This term and model are known as the Heisenberg Hamiltonian and the Heisenberg model, respectively.

When the exchange integral is positive for a given atomic or ionic configuration ($J > 0$), the neighboring spins tend to align parallel and result in a state called ferromagnetism. By contrast, when it's negative ($J < 0$), the spins tend to align antiparallel and result in the state called antiferromagnetism if both the atoms or ions at i and j are the same. Importantly, this is called ferrimagnetism if they're different atoms or ions and don't cancel out each other like the case of antiferromagnetism, Fe^{2+} and Fe^{3+} in Fe_3O_4 which have different magnetic moments for example. This intermediate magnetism between ferromagnetism and antiferromagnetism is significant in the field of magnetism and spintronics as mentioned above.

1.1.2 Spin configurations in ferrimagnets

As mentioned in the previous section, the exchange interaction is the key to the emergence of magnetism but does not always lead to ferromagnetism. What's more, a real solid is often more complex than two particle system. In this case, neighboring atomic spins of different magnitudes can be aligned in a different way to minimize the local many-spin exchange interactions. Such a complex ordering of spins is typically found in oxides.

Here, we take a look at magnetite (Fe_3O_4 ($FeO{\cdot}Fe_2O_3$)) as an example of ferrimagnetic oxides. Single lattice of Fe_3O_4 consists of two ferric ions, Fe^{3+} with the spin quantum number $m_S = 5/2$ and orbital magnetic moment $L = 0$, and one ferrous ion, Fe^{2+} with $s = 5/2$ and $L = 0$. If all of the three moments μ_i were to align parallel like ferromagnets, a total magnetic moment μ would be $\mu = g\mu\Sigma s_i = 2\mu_B(5/2 + 5/2 + 2) = 14\mu_B$, where μ_B refers the Bohr magneton and g refers to the electron spin g-factor. However, it has been experimentally found to be $\mu \approx 4\mu_B$. This discrepancy can be explained by the fact that a ferrous ion and one of the ferric ions located in the octahedron structure align parallel and they're antiparallel to the other ferric ions located in the tetrahedron structure, resulting in $\mu = g\mu\Sigma s_i = 2\mu_B(5/2 +(- 5/2) + 2) = 4\mu_B$. To summarize, there can be two or more two sublattices with different magnitudes of moments that align antiparallel in ferrimagnets. In ferrimagnetic oxides, such interactions to force spins to align antiparallel generally come from superexchange interaction, which is the interaction acting on two atoms or ions with an anion between them. The positive exchange integral, $J > 0$, represents ferromagnetic coupling, and the negative one, $J < 0$, does antiferromagnetic coupling.

Now we assume the ferrimagnets with two sublattices (a and b) and all the exchange interactions between the two sublattices are antiferromagnetic, in inequality, J_{aa}, J_{bb} and $J_{ab} < 0$. The exchange fields acting on the spins of the two sublattices are respectively given as

$$B_a = -\gamma_{aa}M_a - \gamma_{ab}M_b, B_b = -\gamma_{bb}M_b - -\gamma_{ba}M_a \tag{1.5}$$

where all the exchange constants, γ_{ij} are positive ($\gamma_{a,b} = \gamma_{b,a}$ by reciprocity). The associated total energy is therefore given by

$$U = -\frac{1}{2}(M_a \cdot B_a + M_b \cdot B_b) = \frac{1}{2}\gamma_a M_b^2 + \frac{1}{2}\gamma_b M_a^2 + \gamma_{ab}M_a \cdot M_b \tag{1.6}$$

In this way, the energy, U, is minimized when M_a is antiparallel to M_b due to the third term on the right-hand side of Eq.1.6.

1.1.3 Compensation in ferrimagnets

Ferrimagnets have a Curie temperature (T_C) like ferromagnets, at which the magnetization attributable to the exchange interaction vanishes due to strong thermal fluctuations. These fluctuations also induce temperature dependence of the magnetization which differs from the

one in ferromagnets. In the case of ferrimagnets, materials consist of sublattices with different elements or ions, in other words, these sublattices have different temperature dependence on their magnetizations. In some cases, the magnetizations of sublattices cancel out each other and total magnetization consequently becomes zero at a specific temperature below T_C, known as the compensation temperature. Additionally, since the gyromagnetic ratios of sublattices made from different elements are not identical, there's also a temperature at which the total angular momentum becomes zero. In some of them, compensation can be achieved by the modulation of the composition ratio. Figure 1.2 shows examples of the temperature dependence of the magnetization in ferrimagnets. Fig. 1.2(a) is the case in which ferrimagnets show temperature dependence like in standard ferromagnets, increasing the total magnetization at lower temperatures. Fig1.2(b) is the case in which the total magnetization decreases under low temperatures due to the difference in the temperature dependence of magnetizations of the sublattices. Note that the compensation doesn't take place in this case. Fig. 1.2(c) is the case in which the ferrimagnetic compensation can be observed at T_{comp}. In this figure, M_A dominates the total magnetization below T_{comp} while M_B dominates it above T_{comp}. The compensation makes ferrimagnets very appealing for CIDWM, as explained in section 1.4.4.

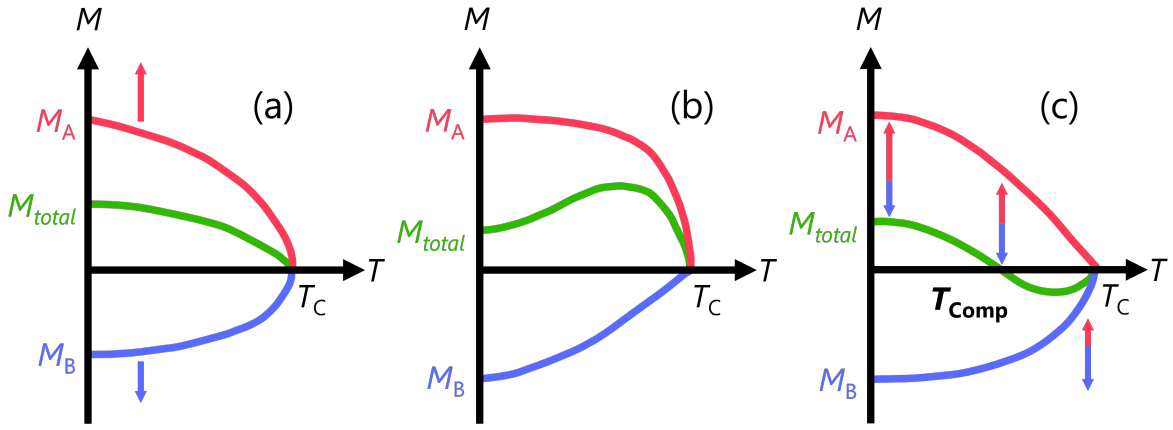

Figure 1.2: *Examples of the temperature dependence of the total magnetization and of each sublattice in ferrimagnets. (a) The case in which ferromagnetic-like behavior is observed. (b) The case in which the total magnetization decreases under low temperature, unlike the ferromagnets. (c) The case in which magnetic compensation takes place by temperature.*

1.2 Magnetic anisotropy

The internal energy in a ferromagnetic or ferrimagnetic domain depends on the direction of its magnetization. Due to the time-reversal symmetry, the magnetization should give the same internal energy as the one reversed along the same axis does (opposite direction). Such energy dependence on the direction of the magnetization is called the anisotropy energy (E_A) which is in the case of uniaxial anisotropy given as

$$E_a = Ksin^2\theta \tag{1.7}$$

where θ is the angle made by the magnetization and the easy axis and K is the anisotropy constant. Magnetic anisotropy is unique and one of the most important properties of ferromagnets to enable the improvement in permanent magnets, HDDs, and so on.

In the following sections, we present the origin of magnetic anisotropies which are crystalline, shape, and interfacial anisotropy. In the end, we explain the advantage of PMA and its

applications.

1.2.1 Crystalline anisotropy

Crystalline anisotropy in ferromagnets mainly derives from the spin-orbital coupling under the lattice structural anisotropy. The energy attributed to spin-orbit coupling can be given as

$$E_{SO} = \gamma_{SO} L \cdot S \tag{1.8}$$

where γ_{SO} is the spin-orbit constant, while L and S are the total orbital and spin angular momentum, respectively. If the atomic orbitals are of spherical symmetry, the orbital angular momentum is zero and the electron thus takes any direction isotropically. In the case of non-zero L_Z under the non-spherical charge distribution, however, the spin angular momentum favors aligning along the specific direction so that E_{SO} is minimized. Although magnetic dipole-dipole interaction can be another significant factor in the case of structures with low symmetry, spin-orbit coupling with non-zero angular momentum is the main origin of crystalline anisotropy. In the case of uniaxial anisotropy, the anisotropy energy U_K is at first order, given as

$$U_K = K(m_x^2 + m_y^2) = K sin^2\theta = -K cos^2\theta + const \tag{1.9}$$

where θ is the angle made by the magnetization and z-axis. For $K > 0$, the energy of the system is lower when the magnetization is aligned with the z-axis. For $K < 0$, the ferromagnet is called to be of easy plane type because the z-axis becomes a difficult axis but the strength of the anisotropy in xy-plane is not strong.

1.2.2 Shape anisotropy

Magnetic anisotropy in ferromagnets is influenced not only by crystalline anisotropy but also by shape anisotropy. The most basic idea of shape anisotropy is that those ferromagnets are easy to get magnetized along the longer direction than the shorter one. We can understand the concept by perceiving that the magnetic field lines prefer to close up at the surface of the samples.

$$divB \equiv div(H + 4\pi M) = 0 \tag{1.10}$$

M is the magnetization of the film which is finite inside it and zero outside. Therefore, the divergence of the field lines is large at the surface if the normal to-the-surface component of the magnetization is not zero. This divergence produces magnetic poles which result in the generation of the demagnetizing field (H_{d}) given by the following equation:

$$divH = -4\pi divM \tag{1.11}$$

The demagnetizing field acts on the magnetization to oppose it and is proportional to the magnitude of the magnetization. This derives from the magnetic poles on the surfaces generated by magnetization. To reflect the effect of the shape, the demagnetizing tensor (N_d) is useful.

Let us assume that the magnetization is homogeneous in a ferromagnetic sample. In the case of an ellipsoid, the energy of the dipolar interaction acting on the magnetization can be given as

$$U_{shape} = -\frac{\mu_0}{2} \cdot M \cdot H_d \tag{1.12}$$

where H_d is given as $-N_d \cdot M$. In the case of a film, this is given by

$$U_{shape} = -\frac{\mu_0}{2} M_s^2 sin^2\theta \tag{1.13}$$

where θ is the angle made by the magnetization and z-axis. Here, the demagnetizing tensors work as $\mu_0 H_{dx} = 0, \mu_0 H_{dy} = 0, \mu_0 H_{dz} = -M_z$. Therefore, if there was no crystalline anisotropy, magnetic films would have strong in-plane magnetic anisotropy.

1.2.3 Interfacial anisotropy

Due to the broken symmetry of the crystalline structure at the interface, magnetic anisotropy at the interface is different from the one in the bulk sample. After the success in the growth of ultrathin magnetic films, the interfacial anisotropy gets attraction because this is not negligible or even sometimes dominant in such system. Note that the contribution of the interfacial anisotropy is antiproportional to the thickness of ferromagnetic layer. Importantly, the interfacial anisotropy often induces PMA, in the case of CoFeB/MgO for example. This is attributable with the elastic stress due to lattice mismatch and hybridization of the $3d$ orbitals of Co and Fe with the p_z orbitals of oxygn at the interface[81–83].

1.2.4 Perpendicular magnetic anisotropy

As mentioned above, PMA has been one of the most significant and practical features for applications even from the viewpoint of magnetic materials engineering. One of the biggest successes is the invention of the perpendicular magnetic recording (PMR) in HDDs, proposed by Iwasaki in 1997[84]. The conventional in-plane magnetic recording had an obstacle in the integration due to the thermal fluctuations of magnetizations in magnetic domains. PMR overtook this problem as shown in figure 1.3 (a), besides, demagnetizing fields in magnets were reduced as magnetic domains become smaller. This was applied to magnetic recording tapes, and HDDs with PMR were commercialized by Toshiba in 2005.

PMA is still taking an important role in recent spintronics. To give an example on CIDWM, Mougin *et al*. theoretically evidenced that magnetic stripes with PMA are more advantageous than the in-plane magnetized ones thanks to the reduction of the threshold current density required for DW motion[49]. Afterward, Emori and Beach reported this reduction with micromagnetic simulation[66]. They attributed this reduction to the simple Bloch DWs in PMA stripes which are more favorable for CIDWM by STTs than transverse or vortex (Néel) DWs in in-plane magnetized stripes. Figure 1.3 (b) shows the graph of DW velocity (v) vs spin-polarized electron velocity (u) which is proportional to current density. Bloch DWs are also suitable for the generation of chiral Néel DWs under strong DMI which is necessary for SOTs-driven CIDWM[27, 85–87].

The detail of the formation of DWs will be explained in section 1.3.2.

1.3 Magnetic domain wall

As discussed in section 1.1.1, if we only consider the influence of the exchange interaction, all the magnetic moments in the ferromagnets would align parallel and have a spontaneous magnetization even under zero magnetic field. However, the macroscopic ferromagnets can be divided into multiple regions with magnetizations in different directions, magnetic domains, as described by Landau and Lifshitz in 1935[88]. In this way, ferromagnets can have zero net magnetization which is called the demagnetized state.

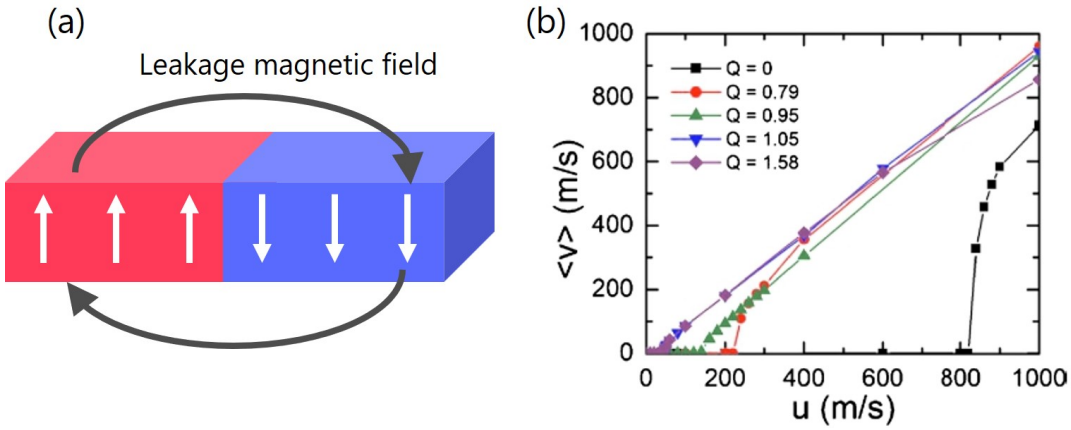

Figure 1.3: *Advantage of PMA for the engineering application. (a) A schematic image of leakage magnetic fields makes a loop with neighboring magnetic domains to reduce the total energy. (b) DW velocity (v) vs spin-polarized electron velocity (u) in microstrips in the simulation. Q represents the degree of magnetic anisotropy, $Q > 1$ for PMA and $Q < 1$ for in-plane magnetic anisotropy[66]*

In the following sections, we discuss the micromagnetic energies which determine the size and the configuration of magnetic domains and DWs. Also, we show some of the DWs' structures and their uses for CIDWM.

1.3.1 Micromagnetic energies

Although there can be other non-negligible contributions in some systems or conditions, we discuss in short about main six types of energies related to micromagnetic energies. The total energy can be given as

$$U = U_{ex} + U_k + U_{me} + U_{ms} + U_i + U_{Zeeman} \tag{1.14}$$

The first term represents the exchange interaction energy as discussed in section 1.1.1 and Eq. 1.3. This is the interaction that aligns the neighboring spins in parallel, thus, U_{ex} can be expanded into

$$U_{ex} \sim -cos\theta_{ij} \sim \left(\frac{\partial\theta}{\partial x}^2\right) \tag{1.15}$$

The second term is the uniaxial magnetocrystalline anisotropy energy which can be derived from section 1.2.1. This is given by

$$U_k \sim -cos^2\theta \tag{1.16}$$

The third term is the magnetoelastic anisotropy energy which is an anisotropy induced by the stress exerted on the material. In this section, we express it in the most simple way, given as

$$U_{me} \sim cos^2\theta \tag{1.17}$$

The fourth term is the contribution from the magnetostatic or shape anisotropy energy which is the interaction between the magnetization and its self-field or demagnetizing field. It

mainly derives from discontinuities in M normal to surfaces or to its volumic charges due to the shape of ferromagnets. It's proportional to M_s^2 and the main factor to form magnetic domains in ferromagnets. This can be given as

$$U_{ms} \sim cos^2\theta \tag{1.18}$$

The fifth term is the interfacial anisotropy energy as mentioned in section 1.2.3. Assuming that we can neglect the effect of the canting spins at the interface, the energy can be given as

$$U_i \sim -cos\theta \tag{1.19}$$

The sixth term is the Zeeman energy which gives the magnetization the preference to align parallel to a magnetic field, and it is given as

$$U_{Zeeman} \sim -cos\theta \tag{1.20}$$

Note that in these equations, Eqs. 1.15 - 1.20, the angle of θ is different for every equation except when the anisotropy axis coincides with the magnetization. These approximations and qualitative discussions for particular cases are used only to illustrate the procedure for finding the microscopic distributions of magnetic moments. These distributions can be derived by finding the magnetization direction (θ) to minimize the total energy given in Eq. 1.14. Here, non-equilibrium distributions of magnetic moments are not considered.

In this discussion, we use a ferromagnet with uniaxial anisotropy in which the magnetization vectors of the adjacent domains align anti-parallel to each other. Thus, there is 180° of transition of magnetization vectors from one domain to the other next to it. This transition region to separate two magnetic domains is called DW. If the ferromagnet is a stripe with PMA, there are two different kinds of DW formations, Néel DWs and Bloch DWs. Figure 1.4 shows the schematic images of Néel DWs and Bloch DWs.

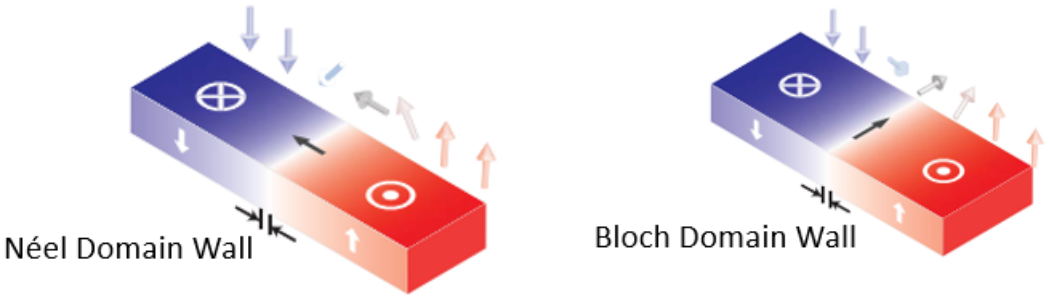

Figure 1.4: *Schematic images of the DW structures in thin films with PMA: (a) Néel DW and (b) Bloch DW.[89]*

Now we focus on Bloch DWs in which spins rotate in the plane parallel to magnetic domains. If the 180° of transition takes place within one lattice spacing in the materials, or neighboring spins rotate 180° in short, there would be no increase in the anisotropy energy as discussed in section 1.2. However, when we take a look at the change in exchange interaction energy for a pair of spins, it's

$$\Delta U_{ex} = -2JS^2 cos\theta_{ij} = JS^2 \tag{1.21}$$

In this assumption, if $J = 4\times\ 10^{-21}$ J (Joules), $\Delta U_{ex}/a^2 \approx 0.25\text{J/m}^3$, which is relatively large and the total energy of the pair of spins should decrease to be stable. In order to minimize

the exchange interaction energy, the transition should be done in a large number of spins with $\theta \approx \pi/N$. When N is a large number, Eq. 1.21 can be expanded as

$$\Delta U_{ex} = -2J^2S^2 cos\theta_{ij} = JS^2\left(\frac{\pi}{N}\right)^2 \tag{1.22}$$

Assuming that all the N spins rotate by the constant angle, the DW energy density is therefore given by

$$\epsilon_{ex} = H\frac{\Delta U_{ex}}{a^2} = JS^2\frac{\pi}{N}^2 \tag{1.23}$$

where a is the lattice spacing (one spin per lattice unit, or lattice constant). Since ϵ_{ex} is antiproportional to N, it's clear that the energy is reduced by extending the DWs.

On the contrary, the anisotropy energy is proportional to N which is derived from Eq. 1.7,

$$\epsilon_k \approx NKa \tag{1.24}$$

where the approximation of $sin^2\theta \approx 1$ was used because each spin in Bloch DWs makes zero angles with a hard axis in the stripe. K is the anisotropy energy density (in J/m^3). Therefore, the combined energy attributed to exchange interaction and anisotropy energy is given as the bottom.

$$\epsilon_{ex} + \epsilon_k \approx JS^2\frac{\pi^2}{Na^2} + NKa \tag{1.25}$$

Minimizing with respect to N, the width of DWs (w_{dw}) can be given as

$$Na \equiv w_{dw} = \pi\sqrt{\frac{JS^2}{Ka}} = \pi\sqrt{\frac{A}{K}} \tag{1.26}$$

where $A \equiv JS^2/a \approx 10^{-11}$ J/m is the exchange stiffness constant.

1.3.2 Formation of DWs

In Eq. 1.26, w_{dw} depends on the magnetic anisotropy. K is around 10^3 J/m^3 for typical soft magnets, leading to $w_{dw} \sim$ 100nm while $w_{dw} \sim$ 10nm for hard magnets.

However, the formation of DWs can change according to the shape anisotropy as well. Néel demonstrated that standard Bloch DWs are not formed if the thickness of a film is close to or smaller than w_{dw}[90]. Technically, Néel DWs or Néel and Bloch-mixed states are preferred in such a system. Néel demonstrated the transition between Néel DWs and Bloch DWs by the effect of shape with a simplified model of DW in an elliptical cylinder. We define the length as W and the diameter as D and the magnetization aligns perpendicular to the direction of the length in the magnetic domains. If simple Bloch DWs are formed, the demagnetizing factor is given as $N_{Bloch} = W/(W+D)$. On the other hand, it is given as $N_{Nel} = D/(W+D)$ when Néel DWs are formed. Therefore, Bloch DWs are more energetically stable when $W < D$, and Néel DWs are stable when $W > D$. Thus, the width of DWs becomes dependent on the exchange length of the stray field ($\Delta_d = \sqrt{A/K_d}$), the exchange length of the anisotropy energy, and the film thickness.

Since the 2010s, the realization of chiral Néel DWs by large DMI has been an intense topic in spintronics. DMI can be obtained through the second perturbation of the spin-orbit coupling interaction, which is in short given as

$$E_{DMI} = -D_{ij} \cdot (S_i \times S_j) \tag{1.27}$$

where D_{ij} is the DMI vector between two spins, i and j[91, 92]. Figure 1.5 shows the schematic image of DMI in the inversion symmetry-broken heterostructure. DMI is zero or negligibly small in the system with inversion symmetry, however, large DMI are reported at the interface with a heavy metal (HM)(Ta, W, Pt, etc.) with a magnetic layer (ML) and in the structure of HM/ML/oxides (MgO, etc.). DMI promotes the realization of Néel DWs with internal chirality, which is a key of CIDWM by SOTs with spin Hall effect from HMs. If Néel DWs don't have chirality, magnetic domains don't propagate in the same directions in ferromagnets. Also, DMI is an important factor for the formation of chiral Néel magnetic skyrmions[21].

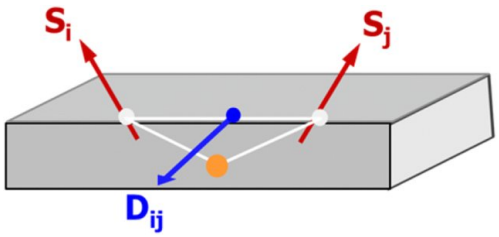

Figure 1.5: *Schematic illustration of interfacial DMI[93].*

1.4 CIDWM

DW motion by the magnetic field is induced by the minimization of Zeeman energy between magnetic moments and the external field, which allows the propagation of domains with the magnetization parallel with the field. However, in the case of CIDWM, torques such as STTs and/or SOTs are exerted on spins localized in the DWs, and the magnitudes of torques components determine the DW velocity and the threshold of the magnetization reversal.

In the following sections, we aim at understanding the magnetization dynamics with Landau-Lifshitz Gilbert (LLG) equation and derive STTs and SOTs. We also mention the CIDWM in ferrimagnets which has been an intense topic in the last decade and the state of the art in CIDWM.

1.4.1 Magnetization Dynamics

LLG equation is the differential equation to give the precession of the magnetization under the magnetic field, which is given as[88, 94]

$$\frac{\partial \boldsymbol{m}}{\partial t} = \gamma_0 \boldsymbol{H_{eff}} \times \boldsymbol{m} + \alpha \boldsymbol{m} \times \frac{\partial \boldsymbol{m}}{\partial t} \tag{1.28}$$

where $\boldsymbol{m}(= \boldsymbol{M}/M_S)$ is the unit magnetization vector, $\gamma_0 = \mu_0 \gamma$ with μ_0 the vacuum permeability, γ is the gyromagnetic ratio and α the phenomilogical damping constant. $\boldsymbol{H_{eff}}$ is the effective magnetic field, not only the external field but also other effects acting on the magnetization such as the magnetic dipole interaction, the exchange interaction, and so on, and this is given as

$$\boldsymbol{H_{eff}} = -\frac{1}{\mu_0 M_s} \frac{\delta E_{total}}{\delta \boldsymbol{m}} \tag{1.29}$$

Figure 1.6 shows the schematic image of the magnetization precession around $\boldsymbol{H_{eff}}$ based on Eq. 1.28. The terms of LLG equation can be considered as torques under the perturbed

system, in which $\boldsymbol{m}$ and $\boldsymbol{H_{eff}}$ vary. The first term of Eq. 1.28 corresponds to the Larmor precession of the magnetic moment around $\boldsymbol{H_{eff}}$. The angular velocity of the precession is proportional to the magnitude of $\boldsymbol{H_{eff}}$ and γ_0. The second term represents the damping torque which corresponds to the relaxation of the magnetic moment. This torque is dissipative in nature and its strength is proportional to α. Considering the relationship of $\boldsymbol{m} = \boldsymbol{M}/M_S$, E_{total} of the magnetic moment is conserved under the magnetic field.

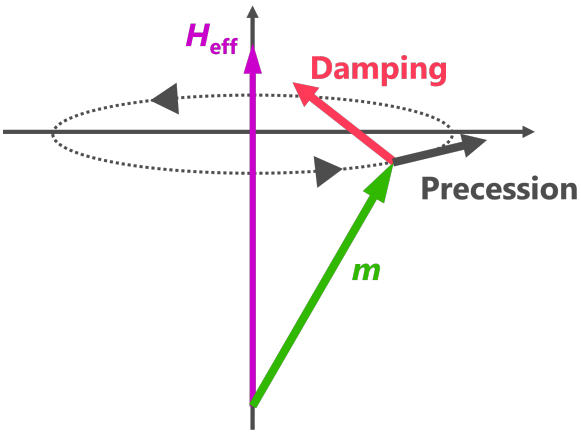

Figure 1.6: *Schematic image of the torques acting on the magnetic moment to induce the precession under the effective magnetic field in Eq. 1.28*

1.4.2 Spin-transfer torques (STTs)

The concept of CIDWM was first proposed by Berger in 1984[35], and it was explained as STTs afterward by Slonczewski[45]. This was based on the *s*-*d* interaction between conduction electrons (*s* electrons) and localized electrons (*d* electrons) which makes the spin angular momenta of *s* electrons and the orbital momenta of electrons align parallel. Therefore, in DWs, spin magnetic moments of *s* electrons change by 180° by passing a DW and transferring their angular momenta to *d* electrons, resulting in DW motion.

The theoretical establishment of this proposal was achieved by expanding LLG equation in Eq. 1.28. First, we deal with the case of the adiabatic approximation[95, 96]. We assume that one conduction electron flow along the x-axis and the unit vector of the magnetic moments in the orbital electrons at the position of x is defined as $\boldsymbol{M}(x)$ and at $x+dx$ is as $\boldsymbol{M}(x+dx)$. The spins follow the direction of the local magnetic moments of d electrons due to *s*-*d* interaction if the spacial change in the magnetic moments is moderate enough. Thus, when we define the unit vector of spin at the position of x as $\boldsymbol{m}(x)$ and the one at $x+dx$ as $\boldsymbol{m}(x+dx)$, the angular momentum transferred to the orbital magnetic moment by one conduction electron is given as

$$given = \boldsymbol{m}(x) - \boldsymbol{m}(x+dx) = -dx \cdot \frac{\partial \boldsymbol{m}}{\partial t} \tag{1.30}$$

Accordingly, Eq. 1.30 can be given as the following equation per unit time and unit area.

$$given = \frac{g\mu_B}{2}\frac{jP}{e}(-dx\frac{\partial \boldsymbol{m}}{\partial t}) \tag{1.31}$$

where g is the g-factor, μ_B is the Bohr magneton, j is the current density, P is the spin polarization of the current and e is the elementary charge. On the other hand, the angular momentum in Eq. 1.31 is all given to the magnetic moment of d electrons in the region with

the thickness of dx in the adiabatic approximation. Therefore, in the time dt, the angular momentum accepted to orbital electrons is given as

$$accepted = \frac{d\boldsymbol{M}}{dt}dx = M_S\dot{\boldsymbol{m}}dx \tag{1.32}$$

Since the Eqs. 1.31 and 1.32 must be equal due to angular conservation, hence, the following equation is acquired.

$$\dot{\boldsymbol{m}} = \frac{g\mu_B Pj}{2eM_S} \cdot \frac{\partial \boldsymbol{m}}{\partial t} \tag{1.33}$$

Since the left side of Eq. 1.33 is equal to that of Eq. 1.28, the adiabatic STTs can be added to LLG equation just by adding the right side of Eq. 1.33 to that of Eq. 1.28. Note that the coefficient part of the right side of Eq. 1.33 has a dimension of the velocity (m/s) which indicates the drift velocity of the spin magnetic moment by the conduction electron. Therefore, this is often called spin-polarized current velocity or spin-drift velocity ($\boldsymbol{u}$)

$$\boldsymbol{u} = \frac{g\mu_B P}{2eM_x}\boldsymbol{j} \tag{1.34}$$

This is a one-dimensional model in which the change in the magnetization is limited only along the x-axis. Thus, in three-dimension, the adiabatic STTs can be generalized in this simple way.

$$\dot{\boldsymbol{m}} = -(\boldsymbol{u} \cdot \nabla)\boldsymbol{m} \tag{1.35}$$

Then, we aim at installing non-adiabatic STTs to LGG equation[46, 97]. The existence of the non-adiabatic STTs has been suggested from the discrepancy in the threshold current density between experimental results and adiabatic simulation, in which the threshold is abnormally large in the simulation compared with the experimental results.

As for the assumption above to derive the adiabatic STTs, when the conduction electron transfer angular momentum to the localized electron, the DW stores energy depending on the angle made by the magnetic moment and x-axis due to the demagnetizing field exerted on the magnetic moment. Such energy storing takes place due to the damping torque in the second term of Eq. 1.28. This term is zero under the condition of a non-magnetic field and current, however, it becomes non-zero when the current is injected and the magnetic moment rotates due to the adiabatic term. The non-adiabatic effect indicates the dissipation of this energy which means non-adiabatic torques should work against the damping torques to minimize the energy.

Thus, LLG equation considering both adiabatic and non-adiabatic torques is given as

$$\dot{\boldsymbol{m}} = -|\gamma_0|\boldsymbol{m} \times \boldsymbol{H_{eff}} + \alpha\boldsymbol{m} \times \dot{\boldsymbol{m}} - (\boldsymbol{u} \cdot \nabla)\boldsymbol{m} + \beta\boldsymbol{m} \times (\boldsymbol{u} \cdot \nabla)\boldsymbol{m} \tag{1.36}$$

where the fourth term represents the non-adiabatic torque and β is the non-adiabatic torque constant. Figure 1.7 shows the schematic image of the STTs exerted on magnetic moments. Note that the third term, the adiabatic torque, is the torque to reverse magnetization while the first term, the precessional torque works against it. What's more, the first term becomes non-zero as a result of the demagnetizing field caused by the second term, the damping torque, which is canceled by the fourth term, the non-adiabatic torque. This effect to prevent the magnetization reversal by the adiabatic torque is called internal pinning and its strength eventually depends on the magnitude of the non-adiabatic torque.

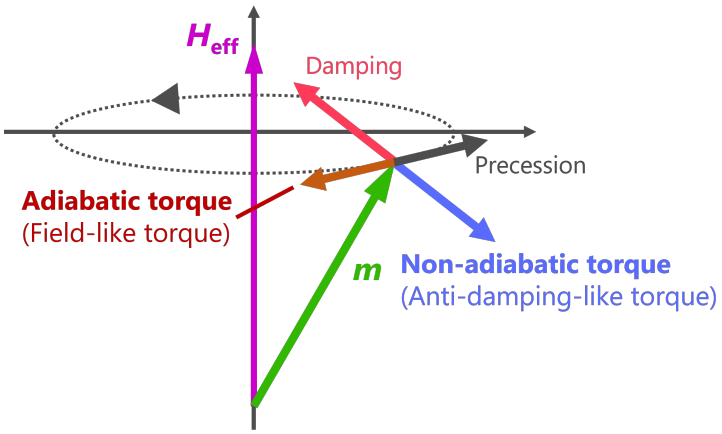

Figure 1.7: *Schematic image of the torques acting on the magnetic moment including STTs in Eq. 1.36.*

1.4.3 Spin-orbit torques (SOTs)

While the spin polarization of conduction electrons is essential for STTs, spin current or spin accumulation through/at the interface between heavy metal (HM) and the magnetic layer (ML) is responsible for SOTs. In such heterostructure, the spin current is generated in the heavy metal by Spin Hall effect (SHE)[15–18, 98] and the spin gets accumulated at the interface by Rashba-Edelstein effect[99, 100]. These spin current and/or spin accumulation acts as an effective field and exerts torques on the magnetic moments in ML, resulting in the magnetization reversal and DW motion.

First, we deal with SOTs by SHE. In SHE, the spin dependent scattering takes place due to scattering which is in the case of extrinsic SHE, and to Berry curvature in k-space which is the case of intrinsic SHE. In HM which has strong spin-orbit coupling (SOC) such as Pt, W, and Pt, the scattering of electrons in the charge current can be converted into a transverse spin current, perpendicular to the direction of the charge current. The SOT generated via SHE is called damping-like or anti-damping-like torque which is in the same direction as the non-adiabatic STT in Eq. 1.36. This torque can be added to the LLG equation as

$$\boldsymbol{\Gamma_{ad}} = \gamma_0 \frac{|g|\mu_B}{2e} \frac{\theta_{SHE}}{M_s t} [\boldsymbol{m} \times (\boldsymbol{m} \times \boldsymbol{\sigma})] \tag{1.37}$$

where, t is the thickness of the ML, θ_{SHE} is the spin Hall angle which is the conversion rate of a charge current into a spin current and σ is the direction of the polarization in the spin current. Figure 1.8 shows the schematic image of the current-induced effective fields by SOTs in the system with SHE.

Then, we move onto SOTs by Rashba effect. This is called field-like torque and is in the same direction as the adiabatic STT in Eq. 1.36. This can be added to the LLG equation as

$$\boldsymbol{\Gamma_R} = \gamma_0 \frac{\alpha_R P}{\mu_0 \mu_B M_s e} [\boldsymbol{m} \times \boldsymbol{\sigma}] \tag{1.38}$$

where α_R is the Rashba coefficient which represents the strength of the Rashba SOC. In fact, both damping and field-like contributions can arise from SHE or Edelstein effect, so the situation is actually a bit more complicated.

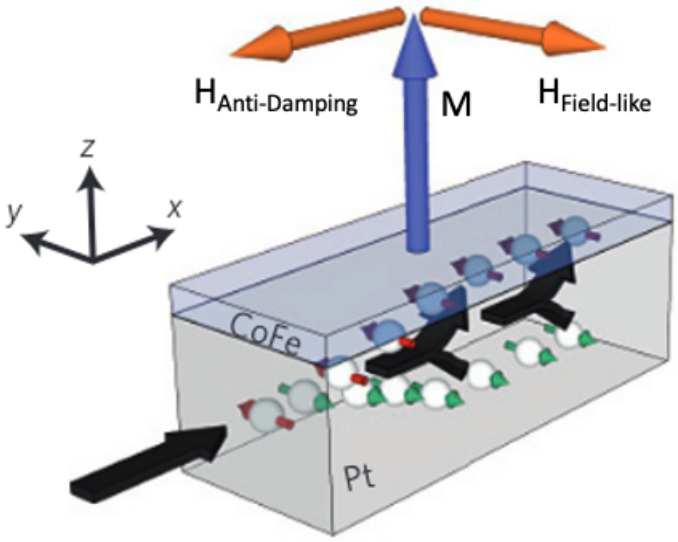

Figure 1.8: *Schematic image of the current induced effective fields by SOTs acting on the magnetization.[101]*

1.4.4 STT in ferrimagnets

In the case of magnets with multiple sublattices, the LLG equation shown above has to be reconsidered and modified[51, 55]. Here, we deal with the case of ferrimagnets in which the sublattices "1" and "2" carry the magnetic moments (m_1 and m_2) always align antiparallel. In this ferrimagnet, we can have two separate LLG equations including STT terms as shown below.

$$[LLG_1]\delta_t\vec{m}_1 = -\gamma_{01}\vec{m}_1 \times \vec{H}_1 + \alpha_1\vec{m}_1 \times \delta_t\vec{m}_1 - (\vec{\mu}_1 \cdot \vec{\nabla}) + \beta_1\vec{m}_1 \times (\vec{\mu}_1 \cdot \vec{\nabla}) \tag{1.39a}$$

$$[LLG_2]\delta_t\vec{m}_2 = -\gamma_{02}\vec{m}_2 \times \vec{H}_2 + \alpha_2\vec{m}_2 \times \delta_t\vec{m}_2 - (\vec{\mu}_2 \cdot \vec{\nabla}) + \beta_2\vec{m}_2 \times (\vec{\mu}_2 \cdot \vec{\nabla}) \tag{1.39b}$$

Here, the $\vec{H}_1$ and $\vec{H}_2$ can be written as the form of Eq. 1.29., however, we need to add the inter-layer exchange coupling between two sublattices (J_{ex}) to the total energy (E_{total}) of the effective field (H_{eff})[55, 102, 103]. Since two sublattices are strongly coupled with exchange interaction, we can expect that there is a very small distance between m_1 and m_2. Thus, we can consider $\vec{m}_1 = \vec{m}_2$ and the effective net magnetization is given as $M_s = M_1 - M_2$, leading to the relationship of $m = m_1 = -m_2$[55]. Now, two LLG equations in Eq. 1.39 can be combined as

$$\begin{aligned}\left(\frac{M_1}{\gamma_{01}} - \frac{M_2}{\gamma_{02}}\right)\delta_t\vec{m} = \frac{1}{\mu_0}\vec{m} \times \frac{\delta E}{\delta\vec{m}} + \left(\alpha_1\frac{M_1}{\gamma_{01}} + \alpha_2\frac{M_2}{\gamma_{02}}\right)\vec{m} \times \delta_t\vec{m} \\ - \left(\left(\vec{\mu}_1\frac{M_1}{\gamma_{01}} - \vec{\mu}_2\frac{M_2}{\gamma_{02}} \cdot \vec{\nabla}\right)\vec{m}\right) \\ + \vec{m} \times \left(\left(\beta_1\vec{\mu}_1\frac{M_1}{\gamma_{01}} + \beta_2\vec{\mu}_2\frac{M_2}{\gamma_{02}}\right) \cdot \vec{\nabla}\right)\vec{m}\end{aligned} \tag{1.40}$$

Eq. 1.40 shows the effective dynamics of the ferrimagnets, and each effective parameter can be expressed as[55]

$$\begin{aligned}
\vec{H}_{eff} &= -\frac{1}{\mu_0 M_s}\frac{\delta E}{\delta \vec{m}} \\
\gamma_{0eff} &= \frac{M_s}{L_s} \\
a_{eff} &= \frac{L_\alpha}{L_s} \\
\beta_{eff} &= \frac{\beta_1 P_1 + \beta_2 P_2}{P_{eff}} \\
P_{eff} &= P_1 - P_2 \\
\mu_{eff} &= \gamma_{0eff}\frac{\hbar}{2e}\frac{1}{\mu_0 M_s}P_{eff} J
\end{aligned} \tag{1.41}$$

where $L_s \equiv \left(\frac{M_1}{\gamma_{01}} - \frac{M_2}{\gamma_{02}}\right)$ is the net angular momentum while $\mathrm{L}_\alpha \equiv \left(\alpha_1\frac{M_1}{\gamma_{01}} + \alpha_2\frac{M_2}{\gamma_{02}}\right)$ is the product of α and L_s ($L_\alpha \equiv \alpha L_s$). Now, the LLG equation can be written in terms of L_s and L_α, given as

$$\delta_t \vec{m} = \frac{1}{L_s}(\vec{m} \times \delta_m E + L_\alpha \vec{m} \times \delta_t \vec{m} + \Gamma) \tag{1.42}$$

and expended as

$$\delta_t \vec{m} = \frac{L_s}{L_s^2 + L_\alpha^2}(\vec{m} \times \delta_m E + \Gamma) + \frac{L_\alpha}{L_s^2 + L_\alpha^2}\vec{m} \times (\vec{m} \times \delta_m E + \Gamma) \tag{1.43}$$

where Γ is the STT term. In Eq. 1.43, the two components of the magnetization dynamics are emphasized. Thus, Γ can be written as

$$\Gamma_{STT} = -(L_s \mu \cdot \nabla)\vec{m} + \vec{m} \times (\beta L_s \mu \cdot \nabla)\vec{m} L_s \mu = \frac{P_{eff} J \hbar}{2e} e_J \tag{1.44}$$

where P_{eff} is the spin polarization effective for CIDWM and Je_J is the current density.

In the $q - \phi$ model of the ferromagnets, the relationship between DW velocity (v) and spin-drift velocity (u) is given as

$$\begin{aligned}
v_{steady} &= \frac{\beta}{\alpha}u \\
v_{precessional} &= \frac{1 + \alpha\beta}{1 + \alpha^2}u
\end{aligned} \tag{1.45}$$

where v_{steady} refers to the DW velocity in the steady regime in which magnetic moments in DWs move continuously according to LLG equation and $v_{precessional}$ refers to the one in the precessional regime in which magnetic moments don't move continuously anymore due to the high current density or the magnetic field. Based on Eq. 1.45 and the discussion above, the relationship between v and u in ferrimagnets is given as

$$\begin{aligned}
v_{steady} &= \frac{\beta}{L_\alpha}L_s u \\
v_{precessional} &= \frac{L_s + L_\alpha\beta}{L_s^2 + L_\alpha^2}L_s u
\end{aligned} \tag{1.46}$$

Going back to Eq. 1.41, we can see that α_{eff} diverges close to the angular momentum com-

pensation point ($L_s = 0$). At this point, the magnetization is instantly aligned to the effective field which is also the result of negligibly small precessional torque on the magnetization. This is why CIDWM in compensated ferrimagnets has been recently an attractive topic.

1.4.5 State of the art in CIDWM

The first experimental report on STT-driven CIDWM was made by Yamaguchi *et al.* in 2004, in an in-plane magnetized permalloy nanostrip[7]. Afterward, the reduction of the threshold current density was achieved in PMA materials from 10^{12} A/m^2 to 10^{11} A/m^2. In 2011, SOT-driven CIDWM was reported by Miron *et al.* in a Pt/Co/AlO_x nanostrip[28]. After this report, SOT became the main focus of CIDWM thanks to the higher performance than those by STTs at that time. Around 2015, the use of compensated ferrimagnets or synthesized antiferromagnets (SAFs) for CIDWM made a breakthrough in this field[54, 102]. Our group demonstrated v = 900 m/s in Mn_4N strips[67] and 3,000 m/s in (Mn, Ni)N purely by STTs under zero magnetic field[71], which are comparable with or even more efficient than one by SOTs. In the 2020s, some records by SOTs via SHE are approaching 6,000 m/s[57], however, they require an external in-plane magnetic field to assist the effective DMI field to form chiral Néel DWs and is disadvantageous for industrial implementation.

We end this introduction chapter by showing the benchmark of CIDWM records in Figure 1.9[28, 57, 61, 67, 71, 102, 104–106]. In the next chapter, research on Mn_4N and its based nitrides, one of the promising candidates for CIDWM, will be presented.

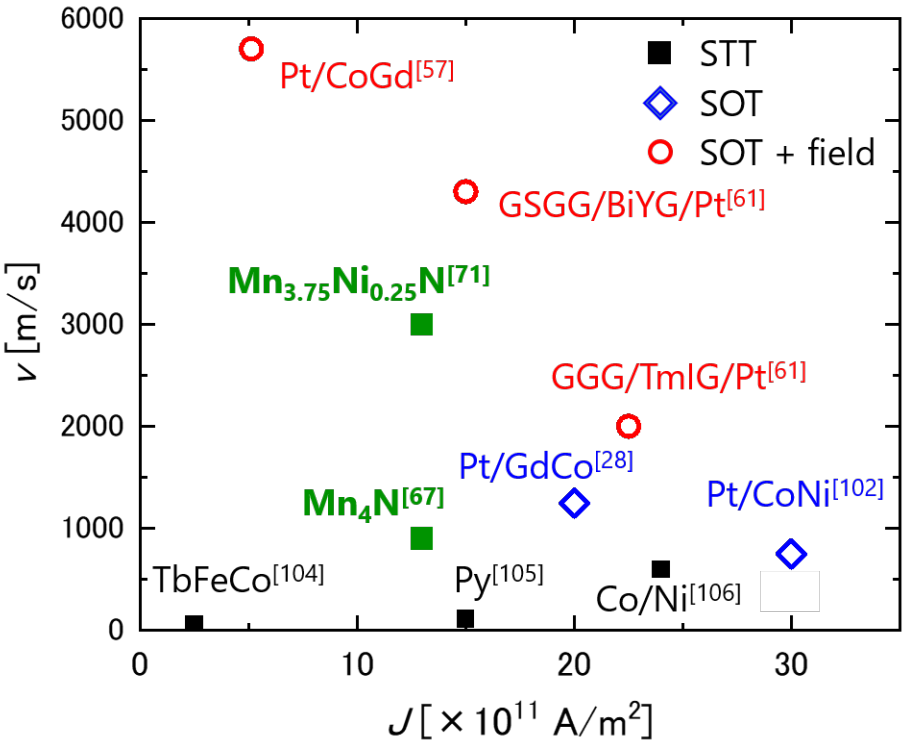

Figure 1.9: *The benchmark of CIDWM in various materials.*

Chapter

Mn_4N-based nitrides and application to CIDWM 2

In this chapter, we introduce the properties and advantages of anti-perovskite magnetic nitrides, especially Mn_4N and $Mn_{4-x}A_xN$, where A refers to another element. The first section shows the brief history of the study on various nitrides, mainly on anti-perovskite nitrides such as Fe_4N, Mn_4N, Co_4N, and Ni_4N with our previous reports. The second section explains Mn_4N for the case of Mn_4N bulks and Mn_4N films, separately. The third section deals with the Mn_4N based nitrides where Mn atoms are partially substituted by other magnetic or non-magnetic elements, especially $Mn_{4-x}Ni_xN$ and $Mn_{4-x}Co_xN$ with compensation composition ratios. The fourth and last chapter introduces our previous study on CIDWM in $Mn_{4-x}Ni_xN$ multiwires. We also show the impact of the compensation in $Mn_{4-x}Ni_xN$ on CIDWM and the things to be improved for more efficient CIDWM in Mn_4N type nitrides. We end this chapter with a summary in the fifth section.

2.1 Nitrides

Nitrides have been important materials thanks to practical applications such as cutting materials. They're often used as semiconductors with wide band gaps or insulators. In this section, we first show the fundamental properties and the previous study of nitrides, especially on compounds made of nitrogens and $3d$ transition metals. Then, we focus on the anti-perovskite nitrides which show unique properties thanks to the hybridization between electrons of nitrogen atoms and those of metals.

2.1.1 Fundamental properties of nitrides

Nitrides are compounds that contain nitrogen with a formal oxidation state of -3. The nitride ions (N^{3-}) tend to strongly donate electrons to metal cations, forming metallic nitrides. They are often categorized as refractory materials, thanks to their high lattice energy which derives from the strong electronegativity of N^{3-}. Boron Nitride[107], Titanium Nitride[108, 109] and Silicon Nitride[110, 111] are representatives of hard nitrides, which are used for hard coatings and cutting metals in our lives[109]. As another important feature, nitrides generally have wide band gaps, and thus are categorized as insulators or semiconductors. One of the most notable successes is Gallium nitride, which has a band gap of approximately 3.4 eV at room temperature (RT) and can be applied to power semiconductors. Also, by doping GaN with

In ions, it functions as blue light emitting diodes[112–114] (Nobel prize in physics in 2014). Therefore, similarly to oxides, nitrides appear suitable for various practical applications.

Most nitrides are made of nitrogens and transition metals. Formulas for such compounds are given as AN, A_2N, A_4N, and so on, where A represents the ion of transition metal ions. In these nitrides, the nitrogen can be interstitial between the atoms or holes, or well located in the crystalline structures. In the case of the latter, they are generally inert, represented by high melting points, hardness, and metallic luster. Importantly, their stability and properties depend on the crystalline structure and on the ratio of nitrogen in the system. $3d$ magnetic transition metals such as Fe, Co, Mn, and Ni also form magnetic nitrides as mentioned. However, these magnetic nitrides are only semi-stable and tend to decompose into substitute elements or compounds, which is also clear from phase diagrams. For example, Fe_2N decomposes at 200 °C[115, 116]. Ni nitrides are also very easy to get denitrided, such as $Ni_4N \rightarrow Ni_8N + Ni$[117, 118]. The stability of such nitride depends on stoichiometry, the composition ratio, and the crystalline structures. In the following sections, we focus on the anti-perovskite nitrides.

2.1.2 Anti-perovskite nitrides

Figure 2.1 shows the structure of anti-perovskites. Typically, anti-perovskites have a formula of AB_3X where A and B are metal ions and X is an anion, generally oxygen, nitrogen, carbon, or boron ions. In this structure, the cation is located at the body-centered site of the crystal lattice, and the anions are at the corner sites (I sites) and the face-centered sites (II sites). For $3d$ magnetic nitrides, the chemical formula is given by A_4N where A is one of the $3d$ transition metals. Additionally, A_4N based magnetic nitrides are often formed, represented by the chemical formula of A_3BN or $A_{4-x}B_xN$ where B is a transition metal different from A, a non-magnetic transition metal such as copper and zinc, or a basic metal such as gallium and tin.

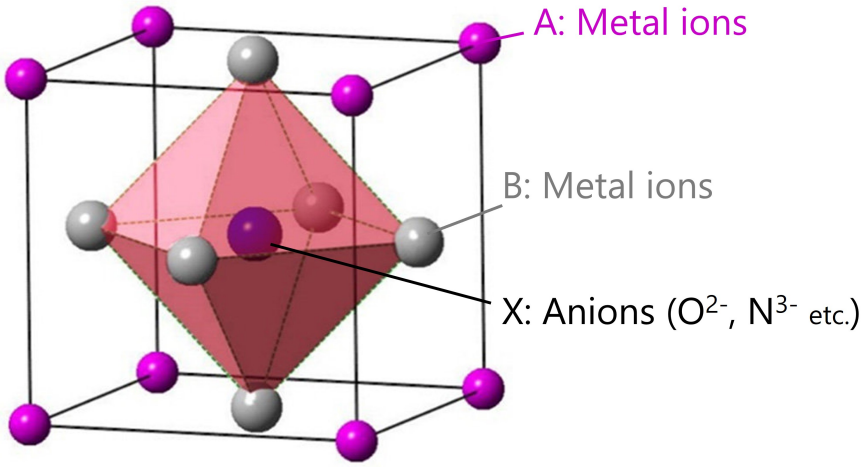

Figure 2.1: *Structure of anti-perovskite crystals. A (at corner sites) and B (at face-centered sites) denote the metal ions and X (at the body-centered site) is an anion such as O^{2-} and N^{3-}.*

Among the variety of anti-perovskite magnetic nitrides, Fe_4N and Mn_4N have been long studied. Fe_4N has been known for a thermally stable and strong ferromagnet with a high Curie temperature (T_C = 767 K)[119] and a large saturation magnetization (M_S = 1100 ∼ 1300 kA/m)[120]. It attracts a lot of attention thanks to the report that it has a theoretically 100 % negative spin polarization of the conduction electrons (P_σ)[121]. Such a large spin polarization was also experimentally proven by point-contact Andreev-reflection measurement ($|P| >$

0.59)[122] and through the existence of a large TMR ratio of 75 % at RT in the heterostructure of CoFeB/MgO/Fe_4N[123]. It was proposed that electrons of Fe(II) are hybridized with those of N due to the smallest interatomic distance in the lattice and that this hybridization causes the shift in the energy states of up-spin $4s$ and $4p$ electrons. Importantly, the hybridization of electrons between metals at II sites and nitrogens at body-centered sites is the source of the unique properties of anti-perovskite nitrides. Likewise, the hybridization between the $2p$ orbitals of the nitrogens and the $3d$ orbitals of the metals is the main source of the electronic transport dominated by the face-centered atoms and their electrons. We focus on Mn_4N in detail in the following sections. In short, Mn_4N has been a research target for a long time because it is the only ferrimagnet among Mn-nitrides. Especially, researchers are nowadays focusing on the application of Mn_4N to CIDWM, manipulation of skyrmions[124], topological Hall effect[125] and so on. In spite of their relative instability, Co_4N and Ni_4N are also recognized as the representatives of $3d$ transition metal nitrides. Like Fe_4N, Co_4N is another nitride with high spin polarization. It was expected to have P_{DOS} of -0.88 according to the first-principle calculations[126]. Although Ni_4N is very easy to get denitrided into stable fcc-Ni as mentioned above[117, 118], fct-Ni_4N was reported to be paramagnetism[127] while fcc-Ni_4N is ferromagnetic (T_C = 121 K)[128, 129].

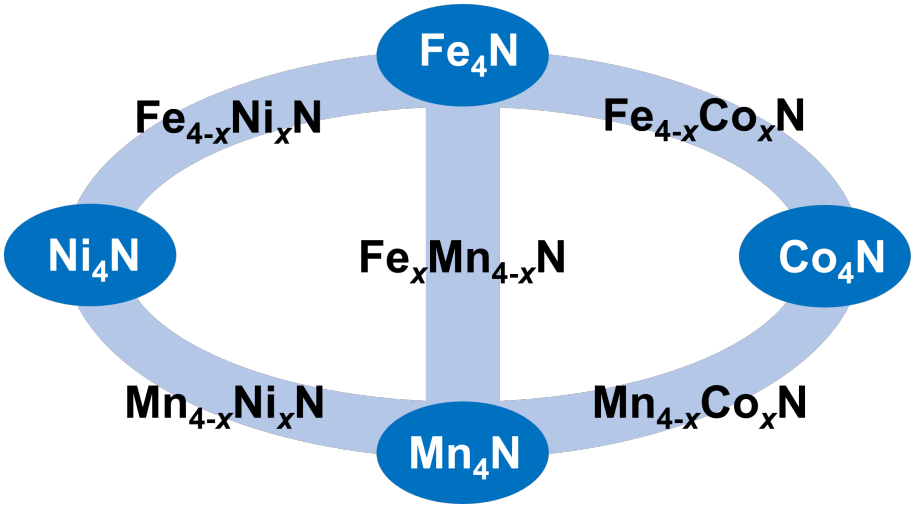

Figure 2.2: *Scheme of the family of anti-perovskite magnetic nitrides made from 3d transition metals. Our group in Univ. Tsukuba succeeded in developing the epitaxial growth of these magnetic nitrides by molecular beam epitaxy.*

Nevertheless, the importance of Co and Ni atoms in anti-perovskite nitrides is that they can be partially substituted with Fe and Mn atoms in Fe_4N and Mn_4N, respectively. Figure 2.2 shows the group of $3d$ transition metal-based anti-perovskite nitrides. Our group in Univ. Tsukuba succeeded in developing the epitaxial growth of such nitrides by molecular beam epitaxy (MBE) by controlling the temperature of Knudsen cells with solid metal sources. We succeeded in modulating not only structural but also magnetic and electric properties by modifying the composition ratio of transition metals. The first case of the anti-perovskite nitrides with mixed transition metals was $Fe_{4-x}Co_xN$ in which a very large spin polarization was expected in the first principle calculation[130–132]. $Fe_{4-x}Mn_xN$ was one of the representatives in which we succeeded in modulating the magneto-transport properties, the transition of P_σ and the change in the magnitude of anomalous Hall effect[133, 134]. In $Mn_{4-x}Ni_xN$ and $Mn_{4-x}Co_xN$, notably, we proved the magnetic compensation (MC) by Ni (Co) composition ratio at room temperature[70, 75], and we experimentally performed the fast CIDWM in $Mn_{4-x}Ni_xN$ microwires with taking the advantage of angular momentum compensation (AMC)[71]. We are

going to deal with these two compound nitrides in detail in section 3.3. In addition, Mn_3AN nitrides such as Mn_3NiN[135, 136], Mn_3CuN[137–139], Mn_3ZnN[140–142] and Mn_3GaN[143, 144] have been intensely studied in the last decade as candidates for negative thermal expansion (NTE) or barocaloric materials. Technically, these nitrides are known to have non-collinear ferrimagnetism or antiferromagnetism, and the transition of their antiferromagnetic modes at a particular temperature is related to NTE.

2.2 Mn_4N

In this section, we focus on the fundamental properties of Mn_4N. Although the main focus of our work is Mn_4N films and related nitrides, we first focus on Mn_4N bulks, then on Mn_4N films. This is because the structural and magnetic properties of Mn_4N bulks and films are different.

2.2.1 Mn_4N bulks

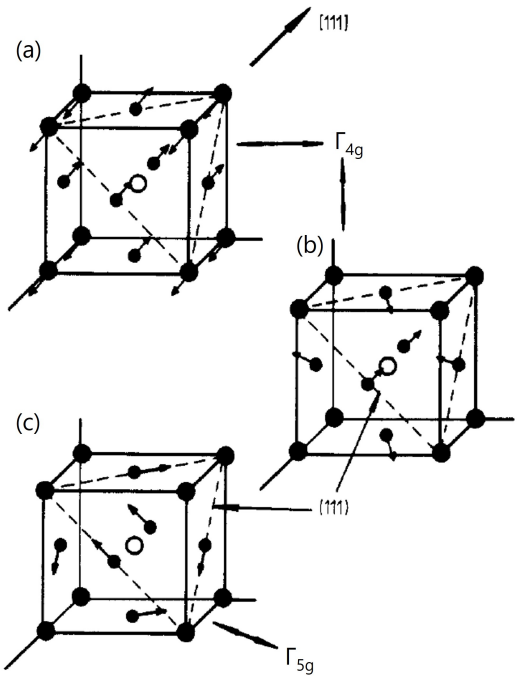

Figure 2.3: *Magnetic structures which can be possibly taken in bulk Mn_4N. (a) Collinear models in which magnetic moments of Mn at corner sites and those at face-centered sites align antiparallel (b) and (c) Non-collinear models in which only Mn at corner sites devote to the magnetization. The structures in (a) and (b) are in a Γ_{4g} mode, and the structure in (c) is based on a Γ_{5g} antiferromagnet mode, respectively.*

Although various types of manganese nitrides had been fabricated by heating Mn metal sources with a stream of N_2 gas[145], the first significant founding was the experimental evidence of ferrimagnetism in Mn_4N bulks by neutron-ray diffraction (NRD)[146, 147]. Figure 2.3 shows the ferrimagnetic structures of Mn_4N bulks based on NRD measurements and their [111] magnetization easy-axis. Fig. 2.3(a) is the model in which we assume that Mn_4N bulk is a collinear ferrimagnet and the magnetic moments of Mn(I) and Mn(II) are antiparallel. On the contrary, Fig 2.3(b) and (c) are based on the assumption that Mn_4N bulk has a non-collinear

magnetic structure, technically, Γ_{4g} mode for Fig 2.3(b) and Γ_{5g} mode for Fig 2.3(c). The magnitude of magnetic moments of Mn(I) were found to be 3.85 μ_B and those of Mn(II) were to be -0.89 μ_B, thus 0.86 μ_B per unit cell[147]. This is reasonable that magnetic moments of Mn(II) are much smaller than those of Mn(I) because $3d$ orbitals of Mn(II) are easy to get hybridized with orbitals of N atoms and become itinerant.

In spite of the special fact that the Mn_4N bulk is the only ferrimagnet among manganese nitrides with a relatively high T_C of 742 K[147], the study of Mn_4N has not been as intense as that of Mn_4N films, which started in the 1990s. However, Mekata already started to work on the Mn_4N based compounds and anticipated the magnetic compensation in $Mn_{4-x}In_xN$ and $Mn_{4-x}Sn_xN$ bulks[148]. These studies afterward opened the gate of the study in Mn_3AN type nitrides for the sake of the realization of NTE materials and so on, as explained in section 2.1.2.

2.2.2 Mn_4N films

The first report on the epitaxial growth of Mn_4N was the case in which the direct current (DC) sputtering method was used and Si(001) was chosen as the substrate[149]. Interestingly, they showed PMA and a slightly strained structure, with in-plane tensile strain, unlike cubic bulk Mn_4N with the easy-axis along [111] azimuth. In this context, Mn_4N films started to attract attention as rare-earth free PMA magnets. The report of the growth of Mn_4N crystalline films on SiO_2[150] (with MnO buffered layer[151]), SiC(0001)[152, 153], GaN(0001)[152, 153], Al_2O_3(0001)[153], MgO(001)[63–65, 124], $SrTiO_3$ (STO)(001)[63, 65, 67, 71] represents this attraction. Additionally, Mn4N films can epitaxially grow onto MgO(110) and (111) substrates, and they show topological Hall resistivity due to the emergence of non-collinear magnetic structures[154, 155]. Meantime, the growth processes have been extended to RF-sputtering (Ar + N_2 supplied)[124], molecular beam epitaxy (MBE) (N-plasma assisted)[63, 65, 67, 71] and pulse laser deposition (PLD)[62].

Figure 2.4 shows the expected magnetic structure of 001 oriented Mn_4N films. Since NRD is effective only when a sample is thick enough and can be considered as a bulk, we do not have direct experimental proof on the magnetic structure of Mn_4N film. Thus, we revealed its structure by the experimental fact that the magnetic moments of Mn(I) and Mn(II) are antiparallel according to the X-ray magnetic circular dichroism (XMCD) analysis[70], and these magnetic moments are aligned along [001] directions which is consistent with the PMA proven by experiments. Besides the structure presented in Fig. 2.4, other magnetic structures such as non-collinear magnetic structures are expected to be formed through the topological properties observed in experiments[125, 154–156]. However, we take the image of Fig. 2.4 as the standard magnetic structure of Mn_4N film in this work because we couldn't find evidence of a non-collinear magnetic structure in XMCD and neither the experimental nor theoretical proof on the stable state of Mn_4N with a non-collinear magnetic structure has been reported. Although the magnitude of the PMA depends on the crystalline quality and thus on the substrates, the uniaxial anisotropic constant (K_U) of Mn_4N films (10-40 nm thickness) is usually 0.1 $\sim$ 0.2 MJ/m^3 when grown on MgO(001) and STO(001)[63–65, 69]. As mentioned above, Mn_4N films are not perfectly cubic with the in-plane tensile strain ($c/a \sim 0.99$). Importantly, this in-plane tensile strain can be observed regardless of the lattice mismatch between Mn_4N and substrates[63], and theoretical calculations also suggest that the cohesive energy of Mn_4N crystals become rather lower with the in-plane tensile (c/a *sim* 0.98)[156]. We will investigate the correlation of the in-plane tensile and PMA of Mn_4N as represented in chapter 3. The M_S of Mn_4N films also depends on the crystalline quality and on the structure of samples. Usually, samples fabricated on MgO(001) and STO(001) substrates with our MBE chamber and method show the M_S of 60 $\sim$ 100 kA/m[63, 64, 67, 69], and the reported values of M_S in Mn_4N films

are smaller than those in bulks. It was suggested that the nitrogen atoms at body-centered sites have an important influence on M_S and K_U of Mn_4N films[64, 156].

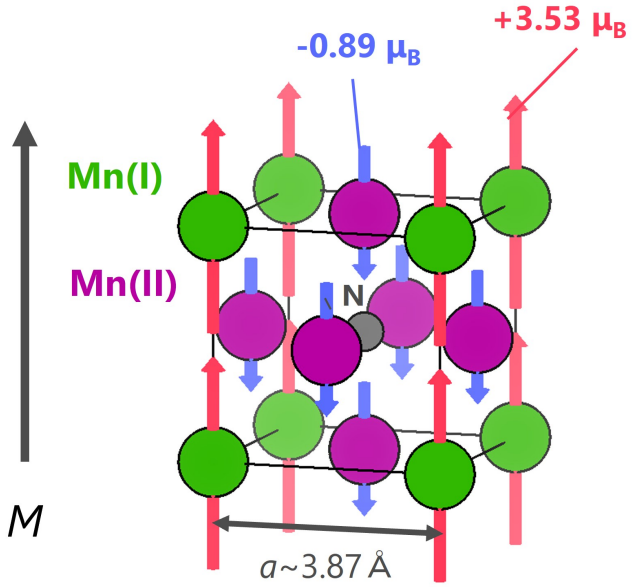

Figure 2.4: *Magnetic structure of Mn_4N film with PMA. The magnetic moments of Mn(I) and Mn(II) are antiparallel. The value of the magnetic moments are based on the ones in bulk Mn_4N.*

Unlike in bulk Mn_4N, electric and magneto-transport properties have been often investigated in Mn_4N films. One of the important features is a relatively large anomalous Hall effect (AHE) represented by a large AHE angle ($\theta_{AHE} = \rho_{AHE}/\rho_{xx} \sim 2$ %)[67, 69]. Generally, the large AHE can be found in materials that include heavy elements with a large spin-orbit interaction (SOI) or in those which have large Berry curvatures such as magnetic Weyl semimetals [157]. However, the origin of the AHE in Mn_4N is still obscure. For example, Shen *et al.*, suggested the main mechanism of AHE is skew-scattering after investigating the correlation between ρ_{AHE} and ρ_{xx}[62], while Kabara *et al.*, anticipated the intrinsic deflection takes an important role from the temperature dependence of ρ_{AHE} and that the anisotropic magnetoresistance (AMR)[158]. By considering this work, we will further investigate the magneto-transport properties of Mn_4N and $Mn_{4-x}Ni_xN$ in chapter 4.

Gushi from our group in Univ. Tsukuba reported that the magnetic and magneto-transport properties in Mn_4N films are related to their crystallininity[65]. Figure 2.5 shows the hysteresis loops of AHE at RT in Mn_4N films and their images of magnetic domains taken when samples were half magnetized at $M = 0$[65]. Here, magnetic domains were observed using a magnetic force microscope (MFM) for Mn_4N/MgO and a magneto-optical Kerr effect (MOKE) microscope for Mn_4N/STO. In Mn_4N/MgO, the nucleation of domains was relatively slow. On the other hand, it was sharp in Mn_4N/STO as judged from the squareness of the loop. Focusing on the magnetization reversals after the nucleation, they were sharper in Mn_4N/STO. According to the images of magnetic domains, they were only 10-100 nm wide in Mn_4N/MgO, while they were often more than 1 mm wide in Mn_4N/STO. Through these results, we concluded that the magnetization reversals initiate with the large density of nucleation sites nucleation followed by the propagation trapped by strong pinning sites in Mn_4N/MgO, while they initiate with the small density of nucleation followed by the smooth propagation in Mn_4N/STO. From the observation of the cross-sectional images with a transmission electron microscope (TEM), we found that Mn_4N/MgO contained more defects due to the large lattice mismatch and that

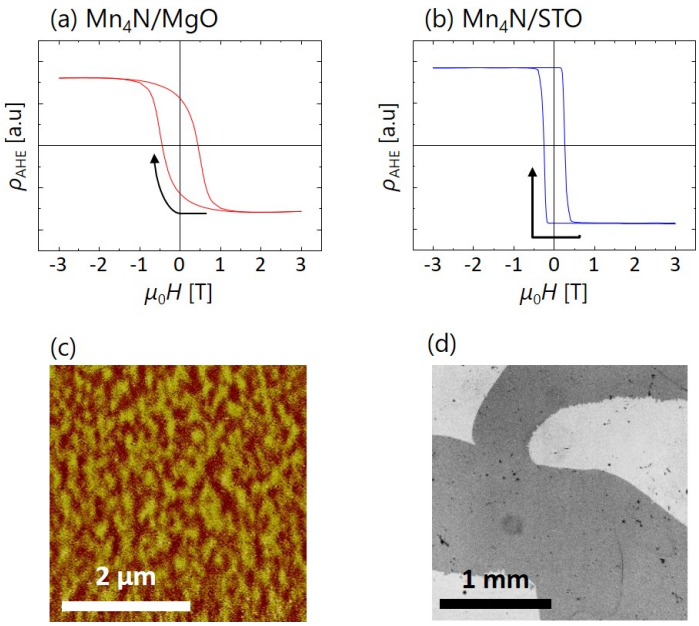

Figure 2.5: *AHE loop taken at RT (a) for Mn_4N/MgO and (b) for Mn_4N/STO, and the images of magnetic domains for (c) for Mn_4N/MgO and (d) for Mn_4N/STO. The domains were observed with a magnetic force microscope for (c) and with a magneto-optical Kerr effect (MOKE) microscope for (d) when the magnetization is half reversed.*

they could function as traps for domains (cf. Figure 3.11 for the cross-sectional TEM images of Mn_4N). We will grow Mn_4N on various substrates which give the different values of lattice mismatch and investigate the change in their properties, especially the PMA in chapter 3.

2.3 Substitution in Mn_4N

The significant feature of anti-perovskite nitrides is that they can consist of more than two types of metals, and Mn_4N is not an exception. Compounded bulk nitrides are generally fabricated by sintering the metallic alloy with nitrogen gas. For films, the growth by MBE is ideal to investigate the composition dependence of the properties because the composition ratio can be easily modulated by the temperature of Knudsen cells. Our group has worked on these compounds fabricated by MBE and has investigated their magnetic, magneto-transport properties, and so on. In this section, we mainly focus on $Mn_{4-x}Ni_xN$ and $Mn_{4-x}Co_xN$, which have the compensation composition ratios at RT. We also introduce bulk $Mn_{4-x}In_xN$ and $Mn_{4-x}Sn_xN$ as the first compensated ferrimagnetic nitrides, and other compounds in which the compensations were demonstrated in bulk samples.

2.3.1 $Mn_{4-x}Ni_xN$

The author of this thesis has worked on the growth and the evaluation of $Mn_{4-x}Ni_xN$ films at Univ. Tsukuba. We discuss $Mn_{4-x}Ni_xN$ films fabricated by MBE with a composition ratio of $x < 0.5$ because $Mn_{4-x}Ni_xN$ with high x is energetically unstable and very easy to get denitrided, which was evidenced by the Mn-Ni alloy phases in the film[68]. Nevertheless, $Mn_{4-x}Ni_xN$ films show the drastic change in their magneto-transport properties and magnetic structures even with small x[69].

Figure 2.6(a) shows the Ni composition ratio dependence of the anomalous Hall angle (θ_{AHE})

and Fig. 2.6(b) exhibits the temperature dependence of the magnetization in $Mn_{4-x}Ni_xN$ films (30 nm deposited on STO(001) substrates)[69]. Mn_4N ($x = 0$) showed the negative value of θ_{AHE}, which correspond to previous reports for Mn_4N/MgO[62]. The value of θ_{AHE} scarcely changes with the Ni composition ratio for $0 < x < 0.2$, however, it drastically changes and its sign reverses for $0.2 < x < 0.25$. There are several factors that could contribute to the change of the sign of AHE: the reversal of the magnetization[159], the change of the conduction carrier[160] and the change of the spin polarization of P_σ[134]. The latter two factors, however, are not likely in the case of $Mn_{4-x}Ni_xN$ because they rather tend to show chronic shifts against the composition ratio. Moreover, the change in the dominant carrier simultaneously causes the sign reversal in the ordinary Hall effect, which we did not observe, and it was found afterward that the sign of P_{sigma} does not change by Ni composition ratio from the first-principle calculation[71]. These inquiries suggested the possibility of the reversal of magnetic moments. This hypothesis was reconfirmed by the result in Fig 2.6(b). While Mn_4N showed a temperature dependence of the magnetization shown in typical ferromagnets, the magnetization decreased with the temperature below approximately 200 K in $Mn_{3.75}Ni_{0.25}N$. Such a change is an indication of ferrimagnetism as shown in Fig. 1.2. Considering that the effect of the magnetic moments of Ni is small due to the small composition ratio, this phenomenon comes from a change of the direction or the magnitude of magnetic moments of Mn atoms.

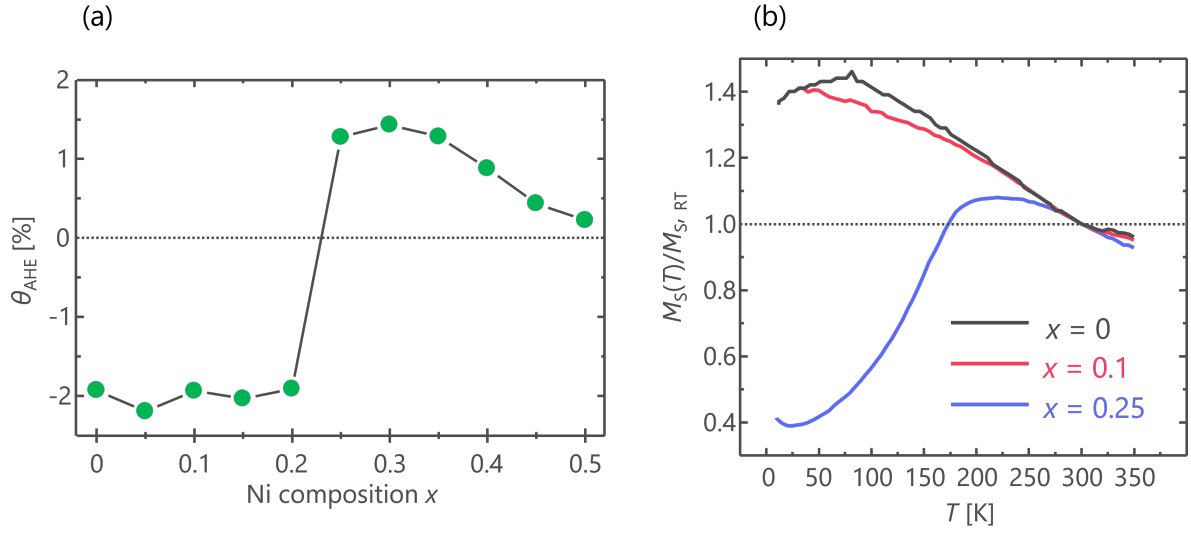

Figure 2.6: *(a) Ni composition ratio (x) dependence of the AHE angle (θ_{AHE}) of $Mn_{4-x}Ni_xN$/STO at RT. (b) Temperature dependence of the magnetization of $Mn_{4-x}Ni_xN$/STO. The measurement was performed under the field cooling (FC), and the magnetizations were normalized by the values at RT (300K).*

In order to confirm the magnetic structures of $Mn_{4-x}Ni_xN$, XMCD measurements and analysis were performed for $Mn_{4-x}Ni_xN$ samples ($x = 0.1$ and 0.25)[70]. Figure 2.7 shows their X-ray absorption spectroscopy (XAS) and XMCD spectra, while Figure 2.8 shows their magnetic structures derived from the spectra in Fig. 2.7. In XAS spectra, we observed several satellite peaks. The peaks pointed by arrows suggest the hybridization between $3d$ orbitals of Mn(II) and $2p$ orbitals of N[161], satellites A (A') originated from manganese oxides[162], and satellites B (B') are reproducible by a one-electron relativistic tight-binding calculation even though their origins are still not revealed[163]. Focusing on XMCD spectra, although the configuration of the XMCD spectra at Mn edges is complex due to the mixing of the effect from Mn(I) and Mn(II), we attributed the sharp peaks marked with "α" to Mn(I) with localized d electrons and the broad peaks, and ones marked with "β" to Mn(II) with itinerant d electrons.

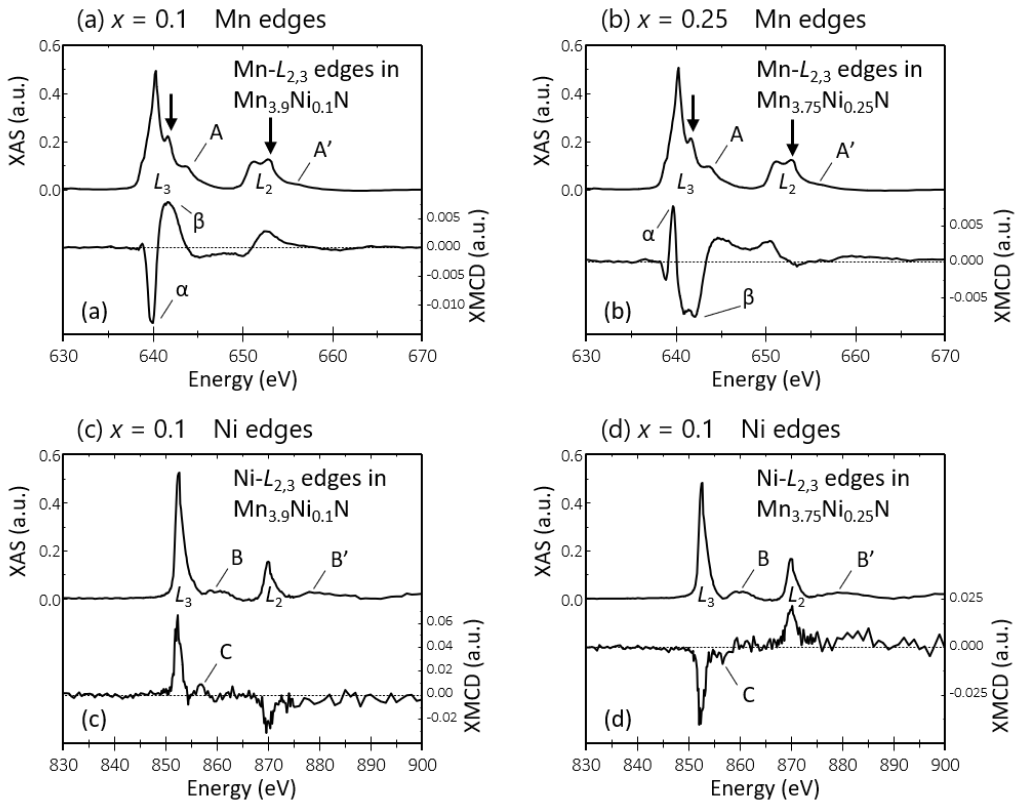

Figure 2.7: *XAS and XMCD spectra of $Mn_{4-x}Ni_xN$ (x = 0.1 (a) (c), 0.25 (b) (d)) under the magnetic field along [001] direction. (a) and (b) are magnified around the absorption edges of Mn and (c) and (d) are around those of Ni.*

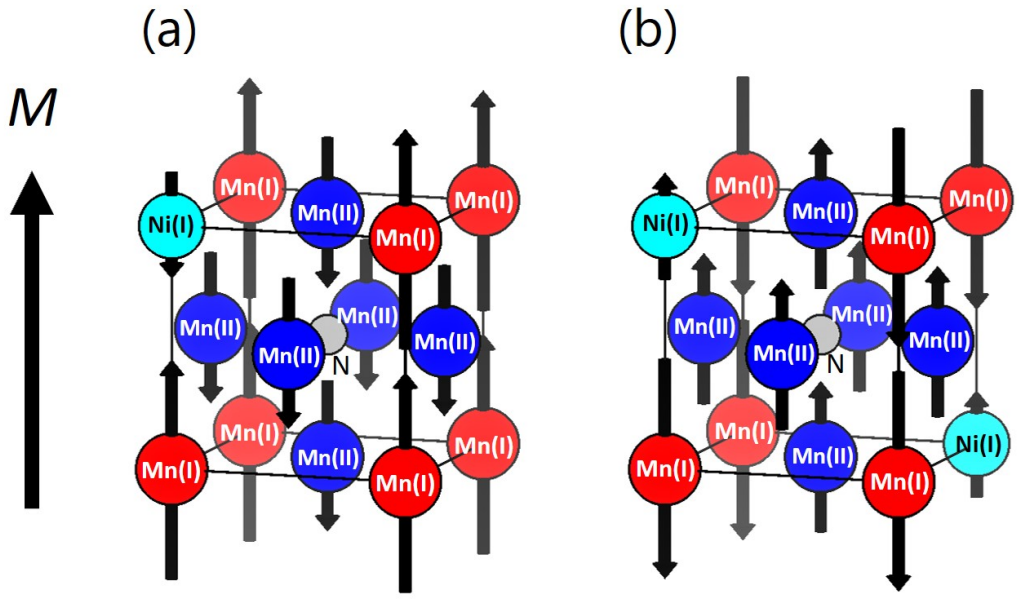

Figure 2.8: *Magnetic structures derived from XMCD measurements and analysis for (a) below and (b) above the magnetic compensation point. The arrow M indicates the direction of the net magnetization.*

This was also verified by the first-principles calculation using the all-electron full-potential linearized augmented-plane-wave (FLAPW) method and Fermi's golden rule[161]. In this way, it is clear that peaks of Mn edges all flip by Ni composition ratio. In the XMCD spectra of Ni, we observed the single streak absorption peak at L_3 and L_2 edges with the satellite peaks marked with C (C'), which are mainly due to the configuration interaction between the final state multiples written by $2p^5 3d^9$ and $2p^5 3d^{10}$[164]. From this, we confirmed that Ni atoms preferentially occupy I sites and the sign of peaks in XMCD spectra of Ni reverse like the case of Mn. Therefore, we proposed that all magnetic moments of $Mn_{4-x}Ni_xN$ flip by Ni composition ratio ($x \sim 0.2$), and the total value of magnetic moments of $Mn_{4-x}Ni_xN$ is zero exactly at this point. In this way, the magnetic compensation in $Mn_{4-x}Ni_xN$ was proven. This is the first rare-earth free compensated ferrimagnet at RT in a single layer. Here, the PMA was preserved in the range of $0 < x < 0.5$, therefore, we have high hope for $Mn_{4-x}Ni_xN$ as a candidate for the CIDWM material.

2.3.2 $Mn_{4-x}Co_xN$

$Mn_{4-x}Co_xN$ is another Mn_4N-based ferrimagnetic nitride, proposed by Ito, Yasutomi, and Mitarai in our group of Univ. Tsukuba. It was first experimentally demonstrated that the composition ratio dependence of M_S in $Mn_{4-x}Co_xN$ ($0 < x < 4$) at RT shows the local minimum value at $x = 0.8$[73]. Also, the PMA is preserved for $x < 0.8$, while it shows very small magnetic anisotropy for a higher Co composition ratio, eventually changing into an in-plane magnetic anisotropy.

Like in the case of $Mn_{4-x}Ni_xN$, its compensation was studied by XMCD as well. Figure 2.9 shows the XAS and XMCD spectra of $Mn_{4-x}Co_xN$ ($x = 0.2$, 0.8, 1.3) and Figure 2.10 shows the magnetic structures derived from the spectra in Fig. 2.9. We classified the peaks in Mn spectra as α and β in the same way as the case of $Mn_{4-x}Ni_xN$. In this way, we discovered that magnetic moments of Mn flipped twice when modulating the Co composition ratio, between 0.2 and 0.8, and 0.8 and 1.3. In Co absorption edges, we also found the reversal of the spectra twice. Moreover, for $x = 1.3$, we observed two absorption peaks with different signs at each L_3 and L_2 edges, marked with A and B at the L_3 edge and A' and B' at the L_2 edge. This result suggested that Co atoms were replaced not only by Mn(I) but also by Mn(II) atoms, which is consistent with the high Co composition ratio ($x = 1.3 > 1.0$). We had also already revealed that $3d$ transition metal at II sites has absorption energy approximately 2 eV higher than that of I sites due to the hybridization states made by $3d$ orbitals of the metal at II sites and $2p$ orbitals of the nitrogen. Therefore, we found that the peaks "A" and "A'" originate from Co(I) and "B" and "B'" originate from Co(II), and proposed the magnetic structures in Fig. 2.10.

These results show that the magnetic compensation presumably takes place both between $x = 0.2$ and 0.8, and between $x = 0.8$ and 1.3. Therefore, $Mn_{4-x}Co_xN$ possibly has two magnetic composition ratios at RT, which is a very unique feature. Kaneyoshi proposed that the existence of two compensation points in a ferrimagnet is theoretically possible by modulating temperature[165], and Zhang nearly observed two magnetic compensation points by modulating the ratio of Mn and Cr in a ferrimagnetic $Co(Cr, Mn)_2O_4$. However, they finally could not evidence a double compensation because of drastic changes in the Curie temperature and crystalline quality[166]. Thus, $Mn_{4-x}Co_xN$ films could be the first ferrimagnets with experimentally proven multiple magnetic compensation points. We assume that multiple compensations could be achieved thanks to Co atoms replaced by Mn(II) atoms, not Mn(I). For the same reason, we also predict that $Mn_{4-x}Ni_xN$ may have more than two compensation points for a higher Ni composition ratio such as $x \sim 1$. However, we have not succeeded in the epitaxial growth of $Mn_{4-x}Ni_xN$ on STO for $x > 0.5$ with our growth system. If we can optimize the growth

condition for a higher Ni composition ratio or adopt the element without the strong preference in the site selectivity for I sites, we may be able to discover other ferrimagnetic nitrides with multiple compensation points.

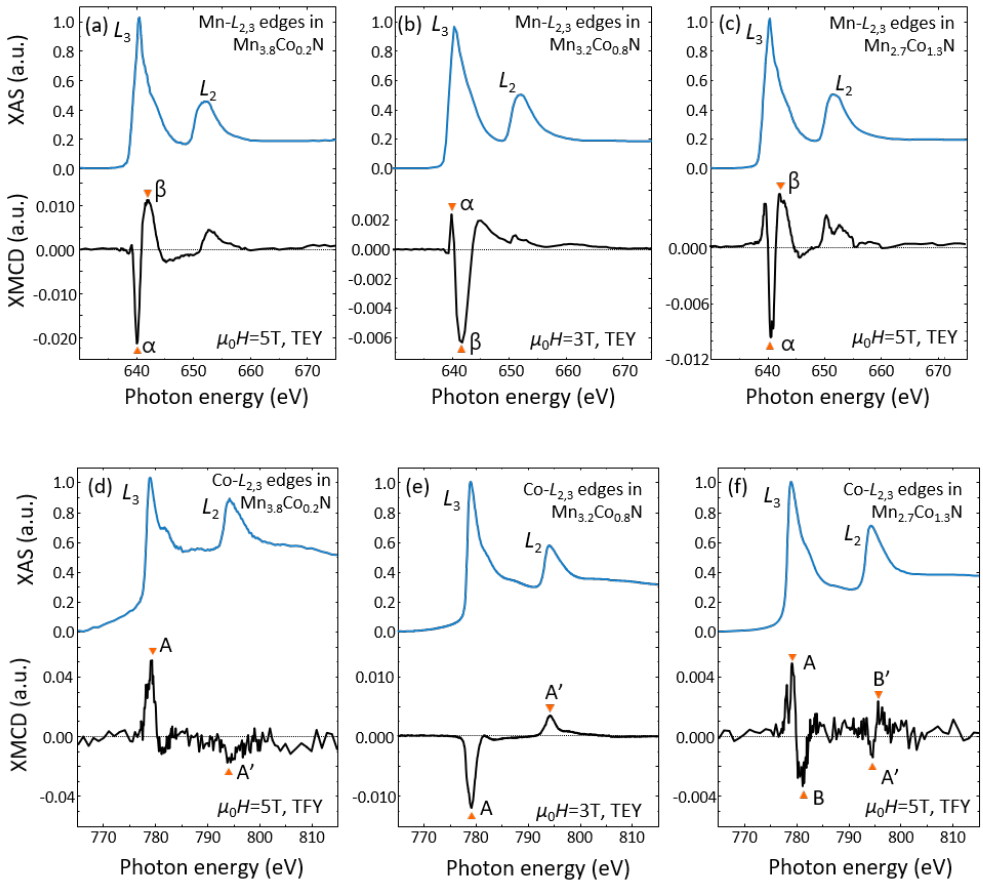

Figure 2.9: *XAS and XMCD spectra of $Mn_{4-x}Co_xN$ ((a) and (d) $x = 0.2$, (b) and (e) $x = 0.8$, (c) and (f) $x = 1.3$). (a), (b) and (c) are magnified around the absorption edges of Mn and (d) and (e) and (f) are around those of Co.[74, 75]*

2.3.3 Other Mn_4N based compounds

Historically, the fabrication and characterization of anti-perovskite nitrides compounds have been attempted even since the 1960s. One of the most noteworthy achievements is the study in bulk $Mn_{4-x}In_xN$ and $Mn_{4-x}Sn_xN$ and the possibility of their compensation by Mekata[148]. In this report, the temperature and the composition ratio dependences of the magnetization were investigated, and the local minimum of the magnetization approaching zero at $x \sim 0.25$ for $Mn_{4-x}In_xN$ and $x \sim 0.38$ for $Mn_{4-x}Sn_xN$ at 0 K was reported. Also, $Mn_{4-x}In_xN$ and $Mn_{4-x}Sn_xN$ showed the changes of the temperature dependences of the magnetization with composition ratios, which was similar to the case of $Mn_{4-x}Ni_xN$ in Fig. 2.6 (b). Although it was the study on bulk nitrides, we anticipate that these films may have magnetic compensation by the composition ratio as well.

Recently, the magnetic compensations in various $Mn_{4-x}Z_xN$ bulks were experimentally demonstrated, where Z indicates the metallic element[167]. Figure 2.11(a) shows the composition ratio dependence of the net magnetic moments in bulk $Mn_{4-x}Z_xN$. In this figure, the magnetic moment crossing 0 suggests the magnetic compensation, and Mn1a and Mn3c are

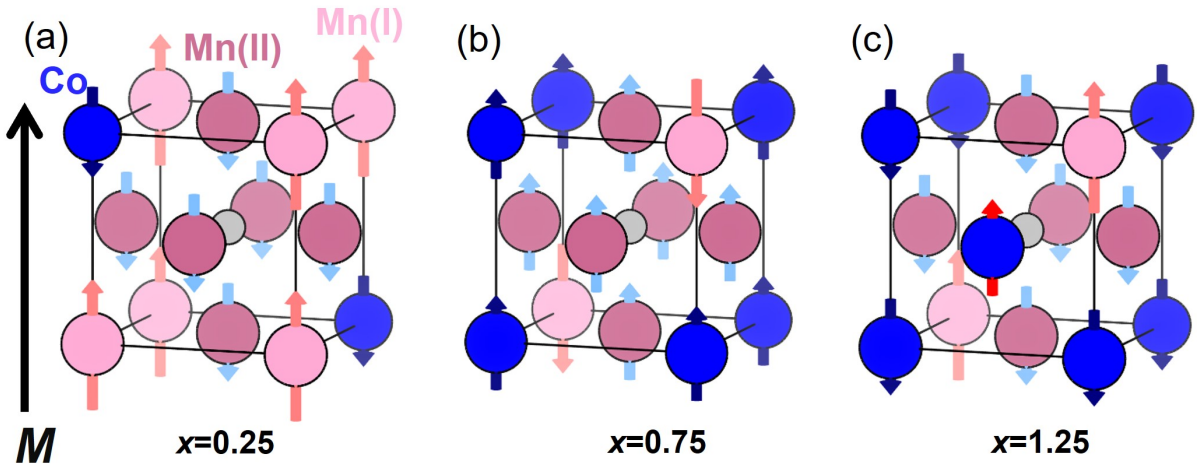

Figure 2.10: *Magnetic structures of $Mn_{4-x}Co_xN$ derived from XMCD measurements and analysis for (a) $x = 0.25$, (b) $x = 0.75$, and (c) $x = 1.25$. The arrow M indicates the direction of the net magnetization.*

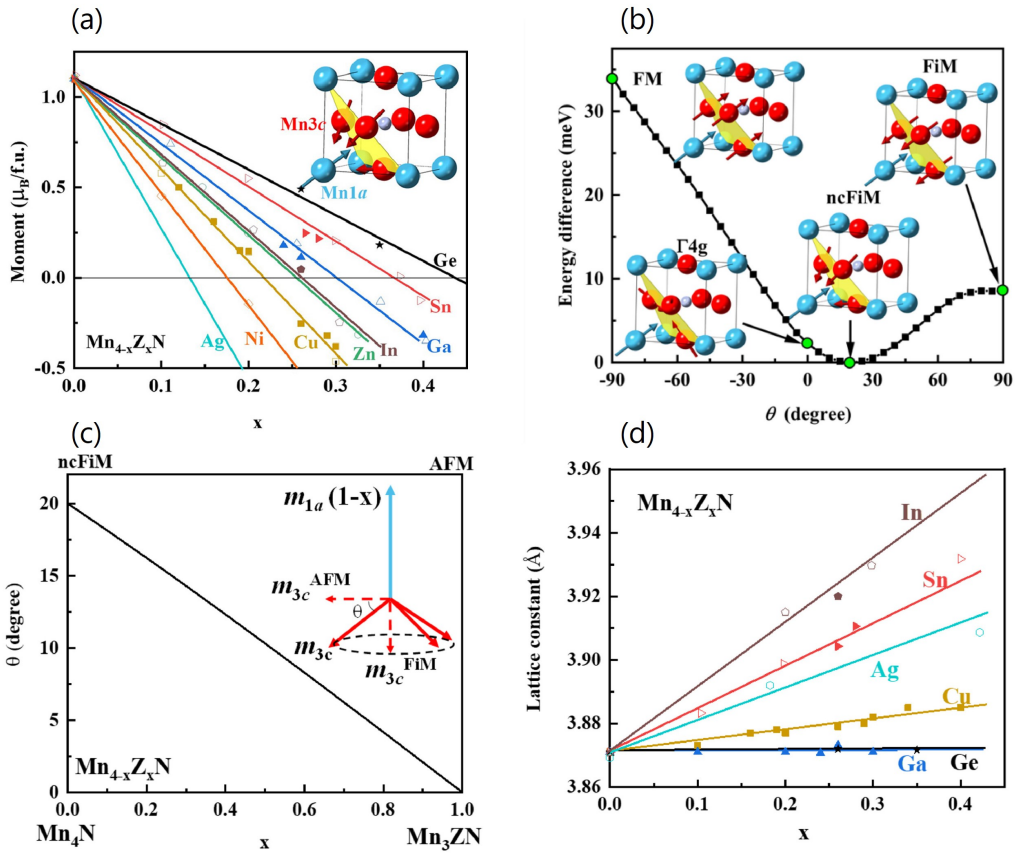

Figure 2.11: *(a) Summary of the net magnetic moment as a function of composition x in bulk $Mn_{4-x}Z_xN$ at RT. (b) Energy difference in the magnetic structure derived by the calculation as a function of tilt angle (θ). (c) Calculated θ versus x. (d) Lattice parameters of $Mn_{4-x}Z_xN$ as a function of x.*

equivalent to Mn(I) and Mn(II), respectively. It is obvious that the magnetic compensation was achieved in various $Mn_{4-x}Z_xN$ bulks with Z of $3d$ transition metals or metallic elements from the 5th period. As mentioned in section 2.2.1, various types of magnetic configurations have been predicted in the cubic bulk Mn_4N. The recent study proposed that magnetic structures of bulk Mn_4N are based on the Γ_{4g} AFM mode, in which magnetic moments of Mn(II) lie in the (111) plane. And what's more, they were found to be the most stable when these magnetic moments are tilted approximately by 20° from the ab-initio calculation. Figure 2.11(b) shows the tilted angle (θ) dependence of the relative cohesion energy in cubic bulk Mn_4N. In such tilted non-collinear ferrimagnet (ncFIM), the magnetic moments of Mn(I) and Mn(II) are not collinear but the net magnetic moments of Mn(I) and those of Mn(II) are antiparallel, leading to the ferrimagnetic Mn_4N. On the other hand, Figure 2.11(c) shows the favorable value of θ which varies by the composition ratio of Z. It was also proposed that the tilted angle decreases as the composition ratio increases in $Mn_{4-x}Z_xN$ in which Z are located at I sites. This change was attributable to the modulation of the exchange interaction between the neighboring Mn(I) and Mn(II) with the replacement of Mn(I) by Z. And at $x = 1$, eventually, $Mn_{4-x}Z_xN$ is expected to completely change into the Γ_{4g} AFM mode.

In spite of our success in the compensated $Mn_{4-x}Ni_xN$ and $Mn_{4-x}Co_xN$, it was suggested that the replacement with Ga would be more favorable for the application as compensated ferrimagnets due to the following reasons. First, especially in the case of Ni, the substitution with Ni causes a drastic change in the magnetic moment of Mn(II), resulting in compensation with a small Ni composition ratio. This is because Ni atoms have 3 more d electrons than Mn atoms do, and these excessive electrons are shared with Mn(II) atoms which are expected to make them behave like Fe with larger magnetic moments than those of Mn. On the contrary, Ga atoms are stable with 10 d electrons and they scarcely share electrons with neighboring Mn(II) atoms. Thus, the Ga atoms do not have a large influence on the magnitude of magnetic moments of Mn, and the modulation of the net magnetization with the composition ratio becomes gentle, which would be beneficial for the better reproducibility of the sample growth. Second, while only $x \sim 0.3$ of Ga is required for the compensation, $Mn_{4-x}Sn_xN$ and $Mn_{4-x}Ge_xN$ require the composition ratio of $x \sim 0.4$ or even more. This is because their doping efficiencies are poor due to their many additional valence electrons. With such a high composition ratio of Sn or Ge, the Curie temperature largely decreases due to their structural instability, which is disadvantageous for the application at RT. In the end, unlikely the elements from the 5th period with a large radius, and ones from the 4th period don't change the lattice constants of $Mn_{4-x}Z_xN$ very much, which is shown in Figure 2.11(d). Therefore, the use of elements from the 4th period would maintain the excellent lattice matching with STO substrates, like the case of $Mn_{4-x}Ni_xN$ films. To conclude, it iss worth attempting the epitaxial growth of these compounds, and the study on the magnetic structures of Mn_4N films.

2.4 CIDWM in $Mn_{4-x}Ni_xN$ and perspectives

In this section, we introduce our the reports of Gushi from our group at Univ. Tsukuba and Ghosh from our group at UGA on CIDWM in $Mn_{4-x}Ni_xN$ microwires and discuss how the compensation affected this CIDWM. Finally, we suggest paths for improvement which will excite the filed of CIDWM more in anti-perovskite nitrides.

2.4.1 CIDWM in $Mn_{4-x}Ni_xN$

The CIDWM in $Mn_{4x}Ni_xN$ films was measured at RT using a polar MOKE microscope, with differential imaging to enhance the magnetic contrast. The samples were fabricated 10 to 30nm

thick on STO(001) substrates and capped with SiO_2 to prevent the Mn_4N layer from oxidation. The films were patterned into 1 μm wide strips using electron beam lithography and ion milling before the deposit of Au/Ti contact pads. Figure 2.12 (a) shows the image of the complete device of microwires and Figure 2.12 (b) is the example of differential MOKE images of DWs with black and white contrasts. We confirmed that the DWs moved in the same direction and the direction of DW motion switched with the current polarity of J. Figure 2.12 (c) shows the DWs velocity (v_{DW}) as a function of the current density (J) in $Mn_{4x}Ni_xN$ microwires. Here, the sample of $x = 0.25$ was above the magnetic compensation point (MCP) and samples of $0 < x < 0.2$ were below it. For composition ratios below the MCP, the DWs moved in the direction of the conduction electrons, and their mobility (dv/dJ) increased as the Ni composition ratio increased, i.e. as the net magnetization decreased in other words. For composition ratios above the MCP, the direction of DW motion reversed, and very large velocities in the direction of the current flow (opposite to the conduction electrons flow), approaching 3,000 m/s, were obtained for a Ni composition ratio around $x = 0.25$ ($M_S \sim 20$ kA/m) and $J = 1.2 \times 10^{12}$ A/m^2. We will discuss the physical background of the reversed CIDWM direction in section 2.4.2. Away from the compensation composition, the DW mobility decreased and eventually reached values similar to those obtained for Mn_4N ($v_{DW} = 900$ m/s). For samples with higher Ni composition ratios, magnetic domains were not observed anymore due to the weak MOKE contrast and the nucleation of very small domains, probably because of worse crystalline quality.

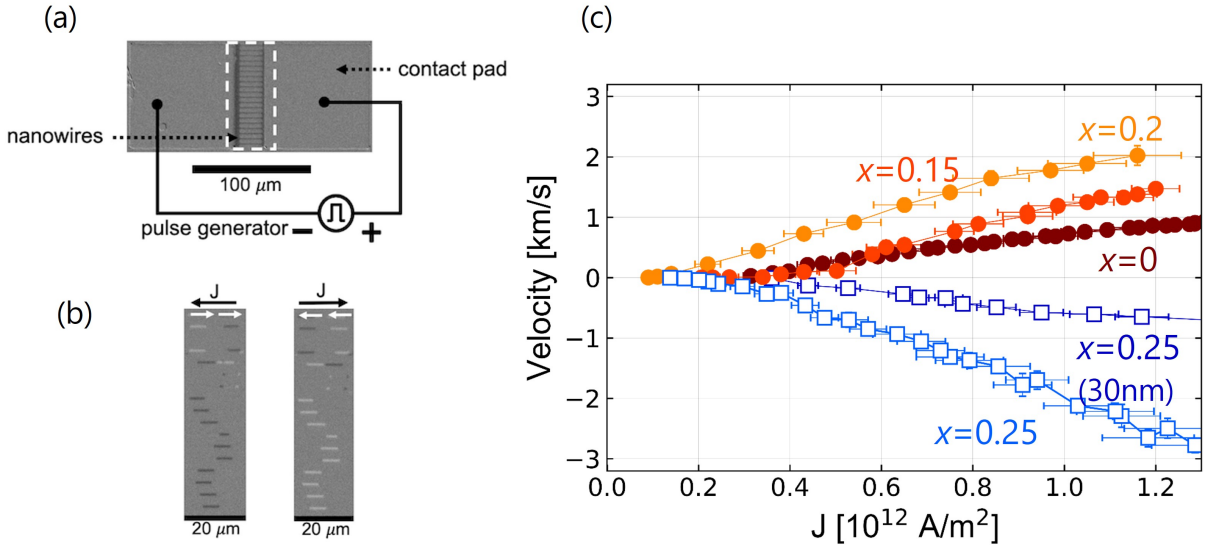

Figure 2.12: *(a) Image of the devices fabricated for the measurement of CIDWM, showing 20 nanowires where DWs are driven by current pulses, together with the contact pads from which the DWs are injected. (b) Differential polar MOKE images, showing the displacement of DWs during the injection of negative (left) and positive (right) current pulses. The white arrows indicate the direct DW displacement. In the device with a composition below the compensation point, the DWs moved in the direction of the electron flow. (c) DW velocity versus current density for $Mn_{4-x}Ni_xN$ films. The thickness of films (wires) was 10 nm if not written. The positive velocity indicates DW motion parallel with conduction electrons*

As mentioned in chapter 1, this v_{DW} approaching 3,000 m/s was comparable to the record of CIDWM achieved in other ferrimagnets. Especially, CIDWM in SiO_2 capped $Mn_{4-x}Ni_xN$ was driven purely by STTs, which was proven by the measurement of zero-DMI, indicated by the isotropic propagation of domains by the out-of-plane magnetic field. Also, other ferrimagnets which show faster and/or more efficient CIDWM rely on in-plane magnetic fields to assist the

formation of chiral Néel DWs, and contain rare-earth elements to enable the compensation at RT. Therefore, we believe rare-earth free $Mn_{4-x}Ni_xN$ films are advantageous for CIDWM application thanks to the possibility of improving the stacks to add SOTs contributions.

2.4.2 Impact of the compensation

In this section, we investigate the DW motion reversal by Ni composition ratio and the effect of compensation on CIDWM in $Mn_{4-x}Ni_xN$. We used the collective coordinate $q-\phi$ (1D) model expanded into a ferrimagnetic system with two sublattices, "I" and "II"[53, 55]. The magnetic moments of "I" and "II" were assumed to be antiparallel. Figure 2.13 shows the schematic image of the alignment in the $q-\phi$ model for the sublattices of $Mn_{4-x}Ni_xN$. In this analysis, we assumed that the influence of the magnetic moments of Ni atoms is negligible because the Ni composition ratios of samples in our interest ($0 < x < 0.25$) were very small, at most 5 %, and magnetic moments of Ni are known to be much smaller than those of Mn according to the sum rule for XMCD spectra[70]. Therefore, sublattice "I" consist of Mn(I) atoms, and sublattice "II" consists of Mn(II) atoms. When physical quantities are defined for each sublattice, the angular momentum of the sublattice (L_i) can be given as

$$L_i = \gamma_i M_i \tag{2.1}$$

where γ_i and M_i are the gyrometric ratios and the magnetization of the sublattice i. Since the value of γ depends on the element of the sublattice, we can assume they meet the formula of $\gamma_I = \gamma_{II}$ by neglecting the effect of Ni atoms in this assumption. Thus, the magnetic compensation (MC) point coincides with the angular momentum compensation (AMC) point.

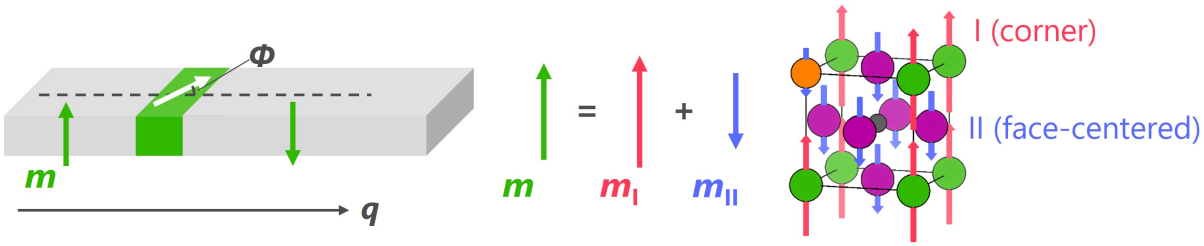

Figure 2.13: *Image of the collective coordinate $q-\phi$ model (1D model) expanded into a ferrimagnetic system with two sublattices, "I" and "II". In the case of $Mn_{4-x}Ni_xN$, we neglected the effect of magnetic moments of Ni, thus, the sublattice I and II consist of Mn(I) and Mn(II), respectively.*

This model allows us to derive the relationship between the DW velocity (v_{DW}), the spin-drift velocity (u), and the angular momentum in the precessional regime, in which the current density (J) in magnets is well above the threshold current density (J_{th}). This relationship can be written as

$$v_{DW} = \frac{L_s + L_\alpha \beta}{L_s^2 + L_\alpha^2} L_s u$$
$$u = \frac{Phj}{2e} \tag{2.2}$$

where L_S and L_α are

$$L_S = \frac{M_I - M_{II}}{\gamma}$$

$$L_\alpha = \frac{\alpha M_I + M_{II}}{\gamma} \tag{2.3}$$

Here, α is the Gilbert damping constant, β is the non-adiabatic STT constant and P is the effective spin polarization given as $P = P_I - P_{II}$[55], L_S is the angular momentum density, and L_α is the product of α and L_S

In Figure 2.14, the maximum experimental DW velocities experimentally acquired in Fig. 2.12(b) are plotted against the saturation magnetization ($M_S = M_1 - M_2 = \gamma L_S$) Fig. 2.14 also shows the best fit of these data plots by Eq. 2.1, which was obtained for $P = 0.65$, $\alpha = 0.013$ and $\beta = 0.002$. Although the value of β in $Mn_{4-x}Ni_xN$ has not been experimentally acquired, the values of P and α did not deviate from those obtained in CIDWM in $Mn_{4-x}Ni_xN$ wires[65] and from the time-resolved MOKE measurements[71]. The value of P was expected not to change significantly because the spin polarization of s orbitals scarcely changed in the range of $0 < x < 0.25$ from the first-principle calculation. Now, taking the $q-\phi$ model into the consideration, from Eq. 2.2, the direction of CIDWM was expected to switch at $L_S = -\beta L_\alpha$. This relationship is supposed to be met just below the AMC point. From the fitting line in Fig. 2.14, indeed, the DW velocity becomes zero just below the experimental MC point. It validates out the assumption that $\gamma_I = \gamma_{II}$ and the MC and ACP points coincided in our system.

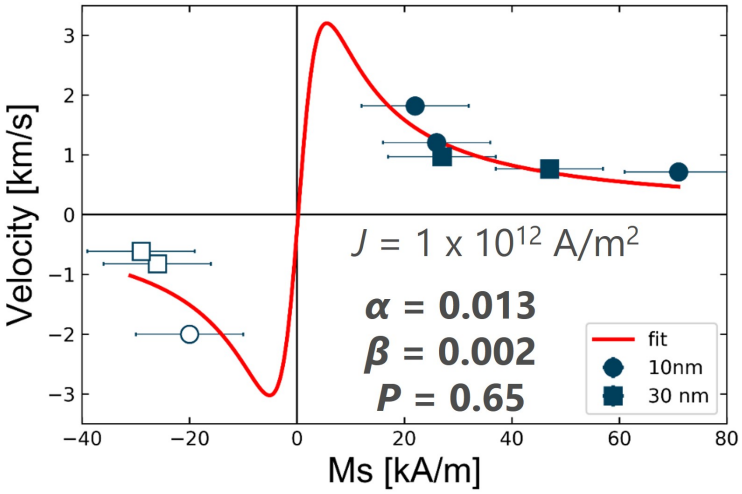

Figure 2.14: *Domain wall velocity versus spontaneous magnetization (M_S). The plots are the experimental data points measured with $J = 1 \times 10^{12}$ A/m^2 and, the red line is the best fit of these points using the q-ϕ model (Eq. 2.2).*

These results revealed that the large STT-driven CIDWM was due to the increase in DW mobility and to the preserved large P when approaching the AMC point. Although the sign of P would also reverse the direction of STT-driven CIDWM, it is not the case in our system, which was evidenced by the small change in the value of P. The composition ratio in the range of therefore, the reversal of the CIDWM $0 < x < 0.25$ direction was related to the relative change in the net spin polarization with respect to the angular momentum after crossing the AMC point. It means that the spin polarization P acts as an effective positive spin polarization below the AMC, while it acts as an effective negative spin polarization above the AMC point.

2.4.3 Room for improvement

The previous sections proposed that $Mn_{4-x}Ni_xN$ films are candidates for CIDWM application. Nevertheless, we expect that we can still improve the CIDWM performance and expand the

possibility of Mn_4N based-nitrides as spintronics materials. Here, we propose two approaches to these goals.

The first approach is the investigation of other anti-perovskite compounded nitrides which have compensation points. As far as we recognize, $Mn_{4-x}Co_xN$ is another candidate at the moment. We expect this material to be advantageous for the CIDWM application thanks to its two compensation composition ratios. This is because it has a wide range of the composition ratio which is close to one of two compensation points, and $Mn_{4-x}Co_xN$ in this range of composition ratios presumably can take the advantage of the compensation for CIDWM, as mentioned in section 2.3.3, represented by little precessions of the magnetizations thanks to the small net angular momentum. This is the feature which $Mn_{4-x}Ni_xN$ ($0 < x < 0.5$) doesn't have. Although further research is required, $Mn_{4-x}Co_xN$ is expected to have a relatively high Curie temperature even with a high Co composition ratio, at least well above RT, which was suggested by the clear magnetic hysteresis loops at RT[75]. In addition, the research on other compounds in films would help to achieve this goal, such as $Mn_{4-x}Sn_xN$ and $Mn_{4-x}In_xN$ in which the compensation by composition ratios in bulk samples have been reported by several groups[148, 167] and $Mn_{4-x}Ga_xN$ which seems to be one of the most suitable candidates as a compensated ferrimagnet as discussed in section 2.3.3.[167].

Another approach is the use of SOTs for the CIDWM in Mn_4N-based nitrides. As written in chapter 1.4.3, the spin accumulation at the interface of ferro(ferri)magnet (FM)/heavy metal (HM) by spin Hall effect (SHE) or Rashba-Edelstein effect is the source of SOTs. Taking the recent research streams into consideration, we rather look for the use of SHE to induce SOTs because of the recent success in SHE-based CIDWM[57, 60, 61]. In order to efficiently apply SHE to CIDWM, chiral Néel DWs should be formed to make magnetizations align along the length direction of the microwire (x-axis). This is because the magnetizations vectors perpendicular with the accumulated spins are more favorable for fast magnetization reversals and the reversals with low current density than magnetizations parallel or antiparallel with accumulated spins[168, 169]. If we find DMI in the system of HM/$Mn_{4-x}Ni_xN$/STO, we can have high hope for SOT-driven CIDWM in $Mn_{4-x}Ni_xN$ microwires. Although high uniaxial magnetic anisotropy constant (K_U) of 0.1-0.2 MJ/m^3 is disadvantageous due to the formation of stable Bloch DWs, its small magnetization may help the formation of Néel DWs even with small DMI effective fields thanks to the low energy barrier between Néel and Bloch DWs. Also, the investigation into the origin of its PMA will lead to the modulation of K_U.

2.5 Summary of this chapter

- Among the various types of nitrides, magnetic anti-perovskite nitrides show unique properties mainly due to the hybridization of d orbitals of metals at face-centered sites (II sites) and p orbitals of nitrogens at body-centered sites. Especially, Mn_4N films attract attention thanks to the small spontaneous magnetizations and the perpendicular magnetic anisotropy (PMA), which are suitable properties for current-induced domain wall motion (CIDWM).

- The crystalline quality of Mn_4N is deeply correlated with the magnetic, electric, and magneto-transport properties. For example, dislocations and defects in Mn_4N crystals function as external DWs pinning. In our previous research, Mn_4N epitaxial films grown onto $SrTiO_3$ (STO)(001) substrates are the most suitable for CIDWM thanks to little dislocation or defects in Mn_4N films which derive from the great lattice matching.

- Like other anti-perovskite nitrides, Mn atoms in Mn_4N can be partially replaced with

other $3d$ magnetic metals, transition metals, or base metals. And even the small composition ratio of these metals basically has a large influence on their fundamental properties. Especially, we proved the magnetic compensation in $Mn_{4-x}Ni_xN$ and $Mn_{4-x}Co_xN$ at RT, which is beneficial for the fast and efficient CIDWM.

- We performed v_{DW} of 900 m/s in Mn_4N and 3,000 m/s in compensated $Mn_{4-x}Ni_xN$ microwires, in which DWs were purely driven by the effect of spin-transfer torques (STTs). These records are comparable even with CIDWM driven by spin-orbit torques (SOTs) under the assistance of the in-plane magnetic fields. Through the analysis based on the 1D model, we proved that the fast and efficient CIDWM and the direction reversal of CIDWM with Ni composition ratio take place when crossing the angular momentum compensation point.

- We anticipate that CIDWM in magnetic anti-perovskites can improve by the research on new materials and the use of SOTs. $Mn_{4-x}Co_xN$ films are one of the candidates from the experimental fact that they have two magnetic compensation points. SOT-driven CIDWM in Mn_4N type nitrides is expected to be achieved by utilizing the spin Hall effect (SHE) in heavy metals.

Chapter

Growth of Mn_4N on various substrates 3

In this chapter, we focus on the epitaxial growth of Mn_4N on various substrates. Previous studies on Mn_4N proved that Mn_4N films grown on MgO and STO substrates have an in-plane tensile strain with a ratio of lattice constants $c/a < 1$[63, 64]. Such an in-plane tensile strain has never been reported in bulk Mn_4N where the magnetization easy-axis is along [111][146, 170], thus, the hypothesis that PMA in Mn_4N is originated from the in-plane tensile strain has been proposed. However, it has not been clear if the in-plane tensile strain in Mn_4N is attributable to the lattice mismatch between Mn_4N and substrates, an extrinsic factor, and/or to the result of the minimization in cohesion energy of crystals, an intrinsic factor. In this context, we attempted to grow Mn_4N on various substrates having different lattice mismatches between Mn_4N and investigated the correlation between c/a and PMA.

Section 3.1 lists the substrates used for the MBE growth in this work and section 3.2 notes the procedure of MBE growth of Mn_4N. Section 3.3 shows the results of crystalline evaluation on the different substrates, section 3.4 shows the results of magnetic and magneto-transport properties and section 3.5 shows the cross-sectional images of Mn_4N. We discuss the correlation of c/a and PMA in section 3.6 and end this chapter with the summary in section 3.7. This study has been published in T. Hirose and T. Komori *et al.*,, J. Cryst. Growth **535**, 125566 (2020)[171], and T. Hirose and T. Komori *et al.*,, AIP Adv. **10**, 025117 (2020)[172]. T. Komori contributed to the assistance of the MBE growth and of the measurements of magneto-transport properties, and the discussion.

3.1 Substrates

Table 3.1 shows the list of substrates used in this chapter, MgO(001), $SrTiO_3$(STO)(001), $LaAlO_3$(LAO)(001), $(LaAlO_3)_{0.3}$·$(Sr_2AlTaO_6)_{0.7}$(LSAT)(001).

Note that although the actual lattice constant of LSAT is 7.736-7.737 Å, we use the halved value to discuss the epitaxial growth of Mn_4N from the viewpoint of the atomic periodicity within the (001) plane. Lattice mismatch between Mn_4N and a substrate was deduced with $(a_{Mn_4N}\text{-}a_{sub})/a_{sub}$. Here are the reasons we choose the substrates above for the study on their dependence on the Mn_4N epitaxial films

1. These oxide substrates can grow onto Si wafers, which is advantageous for the perspectives. Moreover, the growth of Mn_4N films on LAO and LSAT substrates has not been reported so far.

Table 3.1: *Structures and lattice constants of substrates used in this chapter. Lattice mismatch was calculated with the referenced value of a=3.890 Å from a Mn_4N film[63]*

	MgO(001)	STO(001)	LAO(001)	LSAT(001)
Structure	rock-salt (cubic)	perovskite (cubic)	perovskite (pseudo-cubic)	perovskite (cubic)
Lattice constant[Å]	4.212	3.905	3.790	3.868(=$a/2$)
Lattice mismatch[%]	-7.6	-0.3	+2.6	+0.6

2. As mentioned in Chapter 2, an in-plane tensile strain that is unique to Mn_4N thin films has been thought to be the origin of their PMA. Nevertheless, it has not been clear if the in-plane tensile strain is due to the lattice mismatch between Mn_4N and the substrate.

3. Regarding 2., if the in-plane tensile strain is due to the lattice mismatch, LAO and LSAT substrates are expected to give in-plane compressive strain to Mn_4N. Therefore, the investigation of Mn_4N under in-plane compressive strain will reveal the relationship between the strain and PMA for Mn_4N.

More specifically, with 2., Yasutomi grew epitaxial films on MgO(001) and STO(001) substrates with two different thicknesses (t = 10 and 30 nm) and derived the ratio of lattice constants (c/a) which represents the degree of the tensile strain in Mn_4N[63]. Here, c is the perpendicular lattice constant and a is the in-plane lattice constant. In this report, c/a was larger in Mn_4N/MgO (c/a = 0.995: t = 30nm), suggesting weaker tensile strain, compared with Mn_4N/STO with the same thickness (c/a = 0.989: t = 30nm), which is not explained by the lattice mismatch shown in Table 1. Also, c/a is larger on the thicker sample in Mn_4N/MgO while there is little change in Mn_4N/STO. Therefore, the lattice mismatch could not fully explain the origin of the in-plane strain tensile of Mn_4N in this report. In such context, we attempted to grow Mn_4N on various substrates with different lattice mismatches for deeper investigations. Moreover, we observed the cross-sectional view of some samples to observe if there are changes in the lattice constants of Mn_4N at the interface and within the film.

3.2 Growth of Mn_4N by MBE

Table 2 shows the process of substrate cleaning steps used before MBE growth.

Table 3.2: *The process to clean substrates before the MBE growth. The order of the process is from top to bottom*

	MgO(001)	STO(001)	LAO(001)	LSAT(001)
Acetone	5 min	2 min	2 min	5 min
Methanol	5 min	2 min	2 min	5 min
DI-water	no	2 min	2 min	no
Buffered-HF	no	0.5 min	no	no
Pre-anneal	600 $°C$, 30 min	no	no	no

Here, organic treatment and cleaning with deionized (DI)-water were done with ultrasonic cleaning. Buffered-HF consists of HF and NH_4F with a volumetric ratio of 13:110. The purpose

of the treatment with buffered HF is to obtain TiO_2 terminated surface with little roughness for better epitaxial growth[173]. Pre-anneal of the substrate was done in the MBE chamber under a high vacuum ($10^{-8} \sim 10^{-9}$ Torr).

The procedure of MBE growth was common for all substrates. After the annealing (if needed), a Knudsen cell with a Mn solid metal source in it was set at 850 $\sim$ 860 $°C$ so that the flow rate of Mn is set at 1 nm/min, which was checked before samples growth. Before the growth, substrates were heated at 450 $°C$ for the case of MgO, STO, and LAO and at 450-800 $°C$ for the case of LSAT. Also, the nitrogen gas was supplied to the plasma gun so that the flow rate was in the range of 0.9 $\sim$ 1.0 sccm, and the pressure inside the chamber was set at 3.5 $\sim$ 3.6 $\times 10^{-5}$ Torr, then its power was set at 107 W. After the growth, the surface morphology was observed by reflection high-energy electron diffraction (RHEED). Afterward, we wait for the substrate to cool down ($T_S < 100$ $°C$), and SiO_2 was sputtered for the case of MgO, STO, and LAO, or Ti was deposited for the case of LSAT to form a capping layer that prevents oxidation.

Figure 3.1 shows the schematic image of the MBE chamber used in this work. Note that we can perform RHEED observation and the sputtering *in-situ* during the MBE sample process.

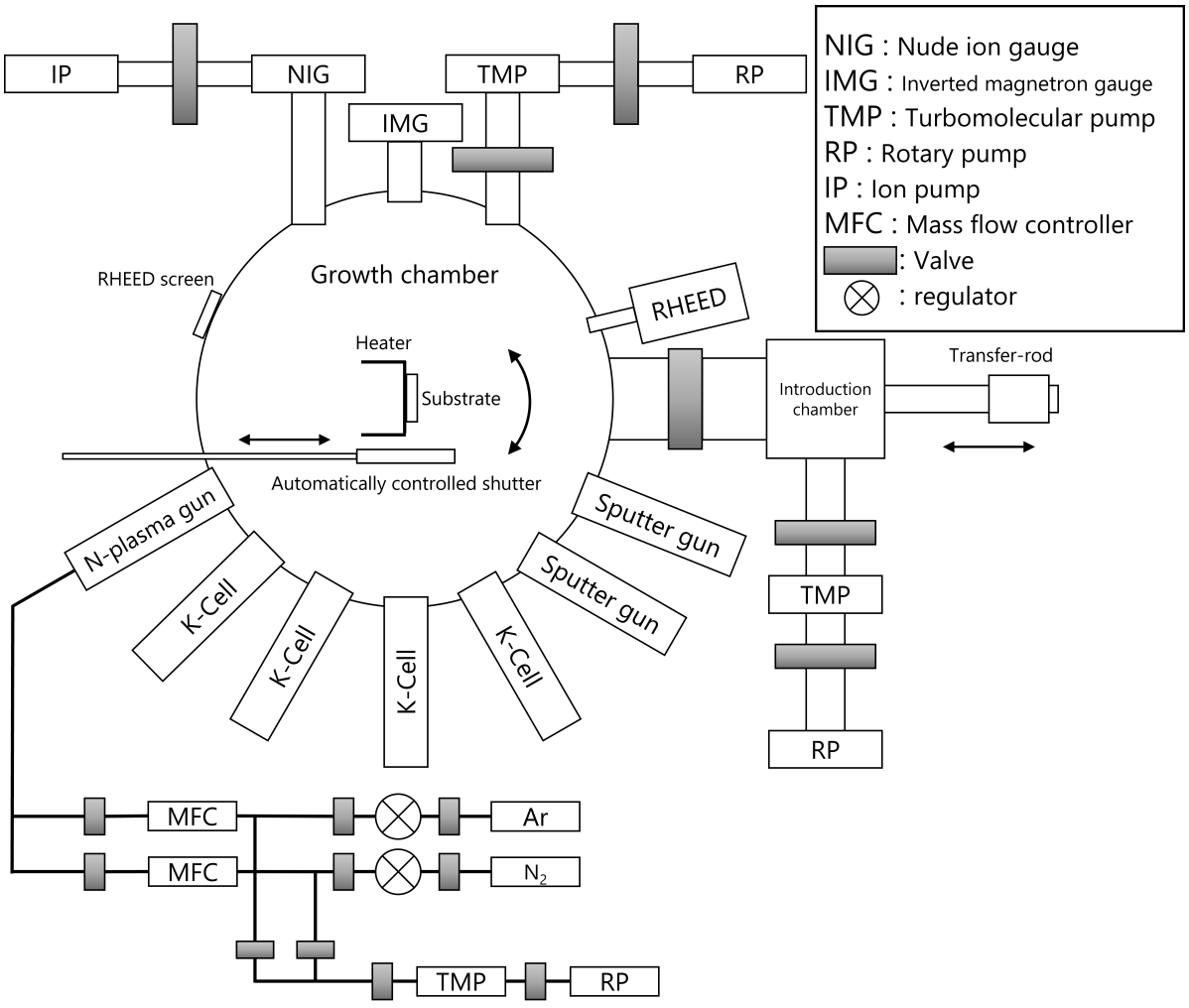

Figure 3.1: *Schematic image of MBE chamber used in this work.*

3.3 Crystalline quality and lattice constants

X-ray diffraction (XRD, Smart Lab, Rigaku, Inc., Japan) was used to assess the crystalline quality of the films while x-ray reflectivity (XRR) was used to evaluate the thickness and the roughness. A Cu-$K_{/alpha}$ radiation source was used for the x-ray and Ge(220) single crystals were used to monochromatize the x-ray beams for the case of out-of-plane XRD and XRR. Lattice constants were calculated from the angles of diffraction peaks in XRD profiles. First, we discuss the case of MgO, STO, and LAO substrates. Table 3.3 shows the list of samples grown on MgO, STO, and LAO substrates. Figure 3.2 shows out-of-plane XRD profiles and RHEED images taken along [100] azimuth.

Table 3.3: *Structural properties of Mn_4N films on MgO(001), STO(001), and LAO(001) substrates. Substrate, thickness of the Mn_4N (t_{Mn_4N}), lattice constants c and a and the ratio c/a are specified.*

Sample	Substrate	t_{Mn_4N} [nm]	c [nm]	a [nm]	c/a
Sample 1	MgO	11.6	0.3856	0.3884	0.9927
Sample 2	MgO	18.4	0.3862	0.3891	0.9927
Sample 3	MgO	42.4	0.3872	0.3890	0.9953
Sample 4	STO	7.4	0.3856	0.3908	0.9866
Sample 5	STO	17.1	0.3863	0.3907	0.9885
Sample 6	STO	39.4	0.3862	0.3911	0.9874
Sample 7	LAO	19.2	0.3866	0.3874	0.9979
Sample 8	LAO	39.4	0.3856	0.3871	0.9962

In Fig. 3.2 (a) and (b), Mn_4N 002 and 004 diffraction peaks appear for the samples grown on MgO and STO substrates (Samples 1-6). Streaky patterns and superlattice diffraction lines in RHEED images, marked by white arrows, were also observed in these samples. The appearance of superlattice diffraction lines implies that a nitrogen atom is positioned at the body-centered position in each lattice, which indicates a highly ordered crystal. Note that the streaky lines in the RHEED images of Mn4N films on STO were sharper than those on MgO, suggesting that Mn_4N films on STO were more highly oriented thanks to the better lattice matching. In Fig. 3.2 (c), we observed Mn_4N 002 and 004 diffraction peaks in the out-of-plane XRD profiles of Mn_4N films on LAO (Samples 7-8), however, they were not as clear as ones in MgO and STO samples (Samples 1-6). Also, 111 diffraction peak was observed in Sample 7, which was not supposed to be observed. Additionally, the RHEED image of sample 7 exhibits a spotty pattern with rings. These results for LAO samples suggest the formation of polycrystalline Mn_4N films.

Figures 3.3 (a)-(c) show the in-plane XRD profiles of Mn_4N films on MgO, STO, and LAO substrates, respectively. In Fig. 3.3(a), Mn_4N 100, 200, and 400 peaks of Mn_4N appeared in all the MgO samples. Regarding the Mn_4N films on STO, the lattices of Mn_4N and STO are matched really well and both of them have a perovskite structure. Hence, the 200 and 400 peaks of STO almost overlapped with those of Mn_4N. For the Mn_4N films ($t_{Mn_4N} = 39.4$ nm) in sample 6, the 400 peak at $2\theta_\chi \sim 105^\circ$ was broader. This is because the peak intensity of Mn_4N increased with t_{Mn_4N}, positioned at a little higher $2\theta_\chi$ angle than that of STO, making the peak broader. Actually, the measured peak profile was well reproduced by two pseudo-Voigt curves, which is a common function to fit XRD peaks, thus we determined the in-plane lattice constant (a) of Mn_4N films in this way. Peaks of manganese oxide were also observed at $2\theta_\chi \sim 41^\circ$ in the profiles of MgO and STO samples. These features might arise from the diffusion of oxygen

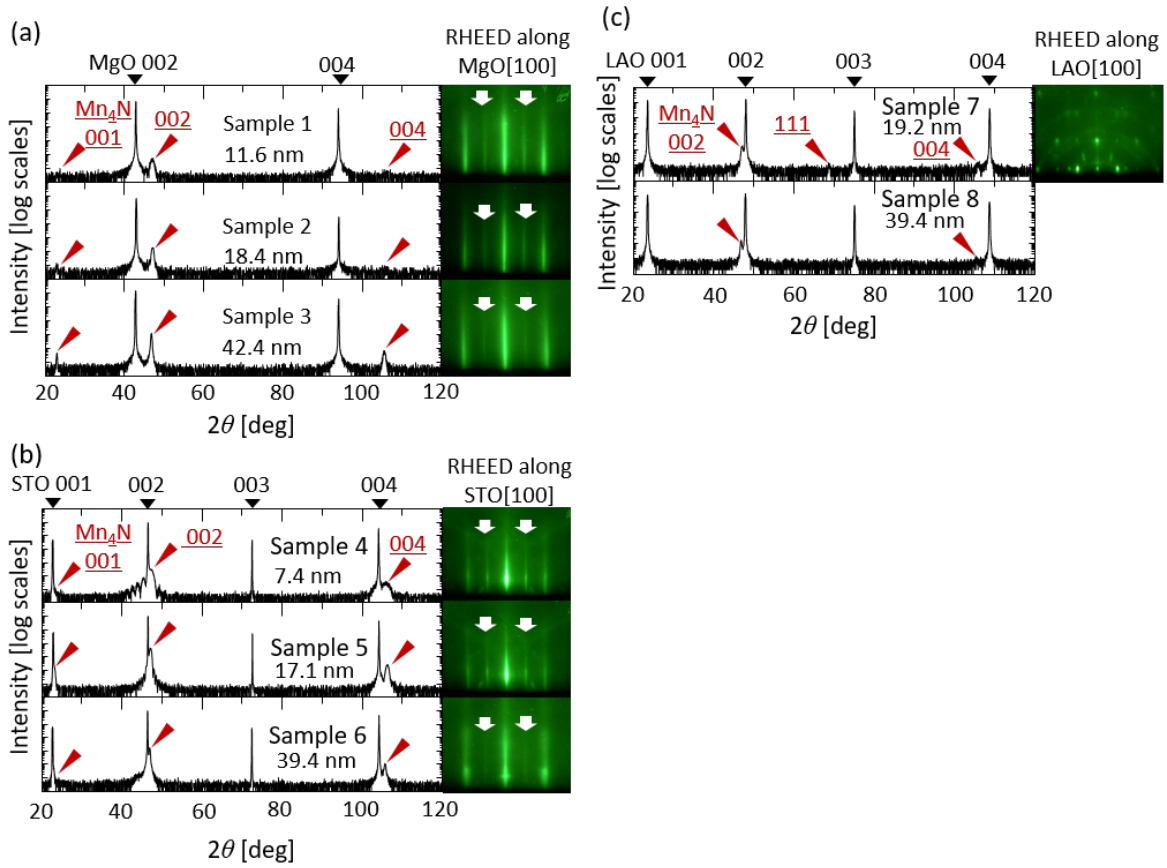

Figure 3.2: *Out-of-plane XRD profiles and RHEED images of Mn_4N films taken along the substrate [100] azimuth on (a) MgO(001), (b) STO(001), and (c) LAO(001) substrates. In the RHEED images, white arrows indicate superlattice diffraction.*

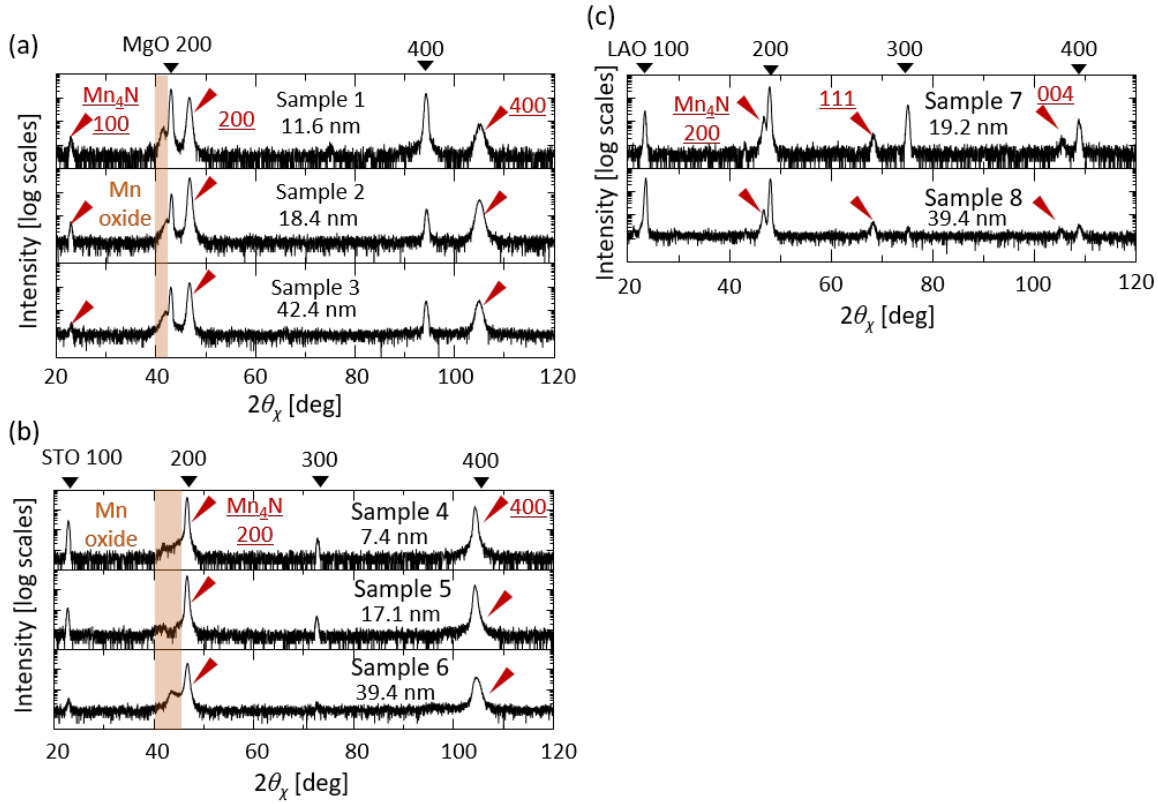

Figure 3.3: *In-plane XRD profiles of Mn_4N films growon on (a) MgO(001), (b) STO(001),and (c) LAO(001) substrates.*

atoms from SiO_2 cap layers or the oxide substrates. In Fig. 3.3(c), the 200 and 400 peaks of Mn_4N appear in samples 7 and 8; however, the 111 peak of Mn_4N also appears, like for the results of out-of-plane XRD. To summarize, we conclude that it is difficult to grow epitaxial Mn_4N films on LAO at 450 $°C$.

Then, we discuss the case of LSAT substrates. Table 3.4 shows the list of samples grown on LSAT. We first show the results of samples of MNLSAT1-6 to explain the growth temperature dependence. Fig 3.4 shows RHEED images taken along [100] azimuth for MNLSAT1-6 and Figs 3.5 (a) and (b) show out-of-plane and in-plane XRD profiles of these samples, respectively.

Table 3.4: *Structural properties of Mn_4N films grown on LSAT(001) substrates. Substrate temperature during the growth (T_S), thickness of the Mn_4N (t_{Mn_4N}), lattice constants c and a and the ratio c/a are specified.*

Sample	T_S [$°C$]	t_{Mn_4N} [nm]	c [nm]	a [nm]	c/a
MNLSAT1	450	16.5	-	-	-
MNLSAT2	550	23.9	-	-	-
MNLSAT3	650	23.3	-	-	-
MNLSAT4	700	33.1	-	-	-
MNLSAT5	750	31.0	0.3859	0.3886	0.9932
MNLSAT6	800	30.6	-	0.3871	-
MNLSAT7	750	10.0	-	-	-
MNLSAT8	750	19.7	0.3859	0.3886	0.9931
MNLSAT9	750	38.7	-	0.3857	-

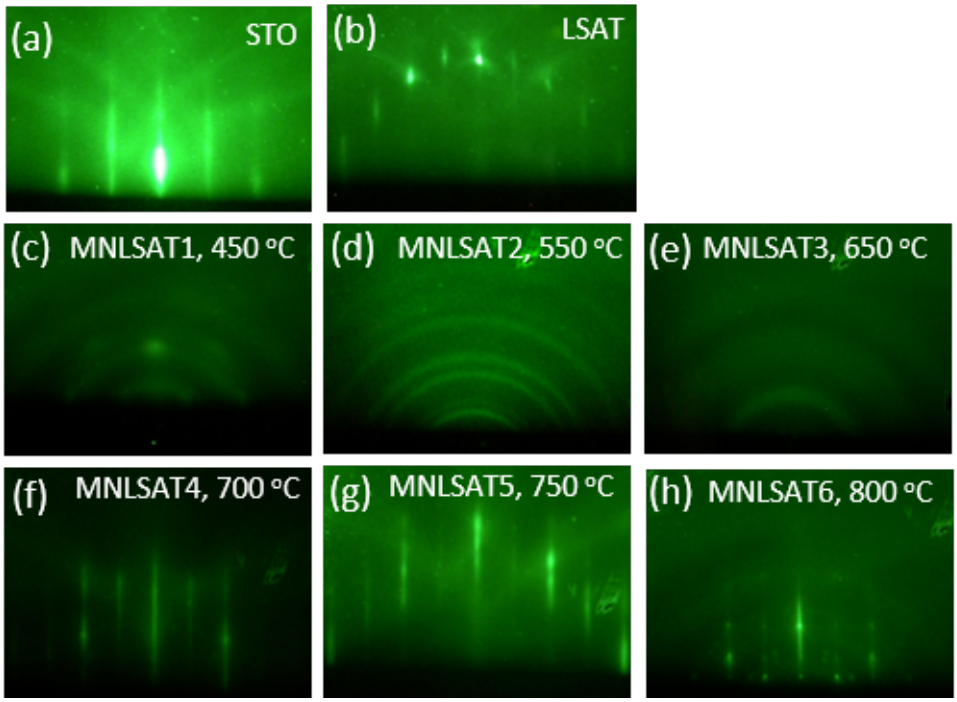

Figure 3.4: *RHEED images of (a) STO(001) and (b) LSAT(001) substrates observed along its [100] azimuth just before the growth of the Mn_4N films. (c)–(h) RHEED images of grown films on LSAT(001) substrates at T_S = 450, 550, 650, 700, 750, and 800 °C (MNLSAT1–6), respectively, recorded along the LSAT[100] azimuth*

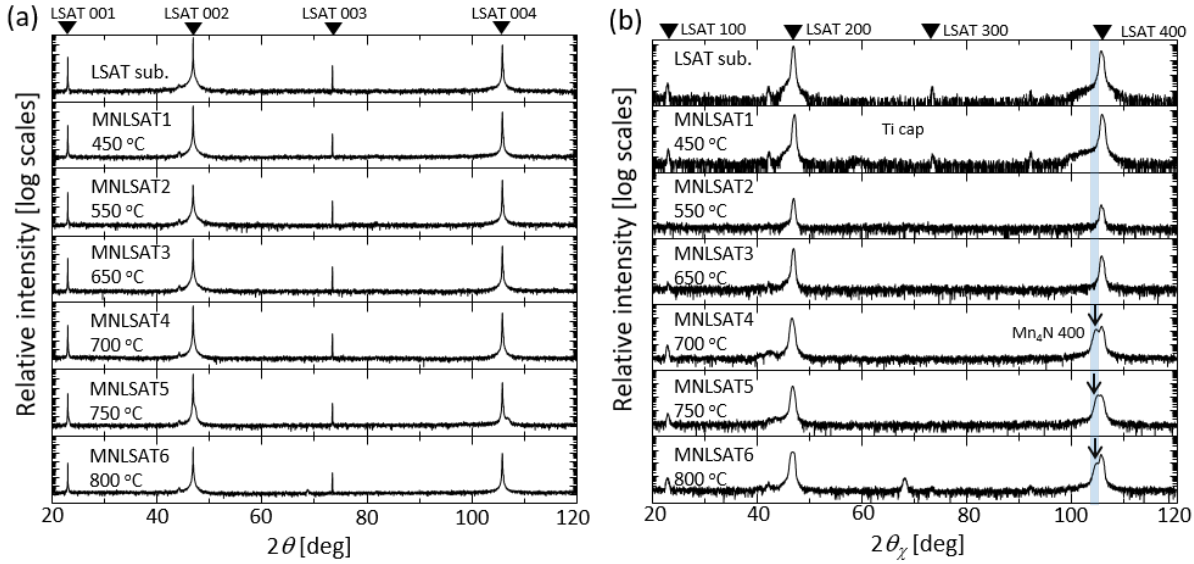

Figure 3.5: *(a) Out-of-plane and (b) in-plane XRD profiles of samples grown on LSAT(001) substrates at T_S = 450, 550, 650, 700, 750, and 800 °C (MNLSAT1–6). The arrows indicate the peak position of Mn_4N 400 diffraction, and the blue lines show the region where 400 diffraction peaks are supposed to be observed.*

The RHEED images in Fig. 3.4 present sharp streak lines for samples grown at T_S = 700, 750, and 800 °C (MNLSAT4-6). However, for samples grown at lower T_S (< 700 °C) (MNLSAT1-3), ring patterns are observed. In Fig. 3.5 (a), the diffraction peaks of the Mn_4N films overlapped with those from LSAT, which is attributable to the same reason as the case

of Mn_4N on STO (Sample 4-6). In Fig. 3.5 (b), we observe the presence of the Mn_4N 400 diffraction peaks marked by arrows for samples grown at T_S = 700, 750, and 800 $°C$ at $2\theta_\chi$ angles a little smaller than those of the LSAT 400 diffraction peaks. Nevertheless, some of the lattice constants can not be calculated due to the failure in the epitaxial growth or insufficient intensity of peaks to be fitted. Together with the streaky RHEED patterns in Fig. 3.4, we concluded that *c*-axis-oriented Mn_4N films were epitaxially grown at T_S = 700–800 $°C$, which is much higher than the optimized T_S for the growth on STO assessed in previous reports[63, 171], and T_S for the growth was optimized at 750 $°C$ from the viewpoint of crystalline quality, which will be reconfirmed from the aspect of magnetic properties as well in section 3.4.

We next investigated the thickness (t_{Mn_4N}) dependence of the quality of Mn_4N films on LSAT(001) substrates at T_S = 750 $°C$. t_{Mn_4N} was varied from approximately 10 to 39 nm. Fig. 3.6(a)-(e) shows t_{Mn_4N} dependence of RHEED images of samples on LSAT(001) substrates grown at T_S = 750 $°C$ observed along the LSAT[100] azimuth. Regarding MNLSAT7 (t_{Mn_4N} = 10 nm), the RHEED images exhibited a mixture of rings and spots with weak and relatively broad streaks. This image suggests that phases other than Mn_4N were formed, which will be discussed again in sections 3.4 and 3.5. In a thicker sample, sharp streaky RHEED patterns with Kikuchi lines appeared in the sample of t_{Mn_4N} = 20-39 nm. Fig. 3.6(f) shows the out-of-plane XRD profiles of these samples. Although some diffraction peaks were not measured well due to the reasons mentioned above, these results suggested that we succeeded in the epitaxial growth of highly *c*-axis oriented Mn_4N films on LSAT substrates in the range of t_{Mn_4N} = 20–39 nm.

Overall, figure 3.7 shows the relationship between the lattice constants a and c, and c/a against film thickness (t_{Mn_4N}). Importantly, values of c/a are smaller than 1 for all the samples regardless of the expected compressive strain in samples on LAO. We next focused our attention on Mn_4N films on MgO and STO substrates, in which we expected that the in-plane tensile strain will be reduced as the film becomes thicker, and that c/a increases with increasing t_{Mn_4N} and asymptotically approaches to 1. Note that c/a is closer to 1 for Mn_4N films on MgO than those on STO, which agrees with the report of Yasutomi[63]. This discrepancy with the magnitude of lattice mismatch is discussed in section 3.4. In contrast, for the samples on LAO, a different trend was observed; c/a decreased with t_{Mn_4N}. This is probably because Mn_4N films on LAO are polycrystalline and the strain caused by lattice mismatch at the interface is not imprinted at the center of the film. Notably, c/a was less than 1 for all samples even on LAO and LSAT substrates. In the case of samples on LSAT, although we couldn't directly compare the value with other samples due to the difference in T_S, the possibility of the emergence of other phases in the films may disturb the effect from lattice mismatch, resulting in c/a <1 despite the expected compressive strain. We attributed this result to the fact that the crystalline structures with $c/a < 1$ are stable in the Mn_4N thin films according to theoretical calculations of the structural relaxation, with $c/a \sim 0.98$ [73, 156].

3.4 Magnetic and magneto-transport properties

In this section, we discuss the magnetic and magneto-transport properties, especially saturation magnetization (M_S), uniaxial magnetic anisotropy constant (K_U), and anomalous Hall effect (AHE) of the different samples. Vibrating sample magnetometry (VSM) was used to measure *M-H* loops at RT. We used K_U to evaluate the degree of PMA. The values of K_U and the effective magnetic anisotropy constant (K_u^{eff}) were derived from the following equations.

$$K_U = K_U^{eff} + \frac{\mu_0}{2} M_S^2 \tag{3.1a}$$

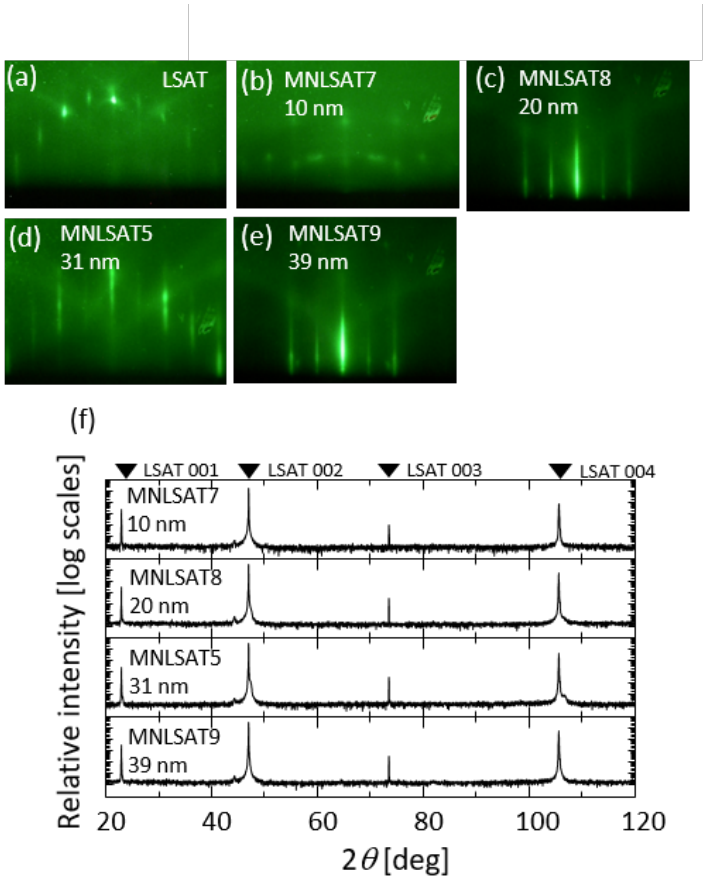

Figure 3.6: *RHEED images of (a) LSAT substrate (t_{Mn_4N} = 0nm) (b) MNLSAT 7 (t_{Mn_4N} = 10 nm) (c) MNLSAT 8 (t_{Mn_4N} = 20 nm) (d) MNLSAT 5 (t_{Mn_4N} = 31 nm) (e) MNLSAT 9 (t_{Mn_4N} = 39 nm) taken along LSAT (Mn_4N) [100] azimuth and (f) out-of-plane XRD profiles of MNLSAT 7, 8, 5 and 9.*

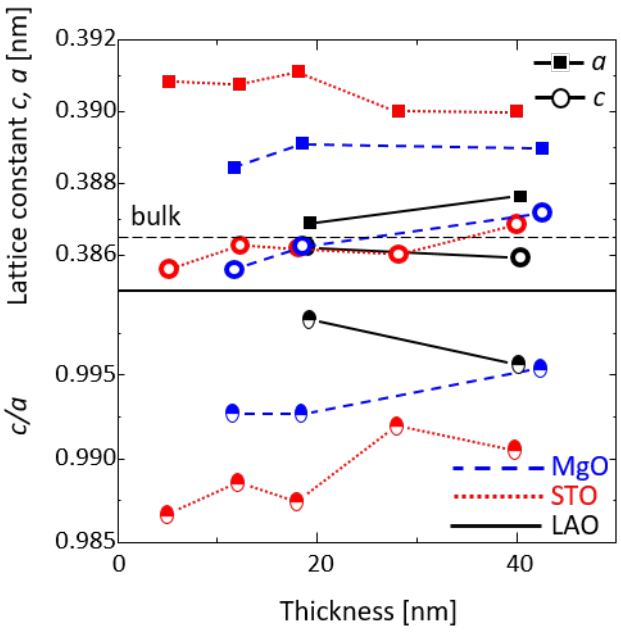

Figure 3.7: *Mn_4N thickness dependence of the in-plane lattice constant a, out-of-plane lattice constant c, and c/a*

$$K_U^{eff} = (\mu_0 \int_0^{M_S} HdM)_{hard} - (\mu_0 \int_0^{M_S} HdM)_{easy} \tag{3.1b}$$

where easy (hard) refers to the easy (hard) magnetization axis. The term of $\frac{\mu_0}{2} M_S^2$ on the right side of Eq. 3.1a is the demagnetization contribution. However, we couldn't correctly calculate these constants from the measured M–H loops by VSM because we could not apply the sufficient magnetic field to make the magnetization saturated in the in-plane direction due to the strong PMA and small magnetization of Mn_4N. To solve this issue, we used the fact that the loops acquired from the anomalous Hall effect (AHE) measurements correspond to M–H loops measured by VSM if the magnetic layers are homogeneous. We calculated the subtractions of AHE loops with Eq. 3.1b and the following equation,

$$M_{||} = M_S \sqrt{1 - (\frac{M_\perp}{M_S})^2} \tag{3.2}$$

where $M_{||}$ ($M_\perp$) is the in-plane (out-of-plane) component of the magnetization. AHE was measured with a physical property measurement system (PPMS) (Quantum Design), where a maximum magnetic field is 9 T. We calculated the Hall resistivity (ρ_{xy}) from the transverse voltage (V_y) with the following equation.

$$V_y = (R_H \frac{B_z}{t} + \frac{\rho_{AH}}{t} \frac{M_\perp}{M_S}) I_x = \frac{\rho_{xy}}{t} I_x \tag{3.3}$$

where R_H, B_z, ρ_{AH}, t and I_x are the ordinary Hall coefficient, the out-of-plane component of the magnetic flux density perpendicular to the sample surface, the anomalous Hall resistivity, the film thickness, and the transverse current, respectively. We did not consider the contribution from the planar Hall effect because the anisotropic magnetoresistance of the Mn_4N film is negligibly small at RT[158].

Table 3.5: *Spontaneous magnetizations (M_S), uniaxial anisotropic constant (K_U), anisotropic field (H_k) of Sample 1-8*

Sample	M_S [kA/m]	K_U [MJ/m^3]	$\mu_0 H_k$ [T]
Sample 1	80	0.052	1.4
Sample 2	63	0.060	1.6
Sample 3	78	0.041	1.2
Sample 4	78	0.215	5.2
Sample 5	73	0.126	3.6
Sample 6	73	0.049	1.2
Sample 7	53	0.045	0.6
Sample 8	59	0.051	0.6

Figure 3.8(a) shows ρ_{AH}-H loops measured under perpendicular magnetic fields for Samples 2, 5, and 7, in other words, Mn_4N films grown on MgO, STO, and LAO substrates, respectively, with t_{Mn_4N} of approximately 20 nm. The loop of Mn_4N films on STO (Sample 5) showed the best squareness (red), followed by those on MgO (Sample 2) (blue). The squareness of the loops was the worst for the samples on LAO (Sample 7) (black). These results suggest that the sharp magnetization reversal takes place in Mn_4N films on STO, whereas a slow magnetization reversal takes place in Mn_4N films on MgO and LAO, highlighting the role of defect and domain wall pinning. The inset of Fig. 3.8(a) shows the relationship between the ratio of the remanence

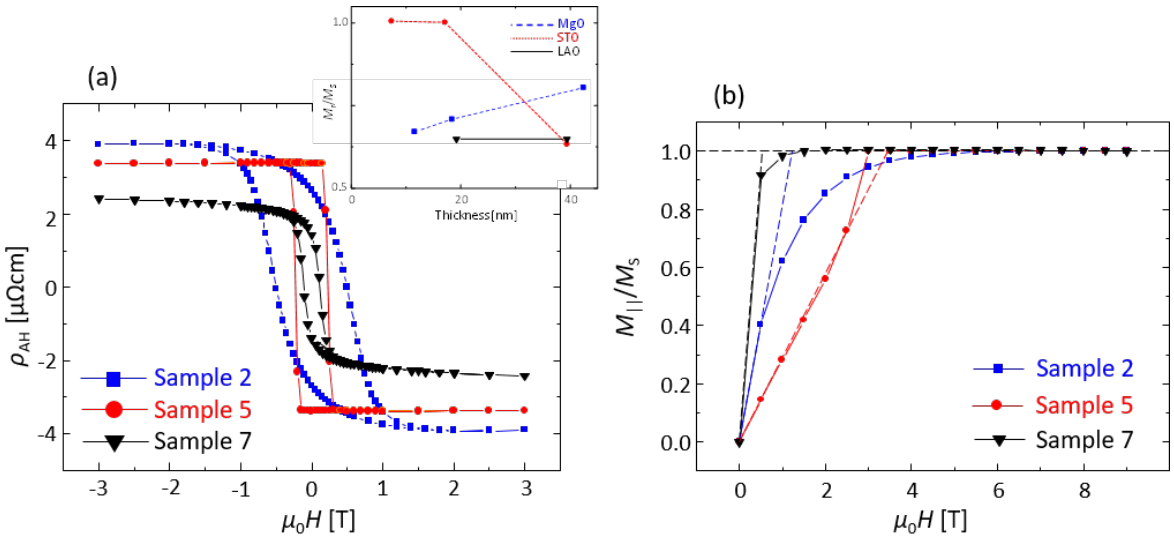

Figure 3.8: *(a) AHE loops measured at RT for Mn_4N films grown on MgO (blue squares, Sample 2, t_{Mn_4N} = 18.4 nm), STO (red circles, sample5, t_{Mn_4N} = 17.1 nm), and LAO (black inverted triangles, Sample 7, t_{Mn_4N} = 19.2 nm) substrates with H applied perpendicular to the plane. The inset shows the ratio of remanence magnetization to spontaneous magnetization (M_r/M_S) dependence on t_{Mn_4N}. (b) In-plane components of magnetization obtained from AHE measurements for samples in (a). Broken lines show the extrapolation from the field of 0 T.*

magnetization to the spontaneous magnetization (M_r/M_S) vs Mn_4N film thickness acquired from AHE for the better understanding of the squareness of loops. Furthermore, the coercivity field of sample 7 was much smaller than those of samples 2 and 5. This trend is attributed to the small K_U and M_S values of the Mn_4N films grown on the LAO substrates, related to the partially pollycrystalized region in the sample as discussed in section 3.3. Figure 3.8(b) shows the normalized in-plane magnetization response when the magnetic field was applied in-plane direction. From figure 3.8(b), PMA appears in all the samples although K_U is higher in Mn_4N films on substrates that induce in-plane tensile distortion, MgO, and STO, supported by Table 3.5. In Table 3.5, the anisotropic field (H_k) was derived from the extrapolation of the gradient at $\mu_0 H = 0$ T, as shown by the broken lines in Fig. 3.8(b)

Now, the discussion moves to the samples on LSAT substrates. Figure 3.9(a) shows the M-H loops of normalized magnetization (M/M_S) for samples MNLSAT4–6, on which we succeeded in the epitaxial growth, and estimated from the AHE loops. The red line and blue broken lines represent normalized magnetization under $H//[100]$ and $H//[001]$, respectively. It is clear that all of MNLSAT4-6 have PMA, however, the squareness of the loop is by far the best in MNLSAT5 (T_S = 750 °C). Figure 3.9(b) shows the T_S dependence of M_S and K_U based on MNLSAT1-6. The values of K_U were obtained only for samples grown at T_S = 700–800 °C (MNLSAT4-6) because the other samples did not show loops that are clear enough to perform the investigation. It was found that M_S increased with T_S and reached maximum at T_S = 700 and 750 °C. This was presumably because the crystalline quality of Mn_4N/LSAT improved at higher T_S, especially the degree of c-axis orientation of Mn_4N. On the other hand, the M_S decreased at T_S = 800 °C. This is because this temperature of 800 °C was close to 860 °C above which Mn_4N becomes unstable and tends to get partially denitrided according to the phase diagram[174]. Note that Mn_4N is the only phase of Mn-nitrides which have non-zero magnetization. Based on these results, we propose that the optimum T_S of Mn_4N films on LSAT was 750 °C.

In the end of this section, we discuss t_{Mn_4N} dependence (t_{Mn_4N} = 10-39 nm) of M_S in

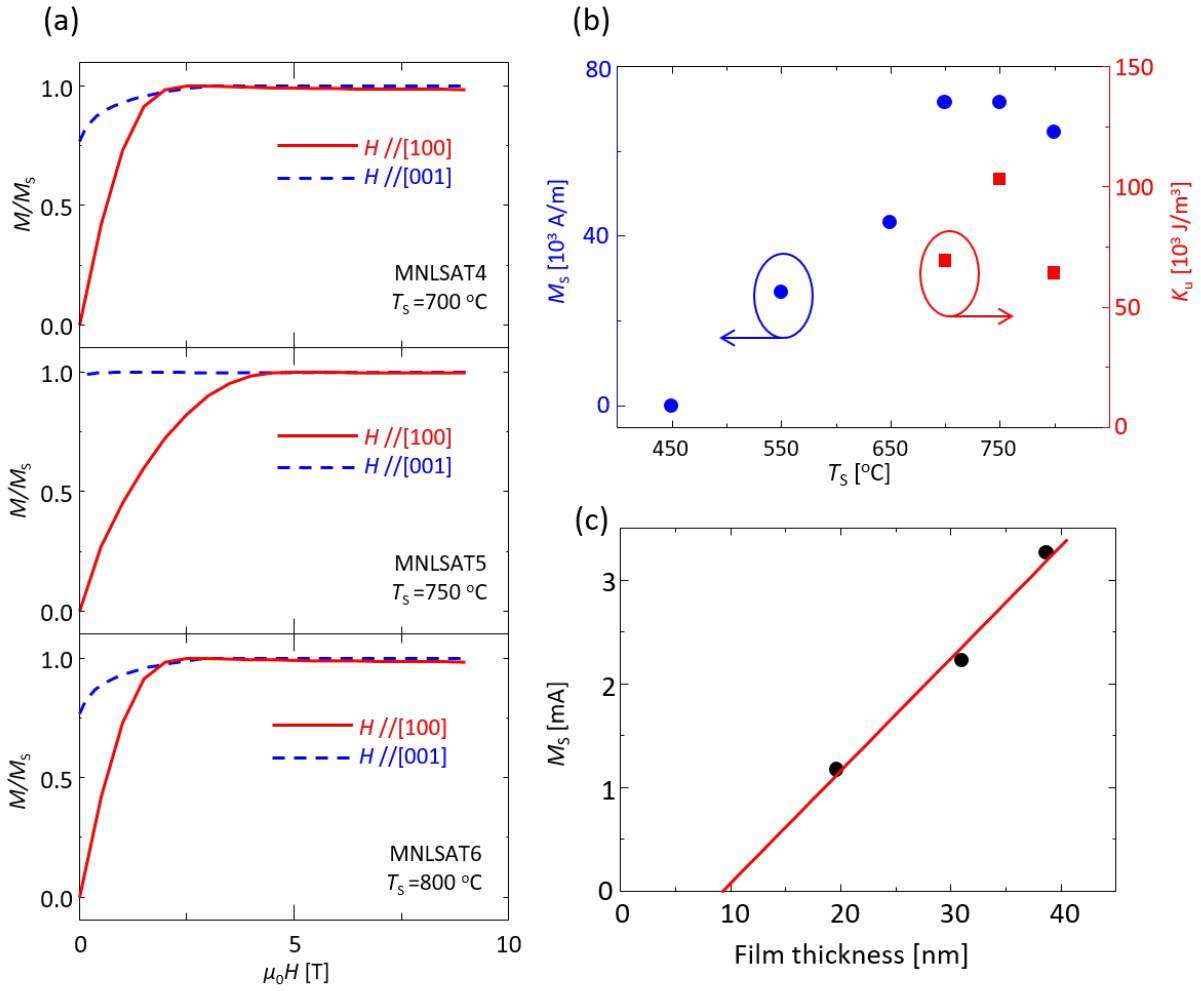

Figure 3.9: *(a) Normalized M-H loops (M/M_S) for MNLSAT4–6 derived from AHE measured by PPMS. (b) Growth temperature (T_S) dependence of spontaneous magnetization (M_S) and uniaxial magnetic anisotropy constant (K_U) of Mn_4N films on LSAT(001). (c) Film thickness dependence of spontaneous magnetization (M_S) of Mn_4N films on LSAT*

Mn_4N/LSAT grown at $T_S = 750\ ^\circ C$ (MNLSAT5,7,8,9). Figure 3.9(c) shows the saturated magnetization dependence of M_S of Mn_4N films grown on LSAT substrates, however, we didn't plot the data of MNLSAT7 ($t_{Mn_4N} = 10$ nm) because we couldn't acquire hysteresis loops with the VSM measurement due to its little magnetization. Note that the values in this figure are the magnetizations per unit area and the contribution of the LSAT substrate to the measured magnetization was already subtracted. We used these values for the discussion because RMS roughness of MNLSAT5,7,8,9 were larger than 2 nm according to the observation with an atomic force microscope (AFM), which makes the calculation of the volume of films difficult especially in thinner ones. Note that RMS of Mn_4N at $T_S = 450\ ^\circ C$ is smaller than 0.5 nm, thus the effect of roughness on the calculation is negligible. The linear extrapolation intersected the x-axis at approximately $t_{Mn_4N} = 11$ nm, indicating the presence of a dead layer of approximately 10 nm in Mn_4N grown on LSAT. This hypothesis supports our experimental fact that we could not observe magnetization hysteresis in MNLSAT7 ($t_{Mn_4N} = 10$ nm). Additionally, the existence of such a dead layer has been reported in CoFeB films as well.

However, since we have not confirmed such a dead layer in Mn_4N on MgO and STO, we discuss the cross-sectional images of Mn_4N on various substrates in the next section.

3.5 Cross-sectional images

Figure 3.10 shows the cross-sectional images of samples of Mn_4N on (a) MgO and (b) STO taken with a cross-sectional transmission electron microscopy (X-TEM). Note that the one on MgO is adapted from the report of Shen *et al.*,[62] and the one on STO is from the report of Gushi *et al.*,[65], from our group, and the one on LSAT is MNLSAT8 fabricated during this Ph.D.

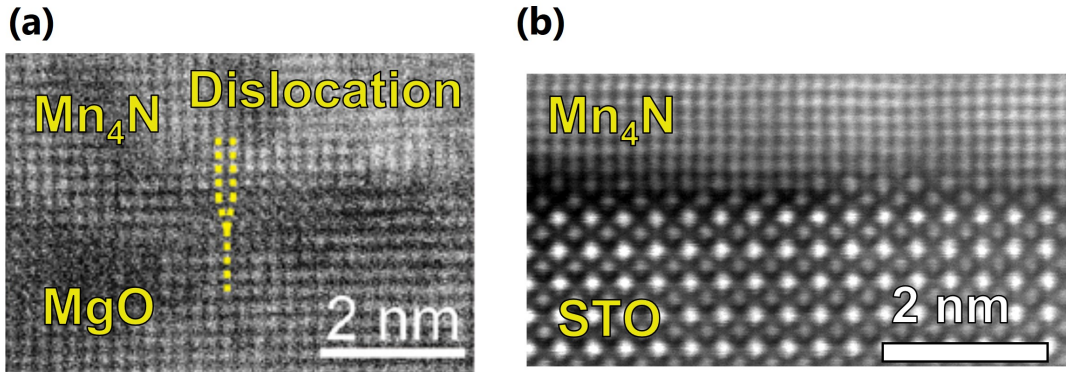

Figure 3.10: *Images of Mn_4N at the interface with (a) MgO[62] and (b) STO taken by the X-TEM[65]. Yellow lines the dislocation*

Since X-TEM images of Mn_4N on MgO and STO substrates have been discussed in our previous reports, we mainly focus on the relationship between lattice mismatch and in-plane strain in this section. In Fig. 3.10(a), the clear dislocations of lattices were observed 1-2 nm above the interface between Mn_4N and MgO. Although Mn_4N would be under a strong in-plane tensile due to the lattice mismatch below the dislocations, it would become relatively weak above the dislocations and there wouldn't be a direct influence from the lattice mismatch at the interface anymore. However, the value of c/a approaches 1 as t_{Mn_4N} increases, which is attributed to the imperfect relaxation of lattice constants at the dislocation. In contrast, Fig 3.10(b) shows no dislocation, even on larger areas (not shown), and evidences a perfect epitaxial growth. Thus, all parts of Mn_4N lattices are expected to be under the influence of the

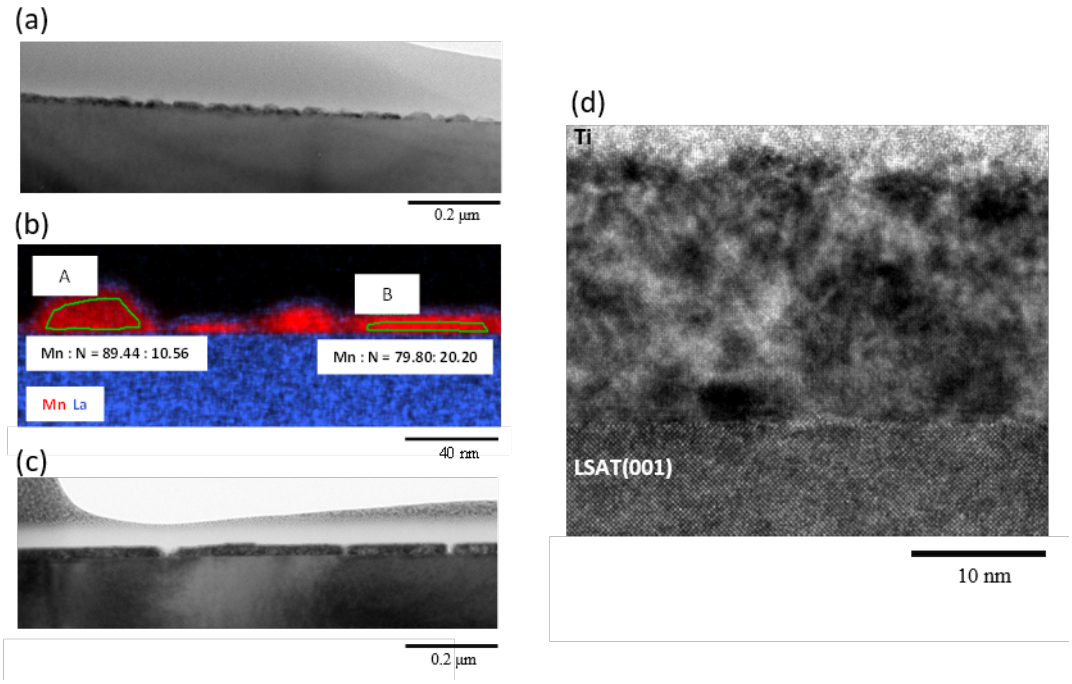

Figure 3.11: *(a) X-TEM and (b) EDX images of Mn and La of MNLSAT7 (t_{Mn_4N} = 10 nm). (c) X-TEM image of MNLSAT8 (t_{Mn_4N} = 20 nm) and (d) magnified view of (c).*

STO lattices, resulting in a mall in-plane tensile strain in all the Mn_4N layers. We concluded this as explains why c/a was smaller in Mn_4N/STO regardless of the relatively small lattice mismatch and that there was little change in c/a with t_{Mn_4N} in Mn_4N/STO.

To discuss the case of Mn_4N on LSAT, we compared X-TEM images of MNILSAT7, 8 (t_{Mn_4N} = 10, 20 nm, respectively) and took an energy-dispersive X-ray (EDX) image for MNLSAT7, as shown in Fig. 3.11. In Fig. 3.11(a) and (b), for t_{Mn_4N} = 10 nm, the Mn_4N film was found to be composed of small grains. The magnified EDX image in Fig. 3.11(b) shows that the Mn_4N film consists of various phases with different composition ratios. For example, the composition ratio of Mn:N was 89.44:10.56 in the region entitled "A", which is far from the ideal ratio for Mn_4N (4:1). On the other hand, it was 79.80:20.20 in the region "B", which is almost the ideal ratio. Figure 3.11(c) shows a large area X-TEM image of MNILSAT8 while Figure 3.11(d) is a magnified one. The Mn_4N lattices were clearly observed especially in Fig. 3.11(d). Considering these results, we concluded that the expected dead layer in Mn_4N/LSAT was attributable to non-ferrimagnetic Mn nitrides other than Mn_4N at the region close to the interface.

3.6 In-plane tensile and PMA

Figure 3.12 shows the relationship between K_U and c/a.

As discussed above, c/a was tuned with t_{Mn_4N} and substrates. We also show the data for Mn_4N grown on LSAT that we couldn't change c/a by t_{Mn_4N} and T_S during the growth and that the growth was different from other substrates. We confirmed that K_U got smaller as c/a approached 1 in all the Mn_4N films, regardless of the substrates except LSAT. We here added one broken gray line as a guide to the eyes so that the relationship between c/a and K_U becomes easy to understand. With this gray line, only Mn_4N on LSAT deviated from the trend of the other substrates. There are several possible factors for this. One is the very high T_S required for the epitaxial growth on LSAT. However, we've already confirmed the decrease

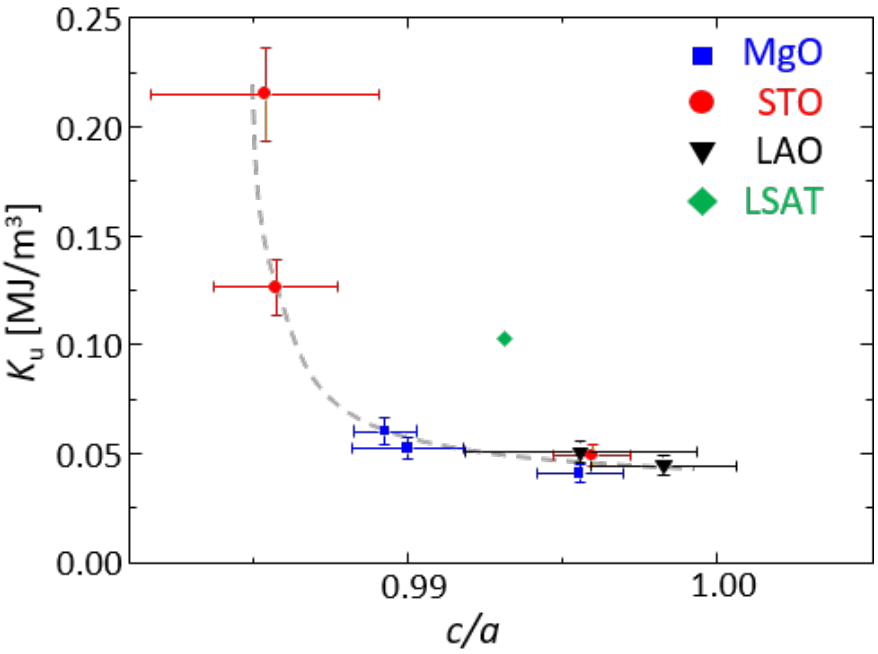

Figure 3.12: *Relationship between K_U and c/a. A broken gray line is a guide to the eyes.*

in K_U for $T_S > 500$ °C on STO, what's more, we have not succeeded in the epitaxial growth of Mn_4N on STO at $T_S > 600$ °C, which we attributed to the change in the morphology of the substrate surface by heat[175]. Another reason would be the less accuracy in the calculated lattice constants due to small XRD diffraction peaks of Mn_4N overlapped with the ones from LSAT. Referring to the plots of samples on MgO, STO, and LAO which grew under the same condition, we concluded that PMA in Mn_4N epitaxial films originated from the in-plane tensile distortion ($c/a < 1$) and there is a strong correlation between K_U and c/a, hence, K_U can be controlled by the magnitude of c/a by changing the growth condition or even by applying the external force.

There are also several hypotheses for the physical background of this correlation. The first-principle calculation suggested that Mn_4N with PMA is stable at $c/a \sim 0.98$ and K_U is strongly influenced by the magnitude of c/a. The change in the electronic states such as crystalline fields may explain this. Also, the complex magnetic structures such as local non-collinear magnetic order caused by dislocations around Mn_4N/substrate interfaces and nitrogen deficiencies, especially in the case of the Mn_4N film on MgO substrates due to the large lattice mismatch, could influence the obtained K_U values as well.

3.7 Summary of this chapter

- We succeeded in the epitaxial growth of Mn_4N on various substrates, MgO(001), STO(001), LAO(001) and LSAT(001), and partially c-axis oriented but polycrystaline growth of Mn_4N on LAO(001). Especially, epitaxial Mn_4N on LSAT, which have smaller lattice constants than those of Mn_4N, was first reported in this work.

- The ratio of lattice constant $c/a < 1$ was confirmed in all Mn_4N samples grown in this work despite of the expected in-plane compressive strain expected by the lattice mismatch with LAO and LSAT substrates. This result experimentally proved that Mn_4N films are

structurally stable at $c/a < 1$. This value can be influenced by the magnitude of lattice mismatch or the existence of dislocations in the films.

- The optimized T_S for the growth of Mn_4N on LSAT was found to be 750 $°C$ while it was 450 $°C$ for other substrates from the perspective of the squareness of hysteresis loops and the values of M_S and K_U. However, even the optimized Mn_4N on LSAT has a large dead layer with a thickness of approximately 10 nm.
- The correlation between c/a and K_U, the degree of PMA, was confirmed. This result will lead to the modulation of PMA in Mn_4N by selecting substrates or even by applying an external force on the film, which can also change the threshold current density for CIDWM.

Chapter

Magneto transport properties in $Mn_{4-x}Ni_xN$ 4

In this chapter, we present the temperature dependence of the magneto-transport properties of $Mn_{4-x}Ni_xN$ thin films, focusing on anisotropic magnetoresistance (AMR) and anomalous Hall effect (AHE). As mentioned in chapters 1 and 2, $Mn_{4-x}Ni_xN$ film is a rare-earth-free candidate for CIDWM, however, its magneto-transport properties have yet to be studied. The study of magneto-transport properties in $Mn_{4-x}Ni_xN$ is very important for a deep understanding of its CIDWM because it originates from the interaction between conduction electrons (s electrons), and localized electrons (d electrons). Their interactions can be investigated by AMR which derives from s-d scattering. Kabara and Tsunoda measured AMR of epitaxial Mn_4N films grown on MgO by sputtering and proposed that the crystal field acting on the Mn_4N films changed from cubic to tetragonal below 100 K[158]. Such transition in AMR ratio was ascribed to a change in the states of d orbitals induced by the temperature. Anzai *et al.*, measured AMR of epitaxial $Fe_{4-x}Mn_xN$ films grown on MgO by MBE and suggested a transition from majority to minority spin transport by increasing Fe content[133]. Also, AHE is another phenomenon that derives from the spin-dependent scattering of electrons with impurities and/or the spin-dependent band curvature, and importantly, the magnitude of AHE is macroscopically proportional to the magnetization. Since Mn_4N films have relatively large AHE angle (θ_{AHE}) of 2 %[67, 69], the investigation into the origin of AHE can lead to a deeper understanding of the magneto-transport properties as well.

Section 4.1 first briefly explains the fundamental theory of AMR and AHE, then section 4.2 lists the information of samples and experiments. Sections 4.3 and 4.4 deal with the results and discussions on AMR and temperature dependence of electrical resistivity, respectively, afterwards, we discuss the s-d scattering in $Mn_{4-x}Ni_xN$ films with the first-principle calculation in section 4.5. In section 4.6, we investigate magneto-transport properties by the analysis of AHE in $Mn_{4-x}Ni_xN$. In the end, we summarize this in chapter 4.7. This study has been published in T. Komori *et al.*,, J. Appl. Phys. **132**, 143902 (2022)[72]. T. Komori contributed to the growth of the samples and all of the experimental measurements. Ab-initio calculations were performed by Associate Prof. S. Honda of Kansai University. T. Komori joined the discussion to make conclusions about this study from the perspectives of both experiments and theories.

4.1 Fundamental theory of AMR and AHE

In this section, we explain the fundamental theory of AMR and AHE. On AMR, we first show its concept and then discuss the effect of the crystal field on AMR curves. On AHE, we mainly focus on the general understanding of the origins of AHE in ferromagnets.

4.1.1 Theory of AMR

AMR effect is macroscopically understood as the change in the electrical resistivity according to the relative direction of magnetization with respect to the electric current. More microscopically, AMR can be explained by the *s*-*d* scattering, in which conduction electrons (*s*, *p*, *d* electrons in the case of 3*d* transition metals) in plane waves are scattered in presence of spin-orbit interaction and into localized *d* orbitals. The resistivity which derives from *s*-*d* scattering is given as[176]

$$\rho_{sd}(\theta) \propto \sum_m \left|(\Psi_m^d|V_{imp}|e^{ik\cdot r})\right|^2 D_m^{E_F} \tag{4.1}$$

where Ψ_m^d is the wavefunction of *d* orbitals, V_{imp} is the potential energy of impurities. Here, the sum (Σ) is taken for all *d* orbitals. Thus, ρ_{sd} changes by the overlap of the wavefunctions of plane waves and *d* orbitals, technically, it depends on the spread of *d* orbitals along the direction of $\boldsymbol{r}$.

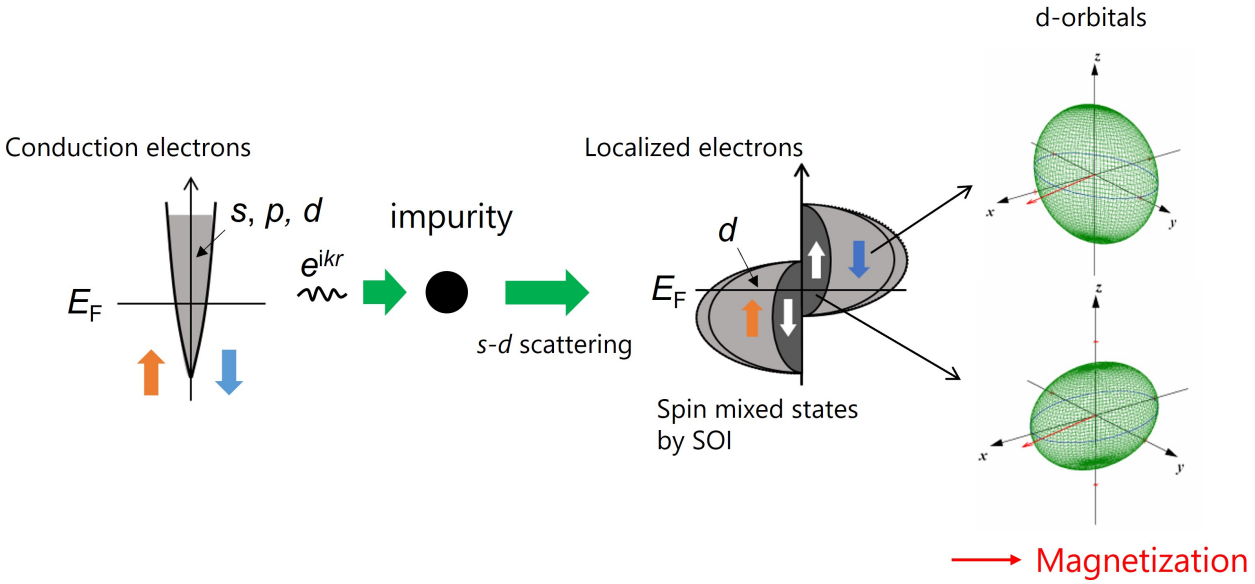

Figure 4.1: *Schematic image of AMR by s-d scattering. SOI hybridizes the DOS of up-spins and down-spins, and these states have d-orbitals with the shape of ellipses that align perpendicular to each other.[177]*

Figure 4.1 shows the explanation of AMR by *s*-*d* scattering. Assuming that there would be no spin-orbit interaction (SOI), the localized *d* orbital would form a sphere. In this case, there's no dependence on the direction of the magnetization. With non-zero SOI, however, the density of states (DOS) of up-spin and down-spin get hybridized, and the *d* orbitals formed in spheres due to the degeneracy will be reformed into ellipses, as shown in Fig. 4.1. Since conduction electrons are scattered into these states by *s*-*d* interaction, these *d* orbitals in ellipses, turned by the direction of the magnetization, induce the AMR effect[178]. In crystalline magnetic

materials, crystal fields also have a large influence on the formation of d orbitals. Figure 4.2 shows the split of d orbitals states and the following changes in the wavefunctions and ρ_{sd}. Here, the mathematical expression of ρ_{sd} is the case in which the spins of the conduction electrons during the scattering, such as in antiperovskite ferromagnetic (ferrimagnetic) nitrides or half-metals, based on Döring equations[179]. Since the d orbital is in a sphere without SOI, ρ_{sd} is constant regardless of the angle of magnetization (θ). It forms an ellipse under SOI and it has two-fold symmetry against the rotation of the magnetization. Therefore, it contributes to a $\cos 2\theta$ term of ρ_{sd}. Under the cubic crystal symmetry, although the configuration of d orbitals change by the split of their energy states, they still have two-fold symmetry and contribute to $\cos 2\theta$ as well. However, the split into d_γ and d_ϵ states results in the change in the probability of s-d scatterings as it depends on the DOS of d orbitals (D^d). This causes the change in the formation of d orbitals by the direction of the electric current, thus, AMR effects come to depend on the crystalline azimuth of the electric current[177, 180]. When the crystals lose the symmetry and they become tetragonal, d orbitals get further split and wavefunctions have four-fold symmetry which contributes to a $\cos 4\theta$ term of ρ_{sd}.

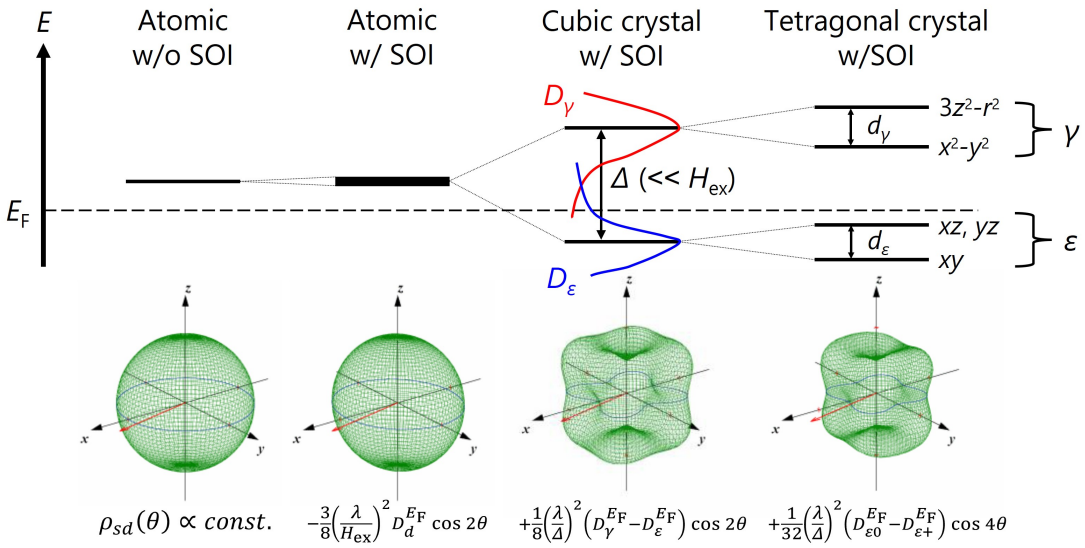

Figure 4.2: *The split of d orbital energy states by SOI and crystal fields, and the corresponding change in the existence probability of wavefunctions. The equations in the bottom line are the different contributions to the AMR effects (ρ_{sd}).*

From the explanation above, the efficiency of the AMR effect, AMR ratio (γ_{AMR}) in other words, can be given as

$$\gamma_{AMR} = (\rho(\theta) - \rho(90°))/\rho(90°) = C_0 + C_2 \cos 2\theta + C_4 \cos 4\theta \tag{4.2}$$

Here, $\rho(\theta)$ is the resistivity at the angle (θ) made by the magnetization direction and the current direction, C_2 is the coefficient of the twofold symmetric term with $\cos 2\theta$, C_4 is the coefficient of the fourfold symmetric term with $\cos 4\theta$, and C_0 is chosen to meet C_2 - C_4 so that the criterion of AMR(90°) = 0 is satisfied. Note that the Eq. 4.2 was first identified from experimental results in various ferromagnets and then physically explained.

One of the most meaningful analyses with AMR curves is the differentiation of the sign of the spin polarization in conduction electrons (P_σ). Kokado *et al.*, stated that γ_{AMR} can be expressed with DOS of $3d$ orbitals by applying the theory of electron scattering by impurities with SOI[178].

$$\gamma_{AMR} \propto -\gamma \cdot [D_{\uparrow}^{(d)} - D_{\downarrow}^{(d)}] \cdot (\sigma_{\uparrow} - \sigma_{\downarrow}) \tag{4.3}$$

Here, γ is a SOI constant, $D_{\uparrow,\downarrow}^{(d)}$ is the DOS of $3d$ orbitals at E_F for up-spin ($\uparrow$) and down-spin ($\downarrow$) and $\sigma_{\uparrow,\downarrow}$ is the electrical conductivity for $\uparrow$ and $\downarrow$ electrons. In $3d$ transition metals or compounds made from them, their total DOS are approximated to partial-DOS (PDOS) of $3d$ electrons. Therefore, the Eq. 4.3 can be rewritten as

$$\gamma_{AMR} \propto -P_D \cdot P_\sigma \tag{4.4}$$

where P_D is the spin polarization of DOS at E_F. Therefore, the sign of P_σ can be derived from the sign of P_D and γ_{AMR}. Figure 4.3 shows the relationship between the sign of AMR ratio and s-d scattering. In bcc-Fe with $P_\sigma < 0$, for example, $s\downarrow$ spin electrons are scattered into the localized $d\uparrow$ spin electrons, resulting in a positive γ_{AMR}. On the other hand, in Fe_4N with $P_\sigma < 0$, $\downarrow$ spin electrons are scattered into the $\downarrow$ spin states, resulting in the negative γ_{AMR}. This negative γ_{AMR} is attributable to the ellipse d-orbitals which give a larger probability of scattering at $\theta = 90°$than at $\theta = 0°$.

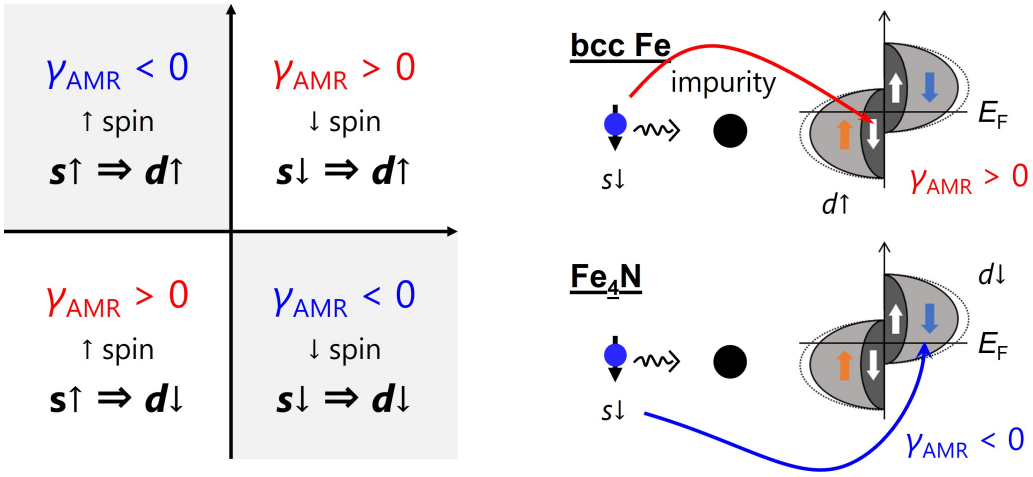

Figure 4.3: *(a) The relationship of γ_{AMR}, spins of majority conduction electrons and the main s-d scattering process. (b) The mechanism of scattering in the cases of bcc Fe and Fe_4N.*

4.1.2 Theory of AHE

Nowadays, thereare three main mechanisms that can give rise to AHE, and spin Hall effect (SHE), intrinsic deflection, extrinsic side jump, and extrinsic skew scattering[181]. Intrinsic mechanisms depend on the details of the whole band structure while extrinsic are scattering on defects. Figure 4.4 shows schematic images of these mechanisms of AHE. The theory of AHE was first proposed by Karplus and Luttinger in 1954[182], in which they evidenced that intrinsic AHE depends only on the band structure and independent from scatterings by phonons or impurities. Importantly, they derived the relationship of $\rho_{xy} \propto \rho_{xx}^2$ by inverting the conductivity tensors. This finding is still the base of the theory of AHE in modern times. The intrinsic contribution to the AHE (xy) conductivity in a perfect crystal can be calculated directly from Kubo formula. In short, it's given as[183, 184]

$$\sigma_{ij}^{AH-int} = -\epsilon_{ijl}\frac{e^2}{\hbar}\sum_n \int \frac{d\boldsymbol{k}}{(2\pi)^d} f(\epsilon_n(\boldsymbol{k}))b_n^l(\boldsymbol{k}) \tag{4.5}$$

where ϵ_{ijl} is the asymmetric tensor, e is the elementary charge, $\hbar$ is the reduced Planck constant, $b_n(\boldsymbol{k})$ is the Berry-phase curvature which is derived by the Berry-phase connection $(b_n(\boldsymbol{k}))$

$$\begin{aligned} \boldsymbol{a}_n(\boldsymbol{k}) &= i \langle n, \boldsymbol{k} | \nabla_{\boldsymbol{k}} | n.\boldsymbol{k} \rangle \\ \boldsymbol{b}_n(\boldsymbol{k}) &= \nabla_{\boldsymbol{k}} \times \boldsymbol{a}_n(\boldsymbol{k}) \end{aligned} \tag{4.6}$$

Note that Berry curvature is equivalent to the magnetic flux in electromagnetics.

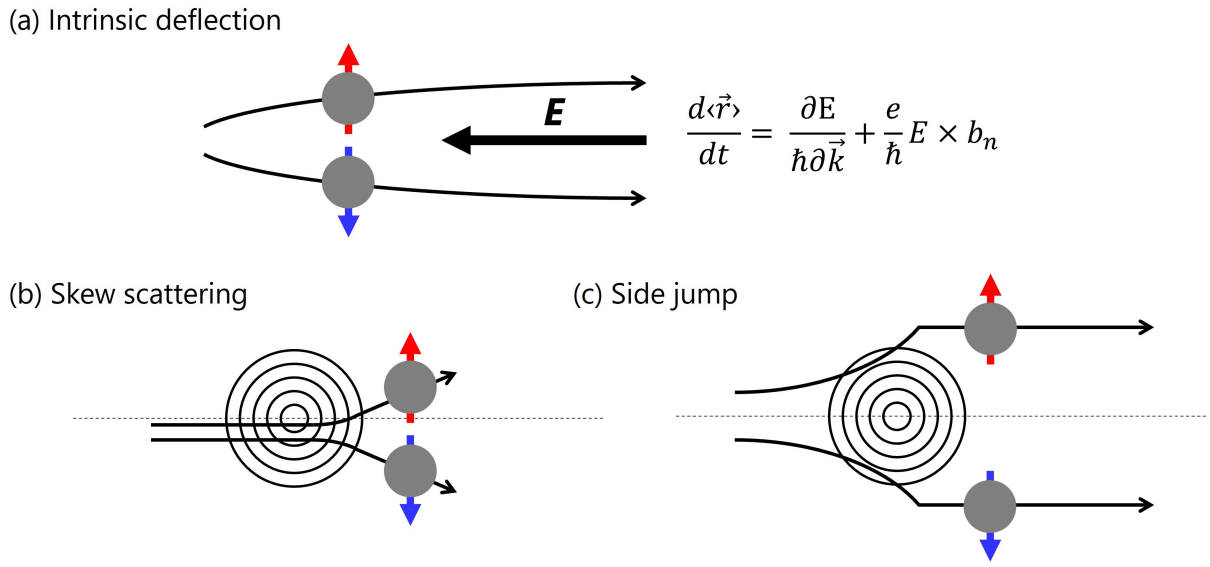

Figure 4.4: *Three main mechanisms that can give rise to an AHE. In any real material, all of these mechanisms act to influence electron velocity.*

Nevertheless, there was criticism of their theory as it lacks a discussion on the scatterings from disorders. In this context, Smit argued that the asymmetric scattering of electrons from impurities by their SOI occurs and derived the relationship of $\rho_{xy} \propto \rho_{xx}$, which is nowadays called skew scattering[185, 186]. Meanwhile, Berger proposed another extrinsic factor, side jump, in which the velocity of an electron is deflected in opposite directions by the opposite electric fields experienced on electrons when approaching and leaving an impurity[187]. The relationship for the side jump effect is predicted to be $\rho_{xy} \propto \rho_{xx}^2$, which is identical to intrinsic AHE. Thus, it's often puzzling to separate intrinsic AHE and extrinsic side jump. Comprehensively, the relationship of the scaling is given as[181]

$$\rho_{AH} = \rho_0 + \alpha\rho^2 + \beta\rho \tag{4.7}$$

where ρ is the longitudinal resistivity which is a function of temperature, α, and β are parameters for fitting, and ρ_0 is the resistivity only by impurities, in other words, ρ_{xx} at the absolute temperature. Recently, this equation was expanded to separate the scatterings by phonons and impurities, which is given as[188]

$$\rho_{xy} = \alpha_I\rho_I\rho + \beta_I\rho_I + \alpha_P\rho_P\rho + \beta_P\rho_P + \gamma\rho^2 \tag{4.8}$$

where ρ_I is the resistivity from impurities $(= \rho_0)$ and ρ_P is the one from phonons. In Eq. 4.8, the first term derives from the side jump by impurities, the second term is from skew scattering by impurities, the third term is from side jump by phonons, the fourth term is from skew scattering by phonons and the fifth term is from intrinsic AHE. However, in $3d$ transition

magnetic metals, the fourth term, skew scattering by phonons is negligibly small and thus often omitted[188].

4.2 Samples and measurements

Table 4.1 lists the structural information of the samples used in this work. The procedure of MBE growth is the same as in section 3.2 for chapter 3. Samples were grown on both STO(001) and MgO(001) substrates with a thickness of approximately 30 nm. The composition ratio of Mn and Ni was controlled by the temperature of Knudsen cells of Mn and Ni solid metal sources based on the rate-check completed before the growth of samples. According to this, the composition ratios of $Mn_{4-x}Ni_xN$ on STO were $x = 0$, 0.05, 0.15, and 0.2. And those on MgO were $x = 0$, 0.1, 0.2, and 0.3. SiO_2 capping layer was sputtered after the MBE growth on all $Mn_{4-x}Ni_xN$ samples.

Table 4.1: *The structural information of the samples used in this chapter. Refer to section 3.2 in chapter 3 for detailed information on the growth procedure.*

Sample	Substrate	Composition ratio (x)	t_{Mn_4N} [nm]
Sample 1	STO	0	30
Sample 2	STO	0.05	30
Sample 3	STO	0.15	30
Sample 4	STO	0.2	30
Sample 5	MgO	0	30
Sample 6	MgO	0.1	30
Sample 7	MgO	0.2	30
Sample 8	MgO	0.3	30

Figure 4.5 shows out-of-plane XRD profiles and RHEED images taken along [100] azimuth. We confirmed the epitaxial growth of $Mn_{4-x}Ni_xN$ in all samples from 001, 002, and 004 diffraction peaks in XRD profiles and streaky patterns in RHEED images. Note that small peaks marked by a red triangle at $2\theta \sim 44.7°$ of samples grown on MgO (Samples 5-8) are attributable to the reflection of X-rays from the stage for a sample. The detailed discussion of crystalline quality from XRD profiles and RHEED images is mentioned in section 3.3 in chapter 3.

For the measurement of magneto-transport properties, the samples were processed into Hall bars with a width of 100 μm. Circuits were patterned with a conventional photolithography system (Heisenberg Instruments: μPG501). AZ5214E (2-methoxy-1-methyl ethyl acetate) photoresist was used as a positive resist and it was spin-coated on the sample surface so that it becomes as thick as 2 μm. After the lithography, the sample was developed with NMD-3 (2.38% of tetramethylammonium hydroxide and 25% of tetramethyl ammonium hydroxide). Dry etching was done with Ar ion milling up to the vicinity of the substrate surface, avoiding over-etching in order to prevent the formation of the conductive 2D electron gases at the surface of reduced STO. Figure 4.6 shows the schematic image of the procedure to fabricate Hall bars.

In this work, all the electric and magneto-transport properties were measured with a PPMS (Quantum Design) as in chapter 3.

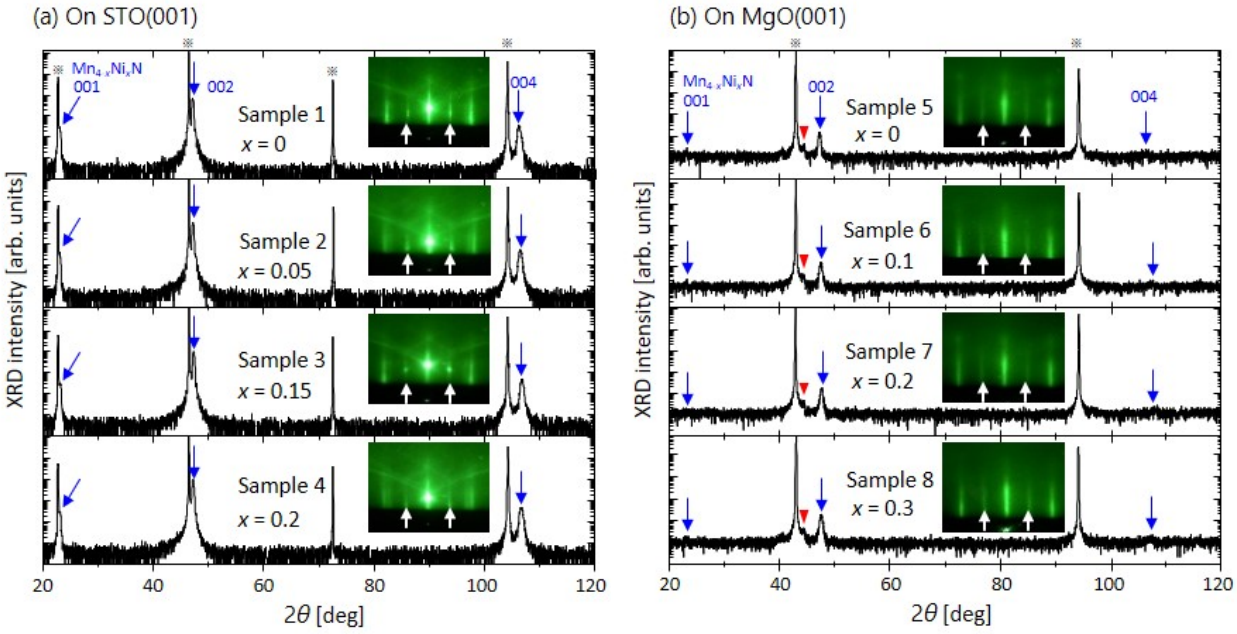

Figure 4.5: *Out-of-plane XRD profiles and RHEED images taken along the [100] azimuth of $Mn_{4-x}Ni_xN$ grown on (a) STO(001) and (b) MgO(001). White arrows in the RHEED images indicate the superlattice diffraction. Asterisks correspond to the diffraction from the substrates.*

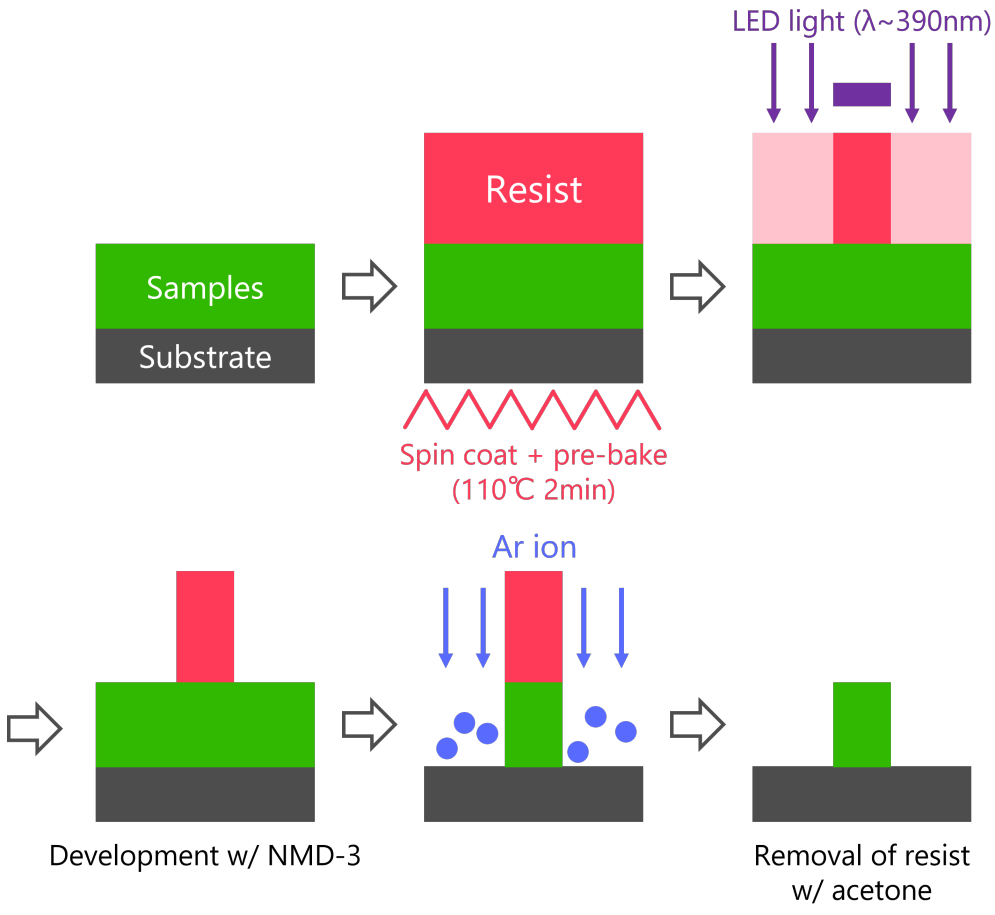

Figure 4.6: *The procedure of the device fabrication used in this chapter.*

4.3 AMR measurements

Figure 4.7 shows the AMR curves of $Mn_{4-x}Ni_xN$ films grown on (a)–(c) STO and (a')–(d') MgO substrates and measured at 5, 20, 60, 100, and 300 K. The AMR ratio was defined as

$$\gamma_{AMR} = (\rho(\theta) - \rho(90°))/\rho(90°) \tag{4.9}$$

where θ is the angle between the electric current along the $Mn_{4-x}Ni_xN$[100] azimuth and the magnetization (external magnetic field). The magnetization rotation was set in the x–y plane. As for Sample 4 ($x = 0.2$ on STO), however, the AMR curves were not correctly acquired because the magnetization was not fully saturated in the in-plane direction even at 9 T, which is the largest magnetic field with our PPMS, due to an extremely large anisotropy field. This is because the Ni composition $x = 0.2$ is at the vicinity of the magnetic compensation point, thus an extremely large magnetic field is required to align the magnetization in-plane from the viewpoint of Zeeman energy. The measurement for this particular sample is thus not shown. (start a new paragraph here).

The AMR curves of $Mn_{4-x}Ni_xN$ films grown on different substrates showed significant θ and T dependence. Briefly, the angular dependence originates from the change of the electron occupation of $3d$ orbitals in the direction of the magnetic moment with respect to the crystal axes. This is because AMR derives from the spin–orbit interaction, giving rise to spin-dependence in the scattering of conduction electrons into $3d$ orbitals. The obtained AMR curves in Fig. 4.7 can be well fitted by using the equation which contains both $\cos(2\theta)$ and $\cos(4\theta)$ terms as discussed later. The $\cos(2\theta)$ term stems from the twofold symmetry of 3d orbitals due to the spin–orbit interactions in a cubic crystal field. Meanwhile, the $\cos(4\theta)$ term arises from the fourfold symmetry of 3d orbitals due to tetragonal distortion. Now, two things are clear from the R curves in Fig. 4.7. First, $|\gamma_{AMR}|$ drastically decreased even with a small Ni composition ratio, showing that the Ni replacement changed the symmetry of $3d$ orbitals from that of Mn_4N. The decrease in $|\gamma_{AMR}|$ was more obvious for $Mn_{4-x}Ni_xN$ films grown on MgO(001) than for those grown on STO(001). We speculate that crystal imperfections such as dislocations caused by the large lattice mismatch between $Mn_{4-x}Ni_xN$ and MgO possibly decreased the magnitudes of their AMR ratios. The second important result acquired from Fig. 4.7 is that AMR ratios were positive at high temperatures like 300 K, whereas negative AMR ratios became dominant as the temperature decreased, especially below 100 K. Similar results have been reported for Mn_4N films on MgO[133, 158]. Since the AMR resistivity comes from the scattering between conduction electrons (s electrons) and localized electrons (d electrons), this change in AMR ratio by Ni composition ratio should be discussed in terms of spin polarization of s electrons and PDOS of d electrons. This will be discussed in section 4.5 with the results of the ab-initio calculation.

Fig. 4.8 shows the Fourier coefficients of the AMR curves in Fig. 4.7 fitted with $\gamma_{AMR} = C_0 + C_2 \cos 2\theta + C_4 \cos 4\theta$ ($C_0 = C_2 - C_4$) represented in Eq. 4.2. First, we discuss the C_2 term. For the cases of $Mn_{4-x}Ni_xN$ films grown on STO, the sign of C_2 reversed from positive to negative around 100 K for $x = 0.05$ and at approximately 40 K for $x = 0$ and 0.15. A similar trend was also observed for $Mn_{4-x}Ni_xN$ films grown on MgO(001). The $3d$ orbitals of anti-perovskite ferromagnets (ferrimagnets) are split into the two states $d\epsilon$ and $d\gamma$ by a cubic crystal field. These states are further split into finer states $d\gamma$ ($d_{3z^2-r^2}$, $d_{x^2-y^2}$) or $d\epsilon$ (d_{xy}, d_{yz}, d_{zx}) by a tetragonal distortion[180], as shown in Fig. 4.2. We assume that the sample and the magnetization were perfectly in the x–y plane and that the current flow in the x direction which is [100] crystalline azimuth. We also consider that the ↑ spin electrons dominate the electrical conduction in Mn_4N on the basis of the experimental results on spin polarization [133]. When

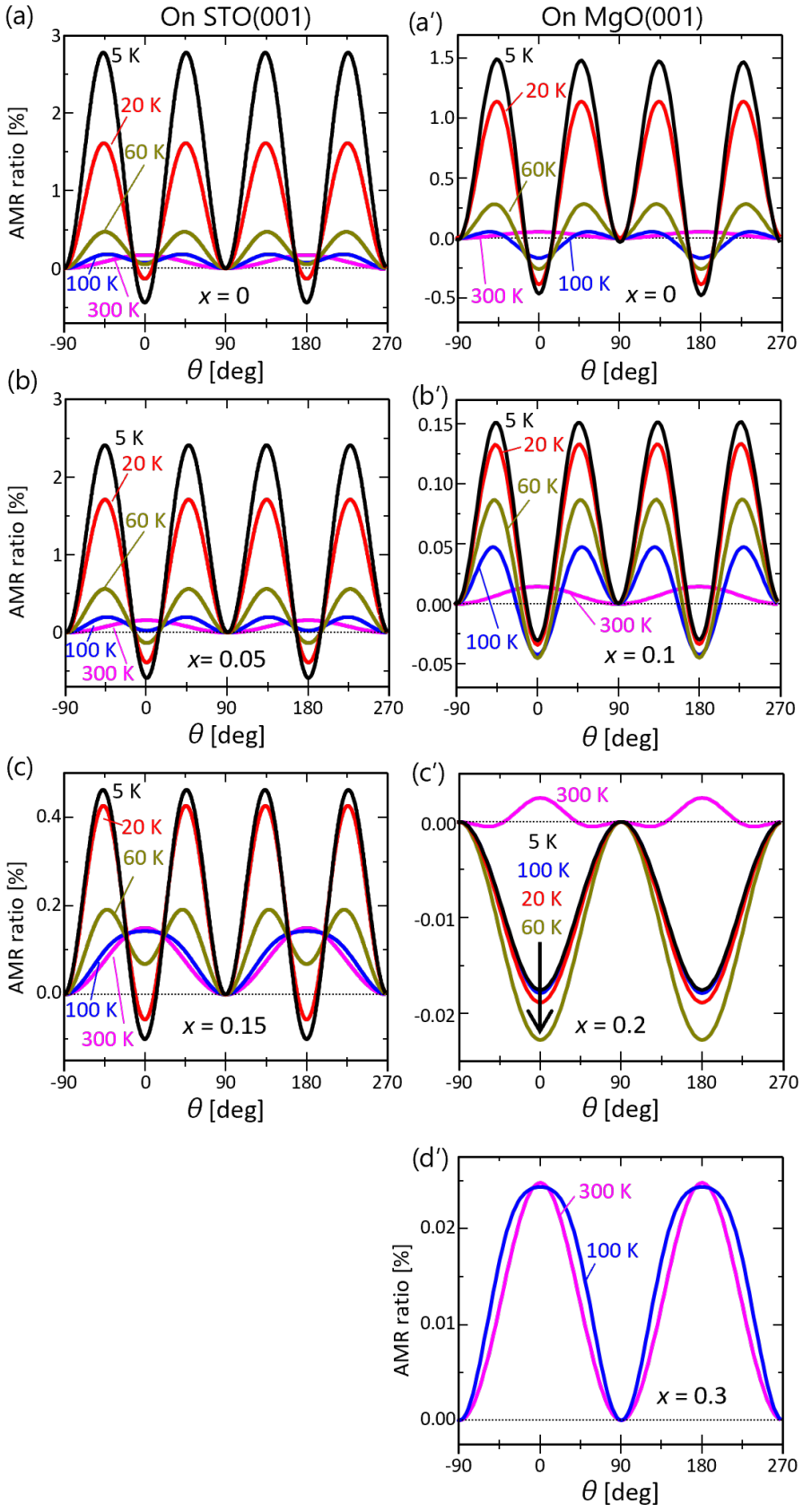

Figure 4.7: *Temperature dependence of ARM curves of $Mn_{4-x}Ni_xN$ films on STO(001) at (a) $x = 0$, (b) $x = 0.05$, and (c) $x = 0.15$ as well as those on MgO(001) at (a') $x = 0$, (b') $x = 0.1$, (c') $x = 0.2$, and (d') $x = 0.3$.*

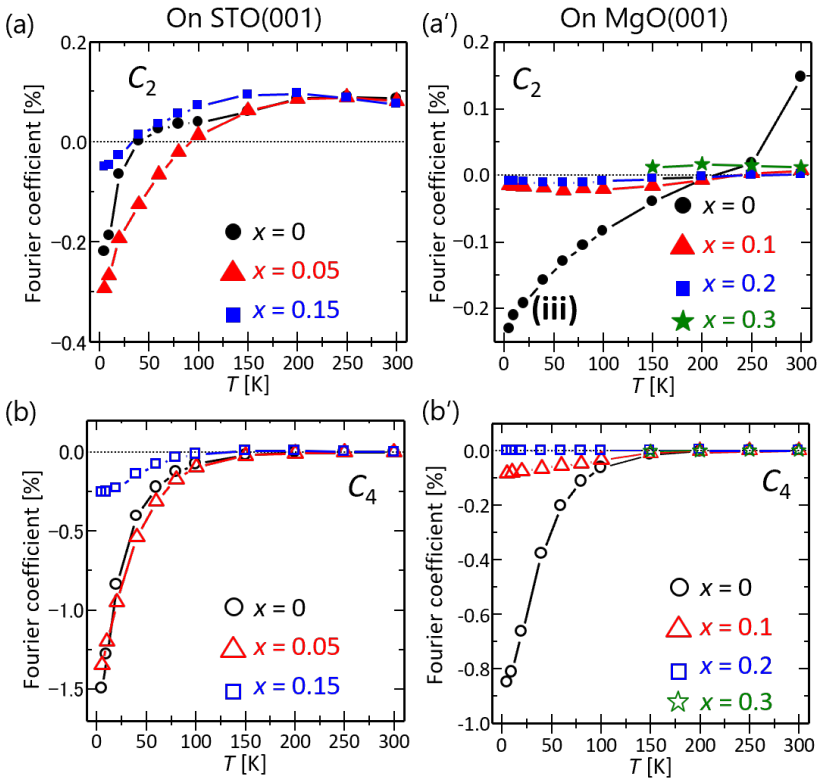

Figure 4.8: *Fourier coefficients of the AMR curves of $Mn_{4-x}Ni_xN$ on STO(001) (x = 0, 0.05 and 0.15) for (a) C_2 and (b) C_4, and on MgO (001) (x = 0, 0.1, 0.2 and 0.3) for (a') C_2 and (b') C_4.*

the dominant s–d scattering process is the scattering of ↑ (↓) spin conduction electrons into ↓ (↑)-spin d bands, C_2 is given as[158]

$$C_2^{\uparrow(\downarrow)\to\downarrow(\uparrow)} \propto \left(\frac{\lambda}{H_A - \Delta}\right)^2 D_{A,\xi_+,\downarrow(\uparrow)} + \left(\frac{\lambda}{-H_B - \Delta}\right)^2 D_{B,\xi_+,\downarrow(\uparrow)} \tag{4.10}$$

where λ is the spin-orbit coupling constant, $H_{A(B)}$ is the exchange splitting of sublattice A (B), Δ is the energy difference between d_γ and d_ϵ, $D_{A(B),\xi_+(\gamma,\delta\epsilon)\zeta}$ is the PDOS of the $d_\xi(d_\gamma, d_{\delta\epsilon})$ orbital with ζ spin at E_F of sublattice A (B) as depicted in Fig. 4.2. Note that this Eq. 4.10 is the expansion of the AMR in ferromagnets into the cases of ferrimagnets with two sublattices A and B. We found that the sign of C_2 is always positive in this case, therefore, it cannot explain the sign reversal of C_2 of the experimental results. However, when the ↑ (↓) spin conduction electrons are preferentially scattered into ↑ (↓) spin d bands, C_2 is expressed as

$$C_2^{\uparrow(\downarrow)\to\uparrow(\downarrow)} \propto \left(\frac{\lambda}{\Delta}\right)^2 \left\{\left(D_{A,\gamma,\uparrow(\downarrow)} + D_{B,\gamma,\uparrow(\downarrow)}\right) - \left(D_{A,\delta\epsilon,\uparrow(\downarrow)} + D_{B,\delta\epsilon,\uparrow(\downarrow)}\right)\right\} \tag{4.11}$$

Eq. 4.11 can give negative values of C_2 at low temperatures because the first term becomes smaller than the second term with the decrease in temperature. The magnitude correlation was reversed at high temperatures like RT due to the shift in E_F, whereby the ↑ (↓) spin conduction electrons are scattered into the ↑ (↓) spin d bands in $Mn_{4-x}Ni_xN$ films.

Then, we discuss the C_4 term. In previous research, the presence of the $cos4\theta$ curve in the AMR curves was interpreted to originate from the tetragonal crystal field[180]. This tetragonal crystal field was hypothetically attributed to the difference in thermal expansion coefficients

between Mn_4N films and MgO substrates[133, 158]. In this work, we confirmed that the $\cos 4\theta$ term appeared both in Mn_4N and $Mn_{4-x}Ni_xN$ films. However, $|C_4|$ significantly decreases only by very Ni composition ratio, even $x \sim 0.05$. It is not likely that such a small amount of Ni atoms (~ 0.5) drastically changed the thermal expansion coefficient of Mn_4N ($Mn_{4-x}Ni_xN$) films. In addition, not only Mn_4N but also $Mn_{4-x}Ni_xN$ films are known to have an in-plane tensile strain, regardless of the substrate (MgO and STO) [68, 69]. Considering these facts, we attribute the presence of the tetragonal crystal field not to extrinsic factors such as strain from lattice mismatch but to intrinsic factors like PDOS modulations of d orbitals. This discussion follows in section 4.5.

4.4 Temperature dependence of the resistivity

Figure 4.9 shows the temperature dependence of the longitudinal electric resistivity (ρ_{xx}) of $Mn_{4-x}Ni_xN$. ρ_{xx} was measured in the range of 2-300 K, and the residual-resistivity ratio (RRR) was calculated with the following equation.

$$RRR = \frac{\rho_{xx}(300K)}{\rho_{xx}(2K)} \tag{4.12}$$

Phonon scattering and impurity scattering of electrons mainly determine the electrical resistivity. While phonon scattering is temperature dependent and suppressed under low temperatures, impurity scattering is scarcely influenced by temperature. Therefore, the RRR calculated with Eq. 4.12 represents how much the conduction electrons in $Mn_{4-x}Ni_xN$ are scattered regardless of temperature. Focusing on substrate dependence, RRR was 15.6 for Mn_4N on grown STO and 4.09 for Mn_4N grown on MgO. XRD profiles and RHEED images revealed that the crystallinity and c-axis orientation of Mn_4N films grown on MgO is not as good as those on STO, which is mainly due to the large lattice mismatch between Mn_4N grown on MgO. The relatively low RRR value of 4.09 in Mn_4N on MgO was, thus, attributable to crystal imperfections such as defects and/or excessive Mn and N atoms.

According to the report of Fe_4N by Kabara *et al.*, it was found that the order of N atoms located at the body-centered sites in Fe_4N (S), which is very sensitive to growth conditions, have an influence on RRR and AMR ratio. In short, the magnitude of RRR, and both C_2 and C_4 of AMR increased significantly for higher S. Nevertheless, cross-sectional TEM images of $Mn_{3.75}Ni_{0.25}N$ on STO had already revealed that a small amount of Ni composition ratio did not cause deterioration of single crystals or induced dislocations. Therefore, the decrease in RRR caused by a small Ni composition ratio of $Mn_{4-x}Ni_xN$ was expected to originate from other factors. To investigate these factors, we scaled ρ_{xx}-T in Fig. 4.9 with the following equation.

$$\rho_{xx} = \rho_0 + A_2T^2 + A_3T^5 - A_4 \ln T \tag{4.13}$$

where ρ_0 is the residual resistivity and A_1, A_2 and A_3 are coefficients used for the scaling. The second term in Eq. 4.13 represents the effect of Fermi liquid or electron-magnon scattering, the third term represents phonon scattering and the fourth term represents the contribution from Kondo effect. Notably, the coefficient of the fourth term (A_4) was zero in Mn_4N regardless of the substrate while it was not approximated to zero in $Mn_{4-x}Ni_xN$ ($x > 0$). This result suggested a non-zero Kondo effect in $Mn_{4-x}Ni_xN$ at low temperatures (< 10 K). The Kondo effect is known to derive from the increase in resistivity caused by the s–d interaction between conduction electrons and localized electrons of magnetic impurities under low temperatures. In the $Mn_{4-x}Ni_xN$ films used in this work, we can consider Ni atoms to be magnetic impurities in Mn_4N owing to the small Ni composition ratio, approximately 5-6% at the largest. This suggests

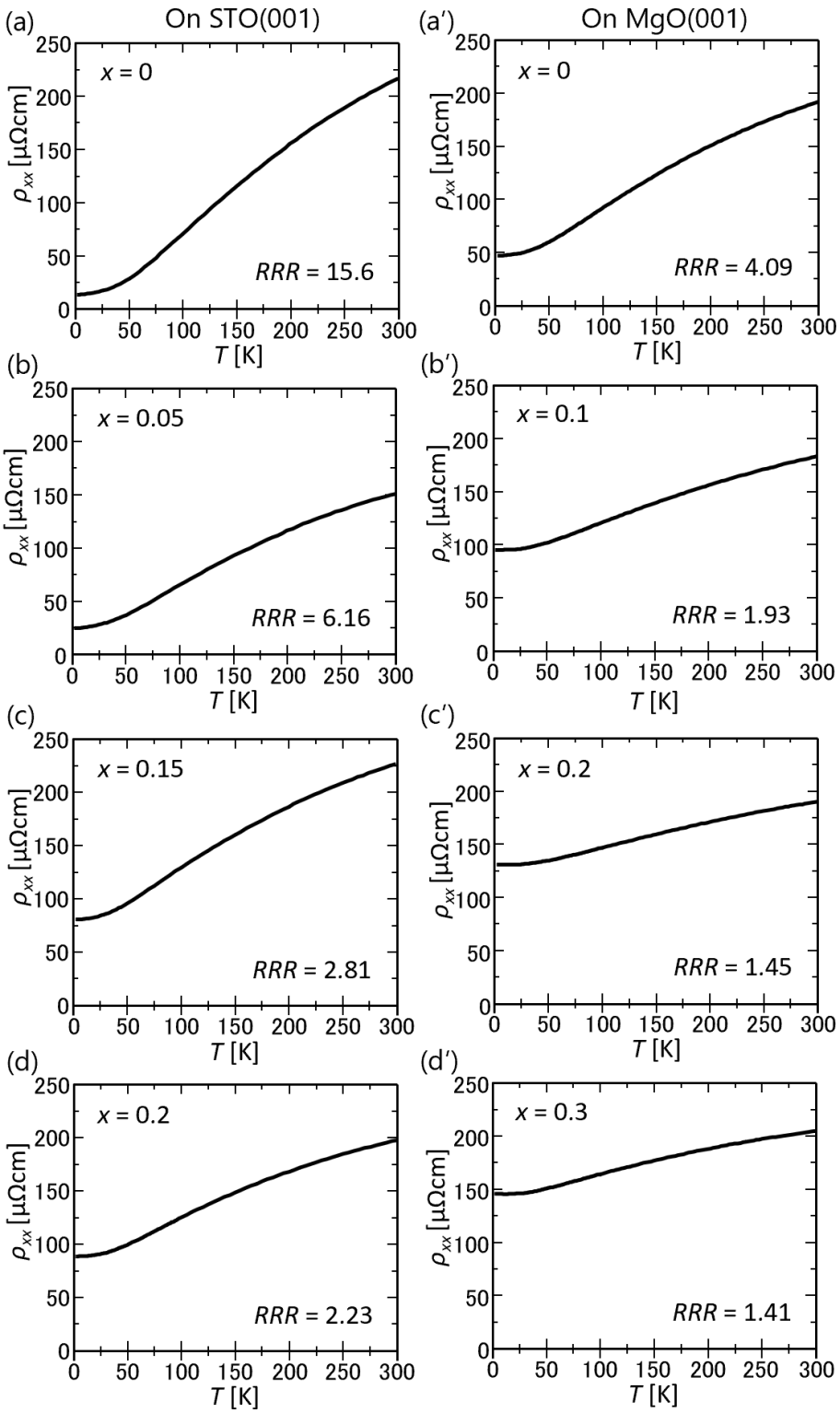

Figure 4.9: *Temperature dependence of longitudinal resistivity (ρ_{xx}) in $Mn_{4-x}Ni_xN$ films on STO(001) at (a) $x = 0$, (b) $x = 0.05$, (c) $x = 0.15$, and (d) $x = 0.2$, and those on MgO(001) at (a') $x = 0$, (b') $x = 0.1$, (c') $x = 0.2$, and (d') $x = 0.3$.*

that there would be no or negligible exchange interaction between electrons of two Ni atoms in the $Mn_{4-x}Ni_xN$ crystals. Our previous study on XAS and XMCD spectra of $Mn_{4-x}Ni_xN$ revealed that Ni atoms occupy corner-sites (I-sites) with magnetic moments antiparallel to those of Mn(I). Considering such magnetic structure, the Kondo effect in $Mn_{4-x}Ni_xN$ is attributable to the coupled spin angular momentum of conduction electrons and localized $3d$ electrons of Ni(I), leading to a non-magnetic state in total. However, further discussion may be needed because the Kondo effect is usually observed in the system which consists of normal metal and a small composition of magnetic impurities.

Regardless of the existence of the Kondo effect, electrical conductance in $Mn_{4-x}Ni_xN$ was expected to be affected by d electrons of Ni atoms even though PDOS of d orbitals are larger at Mn(II) than those at Mn(I), hence Fermi surfaces of electrons are expected to cover Mn(II) atoms[189].

4.5 Ab-initio calculation of PDOS

In order to further discuss the change in d orbital states, we calculated the PDOS of these orbital states by first-principle calculation. The VASP code with projector augmented wave (PAW) potentials in the generalized gradient approximation of the Perdew–Burke–Ernzerhof (GGA-PBE) functional was used to compute the PDOS of d orbitals in $Mn_{4-x}Ni_xN$[190–192]. The cutoff energy was set to 450 eV, and the sampling mesh of the crystal momentum k was set to $(k_x, k_y, k_z) = (17, 17, 17)$. We assumed that all the Ni atoms would occupy Mn I sites, which is based on the XAS and XMCD experimental results[70]. The structure was set to consist of $2 \times 2 \times 2$ cubic cells so that the spatial symmetry would be preserved during the structural optimization. Note that we neglected the effect of the in-plane tensile on $Mn_{4-x}Ni_xN$ discussed in chapter 3 because the result of the calculation didn't get converged in tetragonal systems due to the poor structural symmetry. Figure 4.10 shows the schematic structures of $2 \times 2 \times 2$ of $Mn_{4-x}Ni_xN$ used for the first-principle calculation.

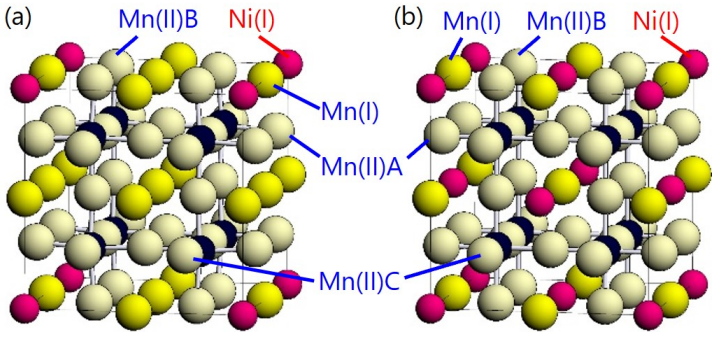

Figure 4.10: *Schematic structure of $2 \times 2 \times 2$ $Mn_{4-x}Ni_xN$ [x = (a) 0.125 and (b) 0.5] used for the first-principle calculation with VASP. Mn atoms are positioned at corner sites (I sites) and face-centered sites (II sites). II sites neighboring Ni and N atoms can be further divided into IIA, IIB, and IIC sites. The spatial symmetry was kept regardless of Ni atoms, and the structure was kept in cubic during the optimization process.*

Figure 4.11 shows the PDOS of d orbitals of $Mn_{4-x}Ni_xN$ at the vicinity of E_F. We first discuss the PDOS of Mn_4N in Fig. 4.11(a)-(d). For Mn(I) sites, in Fig. 4.11(a), the PDOS of d_{xy} (red), d_{yz} (green), and d_{zx} (blue) overlap, and those of $d_{x^2-y^2}$ (black dotted line) also overlap with those of $d_{3z^2-r^2}$ (purple line). This suggests that the degeneracies of d_γ and $d_{\delta\epsilon}$ orbitals are 2 and 3, respectively. On the other hand, for Mn(II)A sites in Fig. 4.11(b), the

PDOS of d_{zx} differs from those of d_{xy} and d_{yz}. Similarly, the PDOS of d_{xy} differs from those of the d_{yz} and d_{zx} for Mn(II)B in Fig. 4.11(c), and the PDOS of d_{yz} differs from those of d_{xy} and d_{zx} for Mn(II)C in Fig. 4.11(d). Through these results, we note that d_γ orbitals are not degenerate at Mn(II) sites. During the structural optimization, the cubic Mn_4N has the same atomic arrangement in the x, y, and z directions. Thus, the total PDOS of the three $d_{\delta\epsilon}$ (d_{xy}, d_{yz}, and d_zx) orbitals overlap, and the sum of those of the two d_γ ($d_{x^2-y^2}$, $d_{3z^2-r^2}$) orbitals also overlap when the PDOS are summed over the unit cell. However, when we classify Mn(II) atoms as Mn(II)A, Mn(II)B, and Mn(II)C as shown in Fig. 4.11, neither the three $d_{\delta\epsilon}$ orbitals nor the two d_γ orbitals are completely degenerate as described above even in the cubic structure of Mn_4N.

Through these considerations, we then discuss the appearance of the C_4 term in the AMR curves. According to the previous report in the AMR of Mn_4N/MgO[158], the C_4 term is proportional to the difference in PDOS between $d_{\epsilon 1}$ (=d_{zx}) and $d_{\epsilon 2}$ (=d_{xy}, d_{yz}) orbitals. Focusing on the PDOS of Mn(II)A sites in the vicinity of E_F in Fig. 4.11(b), the PDOS of $d_{\epsilon 1}$ are almost the same (1.0 eV^{-1} $atom^{-1}$, $orbit^{-1}$ $spin^{-1}$) as those of $d_{\epsilon 2}$ orbitals for the ↑ spin electrons. In contrast, the PDOS of $d_{\epsilon 1}$ are almost zero whereas those of $d_{\epsilon 2}$ orbitals are approximately 0.5 eV^{-1} $atom^{-1}$, $orbit^{-1}$ $spin^{-1}$, contributing to the C_4 term. Similar results were acquired with Mn(II)B and Mn(II)C sites as shown in Fig. 4.11(c) and (d). We conclude that this is the reason why the C_4 term appeared in the AMR curves.

Figures 4.11(e)–(h) show the PDOS of Mn(I), Mn(II)A, Mn(II)B, and Mn(II)C in $Mn_{4-x}Ni_xN$ with $x = 0.125$, respectively, and Figs. 4.11(i)–(l) show those with $x = 0.5$, respectively. We found that the PDOS at E_F are different from those in Mn_4N. In Fig 4.11(e) and (i), the PDOS of Ni(I) and Mn(I) sites are shown together and represented by bright lines with the same color. For the Mn(II) of $Mn_{3.875}Ni_{0.125}N$ in Figs. 4.11(f)–(h) and those of $Mn_{3.5}Ni_{0.5}N$ in Figs. 4.11(j)–(l), the PDOS of the ↑ spin electrons are transited to the high-energy side by approximately 0.1 and 0.5 eV, respectively, compared to those in Mn_4N in Fig. 4.11(a)-(d). This leads to a change in the PDOS, thereby giving rise to the C_4 term. We, therefore, conclude that the tetragonal crystal field induced in Mn_4N and $Mn_{4-x}Ni_xN$ films were not caused by extrinsic factors such as tensile strains, but by intrinsic factors such as the difference in PDOS of d orbitals between Mn(II)A, Mn(II)B, and Mn(II)C sites which is caused by the replacement of Ni atoms with Mn(I) atoms, even by the replacement of 1% of Mn atoms. We found it unique that such a large shift in E_F takes place only by a small Ni composition ratio in $Mn_{4-x}Ni_xN$. This drastic change in the properties can open the door for Mn_4N based nitrides films as a rare-earth-free platform for ferrimagnetic spintronics.

4.6 Temperature dependence of AHE

Figure 4.12 shows the temperature dependence of AHE conductivity (σ_{AHE}) and the longitudinal conductivity dependence (σ_{xx}) of $|\sigma_{AHE}|$ of $Mn_{4-x}Ni_xN$ grown on STO ($x = 0$, 0.05, 0.15, 0.2) (Sample 1-4) and those on MgO ($x = 0$, 0.1, 0.2, 0.3) (Sample 5-8). During the measurement, the temperature was modulated between 5-300 K. For samples of $Mn_{4-x}Ni_xN$ ($x = 0.2$, 0.3) on MgO, however, we successfully measured σ_{AHE} only above 130 K due to the divergence of the coercivity field caused by the magnetic compensation. This is why we have a smaller number of data points. In this work, σ_{AHE} is defined as

$$\sigma_{AHE} = \frac{\rho_{AHE}}{\rho_{xx}^2 + \rho_{AHE}^2} \tag{4.14}$$

First, we focus on the temperature dependence of σ_{AHE} (Fig. 4.12 (a) and (b)). For

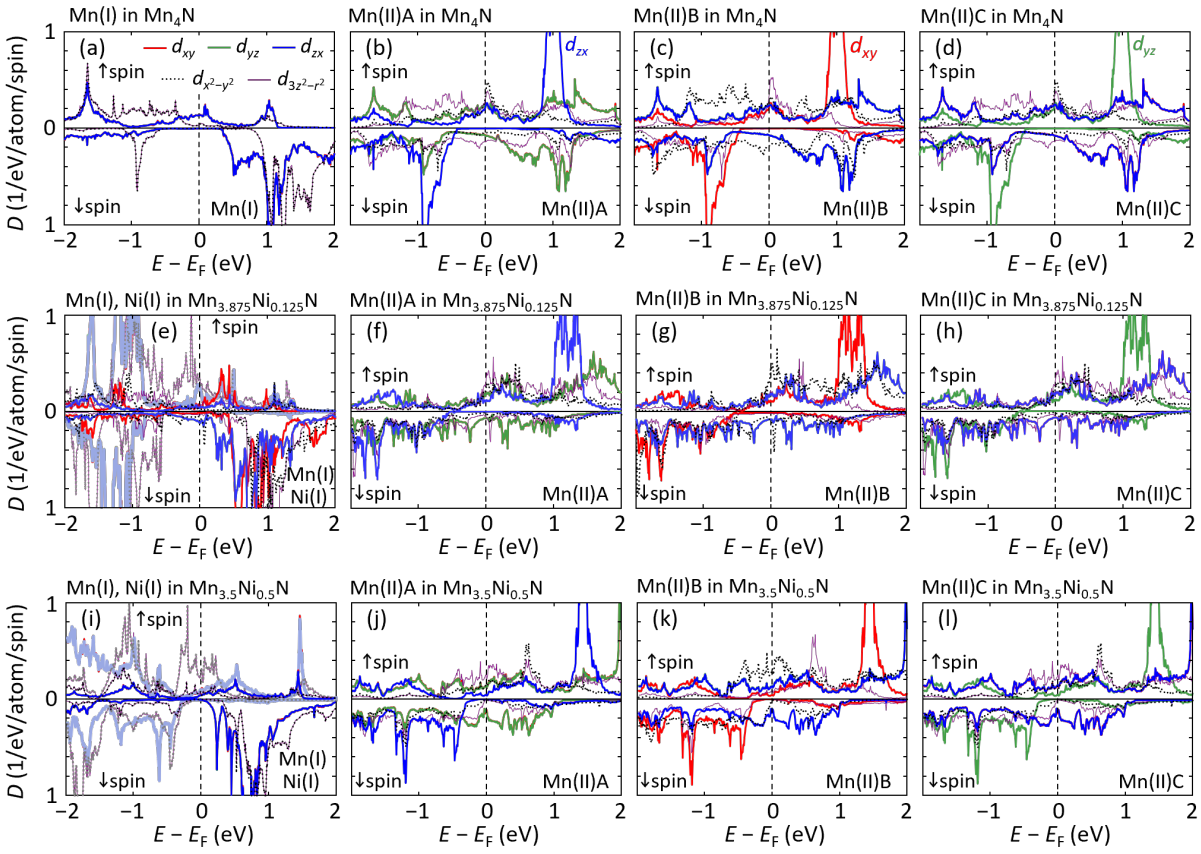

Figure 4.11: *PDOS (D) of each d orbital of Mn_4N at the vicinity of the Fermi energy (E_F) for (a) Mn(I), (b) Mn(II)A, (c) Mn(II)B, and (d) Mn(II)C sites, those of $Mn_{3.875}Ni_{0.125}N$ for (e) Mn(I) and Ni(I), (f) Mn(II)A, (g) Mn(II)B, (h) Mn(II)C, and those of $Mn_{3.5}Ni_{0.5}N$ for (i) Mn(I) and Ni(I), (j) Mn(II)A, (k) Mn(II)B, and (l) Mn(II)C. In (e) and (i), the PDOSs for Ni(I) sites are plotted with soft colors.*

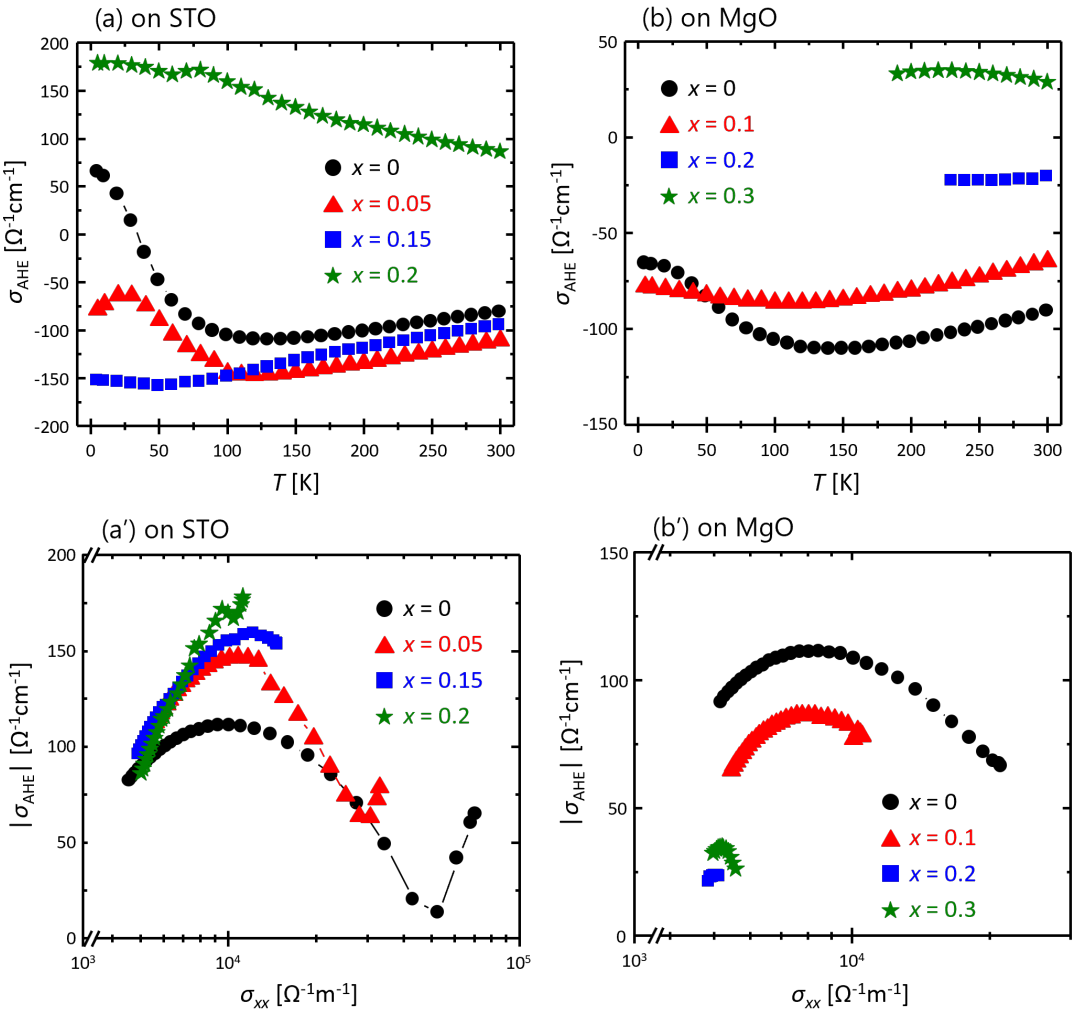

Figure 4.12: *Temperature dependence of σ_{AHE} in $Mn_{4-x}Ni_xN$ on STO (a) and on MgO (b) and the correlation of $|\sigma_{AHE}|$ and σ_{xx} in $Mn_{4-x}Ni_xN$ on STO (a') and on MgO (b'). During the measurement, temperature was modulated between 5-300 K. However, the data points below 130 K are missed in $Mn_{4-x}Ni_xN$ (x = 0.2, 0.3) grown on MgO.*

$Mn_{4-x}Ni_xN$ on STO, the magnitude of σ_{AHE} increased as temperature decreased from 300 K to approximately 100 K. Below 100 K, however, the magnitude of σ_{AHE} decreased for samples with small Ni composition ratio, $Mn_{4-x}Ni_xN$ (x = 0, 0.05) on STO and $Mn_{4-x}Ni_xN$ (x = 0) on MgO, while this effect became less influential and eventually negligible as Ni composition ratio increased ($x > 0.1$). Such decrease in $|\sigma_{AHE}|$ was observed in sputtered Mn_4N films grown on MgO (001) as well, and it was attributable to the emergence of tetragonal crystal field confirmed through AMR measurements[158]. More technically, the intrinsic AHE is connected with not only the Berry curvature but also the electron hopping between d orbital states[193]. The hopping of electrons can take place between two states with the same magnitude of the orbital angular momentum (l_z). In the case of $3d$ transition metal, electrons can make hopping between d_{xz} and d_{yz} ($|l_z| = 1$), or between d_{xy} and $d_{x^2-y^2}$ ($|l_z| = 2$). In crystals, however, the energy states of d_{xy} and $d_{x^2-y^2}$ do not degenerate and the energy gap between them is too large for electrons to make hopping from one to another. Therefore, the electron hopping which induces intrinsic AHE takes place only between d_{xz} and d_{yz}. When the crystal field changes from cubic to tetragonal, d_ϵ states get to be split into two states and d_{xz} and d_{yz} shift to higher energy states, which results in the decrease in their PDOS and a number of electrons which make hopping to induce AHE. Therefore, the decrease in σ_{AHE} can be explained if we assume that the main mechanism of AHE in Mn_4N and $Mn_{4-x}Ni_xN$ under low temperature is intrinsic deflection. We'd like to also mention that we didn't find reproducibility of the sign reversal of σ_{AHE} in Mn_4N grown on STO in different samples with the same structure. We suspect it came from the degree of body-centered N atoms which would affect PDOS of especially Mn(II) from the viewpoint of the distance between the metal atoms and N atoms.

Before discussing the relationship between $|\sigma_{AHE}|$ and σ_{xx}, we explain the empirical approach to investigate the mechanism of AHE with the experimental data in various magnets. We are supposed to investigate the mechanism of AHE not only by analyzing the correlation between σ_{AHE} and σ_{xx} (ρ_{AHE} and ρ_{xx}) but also by focusing on the degree of σ_{xx} (ρ_{xx}). Considering the σ_{xx} in $Mn_{4-x}Ni_xN$, it can be separated into two regions, good metal regime ($\sigma_{xx} > 10^4$ $[\Omega m]^{-1}$) and bad metal-hopping regime ($\sigma_{xx} < 10^4$ $[\Omega m]^{-1}$). In good metal regime, Miyasato *et al.*, first proposed Fe, Ni, and Co within this range of conductivity which mainly originates from either intrinsic AHE or extrinsic side jump[194]. In the scaling of conductivity, this is represented by the constant $|\sigma_{AHE}|$ against σ_{xx}. In a bad metal-hopping regime, on the other hand, the origin of AHE has been still obscure. Nevertheless, the scaling of conductivity is revealed to be usually $\sigma_{AHE} \propto \sigma_{xx}^{\alpha}$ ($\alpha = 1.6 \sim 1.8$), and AHE may originate from inelastic scatterings such as ones induced by phonons[194–196].

Now, we discuss σ_{xx} dependence of σ_{AHE} in $Mn_{4-x}Ni_xN$. In both samples grown on STO and MgO, the plots got into the good metal regime as temperature decreased for samples with a small Ni composition ratio. We found the decrease of $|\sigma_{AHE}|$ against σ_{xx} in the good metal regime, which we can explain with the decrease in the PDOS of d_{xz} and d_{yz} states related to the electrons hopping. Although the investigation with the scaling or previous study on the metals in the good metal regime can seldom distinguish the intrinsic AHE and extrinsic side jump, we proved AHE in $Mn_{4-x}Ni_xN$ in good metal regime (approximately under 100 K with Ni composition ratio of $x < 0.1$) mainly derive from intrinsic AHE with both studies on AHE and AMR. For samples with relatively high Ni composition ratio such as $x > 0.15$, however, the plots scarcely lay on good metal regime even under low temperature, and the decrement of $|\sigma_{AHE}|$ was very small. This result suggests the influence of intrinsic AHE drastically became weaker by a small Ni composition ratio. Further discussion will follow with the scaling of the resistivity in Figure 4.13.

Focusing on the bad metal-hopping regime, we found the relationship of $\sigma_{AHE} \propto \sigma_{xx}^{\alpha}$ in all of the samples except $Mn_{4-x}Ni_xN$ (x = 0.2, 0.3) on MgO in which we couldn't get enough data

points. However, while the value of α is supposed to be in the range of $1.6 \sim 1.8$, we found α was approximately 1.3 for Mn_4N on STO. Although we have not revealed the reason for such a small value of α, it may derive from weak inelastic scatterings and relatively strong elastic scatterings. Further discussion will follow with Fig. 4.13 as well. Meanwhile, for other samples, α was in the range of $1.6 \sim 1.8$. As mentioned above, it's difficult to investigate the origin of AHE from the typical behavior in a bad metal-hopping regime. Still, we can guess that the effect of inelastic scattering is strong and estimate the extrinsic AHE induced by phonons may be the main mechanism of AHE in $Mn_{4-x}Ni_xN$ at high temperature (100 -300 K).

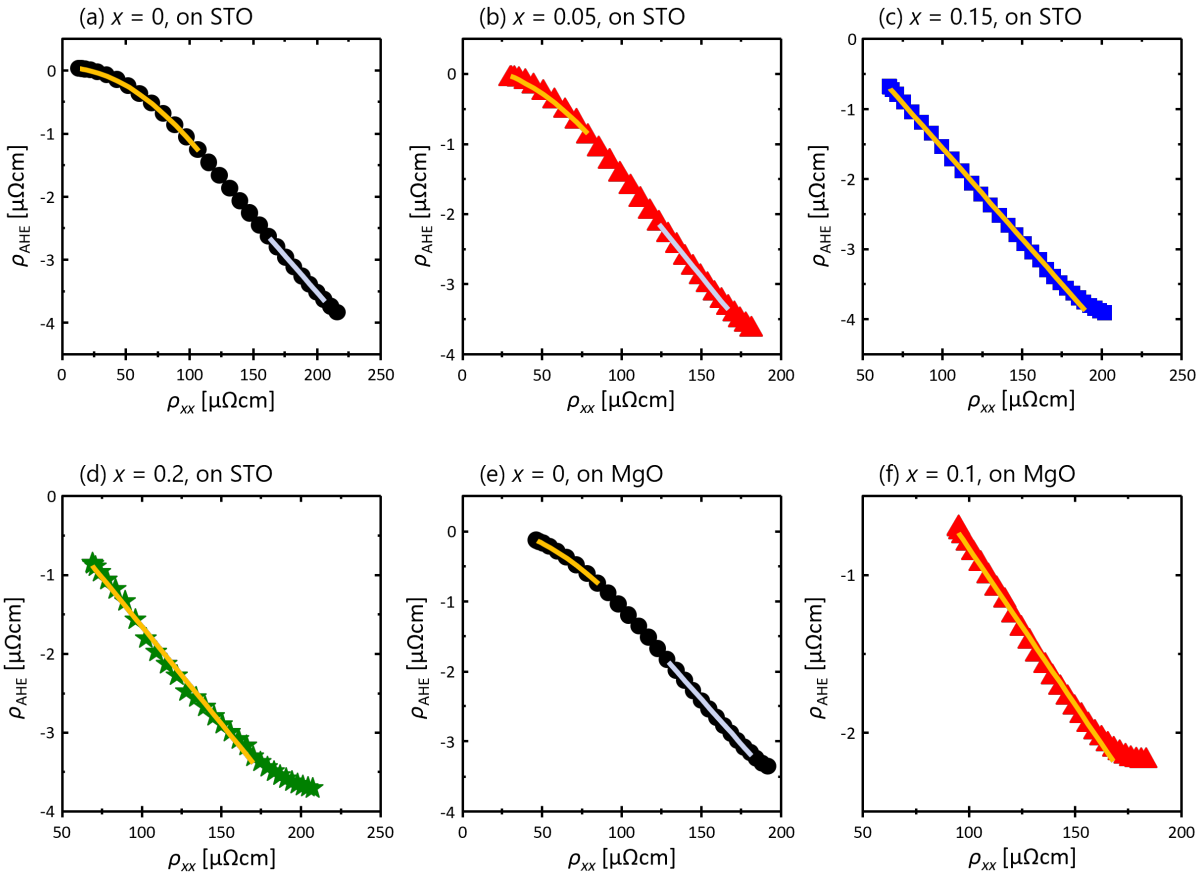

Figure 4.13: *The correlation of ρ_{AHE} and ρ_{xx} in $Mn_{4-x}Ni_xN$. The temperature was modulated between 5-300K during the measurement. The fittings were performed with $\rho_{AH} = \alpha\rho^2 + \beta\rho + C$.*

Figure 4.13 shows the scaling of the ρ_{AHE} and ρ_{xx} and its fitting with $\rho_{AH} = \alpha\rho^2 + \beta\rho + C$ based on Eq. 4.7 where C is a constant and the first and the second term represent the effect of either intrinsic AHE or extrinsic side jump, and extrinsic skew scattering, respectively. Considering that the data points of some samples lay in both good metal regime and bad metal-hopping regime, we performed the fitting separately for lower and higher resistivity sides (in $x = 0$ and 0.1 for $Mn_{4-x}Ni_xN$ on STO, and $x = 0$ for Mn_4N on MgO). Note that we couldn't perform fitting for samples of $Mn_{4-x}Ni_xN$ on MgO with $x = 0.2$ and 0.3 due to the insufficient number of data points. For samples in which we observed the decrease in $|\sigma_{AHE}|$ under low temperature, $Mn_{4-x}Ni_xN$ ($x = 0$, 0.05) on STO and Mn_4N on MgO, we succeeded in the better fitting with ρ^2 component and negligibly small ρ component. This result supported the dominant intrinsic AHE in $Mn_{4-x}Ni_xN$ with a small Ni composition ratio below 100 K, suggested by AMR and the investigation in σ_{AHE}. At high temperatures, however, the ρ component became dominant and the ρ^2 component was scarcely recognized. From this result, we anticipate that skew scattering especially induced by phonons is the main mechanism of AHE in $Mn_{4-x}Ni_xN$ with a small Ni

composition ratio at high temperatures. Even in Mn_4N/STO, skew scattering seems to be the main mechanism of AHE at high temperatures although there was a deviation in the value of the exponent in the scaling, α. Focusing on $Mn_{4-x}Ni_xN$ with a relatively high Ni composition ratio ($x > 0.1$), we could only confirm the region where ρ component is dominant, therefore, skew scattering is the main mechanism of AHE in these samples regardless of the temperature. This skew scattering might be caused by phonons or impurities and deficiencies due to the high Ni composition ratio.

Table 4.2 lists the result of the fitting done in Fig. 4.13. To summarize the results of AHE measurement, When Ni composition of $Mn_{4-x}Ni_xN$ was less than 0.05, the main mechanism of AHE was intrinsic deflection below 100 K and skew scattering which would be caused by phonons at high temperature. Meanwhile, when the Ni composition of $Mn_{4-x}Ni_xN$ was more than 0.1, skew scattering was dominant regardless of the temperature. This change would be attributable to the increase in the number of impurities and deficiencies to induce extrinsic AHE by Ni composition ratio. In addition, considering the smaller RRR values of $Mn_{4-x}Ni_xN$ grown on STO than those grown on MgO in Fig. 4.9, the deficiencies caused by worse crystalline qualities and orientations of samples grown on MgO would show larger extrinsic AHE.

Table 4.2: *The result of fitting of ρ_{AHE} and ρ_{xx} with $\rho_{AH} = \alpha\rho^2 + \beta\rho + C$. Here the value of α and β are listed. "-" is the symbol to denote that the value of the fitted parameter was negligibly small.*

Sample	Substrate	x	Range [K]	α	β
Sample 1	STO	0	5-130	-0.00012	-
Sample 1	STO	0	200-300	-	-0.02312
Sample 2	STO	0.05	5-130	-0.00016	-
Sample 2	STO	0.05	200-300	-	-0.02794
Sample 3	STO	0.15	5-300	-	-0.0259
Sample 4	STO	0.2	5-300	-	-0.02474
Sample 5	MgO	0	5-140	-0.00012	-
Sample 5	MgO	0	180-300	-	-0.02569
Sample 6	MgO	0.1	5-300	-	-0.0198

4.7 Summary of this chapter

- We measured the AMR of $Mn_{4-x}Ni_xN$ films grwon on STO and MgO(001) with the electric current set along $Mn_{4-x}Ni_xN$ [100] azimuth. The AMR ratio drastically decreased even with a very small Ni composition ratio. This is attributable to the emergence of $\cos 4\theta$ (C_4) component in AMR curves under low temperature, the magnitude of which is significantly affected by the Ni composition ratio.

- While $\cos 2\theta$ (C_2) component derives from the d orbital states under the cubic crystal field, $\cos 4\theta$ (C_4) component comes from the tetragonal crystal field. Through the first principle calculation of PDOS of d orbitals, we found the strengh of this tetragonal field effect was modulated by the change in PDOS induced by Ni atoms. We'd like to emphasize that the change in the crystal field effect was caused by the intrinsic factor, not by the extrinsic factor such as the tensile induced by the difference in lattice expansion.

- The temperature dependence of ρ_{xx} in $Mn_{4-x}Ni_xN$ showed a significant decrease in the value of residual resistivity ratio between $\rho_{xx}(300K)$ and $\rho_{xx}(2K)$ by Ni composition ratio. We expected that this comes from the increase in the number of impurities and deficiencies by Ni atoms. Additionally, we found the evidence for the Kondo effect in samples with a high Ni composition ratio, in which we expect Ni atoms to act as magnetic impurities.

- From the first principle calculation with VASP, we confirmed PDOS of d orbitals were much higher at face-centered sites (II sites) than at corner sites (I sites). Although Ni atoms preferentially occupy I sites, the PDOSs of Mn(II) atoms are greatly affected by Ni(I) atoms. Such a change led to the modulation of AMR and the effective crystal field in $Mn_{4-x}Ni_xN$. Notably, E_F of these d orbitals shifted for 0.5 eV even with the Ni composition ratio of $x = 0.5$. Such modulation in d orbitals by composition ratio can lead to further application of Mn_4N based nitrides.

- Through the analysis in AMR curves, the temperature dependence of σ_{AHE}, and the scaling of ρ_{AHE} and ρ_{xx}, we estimate that intrinsic deflection is the main mechanism of AHE under low temperature in $Mn_{4-x}Ni_xN$ ($x < 0.1$) and extrinsic skew scattering have a stronger effect at higher temperatures. In $Mn_{4-x}Ni_xN$ ($x > 0.15$), however, skew scattering seems to be dominant regardless of the temperature. The measurement with angle-resolved photoemission spectroscopy (ARPES) to investigate the band structure of $Mn_{4-x}Ni_xN$ can reveal the strength of intrinsic deflection more clearly.

Chapter

Attempt for SOTs-driven CIDWM in Mn_4N 5

In this chapter, we aim at SOTs-driven CIDWM in the multiwires made from the heterostructure of heavy metal/Mn_4N. In our previous work on STTs-driven CIDWM in Mn_4N multiwires, we achieved DW velocity of 900 m/s, while in $Mn_{4-x}Ni_xN$ multiwires improved it to 3,000 m/s thanks to the angular compensation[67, 71]. Although the latter is by far the fastest purely STTs-driven CIDWM, faster and more efficient CIDWM performances were reported using SOTs, taking advantage of the spin Hall effect (SHE) from a nearby heavy metal layer[57, 61]. While the exchange of the angular momentum takes place between one conduction electron and one localized electron in STTs-driven CIDWM, it takes place between more than one electron due to SHE and one localized electron in SOTs-driven CIDWM. From this point of view, the SOTs are thought to be more suitable for effective CIDWM. In order to apply the SOTs, the formation of chiral Néel DWs supported by Dzyaloshinski-Moriya interaction (DMI) in the heterostructure with the broken inversion symmetry is essential. The effective spin current injection from the heavy metal to the magnetic layer is also an important factor.

Section 5.1 shows the sample fabrication and their crystalline quality. Section 5.2 shows the magnetic and magneto-transport properties of Pt/Mn_4N and W/Mn_4N, and we will compare these results with those of SiO_2 capped Mn_4N. Section 5.3 presents the observation of the magnetic domains in the samples. Section 5.4 shows the result of CIDWM in Pt/Mn_4N multiwires, and we discuss the effect of SOTs by comparing the results in SiO_2/Mn_4N, in which we already confirmed that only STTs is involved in the CIDWM. We end this chapter with the summary in Section 5.5. T. Komori contributed to the growth of the samples and all of the experimental measurements. The fabrication of multiwire devices was completed with the help of Dr. Laurent Vila of SPINTEC. Observation of magnetic domains and CIDWM measurements were performed with the help of Dr. Stefania Pizzini and Dr. Jan Vogel of Institut Néel.

5.1 Sample growth and the crystalline quality

The heterostructures of heavy metal (HM)/magnetic layer (ML)/oxide were fabricated by MBE and sputtering methods (*cf.* Fig. 3.1). STO(001) substrates were used as oxide layers, and 7 or 10 nm-thick Mn_4N films were grown on STO substrates as MLs. The growth condition of MBE is identical to the one mentioned in chapters 3 and 4. After the growth of Mn_4N, the samples were naturally cooled to at highest 100 $^\circ C$, and Pt or W was sputtered onto Mn_4N as the HM. Ar gas was supplied to the growth chamber so that the pressure during the sputtering was set to be around 1.0×10^{-1} Pa, and an electric power of 50 W was applied to the target

source. Table 5.1 shows the list of samples used in this chapter. The thickness of the layer was measured by X-ray reflectivity (XRR), and the longitudinal resistivity (ρ_{xx}) of the samples was measured by the Van der Pauw (VDP) method. The Rietveld refinement was used for the evaluation of the thickness from XRR, in which the error of the density was set to be within $\pm 10\%$ from the value in the database of the Crystallographic Society of Japan.

Table 5.1: *List of samples used in this chapter. The thickness (t) of the layer was analyzed with XRR and its Rietveld refinement, and the longitudinal resistivity (ρ_{xx}) was measured with the Van der Pauw (VDP) method.*

Sample	Heavy metal (HM)	t_{HM} [nm]	t_{Mn4N} [nm]	ρ_{xx} [μΩcm]
Sample A	Pt	3.27	10.42	112.60
Sample B	W	2.98	10.42	186.54
Sample C	Pt	3.30	7.11	465.09
Sample D	W	3.34	7.04	212.36

Figure 5.1 shows the out-of-plane and in-plane XRD profiles, and RHEED images taken along the Mn_4N[100] azimuth before sputtering the heavy metal layer. In the out-of-plane XRD profiles, the diffraction peaks from Mn_4N 002 and 004 were observed, which proves the c-axis oriented epitaxial growth of Mn_4N. However, 004 diffraction peaks in Sample C and D are relatively small and are hardly observed especially in Sample C. This is attributed to the small intensity of the structural factor of 004 diffraction in the anti-perovskite structure. In addition, the crystalline quality of Mn_4N in Sample C is considered to be not as good as that of the other samples, judging from the weak superlattice diffraction in the RHEED image and the abnormally large ρ_{xx}. ρ_{xx} of our typical Mn_4N film is around 200 μΩcm, and that of 3 $\sim$ 4 nm thick Pt sputtered on the magnetic film is around 50 μΩcm[197]. From these results, the poor or excessive nitrogens in the crystals would lead to the worst crystalline quality and act as scattering centers for conduction electrons. We expect that such poor crystallinity in 7 nm-thick Mn_4N is derived from the mechanism of the initial stage of the epitaxial growth of Mn_4N on STO(001) substrates. Figure 5.2 (a) shows the RHEED image of 5 nm-thick Mn_4N taken along Mn_4N [100] azimuth. The red line shows the satellite streaks, which suggests the periodic roughness of the layer[198]. Fig. 5.2 (b) shows the image of the surface of Ti-terminated STO substrate taken by an atomic force microscope (AFM)[199]. The surface forms steps with the length of 200 $\sim$ 500 nm, and each step is delimited by the kink. When we perform the epitaxial growth on such STO substrates, the nucleation of the crystals is initially enhanced along the kinks, and then they tend to grow along them. Therefore, we can state that the crystals favor the uniaxial growth at the initial stage of MBE. They eventually start the isotropic growth, however, the surface of the crystalline film is supposed to form steps and kinks when the film is not sufficiently thick. Such steps and kinks would be reflected by satellite streaks in Fig. 5.2 (a). Figure 5.2 (c) shows the schematic image of the initiation of the MBE growth on the STO(001) substrate which was explained above.

Now, we focus on the in-plane XRD profiles of Fig. 5.1. The asterisks indicate the diffraction from STO, and the black triangle indicates the reflection from the stage to hold the sample. In these profiles, the diffraction peaks were completely overlapped with those from STO because of the small thickness of Mn_4N and the small intensity of the diffraction. In all the samples, we observed the diffraction from either Pt or W, suggesting its crystallization. However, the spin Hall angle (θ_{SHE}) of the crystallized W depends on its phase. In short, α-W (bcc) have small θ_{SHE} while β-W (A15) have large θ_{SHE}[200]. Although it's difficult to distinguish α and β-W from the diffraction peaks in the in-plane XRD profiles, we consider the W layers in our

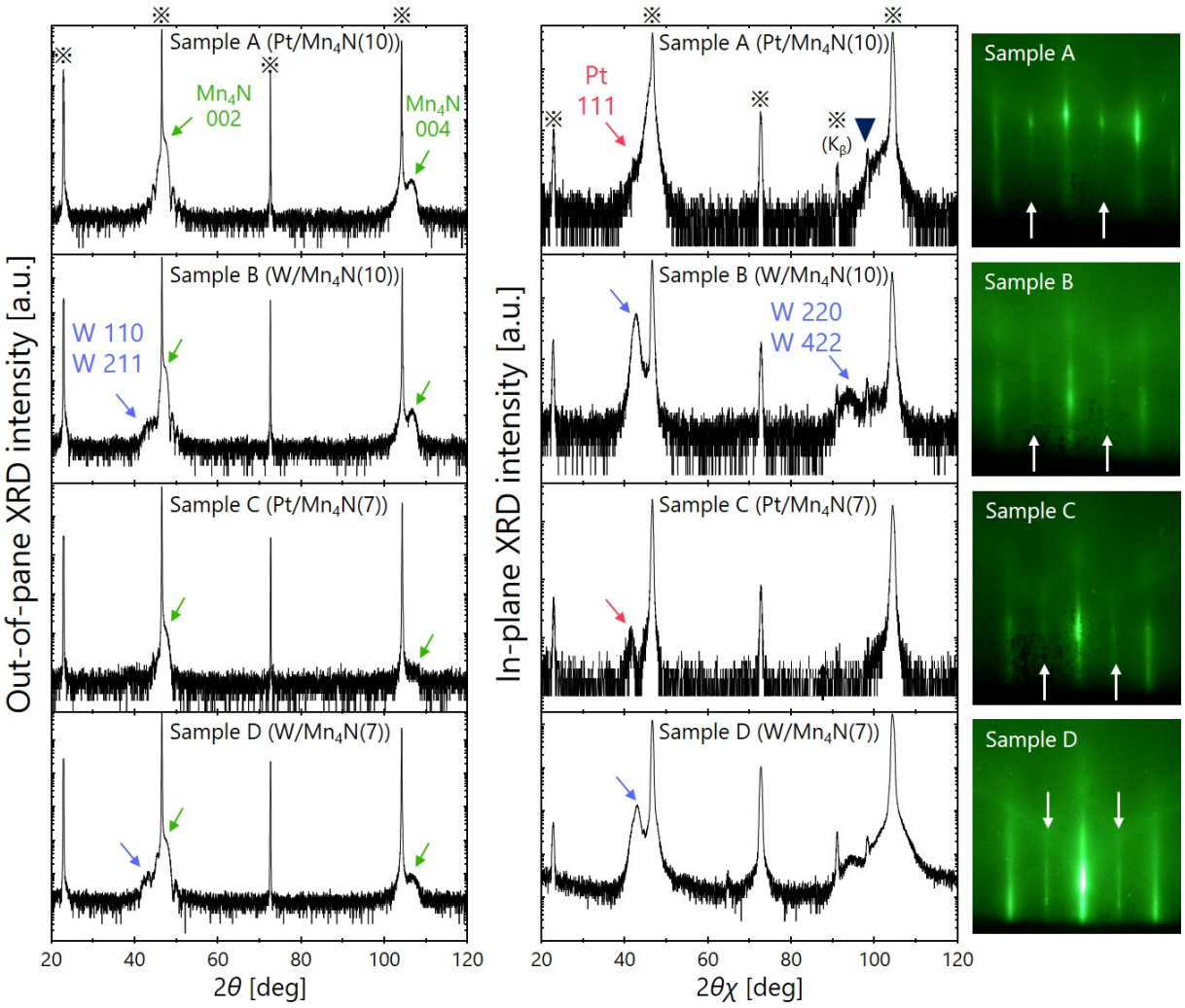

Figure 5.1: *Out-of-plane XRD profiles (left) and in-plane XRD profiles (right) of the Sample A, B, C and D, and RHEED images taken along Mn_4N[100] azimuth right after the growth of Mn_4N films (images on the right side). Asterisks indicate in the XRD profiles indicate the diffraction from STO substrates, and the white arrows in the RHEED images indicate the superlattice diffraction.*

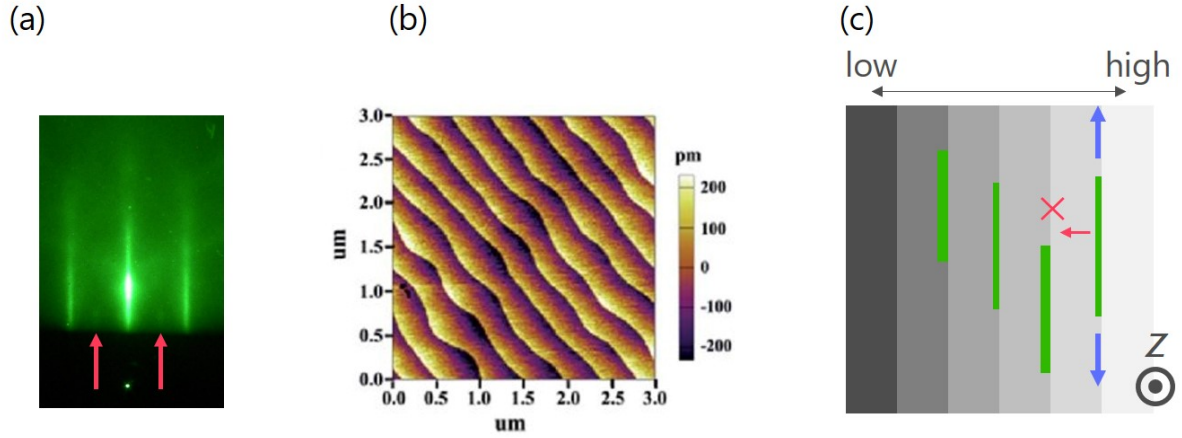

Figure 5.2: *(a) RHEED image taken along Mn_4N[100] azimuth for 5nm-thick Mn_4N/STO. (b) AFM image of the STO(001) substrate treated with buffered-HF. (c) The schematic image of the initial stage of MBE growth on STO(001) substrate.*

samples contain β-W, which greatly support the spin current injection to Mn_4N. This is because the sputtered W films consist of the mixture of α and β-W when the thickness is smaller than about 8 nm, and its resistivity is approximately anti-proportional to the thickness, 200 $\sim$ 300 μΩcm for 3 $\sim$ 4 nm thick W[201, 202]. This value of ρ_{xx} is reasonable with the ρ_{xx} of our samples when we consider ρ_{xx} of Mn_4N to be approximately 200 μΩcm. We note that single β-W film can be acquired only when the films are grown with the supply of oxygen gas.

5.2 Magnetic and magneto-transport properties

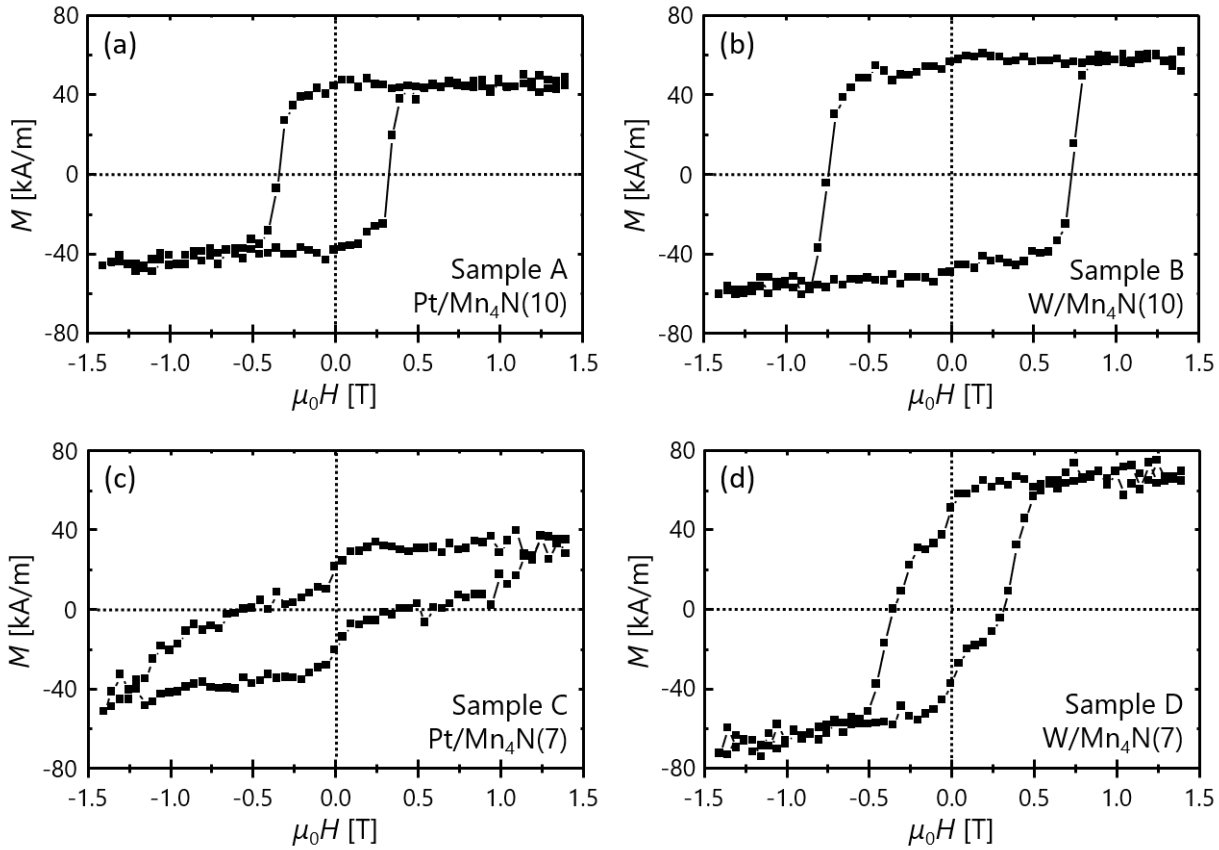

Figure 5.3: *Magnetic loops of Samples A, B, C and D taken at RT by VSM.*

Figure 5.3 shows the magnetic hysteresis loops of the samples measured by VSM at RT. We observed a clear hysteresis loop with smooth magnetization reversals in 10 nm thick Mn_4N samples (Sample A and B). However, their saturation magnetizations (M_S) were about 50 $\sim$ 60 kA/m, which are relatively smaller than 30 nm thick Mn_4N films on STO capped with SiO_2 (M_S $\sim$ 80 kA/m). Although M_S of magnetic nitrides is strongly influenced by the growth condition and the order of body-centered nitrogens, we attributed these smaller M_S to the magnetic dead layer at the interface between HM and Mn_4N and/or between Mn_4N and STO. Especially, the magnetic property of Mn_4N would differ from that of the interfacial layers between HM and Mn_4N due to the damage of Mn_4N during sputtering, to the interfacial diffusion, and so on. These effects on the magnetic properties from the interfacial layer are also suggested by the strong evidence of pinning sites in the magnetization reversals of Sample A, and from the large coercivity approaching 1 T in Sample B, which is generally about 0.3 $\sim$ 0.5 T in Mn_4N on STO. Meanwhile, 7 nm-thick Mn_4N samples (Sample C and D) showed abnormal magnetic properties for Mn_4N on STO. For Sample C, the hysteresis loop was not perfectly closed due to

the strong DW pinnings which hamper the magnetization reversals. Although Sample D shows more smooth magnetization reversals, the reversals in Sample C and D have two steps, unlike Sample A and B. In the first step, the magnetization started to reverse around 0 T, but only resulted in partial reversals. Then, in the next step, the magnetization restarted to reverse and led to 100 % reversal. This magnetization reversal in two steps suggests that the Mn_4N layer consists of the soft and hard magnetic phases. The soft magnetic phase may derive from the interfacial layer between HM and Mn_4N, and the hard magnetic phase is the Mn_4N film which is not influenced by HM or STO. It's reasonable that it derives from the interfacial layers because this magnetization reversal in two steps is obvious in thinner Mn_4N and relatively absent in thicker Mn_4N.

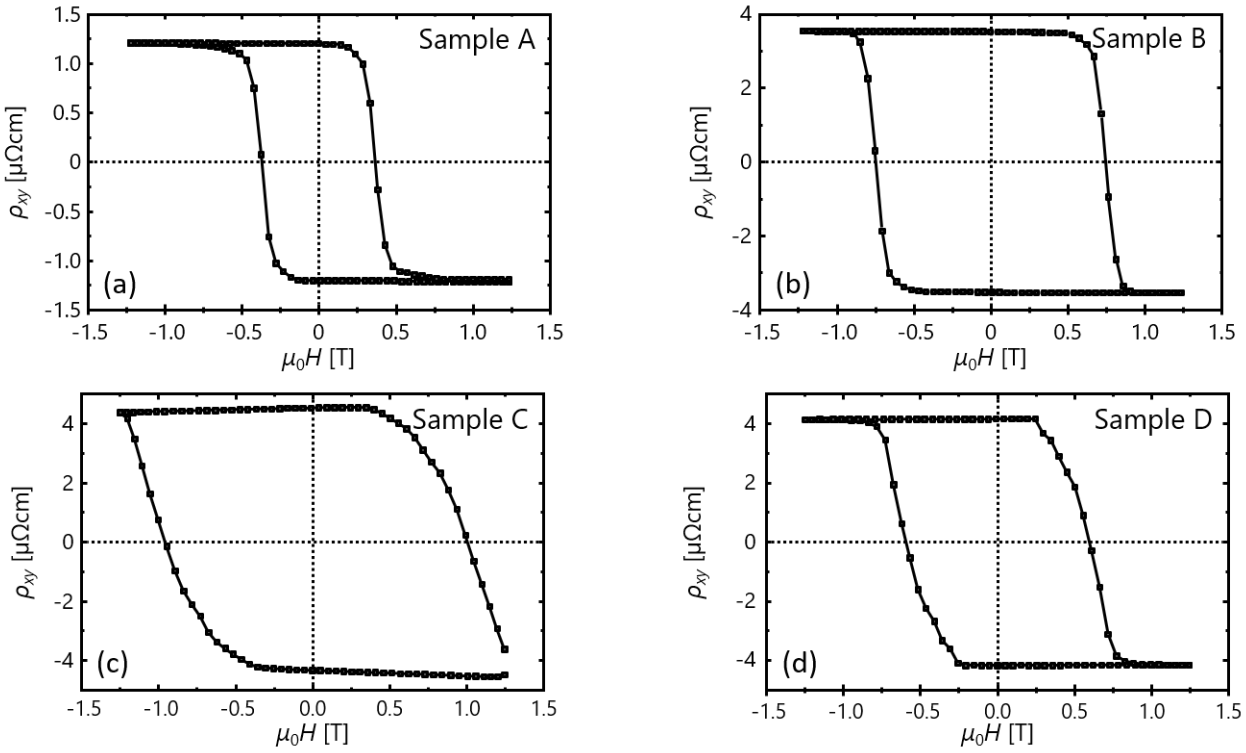

Figure 5.4: *AHE loops of Samples A, B, C, and D taken at RT by PPMS.*

Figure 5.4 shows the AHE loops of the samples measured by PPMS at RT. We observed the clear loops in Sample A and B like in Fig. 5.3. However, compared with SiO_2 capped Mn_4N, we confirmed the effect from DW pinnings around ±0.5 T, at which the magnetization is about to completely reverse. In practical applications, it may decrease not only v_{DW} but also the reliability of the operation. Meanwhile, Sample C showed the AHE loop which is not completely closed due to the large magnetic field required to completely reverse the magnetization. Sample D showed the magnetization reversals with DW pinnings, with a smooth and gradual reversal. We confirmed the magnetization reversal in two steps in the magnetic hysteresis loops in Fig. 5.3 (c) and (d), while it was not observed in the AHE loops in Fig. 5.4(a) and (b). This result may coincide with our consideration that the samples contain both soft and hard magnetic phases if the soft one has high ρ_{xx}. In this case, the electric current wouldn't flow much into the layer of this phase.

Paying attention to the magnitude of ρ_{xy}, W capped samples (Sample B and D) have a value of about 4 μΩcm, which is identical to the one of SiO_2 capped Mn_4N. Since ρ_{xx} of $3 \sim 4$ nm thick W is expected to be approximately $200 \sim 250$ μΩcm or even larger, ρ_{xx} of W and that of Mn_4N in our samples are expected to be very similar, or that the former is larger than the

latter[202]. Thus, the electric current in the samples is expected to have flown homogeneously in the film, or mainly into Mn_4N layer. In this way, we obtained a similar value of ρ_{xy} in W capped Mn_4N and SiO_2 capped Mn_4N. On the contrary, in Pt capped samples (Sample A and C), ρ_{xy} is only about 1.2 μΩcm in Sample A. This change becomes reasonable if we consider that ρ_{xx} of 3 ∼ 4 nm thick Pt is generally about 50 μΩcm, which is the case of Pt for SOTs-driven magnetization reversals in Pt/CoFeB[197]. At least, it is obvious that ρ_{xx} of Pt is much smaller than that of Mn_4N, thus, the electric current is expected to flow mainly in the Pt layer, resulting in an apparent small AHE resistivity of Mn_4N. However, Sample C showed ρ_{xy} as large as that of SiO_2 or W capped Mn_4N. This difference in ρ_{xy} of Mn_4N between Sample A and C is expected to derive from the quality of the crystals and the heterostructure in Samples C, such as abnormally high ρ_{xx}. Considering the relatively weak diffraction peaks from Mn_4N 002 and 004 reflection planes, we expect that the Mn_4N layer has a stronger influence on total ρ_{xx} rather than the Pt layer.

5.3 Magnetic domain observation

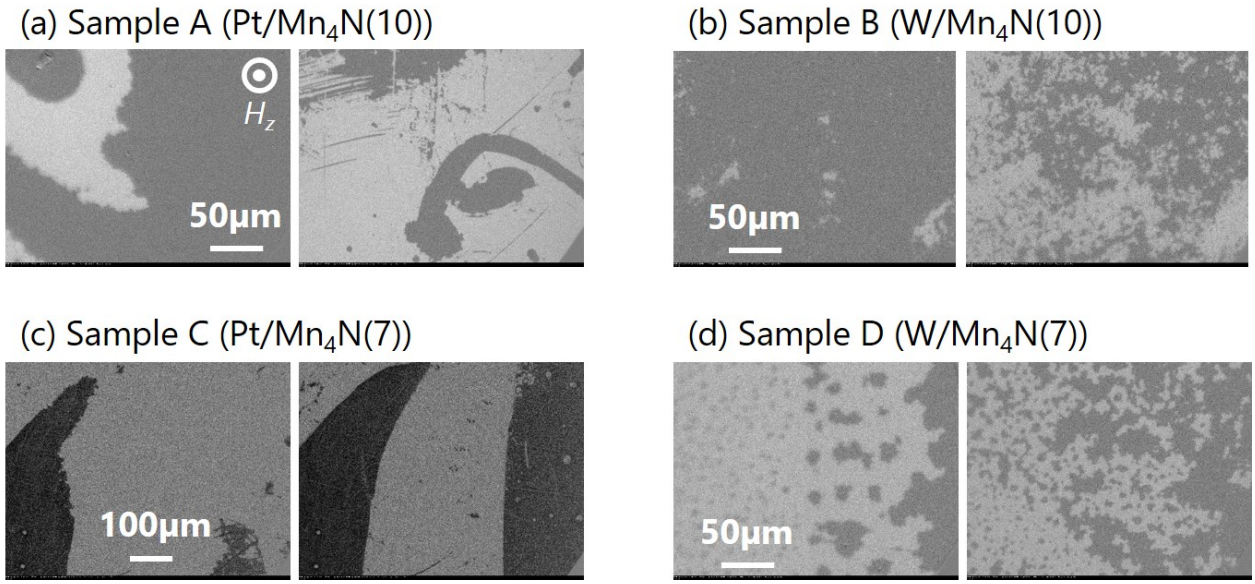

Figure 5.5: *Images of magnetic domains taken by a MOKE microscope. Domains were nucleated by an out-of-plane magnetic field pulse.*

Figure 5.5 shows images of magnetic domains of the samples taken by a magneto-optical Kerr effect (MOKE) microscope. Here, the observation was performed after the magnetization was partially reversed by an out-of-plane pulse field of 200 μs duration. In the samples capped with Pt (Sample A and C), large magnetic domains with a size of approximately 100 μs are observed. These domains are relatively smaller than those in SiO_2 capped Mn_4N on STO but still large compared with typical magnetic materials of similar thicknesses. However, the magnetic domains in Pt capped samples, especially Sample C, are affected by so large pinnings that they were not completely reversed even by a magnetic field approaching 2 T. Although the origin of pinnings havs not been clearly discovered, we expect that they emerged due to the inhomogeneity of the Mn_4N film due to the sputtering of Pt on Mn_4N rather than due to the external scratches on the surfaces. One of the possible causes for the inhomogeneity of the samples is the alloying of Mn and Pt at the interface. According to the phase diagram of Mn

and Pt, they can be alloyed and transformed into paramagnetic metal even though the diagram for lower temperatures (below 100 $°C$) has not been reported[203].

On the other hand, in the samples capped with W (Sample B and D), relatively small and bubble-like domains of the size of approximately 10 µm are observed. Similar to Pt capped samples, W capped samples also show large inhomogeneity, reflected by the difference in the size of domains dependent on the location. Such bubble-like domains are often considered as evidence of the emergence of magnetic skyrmions. Skyrmions in the magnetic film are evidence of the non-zero DMI, a necessary ingredient for the successful SOTs-driven CIDWM thanks to the formation of chiral Néel DWs. In order to investigate these bubble-like domains, we first observed the nucleation and propagation of these domains. Figure 5.6 shows the images of the propagation of domains by an out-of-plane magnetic pulse. From these images, bubble-like domains are found to be pinnings, not nucleation centers in presence of strong pinning. As the magnitude of the magnetic field increases, these domains gradually shrunk but not completely vanished, no 100 % magnetization reversal in other words. It seems that these pinnings strongly disturb the propagation of domains but not as strongly as in the case of W capped samples from the configuration of hysteresis loops and MOKE images of magnetic domains.

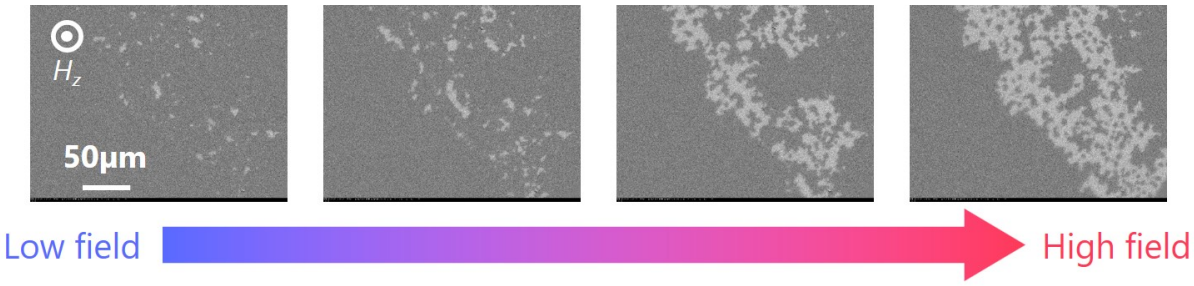

Figure 5.6: *Propagation of domains by an out-of-plane pulse magnetic field pulse in Sample D. Each image was taken after the application of the pulse field of increasing magnitudes.*

Then, we attempted the observation of the propagation of domains under in-plane field in order to judge the existence of the effective DMI field in our samples. When the system doesn't have DMI, a magnetic domain under a constant in-plane field moves by the out-of-plane pulse field along the direction of the in-plane field. During the same period, the DW velocity is proportional to the in-plane field regardless of the chirality of DWs, up/down or down/up, and the domain propagates isotropically. On the other hand, when the system has a certain magnitude of DMI in the xy-plane, the DW velocity is not symmetric against the in-plane field and depends on the chirality of DWs. At the same time, the domain propagates anisotropically. Figure 5.7 shows the propagation of the magnetic domains by an out-of-plane magnetic pulse field under an in-plane constant field ($H_x \sim 250$ mT) in Sample D. Fig. 5.7 (i) is the initial stage of the measurement, which is right after the nucleation of magnetic domains by the out-of-plane field pulse. Then, we applied H_x to the sample and exerted the out-of-plane magnetic pulse field. Fig. 5.7 (ii) is the image taken after the application of the out-of-plane field. Although we applied the largest in-plane magnetic field and the out-of-plane field (> 2 T) to the sample in our system, we couldn't induce DW motion in Sample D. Instead. we observed the displacement of the sample after the out-of-plane pulse injection. This displacement is expected to be caused by the magnetic force between the magnetic field and the iron core of the coil to generate the out-of-plane magnetic field. We note that we succeeded in preventing the sample from displacement by using a smaller magnetic field but we still could not move or propagate the magnetic domains. Also, DW propagation was not observed in Sample B as well, due to the strong pinnings. From these results, we couldn't confirm the presence of DMI in this measurement, at least it's very small. However, if there's non-zero DMI in this system,

we may enhance DMI by fabricating, heterostructures with thinner Mn_4N because the strength of DMI is anti-proportional to the thickness.

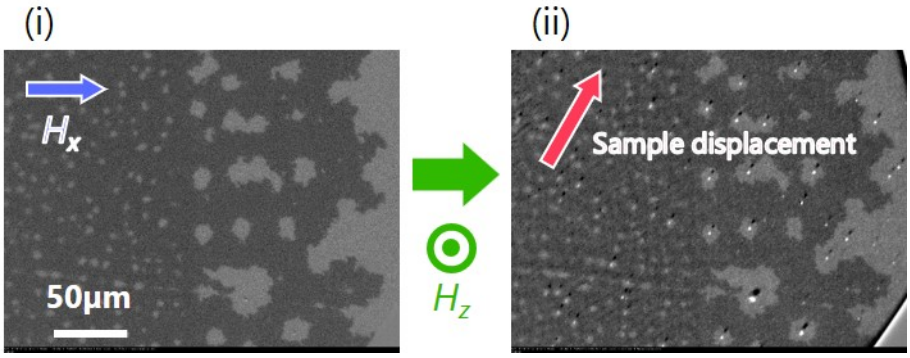

Figure 5.7: *Propagation of domains by out-of-plane magnetic field pulse in Sample D. Each image was taken after the application of the field pulse with the different magnitudes.*

5.4 CIDWM in Pt/Mn_4N

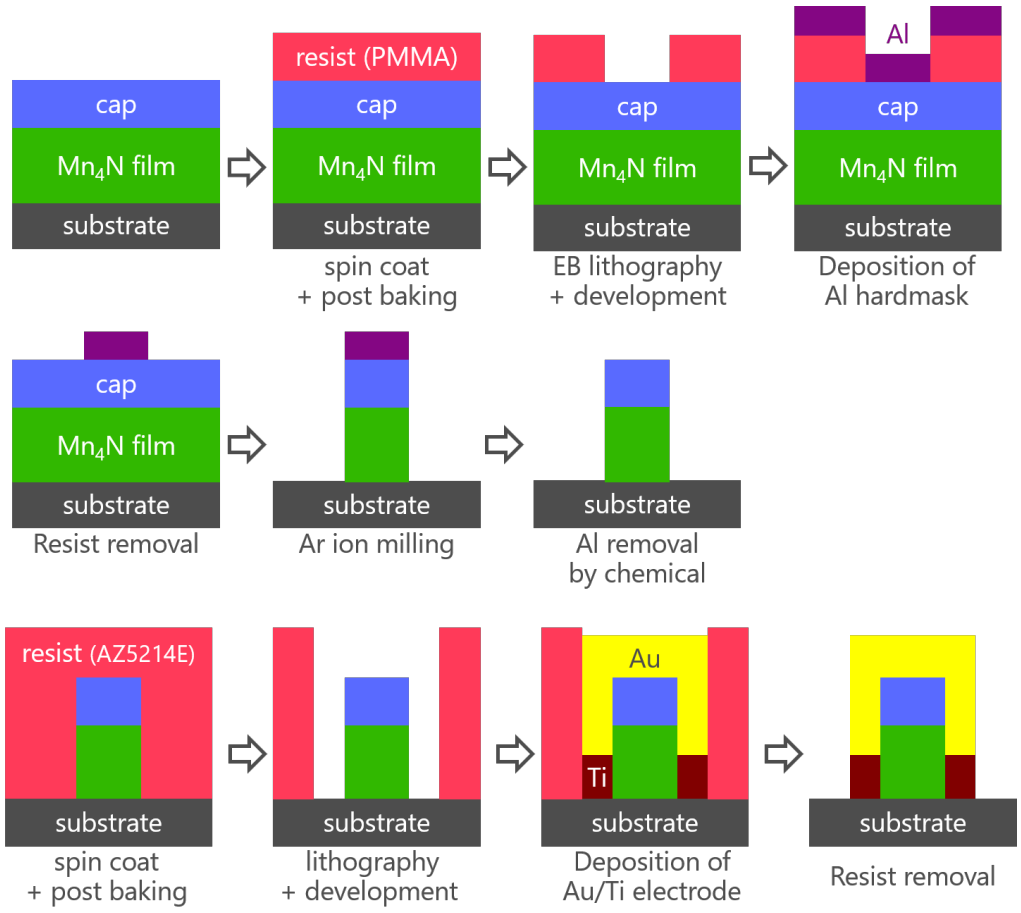

Figure 5.8: *Procedure to pattern our films into devices (the multiwires). The upper and middle rows are about the fabrication of multiwires, and the bottom row is about the fabrication of Au/Ti electrodes on the nucleation pads.*

In order to perform the CIDWM measurement, we processed the films into multiwire devices of 1 µm. They were patterned with an electronic beam lithography system (JEOL6300FS). PMMA (polymethyl methacrylate) was used as a positive resist, and it was spin-coated on the sample surface so that it becomes as thick as 2 μm. After the lithography and resist development by diluted MIBK, a 30 nm-thick Al layer was deposited by the vapor deposition method. Then the sample was dipped in acetone in order to remove the resist and the unnecessary Al. Dry etching was done with Ar ion milling until the substrate surface, avoiding overetching the generation of conductive 2D electron gases at the free surface of STO. In the end, Al was removed with TMAH, and the process for the multiwires was completed. In order to inject the magnetic domains into the multiwires, we attached nucleation pads on both sides of the wires. Also, we put Au/Ti electrodes to bond Al wires to inject the current pulse. AZ5214 resist was coated on the processed device, and the shape of electrodes were patterned with a photomask and MJB4 mask aligner. After the development with NMD-3, 10 nm of Ti and 80 nm of Au were deposited by the vapor deposition method. We completed all the processes after the removal of the resist. Figure 5.8 shows the schematic images of the procedure of the device fabrication. Here, each device has 20 multiwires in parallel, and each multiwire is 1 µm wide and attached to the nucleation pads.

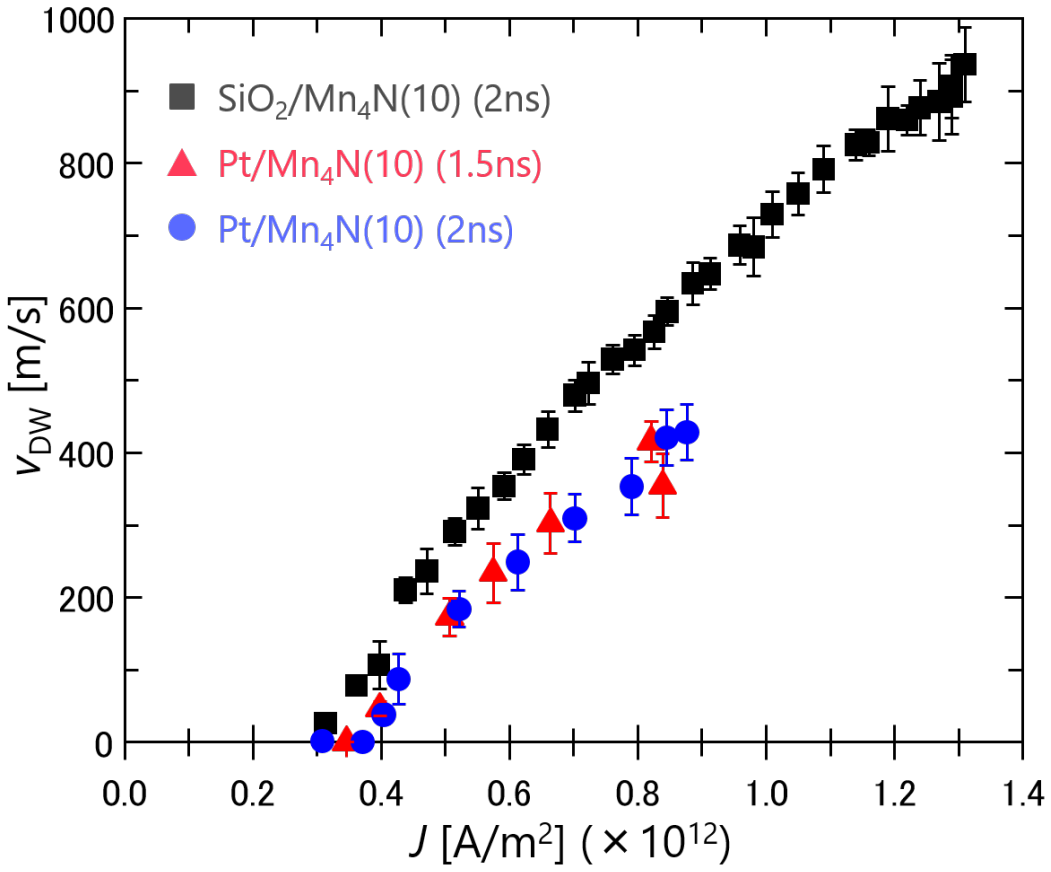

Figure 5.9: *v_{DW} vs J in Pt/Mn_4N and SiO_2/Mn_4N multiwires of 1 µm. The data points for SiO_2/Mn_4N are referred from our previous report, in which we confirmed CIDWM was achieved purely by STTs[67]. The value of J is the estimated current density in the Mn_4N layer.*

Figure 5.9 shows the v_{DW} vs J curves of Mn_4N multiwires recorded at RT in Sample 1. In the CIDWM measurements, the duration of the current pulses was either 1.5 or 2 ns. The value of J in Fig. 5.9 is the current density in the Mn_4N layer calculated from the ratio of ρ_{xx}

of the HM and Mn_4N layer. The data points of SiO_2/Mn_4N refer from our previous report of CIDWM in Mn_4N by pure STTs for comparison[67]. The errors of the data points were derived from the dispersion of induced DW displacement in multiwires. The sign of v_{DW} was defined with respect to the direction of the conduction electrons. For the results of both 1.5 ns and 2 ns, v_{DW} vs J curves are almost identical. However, nucleation of domains took place during the CIDWM with 2 ns duration pulses at the highest current density in Pt/Mn_4N. Figures 5.10 (a) and (b) show the nucleation of domains by the out-of-plane pulse field and the displacement of domains by the current ($J = 8.8 \times 10^{10}$ A/m^2 with the duration of 1.5 ns) for Sample A (Pt/Mn_4N) multiwires, respectively. Here, it is easy to confirm that there is one domain in one wire from the nucleation pad, and there is no nucleation in multiwires. On the other hand, fig. 5.10 (c) shows the image of the multiwires taken with a MOKE microscope after the injection of 8.8×10^{10} A/m^2 with the duration of 2 ns in Pt/Mn_4N. We observed an increase in the number of magnetic domains after pulse injection. On the other hand, this nucleation by the pulse current was not observed with the duration of 1.5 ns, and the measurement in SiO_2/Mn_4N at such current densities. From this result, we attributed this to the thermal effects due to Joule heating from the Pt layer. In SiO_2/Mn_4N, the nucleation by the thermal fluctuation didn't take place even at such high current density pulse, and our group proved that it with a simple analytical expression of Joule heating[204, 205]. In Pt/Mn_4N, on the other hand, approximately 65 % of the electric current flow into the Pt layer. Thus, Joule heating is expected to have been mainly generated in the Pt layer and to have functioned as the heat source.

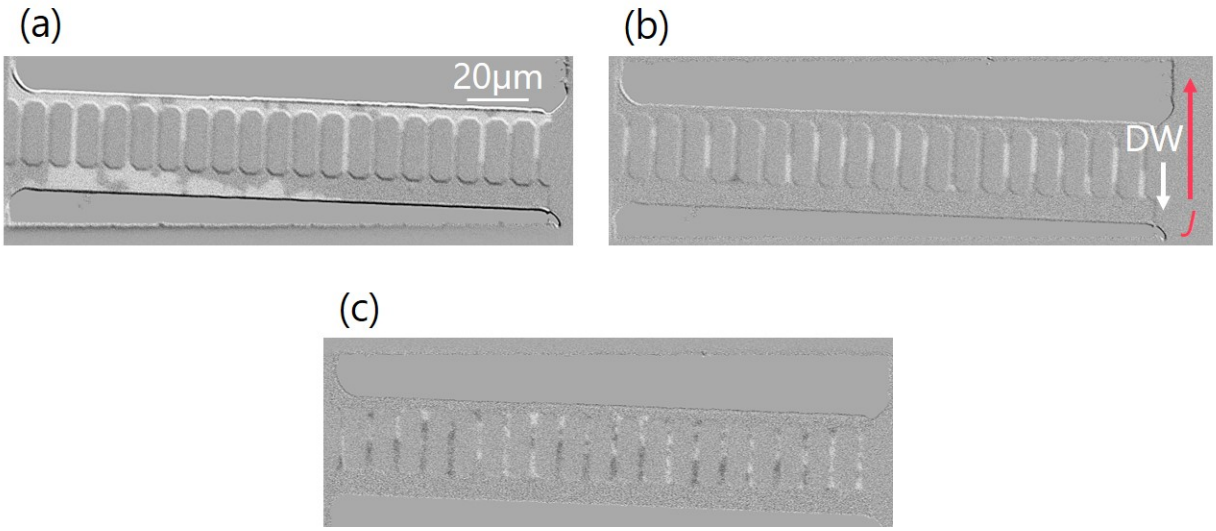

Figure 5.10: *(a) The MOKE image taken after the nucleation of the domains by the out-of-plane magnetic field pulse. Here, white contrast suggests the reversed domain by the field pulse, nucleated from the pads. (b) The MOKE image taken after the DWs displacement by the current pulse of 1.5 ms. The current flew from the bottom to the top, and DWs moved from the top to the bottom, which is shown by white contrasts in multiwires. (c) The MOKE image taken after the injection of the current density of 9.0 × 1011 A/m^2 of 2 ns. More than one domain was observed in the image, suggesting the nucleation of DWs by Joule heatings.*

Discussing v_{DW} of Mn_4N, we found little difference in the magnitude of v_{DW} and in the threshold current density (J_{th}) in SiO_2/Mn_4N and Pt/Mn_4N, and the direction of CIDWM also did not change. In addition, in Pt/Mn_4N, v_{DW} was not saturated with the current we could apply with our pulse generator, which means we could not correctly evaluate the maximum v_{DW} in this sample. This is also attributable to the fact that most of the current flew into the Pt layer. In this work, $v_{DW} \sim 420$ m/s (at $J = 8.8 \times 10^{11}$ A/m^2) was the fastest DW motion

in Pt/Mn_4N, and we expect we could observe faster CIDWM if we could apply higher current density.

After all, we did not clearly confirm the effect of SOTs from this experiment. However, it seems that the effect of SOTs is zero or very small in this sample because there was little change in the trend of v_{DW} vs J curves and in the sign and the magnitude of v_{DW}. The main reason for no or little effect of SOTs is the poor spin injection efficiency from the Pt layer to the Mn_4N layer and/or the failure in the formation of chiral Néel DWs. The former derives from the crystalline quality of the Pt layer on Mn_4N and/or the interfacial condition, which may scatter the spins of the spin current generated by the spin Hall effect. The latter comes from the insufficient strength of DMI field to help Bloch DWs to transform into Néel DWs. We will mention how to investigate these factors and to overtake these obstacles, but in short, the structural optimization and the quantitative evaluation of the spin current in the Pt layer are required to solve the former problems, and the CIDWM measurement under a constant in-plane field and the evaluation of DMI should be performed to investigate the latter.

5.5 Summary of this chapter

- We attempted SOTs-driven CIDWM in Mn_4N by fabricating heterostructures of heavy metal (HM)/Mn_4N. Here, the HM layer is either Pt or W. We confirmed the epitaxial growth of Mn_4N and the crystallization of the sputtered HM layer on Mn_4N.

- From the magnetic and AHE hysteresis loops of the heterostructures, we found that the magnetization reversal occurs with DW pinnings and a relatively large coercivity compared to SiO_2 capped Mn_4N. These DW pinnings are expected to derive from the interfacial layer between HM and Mn_4N, for example, alloying of the HM and Mn_4N, damage on the top layer of Mn_4N by sputtering, and both.

- We observed the effect of the DW propagation with DW pinnings under applications of an out-of-plane magnetic field. Especially, in W/Mn_4N, we observed bubble-like domains, which were found to be due to pinning and numerous nucleation centers. We also performed DW propagation measurements under a constant in-plane field to evaluate the presence of DMI, however, we couldn't confirm it due to the absence of the propagation of the domains.

- We processed Pt/Mn_4N film into multiwire devices to perform the CIDWM measurements. We achieved DW velocity of 420 m/s at the current density of 8.8×10^11 A/m^2. However, we couldn't saturate v_{DW} within the limit of our pulse generator because most of the current flew into the Pt layer. Also, we couldn't clearly observe the effect of SOTs compared with the case of SiO_2/Mn_4N, in which DWs were moved purely by STTs. Further investigation in DMI and the optimization of the structure will be required to realize SOTs-driven CIDWM in a Mn_4N epitaxial film.

Chapter

Summary and future perspectives 6

6.1 Total summary

Current-induced domain wall motion (CIDWM) is one of the most important spintronics research fields because it can be applied to new magnetic devices such as a racetrack memory, spin-transfer majority gate, and so on. They constitute an attractive technology thanks to their non-volatility and fast operation. From material engineering, our group has focused on Mn_4N and $Mn_{4-x}Ni_xN$ films as new candidates for CIDWM. We recorded the DW velocity of 900 m/s in Mn_4N, and 3000 m/s in $Mn_{4-x}Ni_xN$ at the vicinity of its angular momentum compensation (at $x \sim 0.2$) at room temperature. These are the fastest records among CIDWM by pure spin-transfer torques (STTs). In this context, we investigated their magnetic and magneto-transport properties to understand especially the interaction between conduction and localized electrons and attempted to perform SOTs-driven CIDWM for more efficient operation.

Chapter 1 focuses on the theory of magnetism, especially ferrimagnets, and the torques which induce CIDWM. We also showed the advantage of the compensation in ferrimagnets for CIDWM and benchmark CIDWM in the literature.

In chapter 2, we present an overview of Mn_4N and Mn_4N-based compounds. First, we explain the fundamental properties of Mn_4N and concluded that they are beneficial for CIDWM. Then, we present our experiments of CIDWM in Mn_4N and $Mn_{4-x}Ni_xN$, in which we evidence the link between the observed fast DW velocity and the angular momentum compensation of $Mn_{4-x}Ni_xN$. We also introduce previous reports and our own studies on Mn4N-based compounds and explain the compensation in other nitrides such as $Mn_{4-x}Co_xN$.

In chapter 3, we attempt the growth of Mn_4N epitaxial films on various substrates to investigate the origin of PMA in Mn_4N. Our previous study reached the assumption that its PMA derives from the in-plane tensile strain of Mn_4N, however, this correlation was not been proven yet. We succeeded in the modulation of the tensile strain by the thickness and the lattice mismatch between Mn_4N and the growth substrate. In the end, we found a clear correlation between PMA and the magnitude of the ratio of lattice constants of Mn_4N (c/a). We thereby concluded that PMA derives from the spontaneous in-plane tensile strain of Mn_4N films and that it is possible to control its PMA by applying external stress to films.

In chapter 4, we investigate the magneto-transport properties of $Mn_{4-x}Ni_xN$ from anisotropic magnetoresistance (AMR) and anomalous Hall effect (AHE) measurements. From AMR, we found a change of the d electrons state by temperature, which became less effective with Ni insertion. Our ab-initio calculation of PDOSs of $Mn_{4-x}Ni_xN$ proved that it derives from a dras-

tic shift in the Fermi level and the change in the PDOS of Mn even by small Ni composition. Also, we analyzed the scaling of AHE and discovered that large intrinsic deflection contributes to the AHE in Mn_4N at low temperatures while extrinsic scatterings become dominant at high temperatures or in $Mn_{4-x}Ni_xN$.

In chapter 5, we aim at the growth of the heterostructure of heavy metal (HM) (Pt or W) and Mn_4N to attempt SOTs-driven CIDWM from the spin Hall effect. We observed large and stable magnetic domains in these samples, however, we also found that the magnetization reversals are affected by DW pinnings, which may come from the interfacial condition such as alloying and damaging by the sputtering process of the HM layer. We process them into multiwires for CIDWM investigation and achieved DW velocity of 420 m/s. However, we could not find a clear effect of SOTs on CIDWM. We propose that measurements with an in-plane field should be performed to form chiral Néel DWs, a prerequisite for the use of SOTs by SHE.

To conclude, the modulation of PMA by the strain and of the magneto-transport properties by dopants will broaden the possibility of Mn_4N. The use of SOTs for Mn_4N will be attempted with the assistance of the in-plane field and the optimization of the heterostructure.

6.2 Future perspectives

Here, we list our plans and directions for this research project about Mn_4N and Mn_4N-based compounds in the near future.

6.2.1 Modulation of PMA by external force

As concluded in chapter 3, the magnitude of the PMA of Mn_4N is strongly correlated with the in-plane tensile strain, given as c/a. In this thesis, we succeeded in altering c/a between 0.985 $\sim$ 0.998 by modulating the film thickness and the lattice mismatch with the substrate. From this, we found that the uniaxial magnetic isotropy constant (K_U) becomes larger when c/a is smaller. However, we couldn't apply the in-plane compressive strain which makes the crystal into $c/a > 1$ because Mn_4N films are most stable when the crystals were relaxed and set to be around $c/a \sim 0.99$. When we use LSAT(001) substrate to give the compressive strain on Mn_4N crystals, the Mn_4N crystals contain a lot of defects and dislocations, and the strain from the lattice mismatch has little influence on their lattice constants, only to find $c/a \sim 0.995$ at most.

In this context, we expect that we can modulate c/a of the crystals in the wider range by applying the external force, especially by bending samples. This is one of the most common ways to apply external force on the samples in the field of engineering in flexible materials. Although the flexible substrate and the seed layer are required to bend the films, we expect that only small curvature is enough to modulate the magnetic properties of Mn_4N from the drastic change in K_U by the small change of c/a, much less than 1 % for instance. Therefore, we are planning to attempt the deformation of the Mn_4N film by growing it on the thin STO(001) substrate. Our group in Japan succeeded in preparing 50 µm-thick STO(001) substrates thanks to the support of Inc. Furuuchi Chemical, which are generally 300 µm-thick for its products. To make the film curved with the external strain, we made the equipment to distort the film by the difference of the pressure on the top and bottom of the sample's surfaces. Figure 6.1 shows a photo of this equipment. The sample stage is with a hole that is connected to a cylinder with a piston. When we put the sample above this hole and pull the piston to absorb the air from the hole, the sample is distorted, which can be checked with the reflection of the laser beam from the sample's surface. More technically, the sample gets to have a downward curve, giving the crystals the strain of $c/a > 1$. The degree of distortion is evaluated with the position of

the piston, which is fixed with nuts. The K_U of the sample under the external tensile strain can be evaluated by observing its magnetic domain using a MOKE microscope. As explained in section 1.3.1, the size of the magnetic domain depends on the magnetic anisotropy energy. Thus, we anticipate that we can observe the impact of the tensile strain on the crystals by observing the change in the size of the magnetic domain.

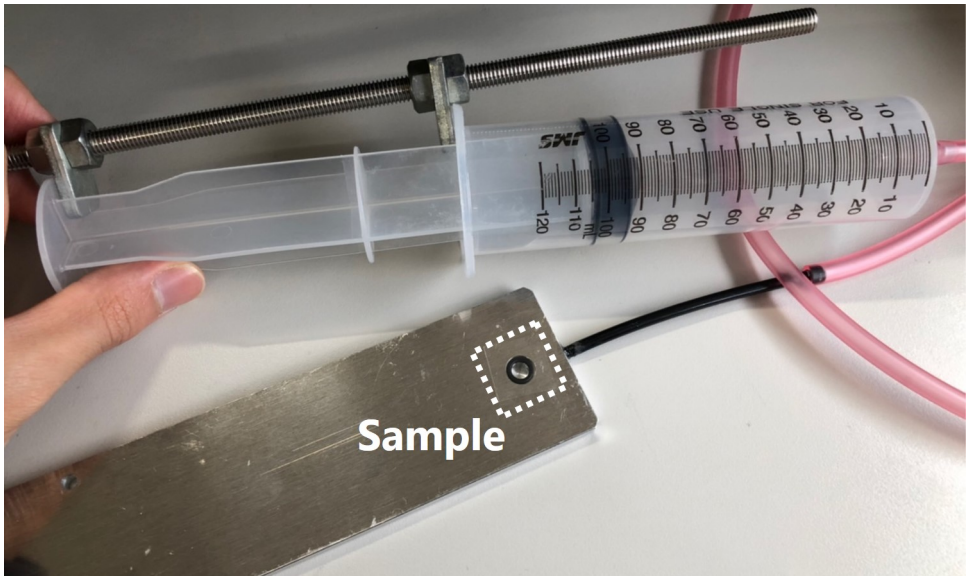

Figure 6.1: *Equipment to give an external strain to the samples. The samples are set at the position marked with the white square. The cylinder will vacuum the space beneath the sample, and the position of the piston is fixed with the nuts.*

The importance of the control of the magnitude of the PMA is to decrease the very high magnetic anisotropy field of the Mn_4N films, which disturbs us from fully magnetizing them in-plane. We consider this as the disadvantage of the study on the magnetic and magneto-transport properties and the CIDWM measurement. For example, the former may be the obstacle for the measurement of the AMR, Brillouin light scattering (BLS), and so on, in which the samples should be fully magnetized in-plane. This will be especially a serious problem in the $Mn_{4-x}Ni_xN$ films which are at the vicinity of the compensation point due to its divergence of the coercivity and the magnetic anisotropy field. The latter can make it difficult to change the formation of the DWs from Bloch to Néel, which is disadvantageous for the SOTs-based application. Thus, this study will open up a further investigation and the application of Mn_4N and its based nitrides.

We're planning to launch this research work with the help of Prof. Wadachi at the University of Hyogo with the measurement with a MOKE. First, we will grow the sample of SiO_2/Mn_4N (10nm)/STO(001), in which the thickness of the Mn_4N film should not be too thick to avoid the gradation of the lattice constants along the [001] azimuth. The size of the magnetic domains of the film will be evaluated with a MOKE by modulating the degree of the in-plane tensile. The position of the piston and the magnitude of c/a will be correlated by the XRD measurement.

6.2.2 Further investigation in the intrinsic AHE of Mn_4N

In chapter 4, we found that the main mechanism of the AHE is intrinsic deflection. However, since the magnitude of the intrinsic AHE is proportional to the Berry's curvature investigation through the scaling of ρ_{AHE} and ρ_{xx} is not sufficient to prove the relatively large AHE in Mn_4N films. In this context, the study on the energy bands of Mn_4N is required. The biggest

obstacle for this study is that the previous reports only reported the case of the cubic Mn_4N crystal, which will mismatch the case of the Mn_4N film in which its crystals are under the in-plane tensile strain and tetragonal distortion. Also, the lattice constants derived from the first-principle calculation after the structural optimization don't match those acquired from the results of the XRD measurements.

To pursue this investigation, the experimental analysis of the band structure with angle-resolved photoemission spectroscopy (ARPES) is expected to be effective. ARPES is based on the photoelectric effect, where an incoming photon with sufficient energy emits an electron from the surface of a film or a bulk sample. By measuring the kinetic energy and the distribution of the emission angles, the electronic band structure and Fermi level can be depicted. Figure 6.2 shows the images of energy bands of PbSnSe measured by ARPES as an example[206]. In this way, we can directly calculate the Berry curvature of energy bands right below the Fermi level.

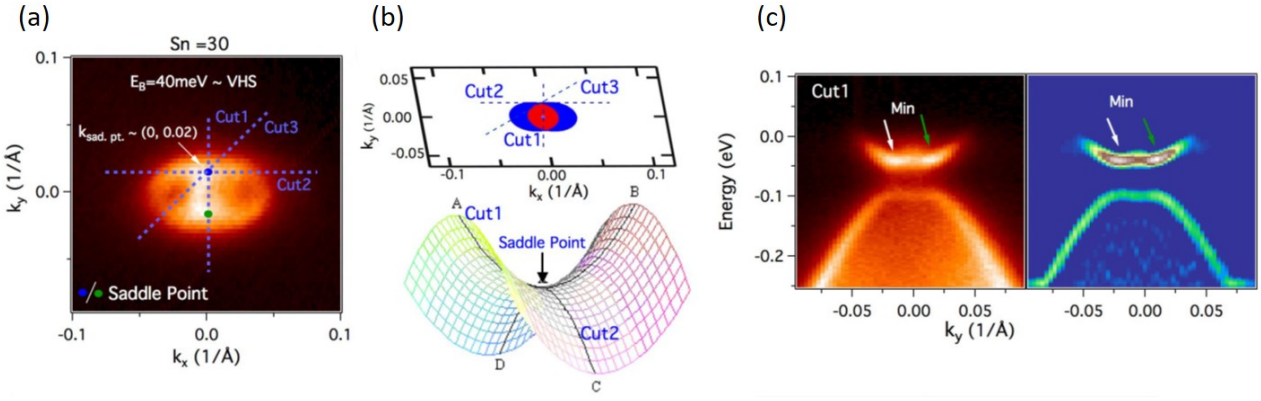

Figure 6.2: *Observation of the energy bands of $Pb_{0.70}Sn_{0.30}Ge$ (a) ARPES constant energy contour in the vicinity of an $\bar{X}$ point in the (001) surface Brillouin zone of PbSnSe at binding energy 40 meV. (b) Surface-state constant energy contour at the saddle point singularity energy by calculation (top), and a three-dimensional illustration of a saddle point (bottom). (c) ARPES dispersion map (left) and its second derivative image (right) along cut 1 depicted in (a) and (b).[206]*

We anticipate that this study has importance not only from the viewpoint of the AHE but also from that of the study on the magnetic structures of Mn_4N. As mentioned in chapter 4, the large AHE in Mn_4N films and other anti-perovskite nitrides such as Fe_4N is abnormal if they have collinear magnetic structures because the AHE is generally large in materials with heavy metal elements, which have large spin-orbit interaction. On the other hand, non-collinear magnets often show large AHE, for example, a Mn_3Sn Weyl semimetal. In the case of Weyl semimetals, very large Berry curvature can be found at the Weyl nodes, at which the energy band of the conduction electron and the valence band cross. And even in other non-collinear magnets, large Berry curvature around the Fermi level can lead to the band structure of the conduction and the valence bands of the topological materials, which correspond with the reports on the emergence of the topological Hall effect in (011) and (111) oriented Mn_4N epitaxial films. Therefore, the investigation of the band structure of the Mn_4N film may open up their application to topological semimetals and so on, and this study can be extended to the Fe_4N films, in which we found the AHE angle of 6 %.

To perform the ARPES measurements, the condition of the samples' surfaces is significantly important, more concretely, the contamination and the oxidation of the surface layer should be prevented before the measurement as much as possible. We're planning two methods to achieve these measurements. The first plan is that we grow a SiO_2/Mn_4N/STO sample, and we install it

into the chamber for the ARPES measurements. Before starting the measurements, the sample is dry-etched by Ar plasma until the Mn_4N surface is reached. In this way, we can remove the oxidized Mn_4N surface before the measurement and initiate the measurements under vacuum. Although the measurement will be performed with the relatively simple procedure in this plan, it will be difficult to completely avoid the damage of the surface by the sputtering, which may affect the results of the measurements. Another plan is, thereby, that we grow the Mn_4N/STO sample without any cap layer, and transfer it to a mobile introduction chamber to keep the sample under the vacancy. Then, it'll be sent to the facility for the ARPES measurements, and the sample will be directly transferred to the equipment. This procedure is costly due to the preparation for the mobile chamber, however, it'll be the best way to avoid all possible contamination and oxidation after the growth of the sample.

6.2.3 Approach to SOTs-driven CIDWM in Mn_4N

Although we attempted to perform the SOT-driven CIDWM in the heterostructure of Pt/Mn_4N multiwires, we could not observe the effect of SOTs compared to our previous result of SiO_2/Mn_4N, in which we proved that domains move purely by STTs. We still need to try CIDWM measurements on other samples we fabricated in this work, however, there are several measurements that should be done for our multiwires.

First, as mentioned in chapter 5, the existence of the DMI in our heterostructures should be evaluated because chiral Néel DWs should be formed for the best use of the SOTs from the SHE in heavy metals. Figure 6.3 shows the relative orientation of the accumulated spins and the magnetization and the reversal of the magnetization. To realize the fast magnetization reversals, Y-type SOT is required, and chiral Néel DWs are essential to achieve this configuration. Since the magnitude of the DMI is anti-proportional to the thickness of the magnetic film, the impact of the DMI of the samples of this work is expected to be very small, which were at most 7 nm-thick. However, if we can find non-zero DMI, we may be able to achieve sufficiently large DMI in thinner Mn_4N films. At this stage, Brillouin light scattering (BLS) is a candidate for the evaluation of the DMI in our samples. The obstacle for the BLS measurement of Mn_4N films is their high magnetic anisotropy field. Here, the modulation of the magnitude of the PMA using the external tensile as mentioned in section 5.2.1, and the use of the substrate which gives relatively smaller PMA to Mn_4N such as MgO(001) and LAO(001) can be solutions.

Also, even though the use of the assistance of the magnetic field is not desirable for the practical application to devices, this can help the formation of the chiral Néel DWs and the experimental performance of the SOTs-driven CIDWM. In fact, the ultrafast DW velocity by SOTs has been achieved with the assistance of an in-plane constant field because the effective DMI field is insufficient to completely transform Bloch DWs into Néel DWs in most of the materials. Since the magnetization of Mn_4N films is small even compared with other ferrimagnets, we expect that the kinetic energy barrier between the Bloch and Néel DWs is small and that the transformation of DWs by the DMI or the assistance of the external field is thus relatively easy, but still limited to 300 mT at the moment.

The other approach is the optimization of the growth condition and the structure of the samples. Although the SHE in heavy metals sputtered on magnetic layers has been reported, especially in the case of the sputtering on amorphous magnets, the case of the sputtering on MBE-grown Mn_4N single crystals is still not clear. In addition, the sputtering gun used in this work is in our MBE chamber, and the pressure is quite low (< 0.1 Pa) for the sputtering condition. Therefore, we may need to independently investigate the SHE of our sputtered heavy metal and work on the optimization of the sputtering condition. Here, the study on the crystallinity of heavy metals with the XRD measurements and the observation using a cross-

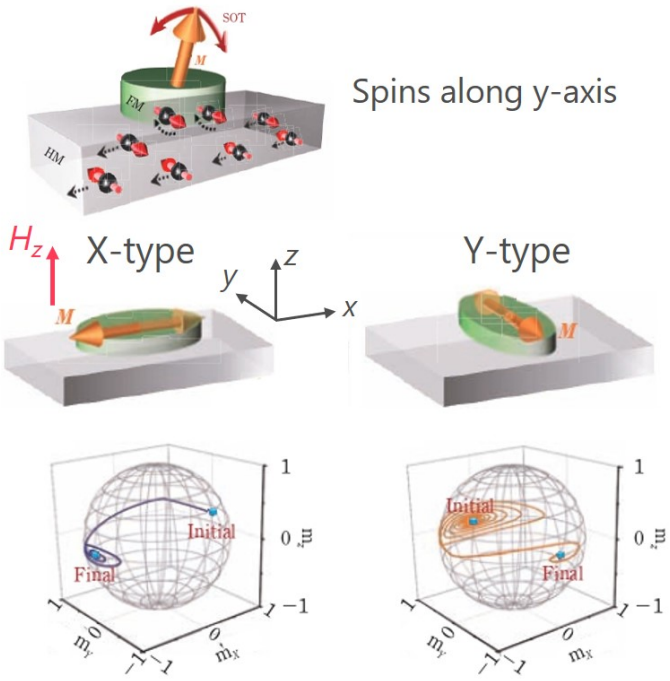

Figure 6.3: *Schematic images of that by SHE in a HM layer. Here, the spins accumulated by SHE are along the y-axis. In X-type, where the magnetization and the accumulated spins are orthogonal, fast magnetization reversals with little precessions are enabled. In Y-type, where the magnetization and the accumulated spins are parallel, the reversals are slower due to the precessions.[169]*

sectional TEM will be required, especially for the case of W to clearly judge its phase which drastically changes the magnitude of SHE.

From the perspective of the structures of the samples, the attempt to refrain from external DW pinning sites should be done. At this stage, we attribute them to the interface between the Mn_4N film and the heavy metal layer such as the alloying of Mn and heavy metal elements, and the damage to the top Mn_4N layer by sputtering. To test the effect of the interfacial condition and to possibly avoid these pinning sites, we anticipate that the insertion of a sacrificial layer between the interface will work. Here, the interfacial layer should be $1 \sim 2$ monolayers thick so that the whole heterostructure can sustain the broken inversion symmetry and the spin current from the heavy metal layer can be efficiently injected into the magnetic layer. The sacrificial layer must be nonmagnetic so that spins of the spin current are not scattered and magnetic moments in the Mn_4N film can be free from the interaction with those in the sacrificial layer. Another option is to cap the Mn_4N layer with a Co/Pt layer, to imprint Néel DWs in the Mn_4N from the large DMI obtained at this interface.

Research outputs and contributions

Contributions of the author

Here, I would like to list my contribution and role in this research project, based on the chapters in this thesis.

In chapter 2, I worked on the MBE growth of $Mn_{4-x}Ni_xN$ films on MgO(001) substrates[68], the growth on STO(001) substrates and their evaluation[69], and the investigation of their magnetic structures[70, 71].

In chapter 3, I assisted the MBE growth, crystalline evaluation with XRD, magnetic measurements with VSM, and magneto-transport properties measurements with PPMS. Here, these experiments were mainly performed by Mr. Taku Hirose of Univ. Tsukuba. I joined in the discussion on the correlation between the tensile and the PMA of Mn_4N[171, 172].

In chapter 4, I mainly performed all of the MBE growth, crystalline evaluation, measurements of magnetic and magneto-transport properties, and their analysis. I also joined the discussion on the results of the ab-initio calculation completed by Asso. Prof. Shuta Honda of Kansai University to conclude this work[72].

In chapter 5, I mainly worked on all of the experiments as in chapter 4. Dr. Laurent Vila of SPINTEC supported me in the process of multiwire device fabrication, and Dr. Stefania Pizzini and Dr. Jan Vogel of Institut Néel gave me technical advice on CIDWM experiments.

List of publications

Reviewed papers

1. A. Anzai, T. Gushi, T. Komori, S. Honda, S. Isogami, and T. Suemasu, "Transition from minority to majority spin transport in iron-manganese nitride $Fe_{4-x}Mn_xN$ films with increasing x", Journal of Applied Physics, **134**, 123905 (2018).

2. S. Isogami, A. Anzai, T. Gushi, T. Komori, and T. Suemasu, "Temperature independent, wide modulation of anomalous Hall effect by Mn doping in $Fe_{4-x}Mn_xN$ pseudo-single-crystal films", Japanese Journal of Applied Physics, **57**, 120305 (2018).

3. T. Komori, A. Anzai, T. Gushi, K. Toko, and T. Suemasu, “Molecular beam epitaxy growth of $Mn_{4-x}Ni_xN$ thin films on MgO(001) substrates and their magnetic properties”, Journal of Crystal Growth, **507**, 163-167 (2019).

4. T. Komori, T. Gushi, A. Anzai, L. Vila, J. P. Attanè, S. Pizzini, J. Vogel, S. Isogami, K. Toko, and T. Suemasu, “Magnetic and magneto-transport properties of Mn_4N thin films

by Ni substitution and their possibility of magnetic compensation", Journal of Applied Physics, **125**, 213902 (2019).

5. T. Komori, T. Hirose, T. Gushi, K. Toko, T. Hanashima, L. Vila, J. P. Attanè, K. Amemiya, and T. Suemasu, "Magnetic reversal in rare-earth free $Mn_{4-x}Ni_xN$ epitaxial films below and above Ni composition needed for magnetic compensation around room temperature", Journal of Applied Physics, **127**, 043903 (2020).

6. T. Hirose, T. Komori, T. Gushi, K. Toko, and T. Suemasu, "Perpendicular magnetic anisotropy in ferrimagnetic Mn_4N films grown on $(LaAlO_3)_0.3(Sr_2TaAlO_6)_0.7$(0 0 1) substrates by molecular beam epitaxy", Journal of Crystal Growth, **535**, 125566 (2020).

7. T. Hirose, T. Komori, T. Gushi, A. Anzai, K. Toko, and T. Suemasu, "Strong correlation between uniaxial magnetic anisotropic constant and in-plane tensile strain in Mn_4N epitaxial films", AIP Advances, **10**, 025117 (2020).

8. H. Mitarai, T. Komori, T. Hirose, K. Ito, S. Ghosh, S. Honda, K. Toko, L. Vila, J.-P. Attané, K. Amemiya, and T. Suemasu, "Magnetic compensation at two different composition ratios in rare-earth-free $Mn_{4-x}Co_xN$ ferrimagnetic films", Physical Review Materials, **4**, 094401 (2020).

9. S. Ghosh, T. Komori, A. Hallal, J. P. Garcia, T. Gushi, T. Hirose, H. Mitarai, H. Okuno, J. Vogel, M. Chshiev, J.-P. Attané, L. Vila, T. Suemasu, and S. Pizzini, "Current-Driven Domain Wall Dynamics in Ferrimagnetic Nickel-Doped Mn_4N Films: Very Large Domain Wall Velocities and Reversal of Motion Direction across the Magnetic Compensation Point", Nano Letters, **21**, 2580-2587 (2021).

10. T. Yasuda, T. Komori, H, Mitarai, S. Honda, S. Ghosh, L. Vila, J.-P. Attané, K. Amemiya, and T. Suemasu, "Ferrimagnetic–ferromagnetic phase transition in Mn_4N films favored by non-magnetic In doping", Journal of Physics D: Applied Physics, **55**, 115003 (2021).

11. T. Komori, H, Mitarai, T. Yasuda, S. Ghosh, L. Vila, J.-P. Attané, S. Honda, and T. Suemasu, "Anisotropic magnetoresistance in $Mn_{4x}Ni_xN$ and the change in the crystalline field", Journal of Applied Physics, **132**, 143902 (2022).

12. T. Komori, T. Horiuchi, H, Mitarai, T. Yasuda, K. Amemiya, and T. Suemasu, "Magnetic structure of 3d-element doped Mn_4N films confirmed by X-ray magnetic circular dichroism-Conditions for magnetic compensation", Journal of Magnetism and Magnetic Materials, **564**, 170050 (2022).

13. T. Yasuda, T. Komori, H, Mitarai, T. Suemasu, "Molecular beam epitaxial growth and magneto-transport properties of $Mn_{4-x}In_xN$ films on $SrTiO_3$(001) and MgO(001) substrates", Journal of Crystal Growth, **582**, 126525 (2022).

Conferences (International)

1. T. Komori, T. Gushi, A. Anzai, S. Isogami, and T. Suemasu, "Significant modification of magneto-transport properties of Mn_4N thin films by Ni substitution", Tsukuba Global Science Week Interdisciplinary Workshop on Science and Patents 2018, IWP048, Tsukuba (Japan), Sept. 21 (2018). (Poster)

2. T. Komori, H. Mitarai, K. Toko, and T. Suemasu, "Magneto-transport properties in $Mn_{4-x}Ni_xN$ films with large current induced domain wall mobility and investigation in their large anomalous Hall effect", IEEE Intermag 2021, IF-02, online, April 26-30 (2021). (Oral)

3. T. Komori, H. Mitarai, T. Yasuda, K. Toko, S. Honda, and T. Suemasu, "Magneto-transport properties in $Mn_{4-x}Ni_xN$ suitable for domain wall motion devices and the origins of its large anomalous Hall effect", MRM 2021, D2-PV22-47, Yokohama (Japan), Dec. 13-17 (2021). (Poster)

4. T. Komori, H. Mitarai, T. Yasuda, K. Toko, S. Honda, and T. Suemasu, "Experimental and theoretical approach to magneto-transport properties in $Mn_{4-x}Ni_xN$ with high domain wall mobility", Joint MMM-Intermag Conference 2022, HOF-11, online, Jan. 10-14 (2022). (Oral)

5. T. Komori, S. Ghosh, A. Hallal, J. P. Garcia, T. Gushi, T. Hirose, H. Mitarai, H. Okuno, J. Vogel, M. Chshiev, J.-P. Attané, L. Vila, T. Suemasu, and S. Pizzini, "Current induced domain wall motion in compensated $Mn_{4-x}Ni_xN$ at room temperature and Ni composition ratio dependence of the properties", Colloque Louis Néel 2022, Obernai (France), June 28- July 1 (2022). (Poster)

6. T. Komori, S. Ghosh, A. Hallal, J. P. Garcia, T. Gushi, T. Hirose, H. Mitarai, H. Okuno, J. Vogel, M. Chshiev, J.-P. Attané, L. Vila, T. Suemasu, and S. Pizzini, "Current induced domain wall motion in compensated $Mn_{4-x}Ni_xN$ at room temperature and Ni composition ratio dependence of the properties", Colloque Louis Néel 2022, Obernai (France), June 28- July 1 (2022). (Poster)

7. T. Komori, S. Ghosh, A. Hallal, J. P. Garcia, T. Gushi, T. Hirose, H. Mitarai, H. Okuno, J. Vogel, M. Chshiev, L. Vila, T. Suemasu, S. Pizzini, and J.-P. Attané, "Reversal of domain wall motion at the angular momentum compensation point in ferrimagnetic $Mn_{4-x}Ni_xN$", 2022 Joint European Magnetic Symposia, Warsaw (Poland), July 24- July 29 (2022). (Oral)

Conferences (Domestic)

1. T. Komori, T. Gushi, F. Takata, A. Anzai, K. Toko, and T. Suemasu, "Epitaxial Growth of $Mn_{4-x}Ni_xN$ thin films by MBE and their characterizations", The 65th Japan Society of Applied Physics Spring Meeting, 19p-D104-18, Tokyo (Japan), Mar. 19 (2018). (Oral)

2. T. Komori, T. Gushi, A. Anzai, K. Toko, S. Isogami, and T. Suemasu, "Significant modification of magneto-transport properties of Mn_4N thin films by Ni substitution", The 79th Japan Society of Applied Physics Autumn Meeting, 18a-131-7, Nagoya (Japan), Sep. 18 (2018). (Oral)

3. T. Komori, T. Gushi, A. Anzai, T. Hirose, K. Toko, S. Isogami, and T. Suemasu, "Temperature dependence of magneto-transport properties of $Mn_{4-x}Ni_xN$ thin films", The 66th Japan Society of Applied Physics Autumn Meeting, 9a-M101-7, Tokyo (Japan), Mar. 9 (2019). (Oral)

4. T. Komori, T. Hirose, K. Amemiya, and T. Suemasu, "Magnetic compensation of $Mn_{4-x}Ni_xN$ confirmed by X-ray magnetic circular dichroism and analysis on its structure ", The 80th Japan Society of Applied Physics Autumn Meeting, 20a-E216-4, Sapporo (Japan), Sep. 20 (2019). (Oral)

5. T. Komori, H. Mitarai, T. Hirose, K. Toko, and T. Suemasu, “Analysis of the magneto-transport properties in $Mn_{4-x}Ni_xN$ films with large current induced domain wall mobility and anomalous Hall effect”, The 81st Japan Society of Applied Physics Autumn Meeting, 11a-Z08-4, online, Sep. 11 (2020). (Oral)

6. T. Komori, H. Mitarai, T. Yasuda, K. Toko, S. Honda, and T. Suemasu, “Examination of magneto-transport properties in $Mn_{4-x}Ni_xN$ acquired by experiment and ab-initio calculation”, The 68th Japan Society of Applied Physics Spring Meeting, 16p-Z19-16, online, Mar. 16 (2021). (Oral)

7. T. Komori, H. Mitarai, T. Yasuda, K. Toko, T. Suemasu, “Evaluation of the properties of ultrathin Mn_4N epitaxial films by growing tilted films with molecular beam epitaxy”, The 82nd Japan Society of Applied Physics Autumn Meeting, 13p-S302-14, online, Sep. 13 (2021). (Oral)

8. T. Komori, H. Mitarai, T. Yasuda, T. Horiuchi, K. Toko, T. Suemasu, “Growth of the Mn_4N epitaxial film with the gradient and the cap and substrate dependence of the properties in the ultrathin region”, The 69th Japan Society of Applied Physics Autumn Meeting, 23a-E205-10, online, Mar. 23 (2022). (Oral)

9. T. Komori, S. Ghosh, A. Hallal, J. P. Garcia, T. Gushi, T. Hirose, H. Mitarai, H. Okuno, J. Vogel, M. Chshiev, L. Vila, T. Suemasu, S. Pizzini, and J.-P. Attané, “Reversal of domain wall motion at angular momentum compensation point in ferrimagnetic $Mn_{4-x}Ni_xN$”, The 83rd Japan Society of Applied Physics Autumn Meeting, 22p-B201-5, online, Sep. 22 (2022). (Oral)

Others

1. T. Komori, H. Mitarai, T. Yasuda, K. Toko, S. Honda, and T. Suemasu, "Significant composition ratio dependence of magneto-transport properties in compensated $Mn_{4-x}Ni_xN$", The 26th Symposium on the Physics and Applications of Spin-related Phenomena in Semiconductors, Tsukuba (Japan), Dec. 20 (2021). (Talk at a symposium)

Acknowledgement

This research project, all experimental results, and this thesis have been completed thanks to support from a lot of people. Here, I acknowledge the people who have contributed to this project.

Supervision

My research activities in this Ph.D. course have been supervised by Prof. Takashi Suemasu of the University of Tsukuba (UT), and Dr. Olivier Fruchart, Dr. Laurent Vila, and Prof. Jean Philippe Attané of SPINTEC, CEA-Grenoble, and Dr. Stefania Pizzini Insititut Néel. Their supervision is represented by regular discussions on the direction of my research, advice for writing papers for journals and conferences, suggestions for presentations including my Ph.D. defense, and admission procedures for the universities, especially for the double degree program (DDP) between UT and Université Grenoble Alpes (UGA).

Double degree program

I would like to acknowledge Prof. Katsuhiro Akimoto and Prof. Etienne Gheeraert who are in charge of the DDP, and secretaries in UT, UGA, and CEA, especially Ms. Adriana Stoenescu of CEA.

Technical advice and experimental support

In Japan, Prof. Suemasu has given me a lot of advice about the growth and characterization of crystalline thin films by MBE and sputtering. Prof. Hideto Yanagihara of UT has spent his time with me for technical discussions and advice on measurements with a VSM. Prof. Seiji Mitani of National Institute for Materials Science (NIMS) helped me with MOKE measurements and introduced me to articles to improve my experimental discussion. Prof. Shinji Kuroda and Prof. Yuzo Ohno kindly gave me advice and hint to brush up on my thesis in my pre-defense. Prof. Kenta Amemiya of Institute of Materials Structure Science, KEK, joined in the discussion on the magnetism of Mn_4N while helping us to perform XMCD measurements. Assoc. Prof. Shuta Honda of Kansai University performed the ab-initio calculation for $Mn_{4-x}Ni_xN$ crystals and provided his consideration to us for the discussion.

In France, Dr. Fruchart gave me many clues to pursue the CIDWM measurements through the discussion. Dr. Vila taught me the processes for nanofabrication and helped me with the various measurements at SPINTEC. Prof. Attané provided me with many hints to brush up on my writing and presentations, especially for the thesis and slides for my defense. Dr. Stefania Pizzini and Dr. Jan Vogel of Institut Néel assisted me with measurements with a MOKE microscope, especially CIDWM measurements, and gave me a lot of technical advice.

Dr. Olivier Boulle of SPINTEC and Dr. Pham Van Tuong of Institut Néel also gave me technical advice and joined our discussion on DMI in our Mn_4N films.

And as my seniors in this DDP, Dr. Toshiki Gushi and Dr. Sambit Ghosh of UT and SPINTEC have given me a lot of advice and practical information for experiments with sharing their experience

Equipments and facilities

Magnetization measurements with a VSM have been performed with the help of Prof. Yanagihara in Japan and Dr. Isabelle Joumard of SPINTEC in France. AMR and AHE measurements with a PPMS have been performed with the help of Assoc. Prof. Tamotsu Koyano of the Cryogenics Division of UT. Device fabrication processes have been held in Nanotechnology Platform of UT in Japan and in la Plate-forme Technologique Amont (PTA) of CEA in France. Measurements with a MOKE, especially CIDWM measurements, have been performed with the help of Dr. Pizzini and Dr. Vogel of Insititut Néel in France.

Research funds

This work was supported in part by the Japan Society for the Promotion of Science (JSPS) KAKENHI (Grant Nos. JP19K21954, JP19KK0104, and JP21H04548). I would like to also acknowledge additional support from the JSPS Research Fellowships for Young Scientists (Grant No. 21J10330). From the French side, we acknowledge the support from the European Union's Horizon 2020 research and innovation program under Marie Sklodowska-Curie Grant Agreement No. 754303 and the support from the Laboratoire d'excellence LANEF in Grenoble (ANR-10-LABX-0051). I was also financially supported by Campus France for my Ph.D. life in France.

Special thanks

My life as a Ph.D. student has been greatly supported by a lot of people concerning not only the research but also my everyday life both in Japan and France. Especially, although world affairs have been difficult to pursue our international research project due to the spread of COVID-19, fortunately, I could continue my research activities and have one year of research experience in France thanks to everyone's kind support.

Prof. Takashi Suemasu has given me a lot of advice and one of the best environments for research. Also, I learned what the ideal researcher is like from him. If I did not join his group, I would not probably choose to go for a Ph.D. course and try this double degree program.

Dr. Olivier Fruchart managed my admission process to UGA. He also showed me the direction of our research project through discussions. Although he must have been busy as deputy director of SPINTEC and president of the EMA, he took care of and helped me a lot.

Dr. Laurent Vila taught me nanofabrication and helped me to decide the policy of the experiment. What's more, he supported me a lot with my life in France such as my accommodation, scholarship, and so on. I'm sure you take the most important role in this double degree program. Also, please tell Hanako-san that her sushi was the best in Grenoble.

Prof. Jean-Philippe Attané gave me a lot of advice on my manuscript and presentations. Especially, I felt confident during my pre-defense thanks to his suggestions and corrections. I hope what you taught me is beneficial even for my future job as well.

Associate Prof. Kaoru Toko taught me what to do for self-growth as a young researcher. He also gave me suggestions about Japanese writing, especially for the application form for JSPS.

Prof. Hideto Yanagihara welcomed our group to his seminar and journal club and gave me a lot of opportunities to study the theory of spintronics. He gave me technical advice as well.

As senior students in this double degree program, Dr. Toshiki Gushi and Dr. Sambit Ghosh helped me a lot with my research and my everyday life. With their aid, my research experience both in Japan and France has been more enriched.

As senior students, Mr. Fumiya Takata and Mr. Akihito Anzai taught me the MBE growth and various measurements. I think what they gave me had an impact on my decision to go for a Ph.D. course.

As junior students, Mr. Tomohiro Yasuda, Mr. Taku Hirose, Mr. Takumi Horiuchi, Mr. Aoi Hatate, and Ms. Haruka Mitarai helped me with my experiments and discussion and motivated me with their earnest attitude toward research.

Owing to all members of Suemasu & Toko laboratory, I enjoyed my student life in Tsukuba with them a lot such as excursions. I'd like to express my special thanks to Dr. Takeshi Nishida (I'm sure you are going to be) as my colleague for 6 years.

Owing to all members of SPINTEC, I enjoyed my Ph.D. student life in Grenoble with them a lot such as drinking, skiing, and going on a hike together. I would like to express my special thanks to Dr. Ryuhei Kohno (I'm sure you are going to be) for teaching me a lot about France.

Throughout my life as a Ph.D. student, owing to Ms. Keiko Suzuki of Bar Dali, Tsukuba, and regular customers there, we shared values of life with drinking. It was a relaxing moment

for me to keep myself motivated for my research project.

Finally, I would like to express my sincere thanks to my family for understanding my decision about my study and work, and for growing me and my student life.

Bibliography

[1]M. N. Baibich, J. M. Broto, A. Fert, F. N. V. Dau, Itoh, and F. Petroff., "Giant magnetoresistance of (001)fe/(001)cr magnetic superlattices", Physical Review Letters **61**, 2472 (1988).

[2]T. Miyazaki and T. Nezuka, "Giant magnetic tunneling effect in fe/al_2o_3/fe junction", Journal of Magnetism and Magnetic Materials **139**, L231 (1995).

[3]J. S. Moodera, L. R. Kinder, T. M. Wong, and R. Meservey, "Large magnetoresistance at room temperature in ferromagnetic thin film tunnel junctions", Physical Review Letters **74**, 3273 (1995).

[4]E. B. Myers, D. C. Ralph, J. A. Katine, R. N. Louie, and R. A. Buhrman, "Current-induced switching of domains in magnetic multilayer devices", Science **285**, 867 (1999).

[5]D. Chiba, Y. Sato, T. Kita, F. Matsukura, and H. Ohno, "Current-driven magnetization reversal in a ferromagnetic semiconductor (ga,mn)as/gaas/(ga,mn)as tunnel junction", Physical Review Letters **93**, 216602 (2004).

[6]S. Yuasa, T. Nagahama, A. Fukushima, Y. Suzuki, and K. Ando, "Giant room-temperature magnetoresistance in single-crystal fe/mgo/fe magnetic tunnel junctions", Nature Materials **3**, 868 (2004).

[7]A. Yamaguchi, T. Ono, S. Nasu, K. Miyake, K. Mibu, and T. Shinjo, "Real-space observation of current-driven domain wall motion in submicron magnetic wires", Physical Review Letters **02**, 077205 (2004).

[8]M. Yamanouchi, D. Chiba, F. Matsukura, and H. Ohno, "Current-induced domain-wall switching in a ferromagnetic semiconductor structure", Nature **428**, 539 (2004).

[9]S. Datta and B. Das., "Electronic analog of the electro-optic modulator", Applied Physics Letters **56**, 665 (1990).

[10]H. Ohno, H. Munekata, T. Penny, S. von Molnár, and L. L. Chang., "Magnetotransport properties of p-type (in,mn)as diluted magnetic iii-v semiconductors", Physical Review Letters **68**, 2664 (1992).

[11]O. H, A. Shen, F. Matsukura, A. Oiwa, A. Endo, S. Katsumoto, and Y. Iye., "(ga,mn)as: a new diluted magnetic semiconductor based on gaas", Applied Physics Letters **69**, 363 (1996).

[12]H. Ohno, D. Chiba, F. Matsukura, T. Omiya, E. Abe, T. Dietl, Y. Ohno, and K. Ohtani., "Electric-field control of ferromagnetism", Nature **408**, 944 (2000).

[13]T. Bergsten, T. Kobayashi, Y. Sekine, and J. Nitta., "Experimental demonstration of the time reversal aharonov-casher effect", Physical Review Letters **97**, 196803 (2006).

[14]A. Oiwa, Y. Mitsumori, R. Moriya, T. Słupinski, and H. Munekata., "Effect of optical spin injection on ferromagnetically coupled mn spins in the iii-v magnetic alloy semiconductor (ga,mn)as", Physical Review Letters **88**, 137202 (2002).

[15]Y. K. Kato, R. C. Myers, A. C. Gossard, and D. D. Awschalom., "Observation of the spin hall effect in semiconductors", Science **306**, 1910 (2004).

[16]S. O. Valenzuela and M. Tinkham., "Direct electronic measurement of the spin hall effect", Nature **442**, 176 (2004).

[17]T. Kimura, Y. Otani, T. Sato, S. Takahashi, and S. Maekawa., "Room-temperature reversible spin hall effect", Physical Review Letters **98**, 249901 (2004).

[18]X. Lou, C. Adelmann, S. A. Crooker, E. S. Garlid, J. Zhang, K. S. M. Reddy, S. D. Flexner, C. J. Palmstrøm, and P. A. Crowell., "Electrical detection of spin transport in lateral ferromagnet–semiconductor devices", Nature Physics **3**, 197 (2007).

[19]T. Yang, T. Kimura, and Y. Otani., "Giant spin-accumulation signal and pure spin-current-induced reversible magnetization switching", Nature Physics **4**, 4 (2008).

[20]Y. Kajiwara, K. Harii, S. Takahashi, J. Ohe, K. Uchida, M. Mizuguchi, H. Umezawa, H. Kawai, K. Ando, K. Takanashi, S. Maekawa, and E. Saitoh., "Transmission of electrical signals by spin-wave interconversion in a magnetic insulator", Nature **464**, 262 (2010).

[21]V. C. J. S. . A. Fert, "Skyrmions on the track", Nature Nanotechnology **8**, 152 (2013).

[22]R. Takahashi, M. Matsuo, M. Ono, K. Harii, H. Chudo, S. Okayasu, J. Ieda, S. Takahashi, S. Maekawa, and E. Saitoh., "Spin hydrodynamic generation", Nature Physics **12**, 52 (2015).

[23]F. Lange, S. Ejima, J. Fujimoto, T. Shirakawa, H. Fehske, S. Yunoki, and S. Maekawa., "Generation of current vortex by spin current in rashba systems", Physical Review Letters **126**, 157202 (2021).

[24]K. Uchida, S. Takahashi, K. Harii, J. Ieda, W. Koshibae, K. Ando, S. Maekawa, and E. Saitoh., "Observation of the spin seebeck effect", Nature **455**, 778 (2008).

[25]T. An, V. I. Vasyuchka, K. Uchida, A. V. Chumak, K. Yamaguchi, K. Harii, J. Ohe, M. B. Jungfleisch, Y. Kajiwara, H. Adachi, B. Hillebrands, S. Maekawa, and E. Saitoh., "Unidirectional spin-wave heat conveyer", Nature Materials **12**, 549 (2013).

[26]I. M. Miron, K. Garello, G. Gaudin, P.-J. Zermatten, M. V. Costache, S. Auffret, S. Bandiera, B. Rodmacq, A. Schuhl, and P. Gambardella., "Perpendicular switching of a single ferromagnetic layer induced by in-plane current injection", Nature **476**, 476 (2011).

[27]A. Thiaville, S. Rohart, V. C. É. Jué, and A. Fert., "Dynamics of dzyaloshinskii domain walls in ultrathin magnetic films", Europhysics Letters **100**, 57002 (2012).

[28]I. M. Miron, T. Moore, H. Szambolics, L. D. B. Prejbeanu, S. Auffret, B. Rodmacq, S. Pizzini, J. Vogel, A. S. M. Bonfim, and G. G. ., "Fast current-induced domain-wall motion controlled by the rashba effect", Nature Materials **10**, 419 (2011).

[29]A. E. LaBonte., "Two-dimensional bloch type domain walls in ferromagnetic films", Journal of Applied Physics **40**, 2450 (1969).

[30]A. Hubert and R. Schäfer., "Magnetic domains: the analysis of magnetic microstructures", 696 (1998).

[31]J. M. D. Coey., "Louis néel: retrospective (invited)", Journal of Applied Physics **93**, 8224 (2003).

[32]T. Ono, H. Miyajima, K. Shigeto, K. Mibu, N. Hosoito, and T. Shinjo., "Propagation of a magnetic domain wall in a submicrometer magnetic wire", Science **284**, 468 (1999).

[33]G. S. D. Beach, C. Nistor, M. T. C. Knutson, and J. L. Erskine., "Dynamics of field-driven domain-wall propagation in ferromagnetic nanowires", Nature Materials **4**, 741 (2005).

[34]K. Fukumoto, W. Kuch, J. Vogel, F. Romanens, S. Pizzini, J. Camarero, M. Bonfim, and J. Kirschner., "Dynamics of magnetic domain wall motion after nucleation: dependence on the wall energy", Physical Review Letters **96**, 097204 (2006).

[35]L. Berger., "Exchange interaction between ferromagnetic domain wall and electric current in very thin metallic films", Journal of Applied Physics **55**, 1954 (1984).

[36]M. Tsoi, R. E. Fontana, and S. Parkin., "Magnetic domain wall motion triggered by an electric current", Applied Physics Letters **83**, 2617 (1978).

[37]M. Kläui, C. A. F. Vaz, J. A. C. Bland, W. Wernsdorfer, G. Faini, E. Cambril, L. J. Heyderman, F. Nolting, and U. Rüdiger., "Controlled and reproducible domain wall displacement by current pulses injected into ferromagnetic ring structures", Physical Review Letters **94**, 106601 (2005).

[38]S. S. P. Parkin, M. Hayashi, and L. Thomas., "Magnetic domain-wall racetrack memory", Science **320**, 190 (2008).

[39]S. S. P. Parkin and S.-H. Yang., "Memory on the racetrack", Nature Nanotechnology **10**, 195 (2015).

[40]A. Brataas, A. D. Kent, and H. Ohno., "Current-induced torques in magnetic materials", Nature Materials **11**, 372 (2012).

[41]D. A. Allwood, G. X. M. D. Cooke, C. C. Faulkner, D. Atkinson, N. Vernier, and R. P. Cowburn., "Submicrometer ferromagnetic not gate and shift register", Science **296**, 2003 (2002).

[42]J. A. Currivan, Y. Jang, M. D. Mascaro, M. A. Baldo, and C. A. Ross., "Low energy magnetic domain wall logic in short, narrow, ferromagnetic wires", IEEE Magnetics Letters **3**, 3000104 (2012).

[43]J. A. Currivan-Incorvia, S. Siddiqui, S. Dutta, E. R. Evarts, J. Zhang, D. Bono, C. A. Ross, and M. A. Baldo., "Logic circuit prototypes for three-terminal magnetic tunnel junctions with mobile domain walls", Nature Communications **7**, 10275 (2016).

[44]Z. Luo, A. Hrabec, T. P. Dao, G. Sala, S. Finizio, J. Feng, J. R. S. Mayr, P. Gambardella, and L. J. Heyderman., "Current-driven magnetic domain-wall logic", Nature **579**, 214 (2020).

[45]J. C. Slonczewski., "Current-driven excitation of magnetic multilayers", Journal of Magnetism and Magnetic Materials **159**, L1 (1996).

[46]A. Thiaville, Y. Nakatani, J. Miltat, and Y. Suzuki., "Micromagnetic understanding of current-driven domain wall motion in patterned nanowires", Europhysics Letters **69**, 990 (2005).

[47]A. Manchon, I. M. M. J. Železný, T. Jungwirth, J. Sinova, A. Thiaville, K. Garello, and P. Gambardella., "Current-induced spin-orbit torques in ferromagnetic and antiferromagnetic systems", Review of Modern Physics **91**, 035004 (2019).

[48]Y. Zhang, Z. Zhang, Y. Liu, B. Ma, and Q. Y. Jin., "Spin-transfer-induced magnetization switching in tunnel junctions with nanocurrent channels", Journal of Applied Physics **99**, 08G515 (2006).

[49]A. Mougin, M. Cormier, J. P. Adam1, P. J. Metaxas, and J. Ferré1., "Domain wall mobility, stability and walker breakdown in magnetic nanowires", Europhysics Letters **78**, 57007 (2007).

[50]M. Imai, Y. Ogata, H. Chudo, M. Ono, K. Harii, M. Matsuno, Y. Ohnuma, S. Maekawa, and E. Saitoh., "Observation of gyromagnetic reversal", Applied Physics Letters **78**, 052402 (2018).

[51]C. D. Stanciu, A. V. Kimel, F. Hansteen, A. Tsukamoto, A. Itoh, A. Kirilyuk, and T. Rasing., "Ultrafast spin dynamics across compensation points in ferrimagnetic gdfeco: the role of angular momentum compensation", Physical Review B **73**, 220402(R) (2006).

[52]M. Binder, A. Weber, O. Mosendz, G. Woltersdorf, M. Izquierdo, I. Neudecker, J. R. Dahn, T. D. Hatchard, J.-U. Thiele, C. H. Back, and M. R. Scheinfein., "Magnetization dynamis of the ferrimagnet cogd near the compensation of magnetization and angular momentum", Physical Review B **74**, 134404 (2006).

[53]K.-J. Kim, S. K. Kim, Y. Hirata, S.-H. Oh, T. Tono, D.-H. Kim, T. Okuno, W. S. Ham, G. G. Sanghoon Kim, Y. Tserkovnyak, A. Tsukamoto, T. Moriyama, K.-J. Lee, and T. Ono., "Fast domain wall motion in the vicinity of the angular momentum compensation temperature of ferrimagnets", Nature Materials **16**, 1187 (2017).

[54]L. Caretta, M. Mann, F. Büttner, K. Ueda, B. Pfau, C. M. Günther, P. Hessing, A. Churikova, C. Klose, M. Schneider, D. Engel, C. Marcus, D. Bono, K. Bagschik, S. Eisebitt, and G. S. D. B. ., "Fast current-driven domain walls and small skyrmions in a compensated ferrimagnet", Nature Nanotechnology **13**, 1154 (2018).

[55]E. Haltz, S. Krishnia, L. Berges, A. Mougin, and J. Sampaio., "Domain wall dynamics in antiferromagnetically coupled double-lattice systems", Physical Review B **103**, 014444 (2021).

[56]J. Han, A. Richardella, S. A. Siddiqui, J. Finley, N. Samarth, and L. Liu., "Room-temperature spin-orbit torque switching induced by a topological insulator", Physical Review Letters **119**, 077702 (2017).

[57]K. Cai, Z. Zhu, J. M. Lee, R. Mishra, L. Ren, S. D. Pollard, P. He, G. Liang, K. L. Teo, and H. Yang., "Ultrafast and energy-efficient spin–orbit torque switching in compensated ferrimagnets", Nature Electronics **3**, 37 (2020).

[58]S.-G. Je, J.-C. Rojas-Sanchez, T. H. Pham, P. Vallobra, G. Malinowski, D. Lacour, T. Fache, M.-C. Cyrille, D.-Y. Kim, S.-B. Choe, M. Belmeguenai, M. Hehn, S. Mangin, G. Gaudin, and O. Boulle., "Spin-orbit torque-induced switching in ferrimagnetic alloys: experiments and modeling", Applied Physics Letters **112**, 062401 (2018).

[59]S. A. Siddiqui, J. Han, J. T. Finley, C. A. Ross, and L. Liu., "Current-induced domain wall motion in a compensated ferrimagnet", Physical Review Letters **121**, 057701 (2018).

[60]C. O. Avci, E. Rosenberg, L. Caretta, F. Büttner, M. Mann, C. Marcus, D. Bono, C. A. Ross, and G. S. D. Beach., "Interface-driven chiral magnetism and current-driven domain walls in insulating magnetic garnets", Nature Nanotechnology **14**, 561 (2019).

[61]L. Caretta, S.-H. OH, T. FAKHRUL, D.-K. LEE, B. H. LEE, S. K. KIM, C. A. ROSS, K.-J. LEE, and G. S. D. BEACH., "Relativistic kinematics of a magnetic soliton", Science **370**, 1438 (2020).

[62]X. Shen, A. Chikamatsu, K. Shigematsu, Y. Hirose, T. Fukumura, and T. Hasegawa., "Metallic transport and large anomalous hall effect at room temperature in ferrimagnetic mn_4n epitaxial thin film", Applied Physics Letters **105**, 072410 (2014).

[63]Y. Yasutomi, K. Ito, T. Sanai, K. Toko, and T. Suemasu., "Perpendicular magnetic anisotropy of mn_4n films on mgo(001) and $srtio_3$(001) substrates", Journal of Applied Physics **115**, 17A935 (2014).

[64]K. Kabara and M. Tsunoda., "Perpendicular magnetic anisotropy of mn_4n films fabricated by reactive sputtering method", Journal of Applied Physics **117**, 17B512 (2015).

[65]T. Gushi, L. Vila, O. Fruchart, A. Marty, S. Pizzini, J. Vogel, F. Takata, A. Anzai, K. Toko, T. Suemasu, and J.-P. Attané., "Millimeter-sized magnetic domains in perpendicularly magnetized ferrimagnetic mn_4n thin films grown on $srtio_3$", Japanese Journal of Applied Physics **57**, 120310 (2018).

[66]S. Emori and G. S. D. Beach., "Enhanced current-induced domain wall motion by tuning perpendicular magnetic anisotropy", Applied Physics Letters **98**, 132508 (2011).

[67]T. Gushi, M. J. Klug, J. P. Garcia, S. Ghosh, J.-P. Attané, H. Okuno, O. Fruchart, J. Vogel, T. Suemasu, S. Pizzini, and L. Vila., "Large current driven domain wall mobility and gate tuning of coercivity in ferrimagnetic mn_4n thin films", Nano Letters **19**, 8716 (2019).

[68]T. Komori, A. Anzai, T. Gushi, K. Toko, and T. Suemasu., "Molecular beam epitaxy growth of $mn_4 - xni_xn$ thin films on mgo(001) substrates and their magnetic properties", Journal of Crystal Growth **507**, 163 (2019).

[69]T. Komori, T. Gushi, A. Anzai, L. Vila, J.-P. Attané, S. Pizzini, J. Vogel, S. Isogami, K. Toko, and T. Suemasu., "Magnetic and magneto-transport properties of mn_4n thin films by ni substitution and their possibility of magnetic compensation", Journal of Applied Physics **125**, 213902 (2019).

[70]T. Komori, T. Hirose, T. Gushi, K. Toko, Hanashima, L. Vila, J.-P. Attanè, K. Amemiya, and T. Suemasu., "Magnetic reversal in rare-earth free $mn_4 - xni_xn$ epitaxial films below and above ni composition needed for magnetic compensation around room temperature", Journal of Applied Physics **127**, 043903 (2020).

[71]S. Ghosh, T. Komori, A. Hallal, J. P. Garcia, T. Gushi, T. Hirose, H. Mitarai, H. Okuno, J. Vogel, M. Chshiev, J.-P. Attané, L. Vila, T. Suemasu, and S. Pizzini., "Current-driven domain wall dynamics in ferrimagnetic nickel-doped mn_4n films: very large domain wall velocities and reversal of motion direction across the magnetic compensation point", Nano Letters **21**, 2580 (2021).

[72]T. Komori, H. Mitarai, T. Yasuda, S. Ghosh, L. Vila, J.-P. Attané, S. Honda, and T. Suemasu., "Anisotropic magnetoresistance in mn_4-xni_xn and the change in the crystalline field", Nano Letters **132**, 2580 (2022).

[73]K. Ito, Y. Yasutomi, K. Kabara, T. GUshi, S. Higashikozono, K. Toko, M. Tsunoda, and T. Suemasu., "Perpendicular magnetic anisotropy in co_xmn_4xn (x = 0 and 0.2) epitaxial films and possibility of tetragonal mn_4n phase", AIP Advances **6**, 056201 (2016).

[74]K. Ito, Y. Yasutomi, S. Zhu, M. Nurmamat, M. Tahara, K. Toko, R. Akiyama, Y. Takeda, Y. Saitoh, T. Oguchi, A. Kimura, and T. Suemasu., "Manipulation of saturation magnetization and perpendicular magnetic anisotropy in epitaxial co_xmn_4xn films with ferrimagnetic compensation", Physical Review B **101**, 104401 (2020).

[75]H. Mitarai, T. Komori, T. Hirose, K. Ito, S. Ghosh, S. Honda, K. Toko, L. Vila, J.-P. Attané, K. Amemiya, and T. Suemasu., "Magnetic compensation at two different composition ratios in rare-earth-free mn_4xco_xn ferrimagnetic films", Physical Review Materials **4**, 094401 (2020).

[76]L. Néel., "Antiferromagnetism and ferrimagnetism", Proceedings of the Physical Society. Section A **65**, 18 (1952).

[77]A. A. Serga, A. V. Chumak, and B. Hillebrands1., "Yig magnonics", Journal of Physics D: Applied Physics **43**, 264002 (2010).

[78]G. Dionne., "A review of ferrites for microwave applications", Proceedings of the IEEE 63 **63**, 777 (1975).

[79]W. Heisenberg., "Mehrkörperproblem und Resonanz in der Quantenmechanik", Zeitschrift für Physik **38**, 411 (1926).

[80]W. Heisenberg., "Relativity quantum mechanics with an application to compton scattering", The Royal Society Publishing **111**, 405 (1926).

[81]B. Rodmacq, S. Auffret, and B. Dieny., "Crossovers from in-plane to perpendicular anisotropy in magnetic tunnel junctions as a function of the barrier degree of oxidation", Journal of Applied Physics **93**, 7513 (2003).

[82]S. Ikeda, K. Miura, H. Yamamoto, K. Mizunuma, H. D. Gan, M. Endo, S. Kanai, J. Hayakawa, F. Matsukura, and H. Ohno., "A perpendicular-anisotropy cofeb–mgo magnetic tunnel junction", Nature Materials **9**, 721 (2010).

[83]S. Peng, M. Wang, H. Yang, L. Zeng, J. Nan, J. Zhou, Y. Zhang, A. Hallal, M. Chshiev, K. L. Wang, Q. Zhang, and W. Zhao., "Origin of interfacial perpendicular magnetic anisotropy in mgo/cofe/metallic capping layer structures", Scientific Reports **5**, 18173 (2015).

[84]H. Iwasaki, "Gmr heads for high-capacity hdd", TOSHIBA REVIEW **52**, 47–50 (1997).

[85]G. Chen, J. Zhu, A. Quesada, J. Li, A. T. N'Diaye, Y. Huo, T. P. Ma, Y. Chen, H. Y. Kwon, C. Won, Z. Q. Qiu, A. K. Schmid, and Y. Z. Wu., "Novel chiral magnetic domain wall structure in fe/ni/cu(001) films", Physical Review Letters **110**, 177204 (2013).

[86]G. Chen, T. Ma, A. T. N'Diaye, H. Kwon, C. Won, Y. Wu, and A. K. Schmid., "Tailoring the chirality of magnetic domain walls by interface engineering", Nature Communications **4**, 2671 (2013).

[87]S. Woo, K. Litzius, B. Krüger, M.-Y. Im, L. Caretta, K. Richter, M. Mann, A. Krone, R. M. Reeve, M. Weigand, P. Agrawal, I. Lemesh, M.-A. Mawass, P. Fischer, M. Kläui, and G. S. D. Beach., "Observation of room-temperature magnetic skyrmions and their current-driven dynamics in ultrathin metallic ferromagnets", Nature Materials **15**, 501 (2016).

[88]L. D. Landau and E. M. Lifshitz., "On the theory of the dispersion of magnetic permeability in ferromagnetic bodies", Collected Papers of L. D. Landau, 101 (1965).

[89]X. Fong, Y. Kim, K. Yogendra, D. Fan, A. Sengupta, A. Raghunathan, and K. Roy., "Spin-transfer torque devices for logic and memory: prospects and perspectives", Journal of Superconductivity and Novel Magnetism **35**, 1 (2016).

[90]L. Néel., "Energie des parois de Bloch dans les couches minces", C. R. Acad. Sci. Paris **241**, 533 (1955).

[91]I. Dzyaloshinsky., "A thermodynamic theory of "weak" ferromagnetism of antiferromagnetics", Journal of Physics and Chemistry of Solids **4**, 241 (1958).

[92]T. Moriya., "Anisotropic superexchange interaction and weak ferromagnetism", Physical Review **120**, 91 (1960).

[93]S. J. Poon and C. T. Ma., "Amorphous ferrimagnets: an ideal host for ultra-small skyrmions", Journal of Superconductivity and Novel Magnetism **33**, 269 (2019).

[94]T. Gilbert., "A phenomenological theory of damping in ferromagnetic materials", IEEE Transactions on Magnetics **40**, 3443 (2004).

[95]Z. Li and S. Zhang., "Domain-wall dynamics and spin-wave excitations with spin-transfer torques", Physical Review Letters **92**, 207203 (2004).

[96]A. Thiaville, Y. Nakatani, J. Miltat, and N. Vernier., "Domain wall motion by spin-polarized current: a micromagnetic study", Journal of Applied Physics **95**, 7049 (2004).

[97]S. Zhang and Z. Li., "Roles of nonequilibrium conduction electrons on the magnetization dynamics of ferromagnets", Physical Review Letters **93**, 127204 (2004).

[98]J. Sinova, S. O. Valenzuela, J. Wunderlich, C. H. Back, and T. Jungwirth., "Spin hall effects", Reviews of modern physics **87**, 1213 (2015).

[99]L. Meier, G. Salis, I. Shorubalko, E. Gini, S. Schön, and K. Ensslin., "Measurement of rashba and dresselhaus spin–orbit magnetic fields", Nature Physics **3**, 650 (2007).

[100]A. Manchon, H. C. Koo, J. Nitta, S. M. Frolov, and R. A. Duine., "New perspectives for rashba spin-orbit coupling", Nature Materials **14**, 871 (2015).

[101]S. Emori, U. Bauer, S.-M. Ahn, E. Martinez, and G. S. D. Beach., "Current-driven dynamics of chiral ferromagnetic domain walls", Nature Materilas **12**, 611 (2016).

[102]S.-H. Yang, K.-S. Ryu, and S. Parkin., "Domain-wall velocities of up to 750ms1 driven by exchange-coupling torque in synthetic antiferromagnets", Nature Nanotechnology **10**, 221 (2015).

[103]T. Okuno, D.-H. Kim, S.-H. Oh, S. K. Kim, Y. Hirata, T. Nishimura, W. S. Ham, Y. Futakawa, H. Yoshikawa, A. Tsukamoto, Y. Tserkovnyak, Y. Shiota, T. Moriyama, K.-J. Kim, K.-J. Lee, and T. Ono., "Spin-transfer torques for domain wall motion in antiferromagnetically coupled ferrimagnets", Nature Electronics **2**, 389 (2019).

[104]H. Awano., "Investigation of domain wall motion in re-tm magnetic wire towards a current driven memory and logic", Journal of Magnetism and Mgnetic Materials **383**, 50 (2015).

[105]M. Hayashi, L. Thomas, C. Rettner, R. Moriya, Y. B. Bazaliy, and S. S. P. Parkin., "Current driven domainwall velocities exceeding the spin angular momentum transfer rate in permalloy nanowires", Physical Review Letters **98**, 037204 (2007).

[106]M. Schöbitz, A. D. Riz, S. Martin, S. Bochmann, C. Thirion, J. Vogel, M. Foerster, L. Aballe, T. O. Menteş, A. Locatelli, F. Genuzio, S. Le-Denmat, L. Cagnon, J. C. Toussaint, and D. Gusakova., "Fast domain wall motion governed by topology and oersted fields in cylindrical magnetic nanowires", Physical Review Letters **123**, 217201 (2019).

[107]G. L. Doll, J. S. Speck, G. Dresselhaus, and M. S. Dresselhaus, "Intercalation of hexagonal boron nitride with potassium", Journal of Applied Physics **66**, 2544 (1989).

[108]D. S. Stone, K. B. Yoder, and W. D. Sproul, "Hardness and elastic modulus of tin based on continuous indentation technique and new correlation", Journal of Vacuum Science Technology A **9**, 2543 (1991).

[109]S. T. Oyama, *Introduction to the chemistry of transition metal carbides and nitrides* (Springer, Dordrecht, 1996), pp. 1–27.

[110]O. N. Carlson, *The n-si (nitrogen-silicon) system* (Springer, 1990-12), pp. 569–573.

[111]"Silicon nitride and related materials", **83**.

[112]I. Akasaki, H. Amano, M. Kito, and K. Hiramatsu, "Photoluminescence of mg-doped p-type gan and electroluminescence of gan p-n junction led", Journal of Luminescence **48-49**, 666–670 (1991).

[113]I.Akasaki, H.Amano, H.Murakami, M.Sassa, H.Kato, and K.Manabe, "Growth of gan and algan for uv/blue p-n junction diodes", Journal of Crystal Growth **128**, 379–383 (1993).

[114]T. Takeuchi, H. Takeuchi, S. Sota, H. Sakai, H. Amano, and I. Akasaki, "Optical properties of strained algan and gainn on gan", Japanese journal of applied physics **36**, L117 (1997).

[115]A. Jain, S. P. Ong, G. Hautier, W. Chen, W. D. Richards, S. Dacek, S. Cholia, D. Gunter, D. Skinner, G. Ceder, and K. A. Persson, "Commentary: the materials project: a materials genome approach to accelerating materials innovation", APL Materials **1**, 011002 (2013).

[116]M. Bykov, E. Bykova, G. Aprilis, K. Glazyrin, E. Koemets, I. Chuvashova, I. Kupenko, C. McCammon, M. Mezouar, V. Prakapenka, H.-P. Liermann, F. Tasnádi, A. V. Ponomareva, I. A. Abrikosov, N. Dubrovinskaia, and L. Dubrovinsky, "Fe-n system at high pressure reveals a compound featuring polymeric nitrogen chains", Nature Communications **9**, 1–8 (2018).

[117]I. Neklyudov and A. N. Morozov, "Formation and decay kinetics of nickel nitrides resulting from nitrogen ion implantation. the nickel–nitrogen phase diagram", Physica B: Condensed Matter **350**, 325–337 (2004).

[118]F. Takata1, K. Ito, S. Higashikozono, T. Gushi, K. Toko, and T. Suemasu, "Epitaxial growth and magnetic properties of nixfe4-xn (x = 0, 1, 3, and 4) films on srtio3(001) substrates", Journal of Applied Physics **120**, 083907 (2016).

[119]G. Shirane, W. J. Takei, and S. L. Ruby, "Mössbauer study of hyperfine fields and isomer shifts in fe4n and (fe,ni)4n", Physical Review **126**, 49 (1962).

[120]K. Ito, S. Higashikozono, F. Takata, T. Gushi, K. Toko, and T. Suemasu, "Growth and magnetic properties of epitaxial fe4n films on insulators possessing lattice spacing close to si(001) plane", Journal of Crystal Growth **455**, 66–70 (2016).

[121]S. Kokado, N. Fujima, K. Harigaya, H. Shimizu, and A. Sakuma, "Theoretical analysis of highly spin-polarized transport in the iron nitride fe4n", Physical Review B **73**, 172410 (2006).

[122]A. Narahara, K. Ito, T. Suemasu, Y. K. Takahashi, A. Ranajikanth, and K. Hono, "Spin polarization of fe 4 n thin films determined by point-contact andreev reflection", Applied Physics Letters **94**, 202502 (2009).

[123]Y. Komasaki, M. Tsunoda, S. Isogami, and M. Takahashi, "75% inverse magnetoresistance at room temperature in fe4n/mgo/cofeb magnetic tunnel junctions fabricated on cu underlayer", Journal of Applied Physics **105**, 07C928 (2009).

[124]C. T. Ma, T. Q. Hartnett, W. Zhou, P. V. Balachandran, and S. J. Poon, "Tunable magnetic skyrmions in ferrimagnetic mn4n", Applied Physics Letters **119**, 192406 (2021).

[125]T. Bayaraa, C. Xu, and L. Bellaiche, "Magnetization compensation temperature and frustration-induced topological defects in ferrimagnetic antiperovskite mn4n", Physical Review Letters **127**, 217204 (2021).

[126]Y. Imai, Y. Takahashi, and T. Kumagai, "Relations of electronic energies and magnetic moments of tetra-3d metal (mn, fe, co and ni) nitrides calculated using a plane-wave basis method", Journal of Magnetism and Magnetic Materials **322**, 2665–2669 (2010).

[127]N. Terao, "Une nouvelle forme du nitrure de nickel: ni4n", Journal of the Physical Society of Japan **15**, 227–230 (1960).

[128]G. J. W. R. Dorman and M. Sikkens, "Structure of reactively sputtered nickel nitride films", Thin Solid Films **105**, 251–258 (1983).

[129]M. Meinert, "Exchange interactions and curie temperatures of the tetrametal nitrides cr4n, mn4n, fe4n, co4n, and ni4n", Journal of Physics: Condensed Matter **28**, 056006 (2016).

[130]T. K. M. Takahashi Y. Imai, "Spin-polarized electronic band structures of the fe4n–co4n system", Journal of Magnetism and Magnetic Materials **323**, 2941–2944 (2011).

[131]K. Ito, T. Sanai, Y. Yasutomi, S. Zhu, K. Toko, Y. Takeda, Y. Saitoh, A. Kimura, and T. Suemasu, "X-ray magnetic circular dichroism for coxfe4xn (x = 0, 3, 4) films grown by molecular beam epitaxy", Journal of Applied Physics **115**, 17C712 (2014).

[132]K. Ito, T. Sanai, Y. Yasutomi, T. Gushi, K. Toko, H. Yanagihara, M. Tsunoda, E. Kita, and T. Suemasu, "Mössbauer study on epitaxial coxfe4xn films grown by molecular beam epitaxy", Journal of Applied Physics **117**, 17B717 (2015).

[133]A. Anzai, T. Gushi, T. Gushi, S. Honda, S. Isogami, and T. Suemasu, "Transition from minority to majority spin transport in iron-manganese nitride fe4 x mn x n films with increasing x", Journal of Applied Physics **124**, 123905 (2018).

[134]S. Isogami, A. Anzai, T. Gushi, T. Komori, and T. Suemasu, "Temperature independent, wide modulation of anomalous hall effect by mn doping in fe4 xmnxn pseudo-single-crystal films", Japanese Journal of Applied Physics **57**, 120305 (2018).

[135]D. Boldrin, A. P. Mihai, B. Zou, J. Zemen, R. Thompson, E. Ware, B. V. Neamtu, L. Ghivelder, B. Esser, D. W. McComb, P. Petrov, and L. F. Cohen, "Giant piezomagnetism in mn3nin", ACS Applied Materials and Interfaces **10**, 18863–18868 (2018).

[136]D. Boldrin, E. Mendive-Tapia, J. Zemen, J. B. Staunton, T. Hansen, A. Aznar, J.-L. Tamarit, M. Barrio, P. Lloveras, J. Kim, X. Moya, and L. F. Cohen, "Multisite exchange-enhanced barocaloric response in mn3nin", Physical Review X **8**, 041035 (2018).

[137]K. Asano, K. Koyama, and K. Takenaka, "Magnetostriction in mn3cun", Applied Physics Letters **92**, 161909 (2008).

[138]T. Shimizu, T. Shibayama, K. Asano, and K. Takenaka, "Giant magnetostriction in tetragonally distorted antiperovskite manganese nitrides", Journal of Applied Physics **111**, 07A903 (2012).

[139]T. Matsumoto, T. Hatano, T. Urata, K. Iida, K. Takenaka, and H. Ikuta, "Hall effect measurements of high-quality mn3cun thin films and the electronic structure", Physical Review B **96**, 205153 (2017).

[140]B. Y. Qu and B. C. Pan, "Nature of the negative thermal expansion in antiperovskite compound mn3znn", Journal of Applied Physics **108**, 113920 (2010).

[141]Y. Sun, C. Wang, Q. Huang, Y. Guo, L. Chu, M. Arai, and K. Yamaura, "Neutron diffraction study of unusual phase separation in the antiperovskite nitride mn3znn", Inorganic Chemistry **51**, 7232–7236 (2012).

[142]S. Deng, Y. Sun, L. Wang, Z. Shi, H. Wu, Q. Huang, J. Yan, K. Shi, P. Hu, A. Zaoui, and C. Wang, "Frustrated triangular magnetic structures of mn3znn: applications in thermal expansion", The Journal of Physcila Chemistry C **119**, 24983–24990 (2015).

[143]Y. Sun, C. Wang, Y. Wen, L. Chu, M. Nie, and F. Liu, "Negative thermal expansion and correlated magnetic and electrical properties of si-doped mn3gan compounds", Journal of the American Ceramic Society **93**, 650–653 (2010).

[144]D. Matusnami, A. Fujita, K. Takenak, and M. Kano, "Giant barocaloric effect enhanced by the frustration of the antiferromagnetic phase in mn3gan", Nature Materials **14**, 73–78 (2015).

[145]A. D. Mah, "The heats of combustion and formation of two manganese nitrides, mn5n2 and mn4n", Journal of the American Chemical Society **80**, 2954–2955 (1958).

[146]W. J. Takei, G. Shirane, and B. C. Frazer., "Magnetic structure of mn4n", Physical Review **119**, 122 (1960).

[147]W. J. Takei, R. R. Heikes, and G. Shirane, "Magnetic study on mn4n and its related compounds", Journal of the Physical Society of Japan **125**, 1893 (1962).

[148]M. Mekata, "Magnetic study on mn4n and its related compounds", Journal of the Physical Society of Japan **17**, 796–803 (1962).

[149]K. M. Ching, W. D. Chang, T. S. Chin, and J. G. Duh, "Anomalous perpendicular magnetoanisotropy in mn4n films on si(100)", Journal of Applied Physics **76**, 6582–6584 (1994).

[150]K.-M. Ching, W.-D. Chang, and T.-S. Chin, "Magnetic properties and structure of mn4n films on glass substrates", Journal of Alloys and Compounds **222**, 184–187 (1995).

[151]W. Li, R. Tanaka, T. Usami, T. Gao, T. Harumoto, Y. Nakamura, and J. Shi, "Growth of mn4n film with enhanced perpendicular magnetization on glass substrate using mno seed layer", Materials Letters **311**, 131615 (2022).

[152]S. Dhar, O. Brandt, and K. H. Ploog, "Ferrimagnetic mn4n(111) layers grown on 6h-sic(0001) and gan(0001) by reactive molecular-beam epitaxy", Applied Physics Letters **86**, 112504 (2005).

[153]Z. Zhang, Y. Cho, J. Singhal1, X. Li, P. Dang, H. Lee, J. Casamento, Y. Tang, H. G. Xing, and D. Jena, "Magnetic properties of mbe grown mn4n on mgo, sic, gan and al2o3 substrates", AIP Advances **10**, 015238 (2022).

[154]Y. K. S. Isogami N. Rajamanickam and Y. K. Takahashi, "Efficient current-driven magnetization switching owing to isotropic magnetism in a highly symmetric 111-oriented mn4n epitaxial single layer", AIP Advances **11**, 105314 (2021).

[155]S. Isogami, M. Ohtake, and Y. K. Takahashi, "Impact of b-doping on topological hall resistivity in (111)- and (110)-oriented mn4n single layers with the non-collinear spin structure", Journal of Applied Physics **131**, 073904 (2022).

[156]S. Isogami, K. Masuda, and Y. Miura., "Contributions of magnetic structure and nitrogen to perpendicular magnetocrystalline anisotropy in antiperovskite mn4n", Physical Review Materials **4**, 014406 (2020).

[157]E. Liu, Y. Sun, N. Kumar, L. Muechler, A. Sun, L. Jiao, S.-Y. Yang, D. Liu, A. Liang, Q. Xu, J. Kroder, V. Süß, H. Borrmann, C. Shekhar, Z. Wang, C. Xi, W. Wang, W. Schnelle, S. Wirth, Y. Chen, S. T. B. Goennenwein, and C. Felser, "Giant anomalous hall effect in a ferromagnetic kagome-lattice semimetal", Nature Physics **14**, 1125–1131 (2018).

[158]M. T. K. Kabara and S. Kokado., "Magneto-transport properties of pseudo-single-crystal mn4n thin films", AIP Advances **7**, 056416 (2017).

[159]D. Rosenblatt, M. Karpovski, and A. Gerber, "Reversal of the extraordinary hall effect polarity in thin co/pd multilayers", Applied Physics Letters **96**, 022512 (2010).

[160]D. Li, G. Wang, H. Li, S. Wu, and S. Li, "Anomalous hall effect with variable-range hopping in mn4-xauxn (x = 0, 0.5) epitaxial films", Materials Research Bulletin **122**, 110646 (2020).

[161]K. Ito, K. Toko, Y. Takeda, Y. Saitoh, T. Oguchi, T. Suemasu, and A. Kimura, "Local electronic states of fe4n films revealed by x-ray absorption spectroscopy and x-ray magnetic circular dichroism", Journal of Applied Physics **117**, 193906 (2015).

[162]J.-S. Kang, G. Kim, H. J. Lee, D. H. Kim, H. S. Kim, J. H. Shim, S. Lee, H. Lee, J.-Y. Kim, B. H. Kim, and B. I. Min, "Soft x-ray absorption spectroscopy and magnetic circular dichroism study of the valence and spin states in spinel mnfe2o4", Physical Review B **77**, 035121 (2008).

[163]K. Amemiya, E. Sakai, D. Matsumura, H. Abe, and T. Ohta, "Anomalous behavior of satellite features at the surface and interface in the ni l-edge x-ray absorption spectra", Physical Review B **72**, 201404(R) (2005).

[164]C. T. C. N. V. Smith, F. Sette, and L. F. Mattheiss, "Relativistic tight-binding calculations of x-ray absorption and magnetic circular dichroism at the l2 and l3 edges of nickel and iron", Physical Review B **46**, 1023 (1992).

[165]T. Kaneyoshi, "The possibility of two compensation points in a decorated ferrimagnetic ising system", Journal of the Physical Society of Japan **70**, 884–888 (2001).

[166]Z. W. H. G. Zhang, E. K. Liu, W. H. Wang, M. Yue, and G. H. Wu, "Site preference and compensation behavior in co(cr, mn)2o4 system", Journal of Applied Physics **117**, 17B735 (2015).

[167]R. Zhang, Y. He, D. Fruchart, J.M.D.Coey, and Z. Gercsi, "Rare-earth-free noncollinear metallic ferrimagnets mn4-xzxn with compensation at room temperature", Acta Materialia **234**, 118021 (2022).

[168]K. Garello, C. O. Avci, I. M. Miron, M. Baumgartner, A. Ghosh, S. Auffret, O. Boulle, G. Gaudin, and P. Gambardella, "Ultrafast magnetization switching by spin-orbit torques", Applied Physics Letters **105**, 212402 (2014).

[169]S. Fukami, T. Anekawa, C. Zhang, and H. Ohno, "A spin–orbit torque switching scheme with collinear magnetic easy axis and current configuration", Nature Nanotechnology **11**, 621–625 (2016).

[170]D. Fruchart, D. Givord, P. Convert, P. l'Heritier, and J. P. Senateur., "The non-collinear component in the magnetic structure of mn4n", Physical Review **9**, 2431 (1979).

[171]T. Hirose, T. Komori, T. Gushi, K. Toko, and T. Suemasu., "Perpendicular magnetic anisotropy in ferrimagnetic mn4n films grown on (laalo3)0.3(sr2taalo6)0.7(0 0 1) substrates by molecular beam epitaxy", Journal of Crystal Growth **535**, 125566 (2020).

[172]T. Hirose, T. Komori, T. Gushi, A. Anzai, K. Toko, and T. Suemasu, "Strong correlation between uniaxial magnetic anisotropic constant and in-plane tensile strain in mn4n epitaxial films", AIP Advances **10**, 025117 (2020).

[173]M. KAWASAKI, K. TAKAHASHI, T. MAEDA, R. TSUCHIYA, M. SHINOHARA, O. ISHIYAMA, T. YONEZAWA, M. YOSHIMOTO, and H. KOINUMA., "Atomic control of the srtio3 crystal surface", Science **266**, 1540 (1994).

[174]H. Okamoto., "Comment on mn-n (manganese-nitrogen)", Journal of Phase Equilibria **15**, 451 (1994).

[175]Y. JunChang and S.-h. Phark., "Atomic-scale visualization of initial growth of perovskites on srtio3(001) using scanning tunneling microscope", Current Applied Physics **17**, 640 (2017).

[176]M. Tsunoda, K. Kabara, and S. Kokado., "Galvanomagnetic Effects of Antiperovskite-Type Transition Metal Nitride Thin Films", Magnetics Japan **11**, 125 (2016).

[177]S. Kokado and M. Tsunoda, "Anisotropic magnetoresistance effect: general expression of amr ratio and intuitive explanation for sign of amr ratio", Advanced Materials Research **750**, 978–982 (2013).

[178]S. Kokado, M. Tsunoda, K. Harigaya, and A. Sakuma., "Anisotropic magnetoresistance effects in fe, co, ni, fe4n, and half-metallic ferromagnet: a systematic analysis", Journal of the Physical Society of Japan **81**, 024705 (2012).

[179]W. Döring., "Dependence of resistance of ni crystals on direction of spontaneous magnetization", Ann. Physik **32**, 259–276 (1938).

[180]S. Kokado and M. Tsunoda, "Twofold and fourfold symmetric anisotropic magnetoresistance effect in a model with crystal field", Journal of the Physical Society of Japan **84**, 094710 (2015).

[181]N. Nagaosa, J. Sinova, S. Onoda, A. H. MacDonald, and N. P. Ong, "Anomalous hall effect", Reviews of Modern Physics **82**, 1539 (2007).

[182]R. Karplus and J. M. Luttinger., "Hall effect in ferromagnetics", Physical Review **95**, 1154 (1954).

[183]F. D. M. Haldane., "Berry curvature on the fermi surface: anomalous hall effect as a topological fermi-liquid property", Phsical Review Letters **93**, 206602 (2004).

[184]X. Wang, D. Vanderbilt, J. R. Yates, and I. Souza., "Fermi-surface calculation of the anomalous hall conductivity", Phsical Review B **76**, 195109 (2007).

[185]J. Smit, "The spontaneous hall effect in ferromagnetics i", Physica **21**, 877–887 (1955).

[186]J. Smit, "The spontaneous hall effect in ferromagnetics ii", Physica **21**, 39–51 (1958).

[187]L. Berger, "Side-jump mechanism for the hall effect of ferromagnets", Physical Review B **2**, 4559 (1970).

[188]V. L. Grigoryan, J. Xiao, X. Wang, and K. Xia, "Anomalous hall effect scaling in ferromagnetic thin films", Physical Review B **96**, 144426 (2017).

[189]Y. Tagawa and K. Motizuki, "Electronic band structures and magnetism of intermetallic manganese compounds mn4x (x identical to n, c)", Journal of Phyics: Condensed Matter **3**, 1753 (1991).

[190]G. Kresse and J. Hafner, "Ab initio molecular dynamics for liquid metals", Physical Review B **47**, 558(R) (1993).

[191]G. Kresse and D. Joubert, "From ultrasoft pseudopotentials to the projector augmented-wave method", Physical Review B **59**, 1758 (1999).

[192]K. B. John P. Perdew and M. Ernzerhof, "Generalized gradient approximation made simple", Physical Review Letters **77**, 3865 (1996).

[193]H. Kontani, T. Tanaka, and K. Yamada, "Intrinsic anomalous hall effect in ferromagnetic metals studied by the multi-d-orbital tight-binding model", Physical Review B **75**, 184416 (2007).

[194]T. Miyasato, N. Abe, T. Fujii, A. Asamitsu, S. Onoda, Y. Onose, N. Nagaosa, and Y. Tokura, "Crossover behavior of the anomalous hall effect and anomalous nernst effect in itinerant ferromagnets", Physical Review Letters **99**, 086602 (2007).

[195]J. S.-Y. Feng, R. D. Pashley, and M.-A. Nicolet, "Magnetoelectric properties of magnetite thin films", Journal of Physics C: Solid State Physics **8**, 1010 (1975).

[196]S. Sangiao, L. Morellon, G. Simon, J. M. D. Teresa, J. A. Pardo, J. Arbiol, and M. R. Ibarra, "Anomalous hall effect in fe (001) epitaxial thin films over a wide range in conductivity", Physical Review B **79**, 014431 (2009).

[197]Y.-C. Lau and M. Hayashi, "Spin torque efficiency of ta, w, and pt in metallic bilayers evaluated by harmonic hall and spin hall magnetoresistance measurements", Japanese Journal of Applied Physics **56**, 0802B5 (2017).

[198]S. Hasegawa, "Reflection high-energy electron diffraction", Characterization of Materials **97**, 1925–1938 (2012).

[199]K. Wang, M. H. Tang, Y. Xiong, G. Li, Y. G. Xiao, W. L. Zhang, Z. P. Wang, Z. Li, and J. He, "Epitaxial growth and magnetic/transport properties of la0.7sr0.3mno3 thin films grown on srtio3 with optimized growth conditions", RSC Advances **7**, 31327–31332 (2017).

[200]D. Choi and K. Barmak, "On the potential of tungsten as next-generation semiconductor interconnects", Electronic Materials Letters **13**, 449–456 (2017).

[201]A. Chattaraj, M. Balal, A. K. Yadav, S. R. Barman, A. K. Sinha, S. N. Jha, S. Joulie, V. Serin, A. Claverie, V. Kumar, and A. Kanjilal, "Unravelling oxygen driven to phase transformation in tungsten", Scientific Reports **10**, 1–10 (2020).

[202]J.-S. Lee, J. Cho, and C.-Y. You, "Growth and characterization of and -phase tungsten films on various substrates", Journal of Vacuum Science and Technology **34**, 021502 (2016).

[203]P. F. Ladwig, Y. A. Chang, E. S. Linville, A. Morrone, J. Gao, B. B. Pant, A. E. Schlutz, and S. Mao, "Paramagnetic to antiferromagnetic phase transformation in sputter deposited pt–mn thin films", Journal of Applied Physics **94**, 979 (2003).

[204]Y. C. Y, I. M. Sung, and B. K. Joe, "Analytic expression for the temperature of the current-heated nanowire for the current-induced domain wall motion", Applied Physics Letters **89**, 222513 (2006).

[205]H. Fangohr, D. S. Chernyshenko, M. Franchin, T. Fischbacher, and G. Meier, "Joule heating in nanowires", Physical Review B **84**, 054437 (2011).

[206]M. Neupane, S.-Y. Xu, R. Sankar, Q. Gibson, Y. J. Wang, I. Belopolski, N. Alidoust, G. Bian, P. P. Shibayev, D. S. Sanchez, Y. Ohtsubo, A. Taleb-Ibrahimi, S. Basak, W.-F. Tsai, H. Lin, T. Durakiewicz, R. J. Cava, A. Bansil, F. C. Chou, and M. Z. Hasan, "Topological phase diagram and saddle point singularity in a tunable topological crystalline insulator", Physical Review B **92**, 075131 (2015).